Quantitative spectral analyses of blue horizontal branch stars

Master's Thesis in Physics

Presented by

Steven Hämmerich

15.01.2020

Dr. Karl Remeis-Observatory
Friedrich-Alexander-Universität Erlangen-Nürnberg

Supervisor: Prof. Dr. Ulrich Heber

”Life is about learning; when you stop learning, you die.”
-Tom Clancy-

Abstract

The horizontal branch is a prominent feature in the Hertzsprung-Russell diagram. Those stars have evolved from the main-sequence and through the red giant branch. Now they are fueled by helium burning in their cores. The blue part, called blue horizontal branch (BHB), is of particular interest spanning a wide temperature range between 8000 K and 20000 K, therefore being found among the spectral types A and B. BHBs are most prominently found in globular clusters (GCs) where they have been studied extensively and show abundance anomalies. Discontinuities in the color magnitude diagrams are found along the BHB. The first jump occurring at an effective temperature of 11500 K separates the A-type and B-type BHBs and is being associated with the transition from convective to radiative atmospheres as well as the on-set of atomic diffusion. A second gap at 20000 K is due to the extinction of hydrogen shell burning and the HeII-convection zone reaching the stellar surface. However, BHBs also exist in the Galactic field but have rarely been studied, although some are much brighter than their siblings in the distant GCs.

In order to further characterize the properties of BHBs in the Galactic field the sample of stars has to be studied in more detail for a large number of stars to allow a detailed comparisons between the field and GC-population to be made. Such investigations will also help to shed more light on long standing questions connected to the morphology of the HB or diffusion. Finally, they will provide important insight into stellar evolution of evolved objects found in different environments.

Only a few stars have been studied before in detail but the analyses were mostly limited to very few elements. In order to increase the number of stars quantitative spectral analyses of potential BHB stars are performed which were chosen from a kinematically selected sample of high resolution spectra. The sets of data are of unprecedented high quality, with respect to signal-to-noise ratio (SNR $\approx$ 200), spectral resolution (R$\sim$ 42000), and wavelength coverage. This allows us to obtain accurate atmospheric parameters and complete abundance patterns. The observations are matched to grids of model spectra computed using a hybrid LTE/NLTE approach into which 22 different elements ranging from helium up to yttrium are incorporated with NLTE-model atoms as well as LTE-line lists. Further, using these results the spectral energy distributions are analyzed ultimately giving the stellar parameters radius, mass, and luminosity. Finally, the orbits of the stars are calculated for three different Milky Way mass models. Accordingly, the stars can be classified based on their atmospheric and stellar parameters, their abundances and the

kinematic characteristics.
The stars studied cover both spectral types A and B and the majority of them can be classified as BHB-stars, however, more peculiar objects could be misclassified as BHBs when only taking one of these steps into account. The abundance patterns derived are different between the spectral types. Helium is found to be around the solar level in A-stars, while it clearly is deficient in the B-type stars which also show a strong enrichment of the ^{3}He isotope due to diffusion acting differently on the isotopes, as well as vertical stratification of the helium content. The abundances of all metals in the A-type stars are below solar and scaling the abundances with iron results in a similar pattern, indicating that iron is a good proxy for the overall metallicity. However, when compared to the solar ratios they vary from star to star, therefore, indicating that the composition and, hence, also the abundance patterns of A-BHB-stars are very different from the solar standard. Amongst the B-stars overabundances of several metals are found, with a slight increase towards heavier elements. The overall abundance pattern, also when considering the elements-to-iron ratios, is very similar to the one observed for subdwarf-stars of spectral type B (sdB) which populate the extreme horizontal branch with effective temperatures even higher than the BHB-stars. This hints at diffusion acting similarly in B-BHBs and sdBs. However, a very prominent difference to the sdBs is an enrichment in phosphorus. Generally the abundances agree with the predictions of diffusion models. The stellar parameters are mostly in agreement with the sample stars being on the HB, however, a few have masses that deviate from normal HB-stars, being either too high or too low. The kinematic analyses using three different Galactic mass models agree well with each other, showing the results to be independent of the mass model used. The A-BHBs all show halo kinematics whereas the B-BHBs predominately belong to the disk. Four peculiar objects include a potentially high mass HB-star, a halo B-BHB, a possible extremely low mass (ELM) helium white dwarf, and a post-HB-star or helium enriched population HB-star.
The analyses presented here are much more detailed and precise than all other published analyses (except for Feige 86). A comparison to the GC-population as well as to other BHB-stars in the field is, therefore, limited, in particular with respect to the chemical abundance pattern. Nevertheless, the results compare favorably to both for the Galactic field and for GCs within errors limits.
The results presented pave the way for future analyses of additional BHBs from the same observational sample or other programs. They show that choosing a similar approach using all kinds of different data and analysis-techniques is suited best for future studies as it allows to determine the evolutionary status of the stars in a robust manner.

Table of Contents

List of Tables

List of Figures

1

Blue horizontal branch stars

During the 17th century the first globular clusters were discovered. Herschel later on was the first astronomer to use this name for these interesting objects. Globular clusters were the first groups of stars in which so called horizontal branch stars were found. In 1900 Barnard noted the presence of stars which were brighter at bluer colors than in the optical. 15 years later Shapley found two color peaks in his data obtained for the globular cluster M 3, one in the red and the other in the blue, the later one at fainter magnitudes. Based on this data ten Bruggencate produced the first color-magnitude diagrams, in which the apparent magnitude of a star is plotted against a color index. In these diagrams ten Bruggencate discovered the presence of a horizontal line at a constant magnitude, therefore calling it the horizontal branch. Subsequently this structure was detected in many more globular clusters (Moehler 2001). However, the physical nature of these stars remained a mystery until later on Hoyle and Schwarzschild (1955) identified the horizontal branch as stars burning helium in their cores. During the same decade the counterparts of these stars were detected in the Galactic field as well. With the introduction of large photometric and spectroscopic surveys the number of stars known to be part of the horizontal branch has increased significantly, so has our knowledge about them, but at the same time more and more new questions dealing with theses stars have come up.

One subset of the horizontal branch is the so called blue horizontal branch. These stars occupy a distinct temperature range and have very interesting properties which can not be fully explained by theory yet (Heber 2016).

This chapter will serve as an introduction to the basic physics of blue horizontal branch stars. First, this group will be discussed in context of the stellar evolution and the other parts of the horizontal branch will also be considered. Secondly, the main properties will be summarized.

Reviews used and covering the main-topics addressed in this chapter include: Catelan (2009); Heber (2016); Gratton et al. (2019).

1.1 Blue horizontal branch stars in the context of stellar evolution and the horizontal branch

1.1.1 Stellar evolution

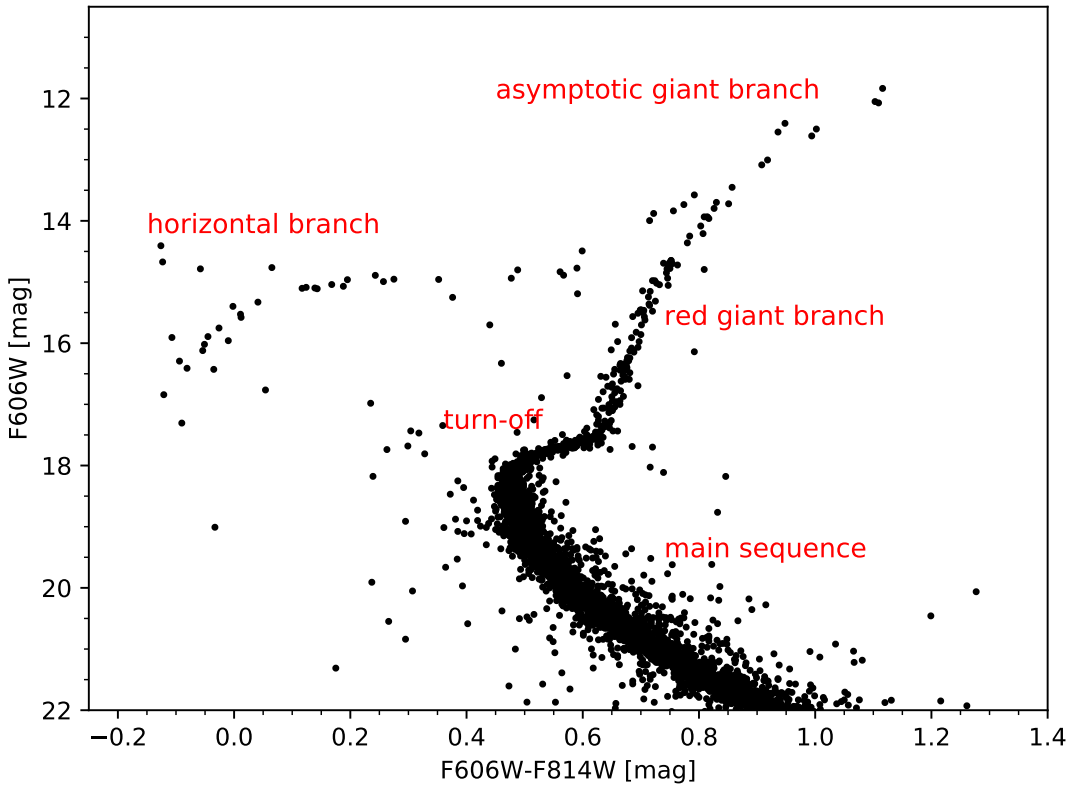

Figure 1.1: Color-magnitude diagram of M 5 using HST-data from the Advanced Camera for Surveys (ACS) Survey of Galactic Globular Clusters (Sarajedini et al. 2007) database [1]

The color-magnitude diagram (CMD) is a powerful instrument for visualizing stellar evolution. In a CMD the apparent magnitude is plotted against a color index, a mathematical expression involving the apparent magnitudes observed with various wavelength filters. Different filter-systems cover different wavelength-ranges. A particularly important system is implemented in the instrumentation of the Hubble space telescope[2] which is also used for the CMDs shown in this chapter. Stars in different evolutionary stages occupy distinct regions in the CMD and those of globular clusters (GC) are especially

[1] https://users.astro.ufl.edu/~ata/public_hstgc/databases.html (last accessed: 11/22/2019, 5:10pm)
[2] http://www.stsci.edu/hst/wfc3/ins_performance/ground/components/filters (last accessed: 01/10/2020, 2:00pm)

suited to illustrate the basic ideas and stages of stellar evolution since all the stars in these objects are assumed to have formed at about the same time compared to the ages of GCs. The different stages can be seen in the CMD of the GC M 5 (Fig.1.1).
Stars form from collapsing interstellar clouds and once fusion of hydrogen to helium sets in within the core of the collapsed proto-star and stable conditions are established, stars are on the main sequence (MS). Stars on the MS generate energy through net-fusion of hydrogen to helium, but stars on the upper MS (>1.15 $M_\odot$) primarily use the so called CNO-cycle, in which carbon, oxygen, and nitrogen are used as intermediaries, in convective cores, whereas stars on the lower MS (<1.15 $M_\odot$) fuse hydrogen to helium through proton-proton chains in radiative cores. Many factors such as metallicity or the age of a stellar population have an impact on the morphology of the MS and all the subsequent phases. Stars born with higher stellar masses are brighter than the low mass ones and evolve faster. In general stars on the MS show an increase in luminosity due to the changes in composition in their interior. The MS is the longest phase of stellar evolution ranging from 10 Myr for high mass stars up to many Gyrs at the low-mass end. Once the hydrogen reservoir in the stellar core is exhausted, hydrogen fusion starts in a shell surrounding the core. Hence, energy production in the core drops causing a contraction which also causes the envelope to expand. Therefore, the star leaves the MS and its position in the CMD changes. The next phase is known as the red giant branch (RGB) phase. Since the surface temperature drops RGB-stars will appear redder. As stars ascend the RGB the helium-core will grow due to the outwards traveling hydrogen burning shell, hence becoming more massive, denser, and heating up. This phase is characterized by the presence of stellar winds. A fraction of stars will not be able to evolve to the next stage due to mass loss and will evolve directly to the white dwarf (WD) cooling sequence which is not visible in the CMD shown in Fig. 1.1.
Once conditions in the core, which is stabilized by electron degeneracy in stars with masses up to 2.3 $M_\odot$, are suited for fusion of helium to carbon and oxygen via the triple-alpha process, the next stage of fusion in the core sets in. This will occur after approximately a billion years spent on the RGB as the star reaches the tip of the branch. Helium burning is ignited in the so called helium-flash in these stars, leading to a enormous release of energy, a strong rise in temperature lifts the degeneracy and allows the core to expand, and stars will move to the horizontal branch (HB). Here they will remain for about 100 Myr. Additionally, the stars will also fuse hydrogen to helium in a shell around the helium-burning core depending on the mass of the hydrogen envelope. Therefore, stars will end up on different parts among the HB. These parts will be discussed in detail later on. Only lower mass stars are able to reach this stage via helium-flash as the cores of stars more massive than 2.3 $M_\odot$ are not electron-degenerate and therefore ignite helium burning quietly as the central temperature rises. These stars will move away from the RGB in loops moving to bluer colors and higher luminosities. For higher stellar masses these loops will be more extended. These stars now form the so called helium main sequence which has a similar slope as the MS, but is located very close to the RGB. Therefore, it is not observationally visible in the CMD. Even more massive stars $\geqslant$10 $M_\odot$ do not go through a HB or loop phase.
A second giant phase, the asymptotic giant branch (AGB) phase, occurs once helium in

the core is exhausted. The carbon-oxygen core is now surrounded by a helium-burning shell. Depending on the mass a hydrogen burning shell can be found atop the helium-burning shell and as these shells advance outwards stars ascend the AGB. During this phase significant mass loss occurs, for example through strong stellar winds, and series of thermal pulses caused by a thermally instable configuration. Lower mass stars are not able to ignite another stage of fusion in their cores and will eventually shed their envelopes forming a planetary nebula and end up as WDs. Stars more massive than 8 $M_\odot$ are able to reach further stages of fusion in their cores as they ascend the AGB. The cores of these stars will eventually collapse after the last possible stage of fusion is completed, resulting in a supernova, leaving a neutron star or black hole, depending on the mass and a few other factors. Such massive stars do no longer exist in populations such as GCs because they evolve quickly. Their progeny, however, is abundant in GCs, in particular WDs, but also neutron stars are found as pulsars and even a stellar black hole has been discovered recently (Giesers et al. 2018).
Another type of star, so called blue stragglers (BS), are visible in CMDs. These stars do not fit into the presented picture of single star stellar evolution. BS are stars brighter and bluer than the rest of the MS and therefore appear as extensions of the MS above the turn-off, hence can be found between the MS turn-off and the HB. It is not yet fully understood how BS are produced, but they have to undergo some kind of interaction. They either originate from binary or multiple star systems and are either produced by mass transfer or are formed through stellar mergers and collisions. Therefore, they will appear younger than the rest of their population. (Prialnik 2000; Boer and Seggewiss 2008)

1.1.2 Globular clusters

Globular clusters are compact, dense (stellar densities of up to 10^5 $M_\odot$ pc^{-3}) and spherical groups of stars and may contain between a few hundred-thousands up to a million stars. Classically a GC is characterized as being compact with typical radii of a few tens of pc and being spherical, due to the gravitational potential (Meylan and Heggie 1997). Their ellipticities are lower than those of elliptical galaxies. This is probably due to the rotation of the cluster and as all GCs show this phenomenon it is most likely linked to their formation (Kamann et al. 2018). Some GCs exhibit one very distinctive feature: a compact core region with high stellar densities (Freeman and Norris 1981). This core region is produced by the internal kinematics of the cluster. In GCs mass segregation is active, which means that due to interactions more massive stars move closer to the core and the less massive ones move outwards. They can also be lost by the GC, therefore, GCs will lose a significant amount of their initial mass. As a consequence of this the core will shrink over time. The core collapse can be staled through additional energy sources, such as the break-up of binary-systems (Ivanova et al. 2005). Another striking characteristic is their age. GCs are very old objects, typically 10 Gyrs or older (Gratton et al. 2004; Krauss and Chaboyer 2003). Generally the stars in GCs are thought to have formed at the same time with similar initial chemical compositions. Since stellar evolution is a slow process from a human viewpoint, it is crucial to study large samples

of stars to test stellar evolution models. Since stars in GCs are thought to have formed under the same conditions at the same time and GCs are very old objects and therefore contain stars in many different evolutionary stages, they from a laboratory for studying stellar evolution.
The Milky Way (MW) contains at least 150 GCs distributed spherically around the Galactic center with center-distances of up to $\sim$ 100 kpc. They are the most prominent objects of the Galactic halo. GCs are found in many other galaxies in the Local group and beyond as well (Harris and Racine 1979). In the MW they exist in the halo, the thick disk and the bulge, but are absent in the thin disk. The role of GCs in the formation of the Galaxy is not fully understood, but as they are old their formation pre-dates most of the stellar formation in the Galaxy. GCs have been linked to galaxy-formation directly as possible building blocks of galaxies, but they also could have formed at the same time as their host galaxies through the same mechanisms which produce other clusters. GCs could also effectively form through galaxy mergers, which produce shock-waves and over-densities. Additionally other scenarios suggest that GCs might also have been acquired from other galaxies or may be stripped cores of dwarf galaxies, as proposed for ω Cen (this GC can be seen in Fig. 1.2) (Krauss and Chaboyer 2003; Giesers 2019). Recent results suggest that only 40% of the MW GCs formed within the MW, and that the remaining were acquired from other dwarf galaxies or result from merger-events (Massari et al. 2019).
Mostly GCs are metal-poor, which is consistent with the picture of them being old. The metallicity of a cluster is linked to its age, where the older clusters have lower metaillicities than the younger ones, and to its position within the Galaxy, as the metal-rich ones tend to belong to the disk. Generally stars in a GC have a relatively small spread in metallicity compared to stars within the galactic field.
However, when taking a closer look this very simple picture is not accurate, GCs are in fact very complex systems and many objects classified as such are only classified based on a few criteria. GCs are known to show chemical inhomogeneities such as correlations and anti-correlations between the abundances of different elements, e.g. the very prominent Na-O anticorrelation among GCs HB-stars (Gratton et al. 2015). These chemical peculiarities can not be explained by the very simple picture of a GC containing only one population of stars and by effects of nucleosynthesis alone. Especially the presence of correlations between light elements prove the presence of multiple populations within GCs. This is also backed up by the fact that multiple sequences are visible in CMDs, e.g. ω Cen having multiple MSs with different metallicities (Villanova et al. 2007). Since chemical inhomogeneities are such a striking characteristic of GCs it has been proposed to use them to classify GCs. In this picture GCs would be intermediate objects between smaller stellar clusters and small compact galaxies.

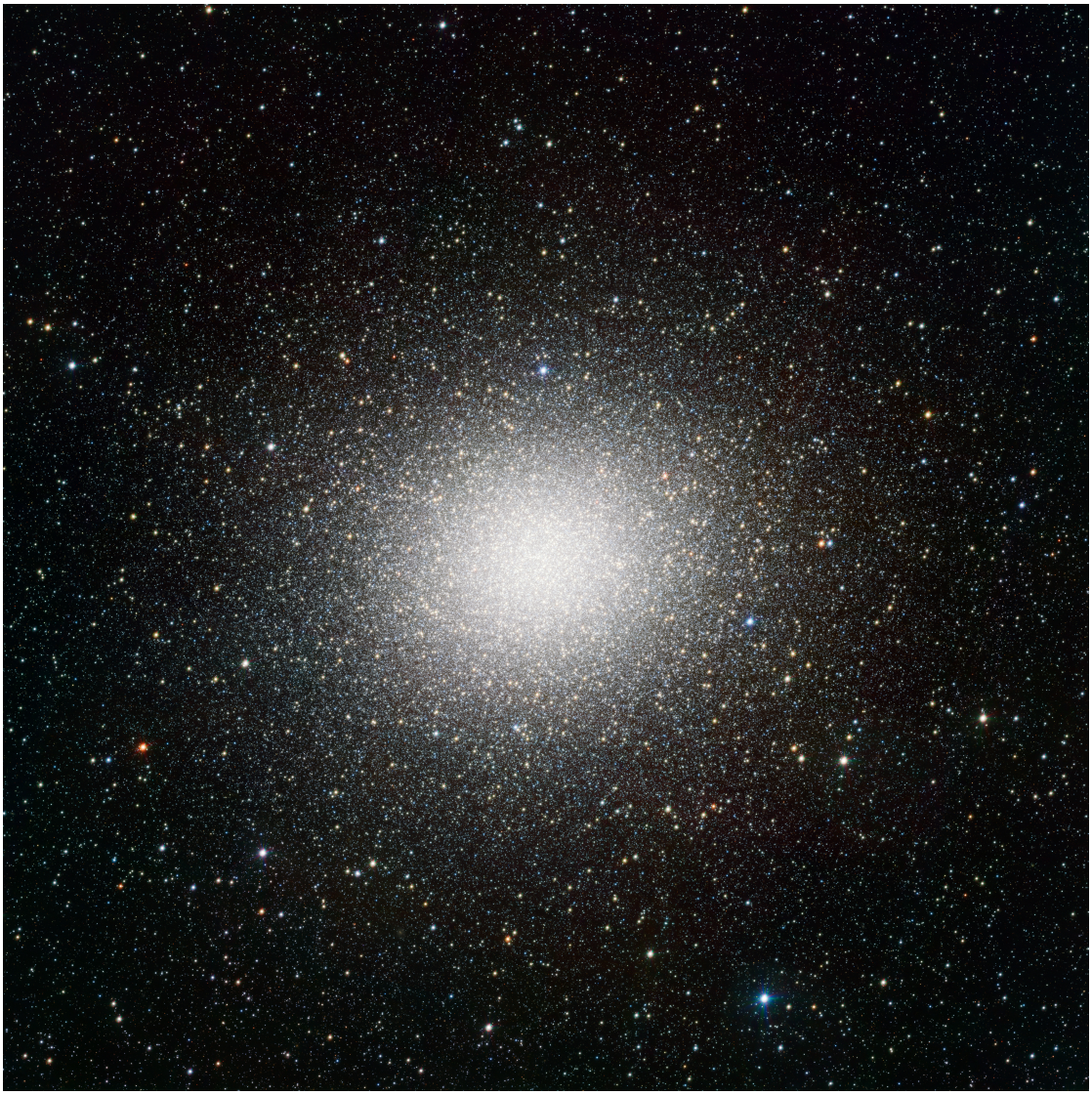

Figure 1.2: Globular cluster ω Cen [3]

[3] https://cdn.eso.org/images/publicationjpg/eso1119b.jpg (last accessed: 11/20/2019, 6:50pm)

1.1.3 The horizontal branch

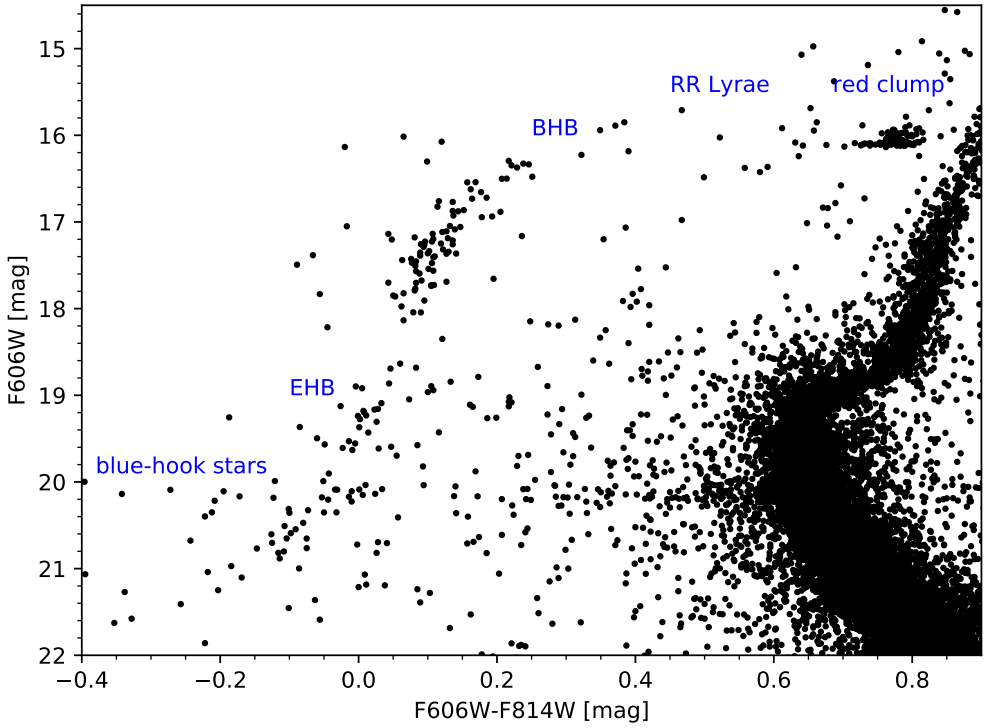

Figure 1.3: CMD of GC NGC 2808 showing the different groups of HB-stars (data from ACS Survey (Sarajedini et al. 2007))

The HB is of special interest since this horizontal feature occurring at a constant brightness allows to determine the distance of GCs and it is important for stellar evolution. It is spread over a wide range of colors, ranging from red to blue parts. Stars on the HB burn helium in their cores. (Brown et al. 2001)
The HB is home to many different kinds of stars. Classically the HB is divided into two parts, the blue and red HB, which parts are separated by the RR Lyrae gap. A classification of GCs builds on the ratio of stars redder than the RR Lyrae gap to that of stars bluer than it. The reddest and therefore coolest group of stars on the HB are the red clump stars. Red clump stars have effective temperatures of about 5,000 K and their name originates from these stars clustering in a rather small area next to the RGB. At slightly smaller masses and in a fainter horizontal structure connected to the clump one can find the red HB-stars. This particular group could also be the offspring of BS-stars. RR Lyrae stars are slightly hotter than the red clump and pulsate, as part of the HB RR Lyrae stars present one of the most long-lived phase of pulsation in stellar evolution. A present relation between the pulsation period and their brightness makes RR Lyrae stars primary tools to determine distances. Moving to bluer colors and higher effective temperatures the so called blue horizontal branch stars (BHB) can be found

staring at the blue end of the RR Lyrae strip. BHB-stars span a vast range of effective temperatures ranging from $\sim$ 8,000 K up to about 20,000 K. In literature they are often divided according to their spectral types, with the cooler end of the BHB corresponding to spectral type A stars, therefore being referred to as HBA stars. Consequently the hotter part of the BHB is also sometimes called the HBB since these stars correspond to a late B type spectral class. The next part in the sequence is the extreme or extended horizontal branch (EHB). These stars can reach temperatures of up to 35,000 K. In contrast to the BHB, stars on the EHB do not have a hydrogen-burning shell. The most extreme objects temperature-wise on the HB can be found among the so called blue-hook (BH) stars, reaching effective temperatures of 60,000 K and higher. (Boer and Seggewiss 2008)

In consequence, the HB is a temperature sequence of the offspring of low mass stars after going through the RGB phase. As stars move up the RGB their helium cores grow and it is expected that the conditions under which helium burning sets in is directly linked to the core mass for electron-degenerate conditions. Once the helium core reaches a mass of approximately $\sim$ 0.5 $M_\odot$ helium burning kicks in and stars move to the HB. Therefore, stars on the HB all share a similar core mass. But since the HB is clearly a sequence of stars with different positions in the CMD something has to be different between the observed groups. One difference between the stars on the HB is their overall mass. Since the core masses are all similar throughout the HB, the HB must be a sequence of envelope mass. The hydrogen-envelope mass decreases with increasing temperature. Red clump stars have the highest envelope mass. The hydrogen envelopes of BHB-stars are massive enough to sustain hydrogen shell burning, the EHB-stars on the contrary are not able to sustain shell burning. The EHB and BH stars have extremely small or no hydrogen-envelopes at all. This also means that the atmospheric parameters and structures of stars among the HB are fundamentally different. (Brown et al. 2001; Dorman 1992)

Since the HB is a sequence of envelope mass this means that mass-loss effects on the RGB have to occur in order to produce the different groups. The differences between the groups are a direct consequence of how much mass is removed before the star moves to the HB. The details of the obviously occurring mass loss are not understood. It is possible that the same mass-loss process is able to remove different amounts of the hydrogen envelope in order to produce the different groups, but the groups could also be produced by different processes each.

The nomenclature presented here refers to the HB stars observed in GCs, but all the different groups have counterparts in other populations, especially in the Galactic field. The Galactic field refers to stars which are not part of GCs, but field stars may be part of the disk or halo. In the field the EHB and blue-hook stars are referred to as sub-dwarfs of spectral types B and O (sdB and sdO). Differences between the GC and the field populations will be discussed later on.

1.1.4 Morphological structure of the horizontal branch

In a single population not every single group of HB-stars has to be present. Some parts of the HB are absent in some GCs or they are less prominent. After all the HB morphology seems to depend on a few different parameters and is not as fixed as the previous section might make it seem. This subsection will deal with the influence of the population first and then shift the focus to differences and distinctions between the groups introduced in the previous section. These groups are not distinguished randomly from each other, but are separated by gaps, jumps, and discontinuities in the CMD. In order to understand those gaps, the main aspects governing them, the structure of the stellar atmosphere and atomic diffusion will be discussed separately and in a very general way. Then the discussed processes will be put into context with the different gaps in the CMD.

1.1.4.1 The second parameter problem

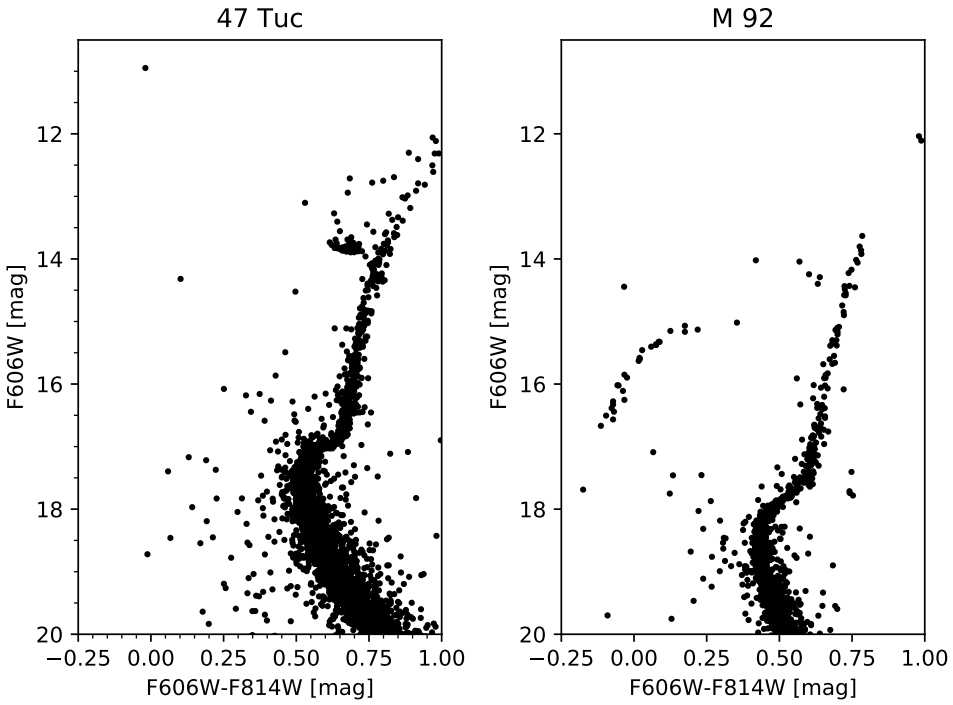

Figure 1.4: CMDs of the GCs 47 Tuc and M 92 (data from ACS Survey (Sarajedini et al. 2007))

The morphology of the HB differs from cluster to cluster. Not all groups are found in all the globular clusters. This gives rise to the question which parameters influences the morphology. Figure 1.4 shows the CMDs of the GCs 47 Tuc and M 92, clearly M 92s HB shows many stars on the blue parts of the HB, especially the BHB and EHB seem to be very prominent in this cluster, and in fact the red parts seem to be missing or these

regions are significantly less populated. 47 Tuc on the other hand lacks the blue parts but shows a pronounced red clump. 47 Tuc is a young metal-rich GC, while M 92 is metal-poor, as can be seen in the iron abundance[4]. The metallicity of 47 Tuc is almost two orders of magnitude higher than the value of M 92, -0.72 dex for 47 Tuc and -2.31 dex for M 92 [5](Harris 1996). This example shows that metallicity is one of the main factors governing the morphology of the HB. Since the metallicity was the first obvious parameter influencing the HB it is often referred to as the first parameter, but as the next comparison shows it can not be the only relevant factor.

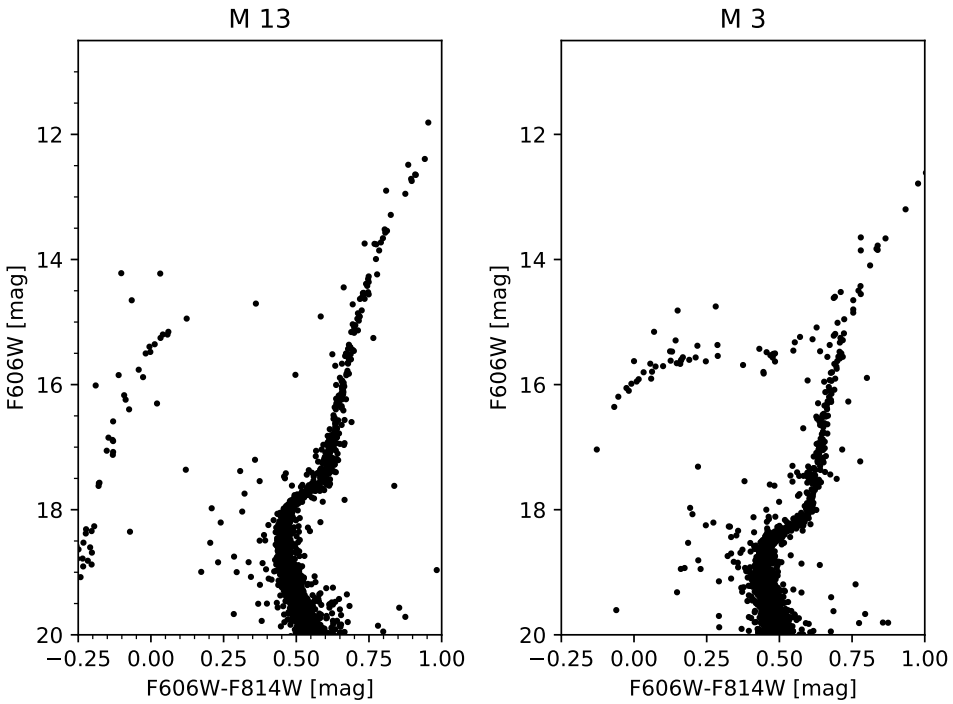

Figure 1.5: CMDs of the GCs M 13 and M 3 (data from ACS Survey (Sarajedini et al. 2007))

Figure 1.5 shows the CMDs of the Hercules cluster M 13 and M 3. This is one of the classical pairs of GCs used to investigate the morphology of the HB. M 13s HB is very densely populated at blue colors but barely shows HB stars in the red parts. On the other hand the HB of M 3 is not as extended to the blue as that of M 13, but in contrast to M 13 this cluster also harbors red HB-stars and has a quite prominent population of RR Lyrae stars. Both clusters share the same metallicity of about -1.5 dex (Harris 1996), but still their HB-morphologies are very different, indicating additional parameters

[4]Metallicity is often approximated using the iron abundance, commonly the iron abundance is given with respect to hydrogen and to the solar value [Fe/H]=log(Fe/H)-log(Fe/H)$_\odot$

[5]values taken form http://physwww.mcmaster.ca/~harris/mwgc.dat (last accessed: 01/10/2020, 2:10pm)

beyond metallicity being important. The lack of knowledge of this one or even more additional parameters having an impact on HB-morphology is also called the second parameter problem.
In the past many different parameters have been suggested to shape the HB, with age being the first one considered in literature. Indeed it seems that younger ages might harbor redder HBs, however significant progress in age determination of GCs showed that it can not be the only additional parameter. Gratton et al. (2010) suggested that if the production of HB-stars is universal for all GCs and scales with metallicity, age is indeed the second parameter. But also this model suggests that at least a third parameter is needed (Dotter et al. 2010; Gratton et al. 2010).
Early on the initial helium-abundance has been suggested to play a role as well. Especially the discovery of chemical peculiarities in GCs and the fact that many GCs host multiple populations have added new fuel to the consideration of the helium content as the main second parameter (Gratton et al. 2010). Helium abundances differing from the primordial abundance can arise from multiple options. Possibly a first generation of stars polluted the later generations with helium via supernovae and multiple episodes of star formation occur in GCs. Other more exotic explanations involve the formation history of GCs, suggesting that a spread of helium abundances is expected due to the formation of GCs since helium might have been more prone to gravitational collapse during formation (Shi 1995). Other scenarios assume no per se enrichment in helium, but suggest that the enrichment could be produced by mixing processes on the RGB induced by tidal forces due to the dense environments. Since stellar spectra very rarely show helium lines, the helium content can not be observationally constrained. However, evolutionary models involving populations with different helium contents are able to reproduce the observed features of the GC CMDs, including the HB-morphologies, quite well (Yi 2008). Figure 1.6 shows the result of a simulation considering multiple populations differing in helium. The simulations fit the observation considerably well. In this scenario the bluer HB-stars are produced by a population of stars with higher helium content. Generally MS stars with higher helium content will lead to the production of hotter HB-stars, which also means that the stellar masses of the stars produced by this population will be lower. The helium enhancement will also lead to the HB-stars exhibiting higher luminosities due to the higher energy output of their hydrogen burning shells and their decreased envelope opacities (Sweigart 1987; Brown et al. 2016).
Nevertheless, the list of other parameters that could be involved in this issue is long. It includes evolutionary effects such as mass loss, variations of the mass during the helium core flash or mixing processes, cluster properties like ellipticity, stellar density (Dotter et al. 2010), the formation of chemical anomalies such as the Na-O anti-correlation or a trend with C, N, O abundances, or stellar parameters such as rotation or the presence of planets. But in the end there is always some detail which every model only considering one parameter besides metallicity fails to explain. That is why many theories consider more than two parameters to be responsible and various combinations are explored. Future research involving observations and advanced simulations are needed in order to settle the second parameter problem (Gratton et al. 2010).

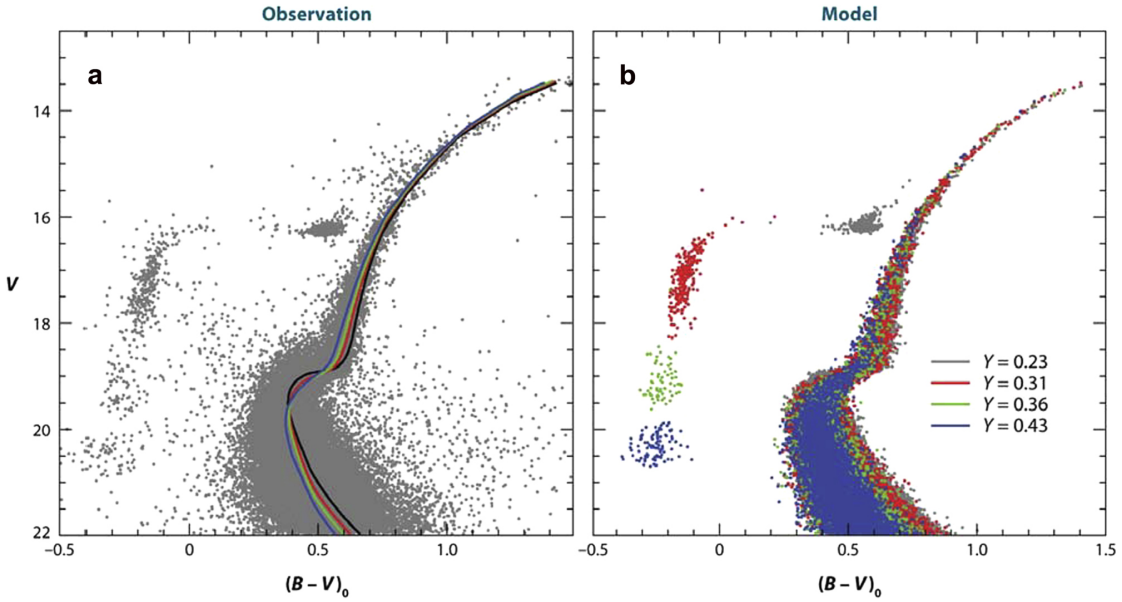

Figure 1.6: Panel a) displays the observed CMD of the GC NGC 2808 whereas panel b) shows the result of a simulation of different populations with the helium content being color coded (Yi 2008)

1.1.4.2 Atmospheric structure

The cores of horizontal branch stars are all very similar and convective, since the helium burning reaction is very sensitive to temperature (Spruit 2015). As the structure of the core seems to be universal along the HB the outer structure should be more influential. The HB is a sequence of hydrogen envelope mass and the mass decreases with temperature implying the relevance to search for structural changes along the HB since the total mass has a direct impact on the stellar structure, especially the structure of the atmosphere. The structure again will have an impact on several different properties of the stars, including their position in the CMD and the chemical composition. The structure also has major implications for the energy transport towards the surface.
The cooler HB-stars with massive envelopes have deep convection zones, so energy transport happens through convection in their outer layers. As the effective temperature increases and the envelope mass decreases the depth of the convection zone decreases, too. As the temperature passes $\log(T_{\rm eff}) \sim 3.8$ the deep convection zone breaks down into three smaller disconnected zones, each of them being associated with the ionization of hydrogen and helium. This is illustrated in Fig. 1.7. At $T_{\rm eff} \sim 11{,}500$ K the H convection zone, which has up to this temperature always reached the stellar surface, breaks down, leaving only small layers of convection deeper in the envelope. The HeI-convection zone, which is driven by the ionisation of HeI, will break down at slightly higher temperatures, but with increasing temperature it moves closer to the surface. The HeII-convection zone, driven by the ionisation of HeII, is the last one to break down as the temperature

increases. The thickness of every zone decreases as well (Sweigart 2002; Caloi 1999). In this process the atmosphere becomes more stable and energy transport will be taken over by radiative transport.

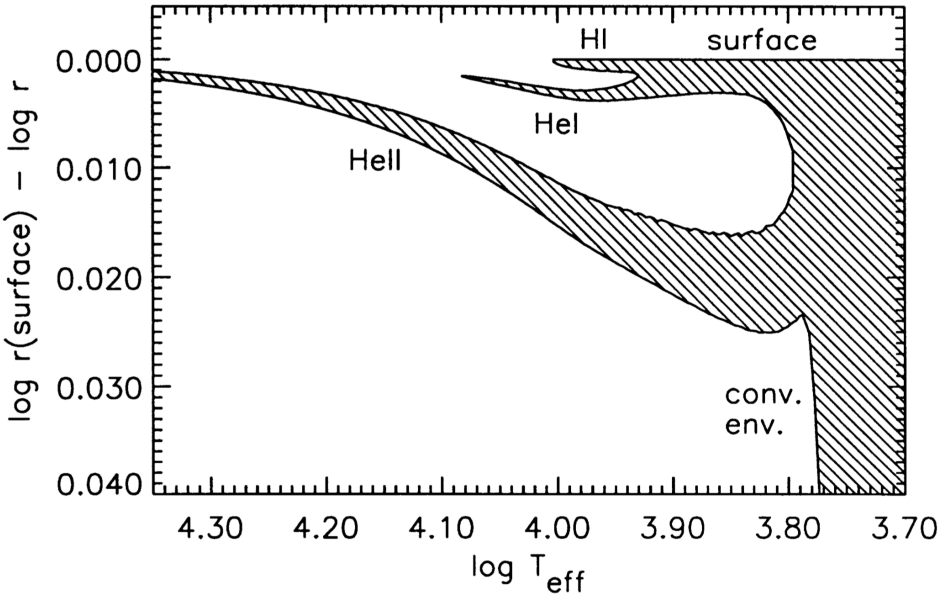

Figure 1.7: The envelope convection zones (shaded area) as a function of temperature with the shaded area being convective. Model calculated for fixed metallicity of [Fe/H]=-1.6, computed for one canonical HB (Sweigart 2002)

This structure is not universal in every detail but depends on a few parameters. The metallicity for example has an impact on the termination temperature of the H and HeII convection zones. For higher metallicities the H zone is terminated at higher temperatures than in low metallicity environments. The HeII zone will be terminated at higher temperatures as well and will also be able to reach depths closer to the surface. Another parameter influencing the structure is the initial helium content. The helium content does, however, not impact the H and HeII zones, but it has a major influence on the HeI convection zone. At higher helium contents the star is able to sustain convection up to higher effective temperatures. Additionally, the zone is able to penetrate layers closer to the surface. The influence of these parameters is illustrated in Fig. 1.8, where the extend of the convection zone is shown as a function of temperature. The upper panel is representing the metallicity of the GC NGC 2808 (-1.36 dex) and the lower one the high metallicity of GC NGC 6388 (-0.6 dex). Different helium contents are shown as well. The presence of convective zones has implications for the chemical composition, since the matter in the zone is constantly mixed, resulting in a homogeneous chemical composition and representing the original composition (Brown et al. 2016).

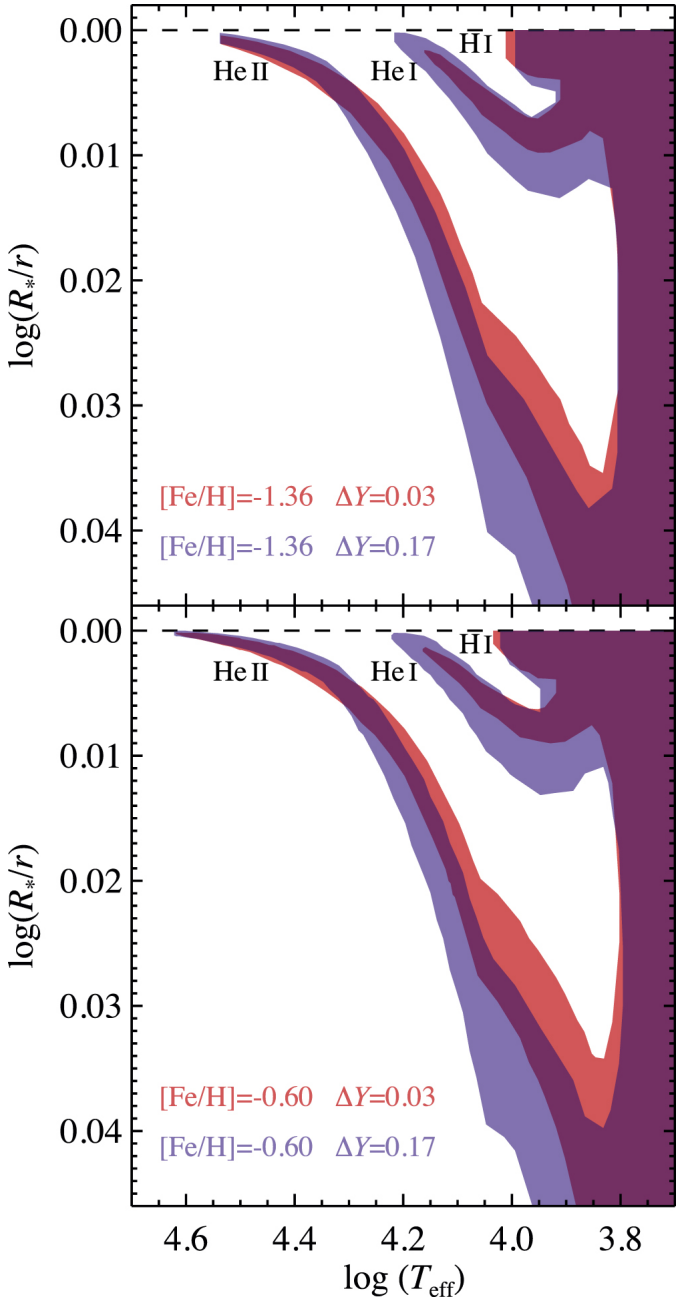

Figure 1.8: The extend of the convection zone as a function of effective temperature assuming the metallicity of NGC 2808 (upper panel) and that of NGC 6388 (lower panel). The color shading represents the respective initial helium content (either ΔY= 0.03 dex or ΔY= 0.17 dex) (Brown et al. 2016)

1.1.4.3 Atomic diffusion

For atomic diffusion to play a significant role the outer envelope of a star has to be hydrodynamically stable enough for mixing not to occur since diffusion velocities are smaller than macroscopic movements, e.g. convection (LeBlanc et al. 2010). As seen in the previous section the envelopes of HB-stars hotter than 11,500 K stop to be convective, therefore becoming stable and giving rise to diffusion processes. Diffusion refers to a net movement of atoms, in particular chemical species, from one region of higher concentration to one with an initially lower one. In stellar atmospheres the processes mainly responsible for the net moment are gravitational settling and radiative levitation. Gravitation and radiation pressure are the two forces having an influence on the atoms. This influence, especially which of the forces is dominating, depends on the chemical species. The radiative acceleration of atoms depends on the number and strength of their spectral lines. Also the domain of the electromagnetic spectrum in which the majority of spectral lines occur has a large impact. Since the radiation flux is the highest in the UV for the stars under consideration the acceleration will be greater for species with more spectral lines in the UV, because the flux distribution of a hot star peaks there. This is primarily the case for metals. Helium for example lacks transition lines in the UV compared to metals, which means that for helium the gravitational force is larger than the radiative force experienced by interaction with photons mainly through absorption processes. Consequently, helium will sink towards the stellar interior. Metals on the other hand will, depending on the species and the number of spectral lines an individual species exhibits, experience a greater radiative force, therefore being transported outwards. The acceleration also depends on the stellar layer under consideration. Consequently, the abundances seen at the stellar surface do not represent the initial chemical composition. Diffusion will lead to abundance anomalies and stratification of species (Moehler et al. 2014; Hui-Bon-Hoa et al. 2000).
There are processes that can counterbalance or slow down diffusion. Stellar rotation is known to play an important role, as fast rotation can suppress the effects of diffusion (Michaud et al. 2011). Mass loss, for example through a radiatively driven stellar wind, could also be able to slow down diffusion by damping the gravitational settling of elements. Diffusion does not only effect the atmospheres of stars but is also an important process active in layers beneath the photosphere. For some stars diffusion is also responsible for pulsations as diffusion alters the abundances creating an opacity bump of iron-peak elements, which then drives pulsations. The presence of pulsation in some stars has led to considering truculences in the outer layers being present, which will also slow down diffusion processes.

1.1.4.4 Discontinuities in the sequence

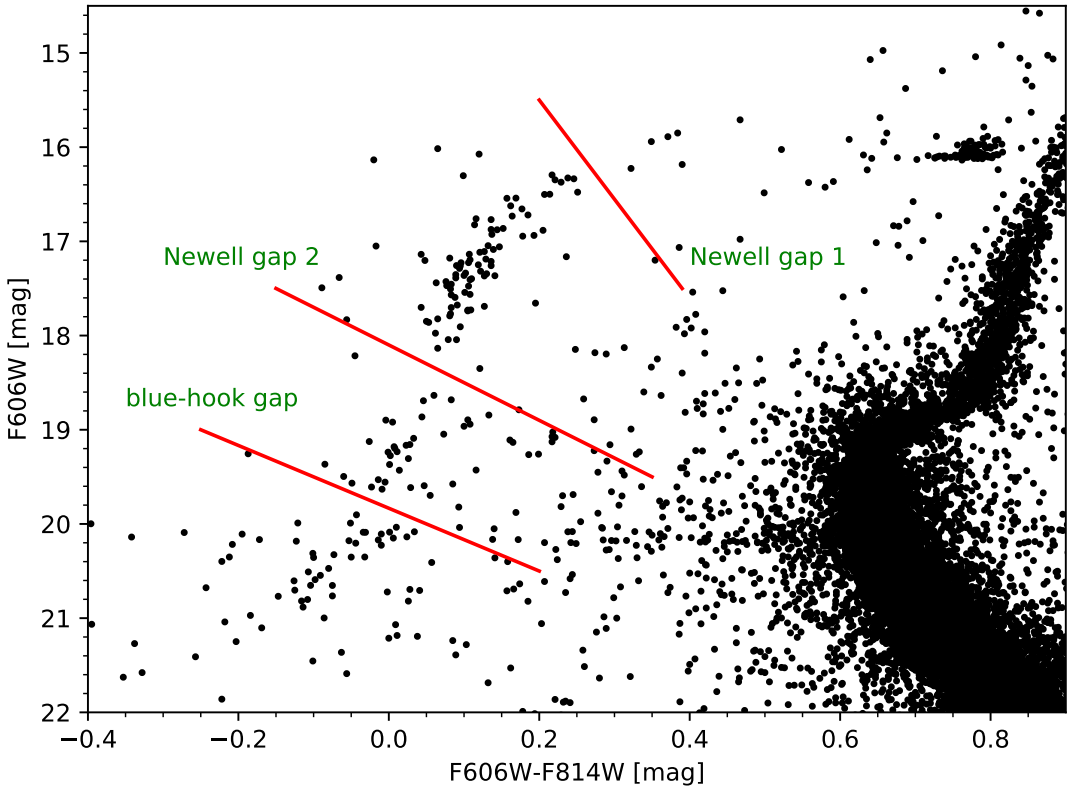

Figure 1.9: CMD of the GC NGC 2808 showing the different gaps in the HB (data from ACS Survey (Sarajedini et al. 2007))

The different groups of stars along the HB and their distinctions, as presented in Sec.1.1.3, are not random but based on physical differences. The physical processes leading to these differences are not completely understood yet, but they seem to be omnipresent (Brown et al. 2016). The distinctions become evident in the CMD where they, depending on the colors used, manifest themselves as gaps, jumps, or discontinuities, see Fig. 1.9 for a CMD of NGC 2808.
The previously mentioned RR Lyrae strip presents itself as the reddest gap in the HB. This gap is understood not as a gap due to a change in physical processes, but as region underrepresented in CMDs due to measurement times being insufficient. The blue end of the RR Lyrae strip extends into the BHB. The red end of the BHB (stars here are also named HBA stars in literature) starts at effective temperatures of typically $\sim 8,000$ K. This sequence of A-type BHB (A-BHB) stars extends up to effective temperatures of $\sim 11,500$ K. At this position the first gap along the HB occurs, the so called Newell gap 1 (NG1) which was first described by Newell (1973), but it is often called Grundahl jump (Grundahl et al. 1999). The NG1 is observed in the field and the GC population (Newell

and Graham 1976). This corresponds to effective temperatures of about 11,500 K which is also confirmed by observations of GCs spread over many different types differing in mass and metallicity. Therefore, this gap seems to be at $T_{eff} \geq 11{,}500$ K (Brown et al. 2016). The NG1 has been associated with atomic diffusion setting in and, therefore, an increase of metal abundances at the stellar surface due to radiative levitation (Grundahl et al. 1999). The presence of effective atomic diffusion implies that the atmosphere must become more stable at the NG1 and as shown in Figures 1.7 and 1.8 the H and HeI convection zones disappear. This theory is also backed up by the decrease of helium abundance most likely due to gravitational settling at temperatures corresponding to the NG1. This suggests that the gap and the onset of diffusion could be due to one of the disappearing convection zones or even due to both (Brown et al. 2016). Empirical evidence for these claims come from spectroscopic analyses showing higher metal abundances at colors bluer than the NG1 (Geier et al. 2010) again hinting at the presence of atomic diffusion. The spectroscopic conformation that the projected rotational velocities of stars beyond the NG1 drop significantly (Geier and Heber 2012), implies more stable atmospheres. In many GCs the NG1 is observed at similar temperatures, but Brown et al. (2016) observed the gap at slightly higher temperatures in two metal-rich clusters. They suggest that the higher temperature of the gap is due to helium enrichment. This would make the disappearance of the HeI the most likely explanation, since the H convection is not effected by helium content and therefore could not explain the higher temperatures. However, the disappearance of the relevant convection zones does not entirely coincide with the occurrence of the NG1, suggesting either that the gap is not due to one zone only or that another parameter has to be considered additionally to convection (Brown et al. 2016). Michaud et al. (2011) suggested a mixed outer layer at the surface driven by turbulence or mass loss as an additional parameter, yielding good agreement with expectations.

The next gap, the so called Newell gap 2 (NG2), also first described by Newell (1973) and Newell and Graham (1976) and often called the Momany jump (Momany et al. 2002), corresponds to temperatures between 18,000 K and 20,000 K. This gap marks the transition from the hotter BHB stars (called HBB in literature), which are late type B stars (B-BHB), to the EHB in GCs or the sdB-regime in the field. Again, this gap is observed in GCs as well as the field, thus indicating a universal nature. However, compared to the NG1 so far no variations of the occurrence-temperature have been observed in GCs even over a wide spread of different population parameters (Brown et al. 2016, 2017). Stars on both sides of the NG2 show metal-enrichment, but stars on the red side have higher iron abundances than stars on the blue side, although they are also enriched (Brown et al. 2017). The same is observed for field B-BHBs and sdBs (Geier et al. 2010). The change of iron abundance is also supported by calculations (Michaud et al. 2011), but physical processes responsible for this change in abundance remain unknown. A link to the HeII convection zone could exist, as this zone is pushed towards the surface at temperatures close to the NG2 (Brown et al. 2016). The gap also marks the temperature at which the hydrogen envelope mass drops to a limit so that the hydrogen burning shell ceases to exist.

The third gap occurring separates the blue-hook stars from the EHBs. These stars have

temperatures of 35,000 K or higher and can not be produced by canonical evolution models. It is proposed that these stars are not the direct progeny of RGB stars but of stars undergoing a delayed helium flash when they have already reached the WD cooling sequence.
The discontinuities along the HB, especially the NG1 and NG2, seem to have a universal character and might be associated with atmospheric changes in HB-stars. This is also backed up by the fact that the transitions are observed among different populations (Brown et al. 2017).

1.1.5 Evolution of horizontal branch stars

In order to explain all the different types of HB-stars many different formation scenarios have been suggested in the past. The most simple models in context of the simple picture of stellar evolution, presented in Sec. 1.1.1 are canonical models. These models are considered to be valid for a wide range of different HB-stars, including BHBs. Canonical models assume that stars evolve up the RGB while losing mass due some mass loss process or multiple processes. A hydrogen burning shell around the helium core, which is degenerate, advances outwards. Hence, the helium core will grow in size. At the tip of the RGB, which depends on metallicity and helium abundance (Sweigart 1987), the core is massive enough to ignite helium, which happens at a core-mass in the range of 0.47 $M_\odot$ to 0.5 $M_\odot$. Helium is ignited off-center in the so called helium core flash event, a violent set in of helium burning lifting the degeneracy of the core. The result is a He-core burning HB-star. As pointed out previously, the position on the HB depends on the envelope mass which means that stars have to lose mass while on the RGB (Dorman et al. 1993). Clearly, stars lose different amounts of mass while on the RGB, for example through stellar winds. However, until today it is not clear what causes the different amounts of mass lost on the RGB or which mass loss processes are indeed present. The mass loss could also be linked to helium enhancement, tidal forces, rotation, or binary interaction which are not considered for canonical models. Assuming just fixed mass losses along the RGB canonical models are able to explain many HB-stars without further characterizing the mass loss.
The presence of hot EHB-stars which have essentially lost their entire hydrogen envelopes is a big challenge for canonical models, since no process is known to be able to remove the envelope completely. Therefore, many other scenarios which are also able to explain BHB-stars, have been evoked as well. Helium mixing on the RGB assumes that the convective envelope is somehow able to penetrate the hydrogen burning shell, bringing helium into the envelope and causing a higher energy-output and luminosities, which are linked to higher mass loss rates. Depending on how strongly helium is mixed into the envelope different amounts of mass can be lost (Sweigart 1997). The penetration of the hydrogen shell could be linked to rapid rotation or tidal forces.
Other scenarios, especially those explaining the hottest EHB and blue-hook stars are more exotic. If a significant amount of mass is lost on the RGB, stars can depart from the RGB without undergoing a helium flash, which then can happen later on. The flash

might occur shortly after leaving the RGB, then being called a early-hot flasher, the stars would then result in an average EHB-star. Or the flash may occur later while the star is already moving towards the WD cooling sequence (late-hot flasher). Depending on the mixing different elements then will be dredged up into the envelope (Brown et al. 2001, 2012). Again other scenarios assume the stars are or have been part of a binary system. EHB-stars can also be produced by Roche-lobe overflow, common envelope, a combination of these, or mergers especially of WDs. The evolutionary tracks of the most relevant scenarios are shown in Fig. 1.10.
Once stars reach an equilibrium core-helium burning state, shortly after the RGB has been left, they are on the zero-age HB (ZAHB). Stars spend about 100 Myr there. When helium-core burning ceases they reach the terminal age HB (TAHB). The subsequent post-HB evolution is short compared to the HB-lifetime. The effective temperatures and luminosities will increase. BHB-stars will progress to the AGB, where the more massive ones enter into the thermal pulsing phase. EHB- and BH-stars on the other hand immediately move towards the WD-cooling sequence and ultimately end up as WDs. These formation scenarios are thought to be valid for the field as well as the GC population.

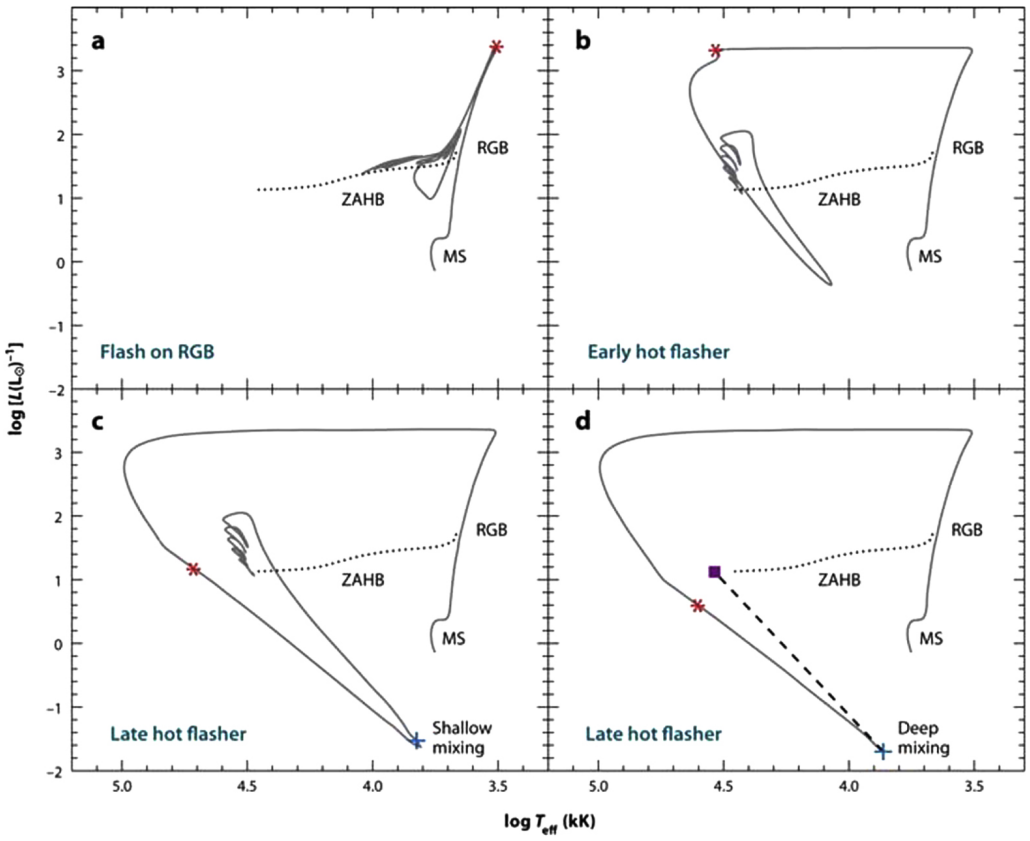

Figure 1.10: HRDs showing the tracks of different evolutionary scenarios. Drawn line shows the evolutionary track, dotted line the HB. (Heber 2016)

1.2 Properties of blue horizontal branch stars

Most studies in the past have focused on the GC population of BHB-stars and, therefore, most of our knowledge is based on GC and not field BHBs. However, during the past two decades a few studies have been conducted in the field as well, making comparisons between the populations in principal possible. First the basic properties of BHB-stars, including A-BHB and B-BHB, will be reviewed, mostly focusing on the field population. Then the field population will be compared to the GC BHBs.

1.2.1 Atmospheric properties

1.2.1.1 Stellar structure

As previously mentioned the cores of HB-stars are convective and powered by helium burning. The core is surrounded by a hydrogen burning shell and the envelopes are radiative (Faulkner 1966). However, the sub-surface layers differ among BHB-stars. The A-BHB-stars have surface convection zones, mixing the outer regions of the star and making the star stable towards diffusion. Surface-convection breaks down at the transition to the B-BHBs (see Sec. 1.1.4.2). These stars have radiative surface-zones, although a sub-surface HeII convection zone is present (Brown et al. 2016). Hence, diffusion will influence the abundances and therefore also the structure. Diffusion can lead to vertical stratification in B-BHB-stars, meaning the abundance of a certain species will differ throughout the outer layers, since the radiative acceleration also depends on the layer diffusion is operating in. Stratification will lead to structural changes induced by opacity changes in the respective layers. These structural changes will be detectable in photometric anomalies (jumps in CMDs) and lower surface gravities than when assuming a homogeneous distribution of elements in the stellar atmosphere (LeBlanc et al. 2010).

1.2.1.2 Rotational properties

The projected rotational velocity of a star v·sin(i), with the inclination i, is an important parameter to characterize a lot of properties of HB-stars. Rotational velocities can be measured from spectroscopy, where rotation will broaden the absorption lines, or from astroseismology. The rotation of HB-stars has been subject to many studies. Generally HB-stars show low rotation velocities compared to MS stars. Since theses stars have gone through several steps of evolution it is not surprising to find lower rotational velocities, as they have had opportunities to lose angular momentum, for example through stellar winds. Typical rotational velocities are a few 10 km/s at most. One interesting observation is a drop in projected rotational velocity coinciding with the NG1, stars to the red of the gap show velocities of up to 40 km/s while stars on the blue side rotate with velocities of typically 10 km/s or less (Geier and Heber 2012). This distribution with a smooth transition from A-BHB to B-BHB-stars can be seen in Fig. 1.11. The transition to the EHB is smooth too. The same holds for the angular momentum which decreases with effective temperature (Geier and Heber 2012).
Slow rotation is considered to be a requirement for diffusion, since the atmosphere will

be more stable and mixing through circulation induced by rotation should then be negligible. For stars near the NG1 a projected rotational velocity of 20 km/s or higher would be needed to counterbalance diffusion (Quievy et al. 2009). An explanation for the distribution of rotational velocities has not been found yet. Some theories propose that the low rotation HB-stars originate from slowly rotating MS stars. Diffusion could also be important, since radiative levitation, especially of iron, might be able to induce a stellar wind leading to a loss of angular momentum (Sweigart 2002). The rotation rates could also be linked to the convective zone, which should, when present, account for a significant amount of the envelopes angular momentum. Once the convective zone disappears the stars will rotate slower (Brown et al. 2008; Geier and Heber 2012).

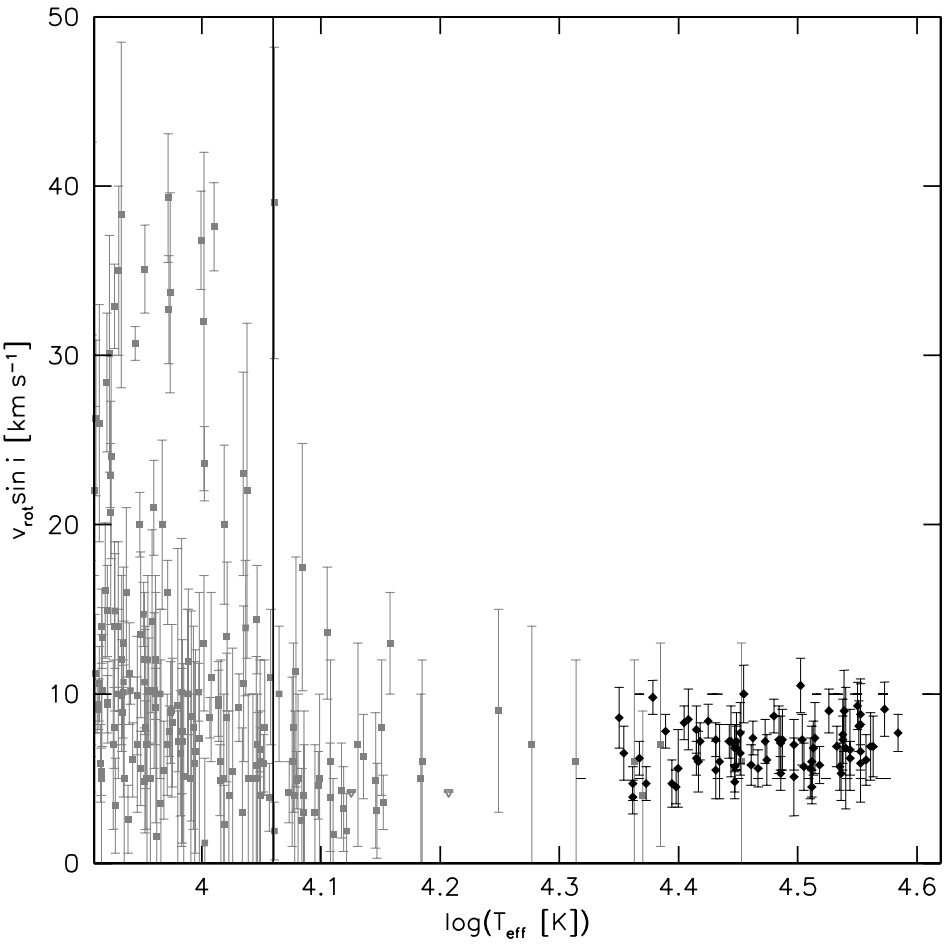

Figure 1.11: Projected rotational velocity as a function of T_{eff}, the solid line marks the temperature of the NG1 (Geier and Heber 2012)

1.2.1.3 Atmospheric parameters

The atmospheric parameters effective temperature T_{eff} and surface gravity log(g) are very important to characterize stars and to classify them as HB-stars. In the log(g)-T_{eff} plane HB-stars will be found on the HB-band, spanned by the ZAHB and TAHB. The position of this band also depends on metallicity and helium abundance. Higher helium abundances will result in higher luminosities and lower gravities, hence shifting the band upwards (Moehler 2001).
ABAHB stars have typical effective temperatures between 8,000 K and 11,500 K and log(g)-values between 3.0 and 4.0. The values derived from spectroscopy, usually, agree quite well with the stars being on the HB-band (Kinman et al. 2000). Often the effective temperature is also given as a logarithm. The field sample studied by Kinman et al. (2000) is shown in Fig. 1.12.
B-BHB-stars have a temperature range bracketed by the Newell gaps, so they span a temperature range from 11,500 K up to 20,000 K. The surface gravities range between 4.0 and 5.0. For B-BHB-stars the log(g)-values from spectroscopy are often lower than predicted by canonical models, when metallicity agrees with the population metallicity (Grundahl et al. 1999). Using models with higher metallicities on the other hand will yield better agreement with the HB-band, which is also consistent with the picture of these stars being metal-enriched by diffusion (Moehler et al. 2014).

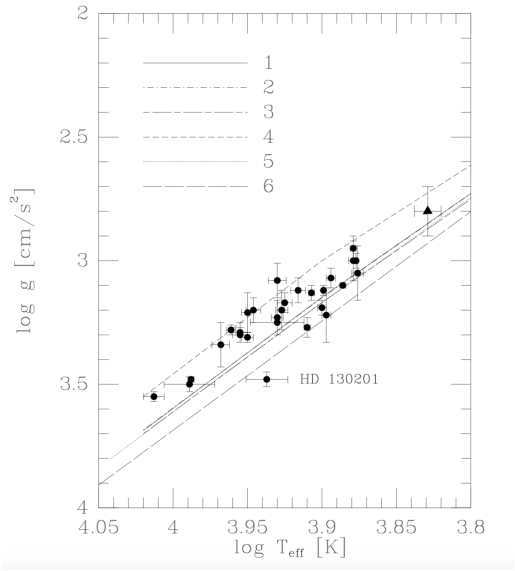

Figure 1.12: log(g)-log(T_{eff}) plane containing a sample of field A-BHB-stars, the lines correspond to ZAHBs calculated for different metallicities (Kinman et al. 2000)

1.2.2 Chemical properties

1.2.2.1 Helium abundance

The helium abundance has a major influence on stellar structure and parameters and on a star's position on the HB-band. The strengths of the helium lines decrease with decreasing T_{eff} and lines vanish at temperatures of about 8,000 K. Since in this temperature-range the helium lines are below the noise-level, little data on stars in this range exist. However, above 8,500 K the photosphere reaches temperatures high enough for weak helium lines to appear in the spectrum. For the A-BHB-stars the helium abundance is similar to the solar value (Adelman and Philip 1996; Kinman et al. 2000; Behr 2003a).
For the B-BHB-stars the picture is different. The helium abundance at the surface decreases with temperature. This is probably due to diffusion being active in the atmospheres of B-BHB-stars. Helium is depleted because it is prone to gravitational settling (Behr 2003a). The helium abundance decreases and reaches its minimum at about 15,000 K, beyond which the helium abundances increase again, but helium remains strongly under-abundant with respect to the sun. Since a similar trend is observed for the iron abundance it may suggest that the efficiency of diffusion varies with temperature, with the highest efficiency reached at the minimum helium-abundance (Moni Bidin et al. 2012). This general trend for B-BHB-stars is shown in Fig. 1.13.
On the EHB the helium abundance increases again as a function of temperature. There are two distinct sequences of EHB-stars showing this behavior. A small fraction of stars is helium poor and shows an increase, whereas the majority of stars can be found on a helium-rich sequence exhibiting the same behavior (Edelmann et al. 2003). This is not yet fully understood but could be linked to diffusion as well.
Typically, helium abundances are derived assuming that helium is mainly present as ^{4}He (two protons and two neutrons in the nucleus). But for some stars on the B-BHB (Hartoog 1979) and a few sdBs (Heber 1987) the ^{3}He content has to be considered as well, since signatures of this isotope can be visible in the spectrum. In these cases helium lines show clear wavelength-shifts, since the ^{3}He transitions are shifted due to the different masses of the isotopes leading to a general shift. An additional shift is introduced by the wave function of a two electron system which can only become non-zero for P-orbital transition terms (Schneider et al. 2018). Since ^{3}He is seen in the spectrum this also indicates that the isotopic ratio is very different from the solar value. Generally it is expected that ^{4}He experiences a stronger gravitational pull than ^{3}He, thus leading to a isotopic separation and an enrichment in ^{3}He which is often associated with diffusion. However, the isotopic differences in gravitational settling are not strong enough to explain the observed enrichment. At least in the B-BHB-stars showing this anomaly, it is not possible to match the helium lines when assuming a homogeneous distribution of helium throughout the atmosphere, therefore indicating that helium might be stratified with the helium content increasing with atmospheric depth (Schneider et al. 2018).

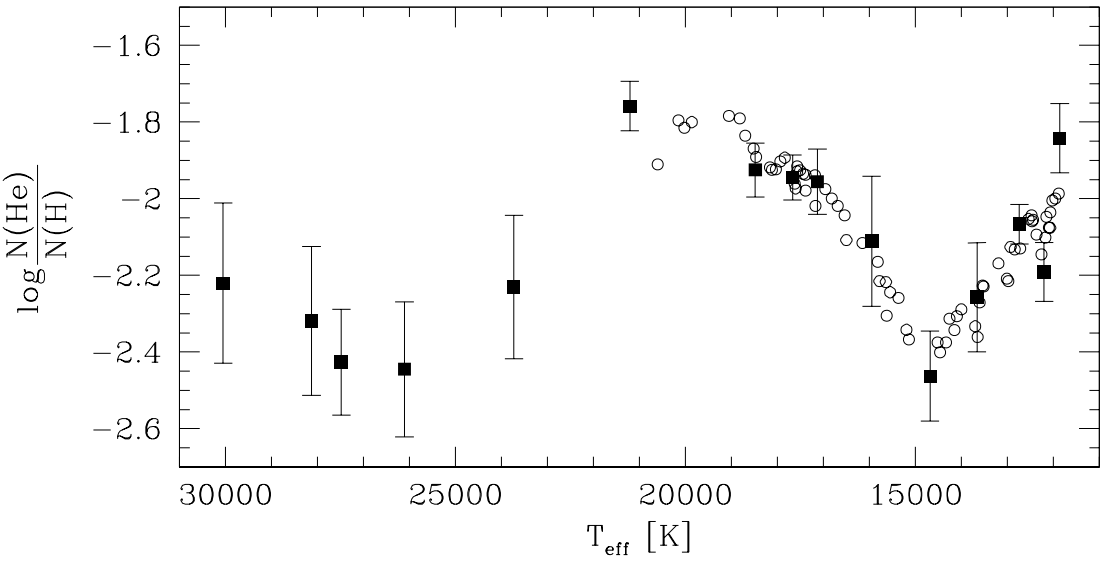

Figure 1.13: Helium abundance as a function of effective temperature, binned data for many stars in the GC ω Cen is shown (Moni Bidin et al. 2012)

1.2.2.2 Metal abundances in A-BHBs

The abundance patterns of the A and late-B type BHB-stars are very different from each other, as already indicated by the helium abundances. Therefore, they will be discussed separately.
The abundances of the A-BHB-stars agree well with the abundances observed in their respective populations (Behr 2003a). While helium is comparable to the solar value (Adelman and Philip 1996) metals are mostly under-abundant (Kafando et al. 2016).
A slight enhancement of α-elements (C,O,Ne,Mg,Si,S,Ar,Ca,Ti) in contrast to the other elements has been known to exist in metal-poor stars for a long time (Wallerstein et al. 1963), although in A-BHBs neon, sulfur and argon have not been observed before. The α-enhancement originates from massive stars going supernova and therefore enriching the interstellar medium (ISM) with these elements for the next generation of stars to form. While carbon, if visible in the spectrum, is highly under-abundant, oxygen is found to be sub-solar or at most at solar level (Kafando et al. 2016). Magnesium shows only a slight or no enhancement at all compared to the population abundance. However, this is not conclusive, since some studies find Mg to have the typical α-enhancement (Kinman et al. 2000) and others find slightly higher abundances, especially at temperatures close to the NG1. Mg is usually used as a proxy for α-elements, as is iron for metallicity. Therefore, the correlation between Mg and iron is often investigated. Silicon is found to have a similar behavior as Mg, and some studies find a large scatter among sample stars. The calcium abundances scatter around the population value. Titanium generally exhibits an enhancement with respect to the population (Behr 2003a; For and Sneden 2010; Hubrig

et al. 2009).
Odd-Z elements (N, Na, Al, P) are also found in HB-stars. Nitrogen is slightly sub-solar (Kafando et al. 2016). At least from optical spectroscopy it is not that easy to derive reliable abundances for sodium, since the only lines are often contaminated by interstellar lines. Therefore, these lines can only be used if the stellar and interstellar lines are well separated. In these cases sodium is found to be sub-solar. Aluminum is not detected in all A-BHBs (For and Sneden 2010) and Phosphorus has not been observed in A-BHBs (Behr 2003a).
Iron-peak elements (Sc, V, Cr, Mn, Co, Ni) are detected in BHB-stars as well. The abundances of scandium, vanadium, manganese, cobalt, and nickel scatter around the population value, when present. Chromium is detected in more stars than other iron-peak elements and is also consistent with the population abundance (Behr 2003a; For and Sneden 2010; Hubrig et al. 2009).
Also n-capture elements (Sr, Y, Zr, Ba, La) are present in BHBs. They are generally under-abundant but not found in all stars. Strontium is detected more often than the other elements. Yttrium and zirconium are found to be only slightly below solar, if present, and the abundances increase towards the NG1. Barium is only observed in a few stars and lanthanum has not been observed so far (For and Sneden 2010).
No information regarding the abundance of cer in BHBs can be found in the literature. The abundance of iron is consistent with the population-abundance and is sub-solar but can show some scatter (Behr 2003a; Kafando et al. 2016).

1.2.2.3 Metal abundances in B-BHBs

The metal-abundance patterns of B-BHB-stars are different from those derived for the A-type stars, which is expected since diffusion could be active in the former. The metal abundances are often enhanced compared to the mean abundance of the population, some elements even reach abundances higher than solar.
Carbon is found to be under-abundant with respect to solar, but the values can have quite some star-to star scatter, while oxygen, if detected, can reach solar abundances. Neon can be found close to solar as well. Magnesium, silicon and sulfur are all sub-solar and while Si and S only show a very little enhancement over the population abundance, Mg is fully consistent with the respective population. Argon shows clear overabundances. The calcium abundance corresponds to the solar value, while titanium is overabundant with respect to the solar and the population abundances (Bonifacio et al. 1995; Behr 2003a; Kafando et al. 2016; Németh 2017).
While nitrogen, sodium, and aluminum are sub-solar when detected, phosphorus is quite different. While being enhanced over the population value, it is also strongly enhanced with respect to solar and shows stratification in some stars. The enrichment of P is much stronger than the one found for iron which shows the largest enhancement observed (Behr 2003a; Kafando et al. 2016; Németh 2017).
Among the elements scandium, vanadium, chromium, cobalt, and nickel abundances are all higher than the population abundance and have values close to solar. Manganese may even be more abundant than in the sun (Bonifacio et al. 1995; Kafando et al. 2016).

Almost no data is available for Sr, Y, Zr, Ba, La, and Ce, but Y and Zr seem to have solar abundances in the cooler stars close to the NG1 (Hubrig et al. 2009).
Iron is more abundant than in the respective population and is mostly at a solar level, but it can also be enriched compared to solar (Behr 2003a).
The abundances of many metals are a function of effective temperature along the HB. The iron abundances derived for different GCs by Behr (2003a) are shown in Fig. 1.14. The dashed line indicates the population abundance and it is clear that once the NG1 is crossed the abundances are higher. The presence of vertical stratification (Kafando et al. 2016) and overabundances of some metals plus isotopic anomalies hint at the presence of diffusion in late B-type BHB-stars. However, one should not put too much weight on the abundances for many elements, since they are based on a few stars only.

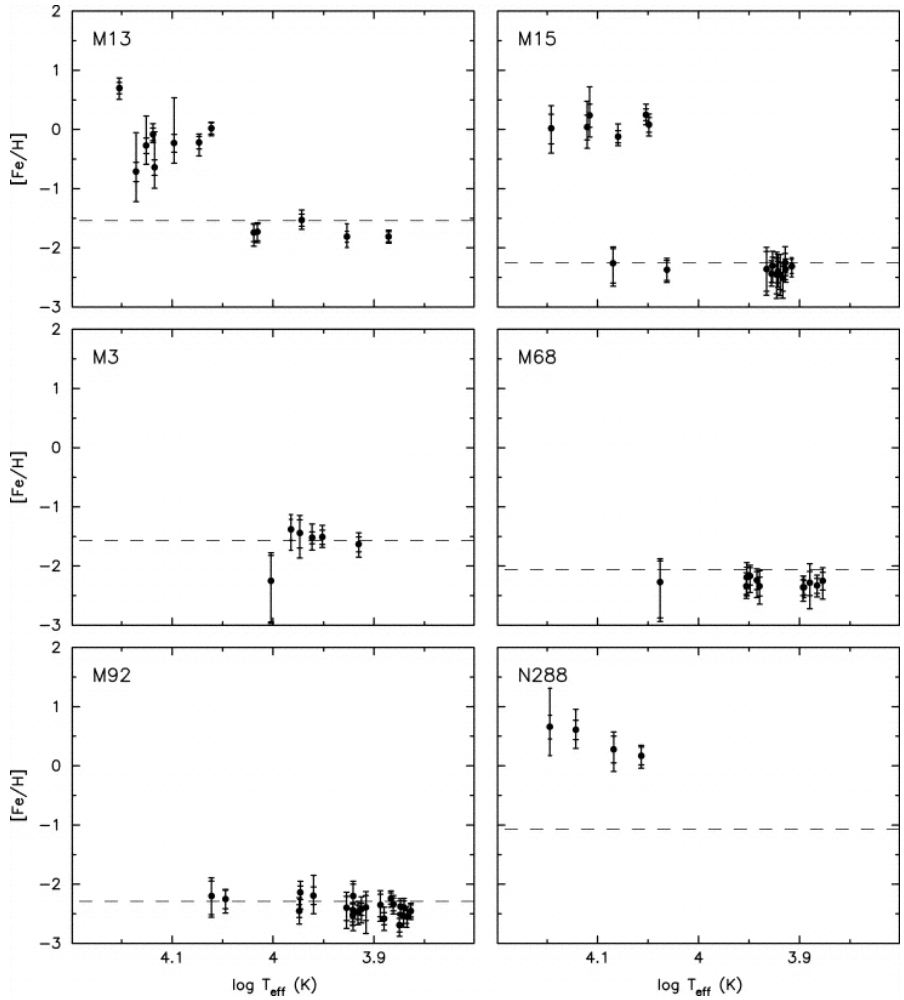

Figure 1.14: Iron abundance as a function of effective temperature in six GCs (Behr 2003a)

1.2.2.4 The sdB abundance pattern

Since diffusion is expected to be important in B-BHBs and EHBs it is crucial to compare the abundances of both groups as well. Therefore the abundances of the cooler EHB-stars will be reviewed, as summarized in Fig. 1.15 (Naslim et al. 2013).
Nitrogen and carbon show very different abundance patterns although levitation effects are predicted to be similar. Nitrogen is subsolar in most stars and the scatter is rather small. Carbon, on the other hand has a much larger spread, from strongly sub-solar to super-solar. Oxygen displays a smaller spread than carbon but shows more variation than nitrogen. A correlation between carbon and nitrogen abundances with the helium-abundance emerges if the results for sdB and sdO stars are combined (Naslim et al. 2013).
Magnesium is mostly sub-solar and shows little scatter. Iron displays almost the same scatter but is mostly found to be at solar level. Intermediate mass elements, such as silicon or aluminum, are depleted and show large star-to-star variations. Heavier elements, such as titanium for example, are strongly enriched compared to solar level. Some of these elements have been detected in a few stars only, but if detected, they are strongly enriched with respect to solar. In general, elements heavier than Ar are all enriched, except for iron, and show an increase with temperature. Lead is an element present in many sdB-stars and it is one of the most important elements to study nucleosynthesis since it is produced in very distinctive processes (Naslim et al. 2013).

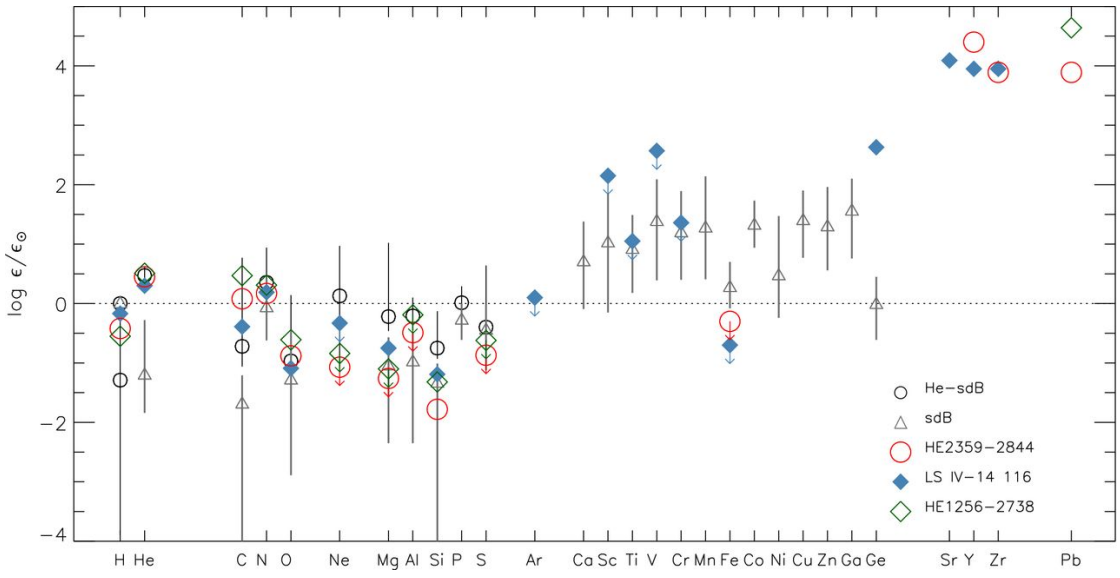

Figure 1.15: Abundances relative to solar for different EHB-stars, triangles show the mean sdB abundances (Naslim et al. 2013)

1.2.3 Fundamental stellar parameters

The stellar parameters radius, mass, and luminosity are important indicators for the evolutionary status of stars. As discussed previously the HB is a sequence of hydrogen envelope mass and therefore also of total mass. Typical values for A-BHBs are in the range of 0.5 $M_\odot$ to 0.7 $M_\odot$ (Dorman 1992). However, some measurements also find masses slightly higher (De Marco et al. 2005). For B-BHBs the masses should be closer to 0.5 $M_\odot$ and a further decrease towards the EHB is expected since sdB and sdO masses should center around the canonical mass of 0.47 $M_\odot$ (Fontaine et al. 2012), which means that the hydrogen-envelope is very small or absent.
The stellar radius should also decrease with temperature. The radii of BHB and EHB stars are significantly different (Geier and Heber 2012), with the coolest BHBs having radii up to one order of magnitude larger. On the low mass end radii are typically in the solar range (Dorman 1992), but some studies find radii ranging up to 3 $R_\odot$ for the coolest (De Marco et al. 2005), whereas sdBs radii will be in the range of 0.15 $R_\odot$ (Fontaine et al. 2012).
At the lower mass end of the A-BHB stars may exhibit luminosities of up to 50 $L_\odot$. The luminosity will decrease with temperature and the hottest A-BHBs will have luminosities of 20 $L_\odot$. The coolest sdBs are expected to have luminosities of 10 $L_\odot$ (Dorman 1992).

1.2.4 Kinematic properties

In the Galactic field the kinematics of a star can be used to classify its population-membership. The Milky Way consists of three distinct stellar populations, the thin- and thick-disks and the halo. Thin-disk stars have orbits of small eccentricities and staying close to the Galactic disk. They orbit the Galactic center at a velocity similar to that of the sun. Thick-disk stars lag behind the thin-disk ones and their orbits are moderately eccentric and not strictly contained within the disk of small eccentricity. The orbits of Halo-stars are not within the disk. They extent well above and below the disk and are extremely eccentric. The halo population does not show a net rotation. Based on a few basic parameters stars can be matched to the different populations.
A few studies have calculated the orbits of HB-stars and there seems to be a kinematic trend among the field HB-stars. RR Lyrae stars show halo as well as disk kinematics, but there seems to be a trend with metallicity. The metal-poor ones have halo-like orbits whereas the metal-rich ones belong to the disk. The A-BHB-stars have orbits extending well over the Galactic disk, therefore they are most likely halo members. B-BHBs on the other hand show a different behavior. Their orbits are contained within or are very close to the disk, indicating a disk-membership (Altmann and de Boer 2000). The orbits of sdBs are mostly found to be similar to those of B-BHBs (Altmann et al. 2004). Orbits of different HB-stars are shown in Fig. 1.16.
Although the single samples used are limited in number, every study agrees on the halo-membership of A-BHBs and disk-membership of B-BHBs (Kinman et al. 2009).

These results pose interesting questions for the origin of field BHBs and whether different processes produce them in the respective populations or if the same process is governed by environmental parameters such as metallicity. The kinematics is also important for aspects concerning Galactic evolution. Stars could possible originate from tidally disrupted satellite galaxies or GCs or might possibly have been acquired from GCs, and in fact models predict that GCs have lost ∼70% of their primordial stars during their lifetime by internal mass segregation and tidal forces. Hence, some field BHB-stars may originate from GCs. Further kinematic and chemical analysis of local stars with similar properties would be needed to shed more light on this issue (Altmann et al. 2005).

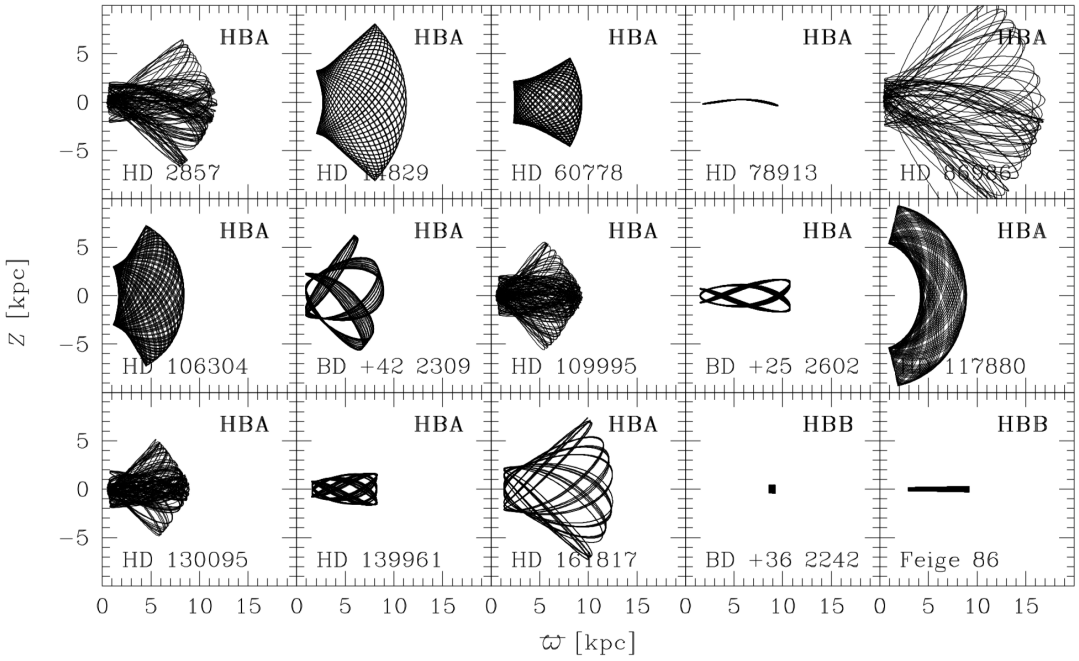

Figure 1.16: Orbits of different types of HB-stars, Z is the height over the Galactic plane and ϖ denotes the distance from the Galactic center (Altmann and de Boer 2000)

1.2.5 The prototype B-BHB-star - Feige 86

The field B-BHB-star Feige 86 could be considered the arche-typical B-BHB-star, because it is probably the most studied HB-star, since it is the brightest known star of its type. Its orbit calculated by Altmann and de Boer (2000) indicated that Feige86 is a disk star (lowest right panel in Fig. 1.16), which is expected for the B-BHBs. Published atmospheric parameters differ depending on the method used. Effective temperatures between 15,000 - 18,000 K have been derived while the surface gravities differ enormously (from 3.75 to 4.75) (Baschek and Sargent 1976; Bonifacio et al. 1995; Behr 2003b; Németh

2017).
Feige86 is known to exhibit many chemical peculiarities, similar to HgMn-stars. A high isotopic shift for helium is observed (Hartoog 1979), hence the spectrum must be strongly enhanced in ^{3}He. Helium is under-abundant, as expected. Furthermore Feige 86 shows overabundances for many metals, including P, Cl, Ar, Ti, Mn, Fe, Cu, Zn, Ga, Pt, Au and Hg. Other elements are close to solar (e.g. Ne) or under-abundant (e.g Mg and C), especially the lighter elements. Iron might be stratified with depth (Bonifacio et al. 1995; Kafando et al. 2016; Németh 2017). The abundance pattern of Feige86 is shown in Fig. 1.17.
These observations hint at the presence of diffusion processes in Feige 86 and make it a prime target for the investigation of hot stellar atmospheres, NLTE effects, atomic data, diffusion and nucleosynthesis (Németh 2017).

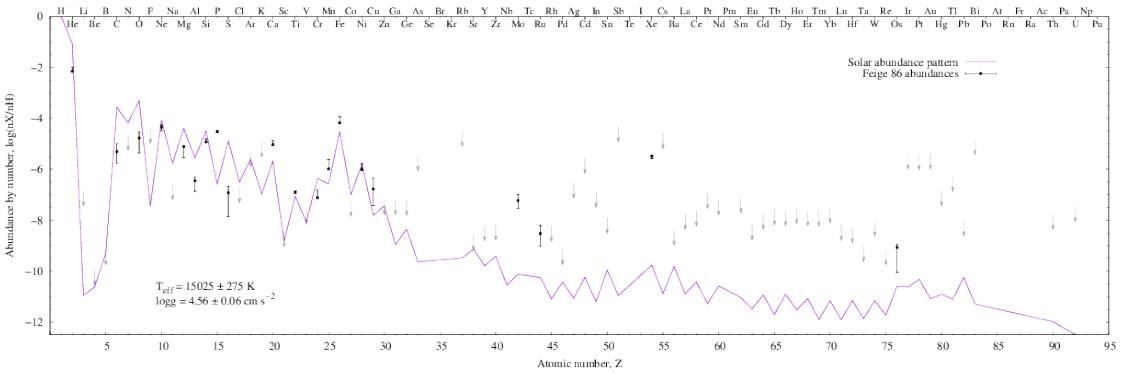

Figure 1.17: Abundance pattern of Feige 86 compared to the solar-abundance pattern (Németh 2017)

1.2.6 Comparison between the field and globular cluster populations

Unfortunately, the number of field BHBs that have been analyzed in detail, is small. Hence, the properties in this chapter are sketchy and an in depth comparison between the field and the GC populations is not possible. Up to now we are restricted to the general trends and very few chemical species, mostly Mg and Fe, which seems to be similar in the field and GCs (Magurno et al. 2019) (see Fig. 1.18). The abundance patterns of A-BHBs and B-BHBs observed in the field and in GCs seem to show similar trends. Based on the lack of detailed information differences can not be observationally constrained, but no significant difference has been found so far (Kafando et al. 2016).
For EHB-stars the field and the GC population also seem to be in agreement with each other. However, since expect for He there is not much abundance information available for GC EHBs. In addition the picture is also not conclusive for the EHB. However, GCs lack the helium-rich sdOs found in the field.
This calls for a detailed analysis of field BHB stars, covering as many elements as possible

and using a big variety of available information for each star.

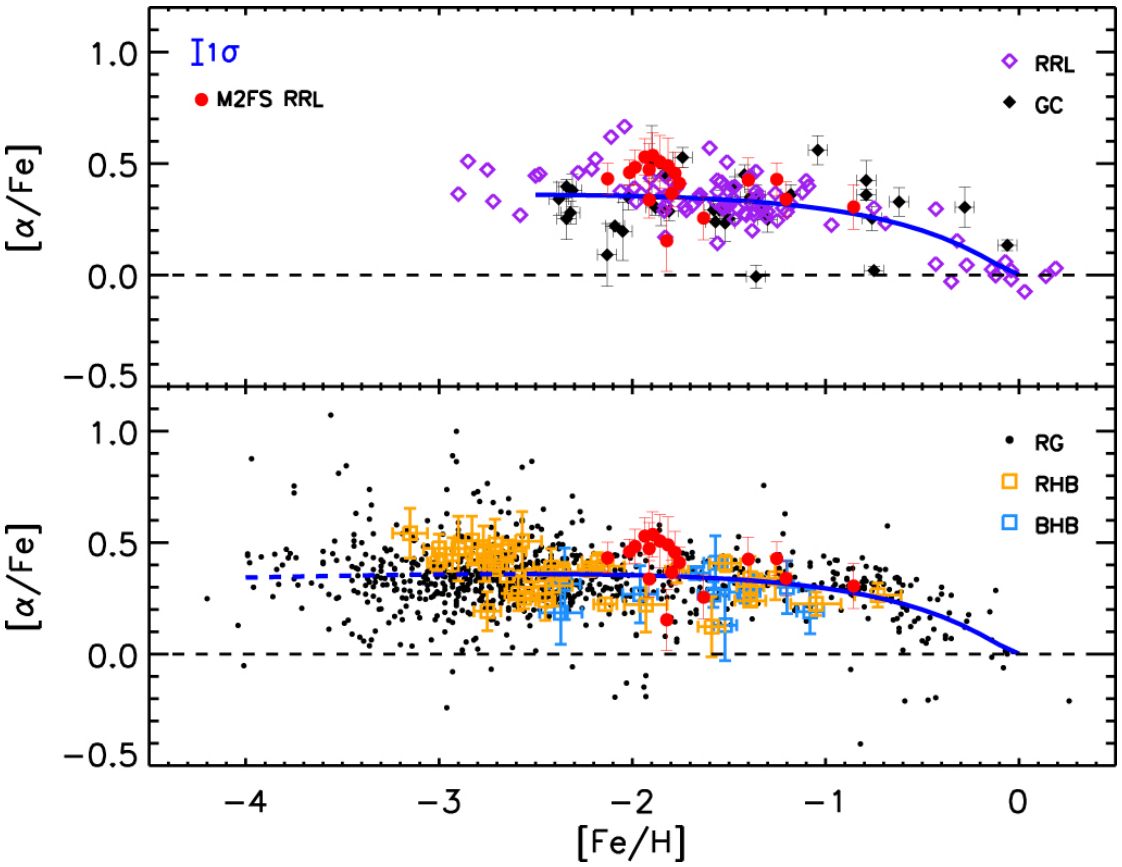

Figure 1.18: α-element abundance as a function of metallicity for GC (upper panel) and field (lower panel) stars,
red dots: RR Lyrae stars of ω Cen, purple diamonds: field RR Lyrae stars, black diamonds: GCs, black dots: halo giants, blue-orange squares: HB-stars from For and Sneden (2010) (Magurno et al. 2019)

2

Observations and instruments

This thesis is based on high-resolution spectroscopy from several spectrographs and telescopes, and high-precision astrometry from the Gaia mission.
Spectroscopy is one of the most important utilities in modern astrophysics to gain knowledge about astrophysical sources. The flux of the source is measured as a function of wavelength, frequency, or energy of the photons emitted by the source. For this purpose spectrographs are used in order to disperse the light of a source and sort it according to wavelength.
Hence, spectroscopy allows us to determine many fundamental parameters of a source such as dynamical, chemical, or other parameters. In stellar astronomy spectra are used for various purposes. They can be used to measure atmospheric parameters, the radial velocity, or chemical abundances from absorption lines in the spectrum. In order to obtain a detailed picture of a star, accurate spectra containing as much information as possible are essential.
The information obtained from spectra can be used as an input for other types of analysis. In order to derive stellar parameters and carry out kinematic analyses, astrometric measurements are needed, which became available recently by the Gaia mission. Therefore, further analysis steps heavily rely on Gaia.
The number of field BHB stars studied in detail, especially regarding the chemical abundances, is small. In order to increase the number of stars studied in detail and hence obtain a clearer picture of the properties of BHB stars, it is crucial to make use of available high quality spectra and Gaia-data.
This chapter will, therefore, discuss the spectroscopic and astrometric observations. The sample selection, the spectrographs used and the Gaia mission will be described.

2.1 Target selection

The stars studied were compiled from two separate samples. These will be explained individually and then as a whole new sample.

2.1.1 Altmann-Catelan sample

The vast majority of the stars were taken from a large sample of potential field BHB stars compiled by Martin Altmann and Marcio Catelan who obtained spectra with the UVES spectrograph at the ESO VLT.
The goal of this observing program is to study the kinematics of local halo BHB stars, therefore targeting relatively bright ($8 \leq V[\mathrm{mag}] \leq 11$) high-proper motion A and B type stars. High resolution and signal-to-noise spectra are needed for such studies, since they allow to determine precise radial velocities, derive abundances, and check if the stars observed are in fact BHB-stars. The analysis of such spectra will allow us to further characterize the structure and formation of the galactic halo.
In order to get a sample of local halo BHB-stars as clean as possible, criteria are needed for the target selection. These were all based on the Tycho catalog recorded by the Tycho-instrument aboard the Hipparcos satellite (Høg et al. 2000). A color-cut was applied: $B_T - V_T \in [-0.16, 0.22]$. This color-range corresponds to the colors of A and late-B type stars, which is appropriate for BHBs. The cut-off at blue colors also avoids the contamination of the sample with EHB-stars. However, more criteria are needed to target the BHB. A magnitude cut was applied to limit the sample to stars with reliable data $V_T < 11.0$ mag, since the Tycho catalog tends to become unreliable for fainter stars. Applying only these two criteria, will still leave a gigantic sample that will also contain many MS stars primarily from the Galactic disk. The kinematic properties of field BHBs have been studied before and higher proper motions would be expected for BHB stars than for MS stars belonging to the disk. Of course also radial velocities would be required for a clean kinematically chosen sample, but for radial velocities spectra are needed, thus the proper motion has to be used for a kinematic cut. To get a sample reasonable in size and to avoid contamination with nearby high proper motion MS-stars a proper motion cut was: $\mu_{\mathrm{tot}} \geq 50$ mas/yr (Altmann, priv comm.).
These criteria leave a sample of stars which were observed with UVES. All spectra were classified by eye and the 10 stars appearing to be the hottest were selected for further analysis. The criteria used for the by-eye inspection are the strength of the helium-lines, the form of the Balmer-lines and the amount of metal-lines visible in the spectrum.

2.1.2 Additional late B-type stars

The quantitative spectral analyses of the first sample revealed that their effective temperatures are lower than anticipated, except for the star HD 110942 all stars have T_{eff} lower than the NG1. In order to analyze stars with temperatures higher than the NG1, additional stars were selected from the literature and other observational programs.

The spectrum of BHB-star HD 110942 found in the first sample resembles the one of well-studied BHB-star Feige 86 quite well. Since both stars have similar spectroscopic characteristics and Feige 86 has been studied very extensively in the past (Baschek and Sargent 1976; Hartoog 1979; Bonifacio et al. 1995; Behr 2003b; Kafando et al. 2016; Németh 2017), hence also allowing for the comparison of the analysis strategy and the characterization of its validity, the latter was added to the second sample.
The presence of ^{3}He in the spectra of these two stars made a further and detailed analysis of ^{3}He in BHB stars possible. For this reason the two known ^{3}He BHB-stars PHL 382 and PHL 25 were added to the sample as well hereby also presenting the opportunity to later compare the results with those from the literature (Heber 1987; Schneider et al. 2018).
Beers et al. (2007) suggested that the star Feige 6 could be a BHB-star as well, probably of late-spectral type B. The availability of high quality UVES observations and an ESI spectrum of this star allows the verification of the assumption that Feige 6 is, in fact, a BHB-star additionally analyzing the abundances in this star. Therefore, Feige 6 was added to the sample.

2.1.3 Final sample

The selection from the sample described in Sec. 2.1.1 and from other sources leaves a sample of 14 stars to analyze. For these high-resolution, high signal-to-noise spectra from various instruments are available. The stars are spread over a range of different spectral types, hence potentially sampling the BHB on both sides of the NG1. This sample containing A-BHB-stars as well as B-BHB-stars allows for a very detailed spectroscopic analysis from which the atmospheric and the chemical properties of the stars can be derived, leading to an increase of the number of field BHB-stars studied. Additional data for all program stars are available from Gaia DR2 and multiple photometric surveys. This allows the stars to be analyzed not only based on spectroscopy, but also enables kinematic and photometric studies. The stars, their positions, and the spectrograph used for the analysis of the star are listed in Tab. 2.1.

Table 2.1: Program-stars and the spectrograph used to study them

star	right ascension	declination	spectrograph
CD-38 8806	13h 47m 39.963s	-39° 10' 18.707"	UVES
CD-48 14233	22h 31m 50.633s	-47° 29' 38.289"	UVES
HD 8269	01h 21m 47.688s	-15° 3' 5.488"	UVES
HD 12655	02h 03m 38.344s	-18° 37' 22.603"	UVES
HD 23342	03h 43m 27.326s	-28° 28' 11.024"	UVES
HD 156758	17h 19m 08.766s	05° 38' 56.733"	UVES
HD 209292	22h 02m 38.463s	-19° 23' 08.383"	UVES
TYC 1914-687-1	07h 31m 35.426s	24° 40' 12.733"	UVES
TYC 6036-1933-1	09h 13m 36.469s	-20° 31' 40.352"	UVES
HD 110942	12h 45m 58.963s	-43° 05' 21.717'	UVES
Feige 86	13h 38m 24.766s	29° 21' 56.007"	UVES
PHL 25	21h 31m 55.937s	-17° 19' 32.621"	HRS
PHL 382	22h 43m 6.037s	-14° 50' 37.772"	FEROS
Feige 6	0h 43m 2.533s	-8° 46' 32.297"	UVES and ESI

2.2 The UVES spectrograph at the ESO VLT

UVES is the most used instrument for the sample, therefore, this particular instrument will be reviewed in more detail than the others.

2.2.1 The instrument

The Ultraviolet and Visual Echelle Spectrograph (UVES) is an echelle spectrograph located at the Very Large Telescope (VLT) which is operated by the European Southern Observatory (ESO). The instrument (see Fig. 2.1) is mounted at the Nasmyth focus of unit telescope 2 (UT2, Kueyen) and started operation in April 2000. UVES is designed to deliver high-quality and high-resolution spectra covering a spectral range from 3000 Å up to 11000 Å. At the lower end the wavelength is restricted by the atmosphere, and at the higher one the size of the CCDs is the limiting factor. The instrument has two arms, separating the UV/blue part from the visual/red one, allowing for a higher efficiency to be reached. The maximum resolving power R of UVES is $\sim 80,000$ and $\sim 110,000$ for the blue and red arms, respectively, and $\sim 40,000$ in narrow slit mode (Dekker et al. 2000; Mieske 2019).
The light of the source collected by the 8m unit telescope enters the pre-slit unit of UVES through the telescope shutter. The single stations on the light path through UVES are illustrated in Fig. 2.2. The light then enters the calibration unit which consists of a mirror system and a Th-Ar calibration lamp used for wavelength-calibration. This unit is used to ensure that the calibration light and the source light enter the instrument in the exact same way. The derotator parallelizes the beam and compensate for losses introduced through rotation of the telescope. Next, the beam will pass through the filter-wheel which offers to apply different filters using the Johnson-system. The atmospheric dispersion corrector (ADC) will reduce atmospheric dispersion effects. After that a depolarizer can be used to get rid of polarization introduced by the telescope, and the pupil-stop prevents stray light from entering the setup. Before the light enters the actual spectrograph the spectral-arm has to be chosen. Different modes can be used in UVES. The spectrograph can be run in single-arm mode, selecting the red or blue arm only. UVES also offers two different two arm-modes, enabling observations with both arms simultaneously making use of dichroic beam splitters. The two two-arm modes, DICHR#1 and DICHR#2, differ in wavelength-coverage (Dekker et al. 2000; Mieske 2019).
Both arms are built in a similar way. Light enters the spectrograph through the slit units and is then reflected to the main collimator by a mirror. The slit unit consists of a filter wheel and interference filters in order to reject stray light and to isolate certain echelle orders. Once the beam is collimated it is directed towards the echelle grating, where the light is diffracted and separated into overlapping refraction orders which match the upcoming CCDs in width, and then back to the collimator. A small fraction of the light is directed to the exposure-meter which is used to monitor the total amount of light entering the instrument, before hitting the grating. The now dispersed beam is directed towards the crossdisperser unit which is used to disperse the beam again in order to separate the higher orders from each other. The beam then enters the cameras through

a focusing module and is then recorded by the CCD (Dekker et al. 2000; Mieske 2019).

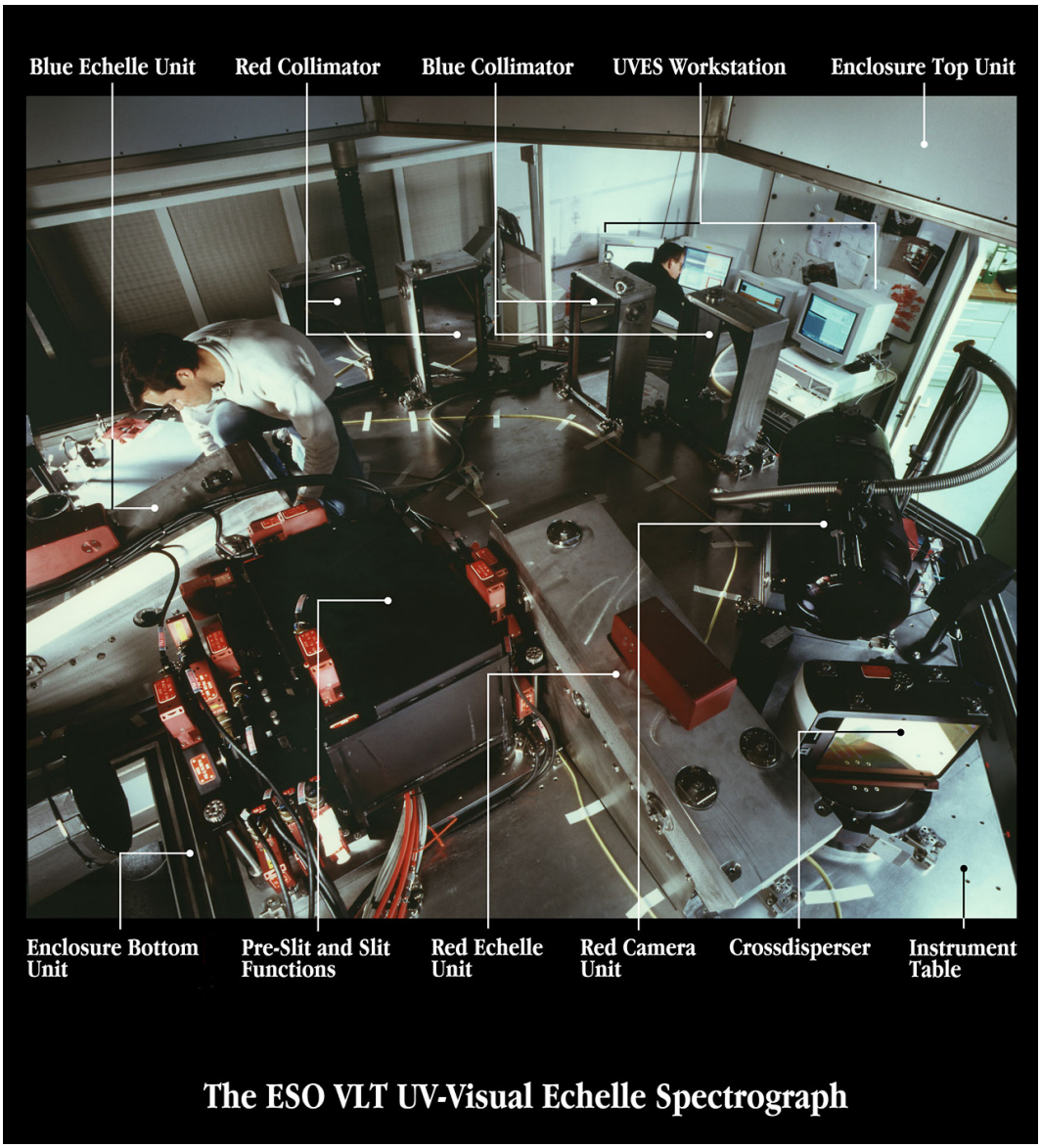

Figure 2.1: The UVES spectrograph [1]

[1] https://www.eso.org/public/images/eso9854b/ (last accessed: 12/16/2019, 3:05pm)

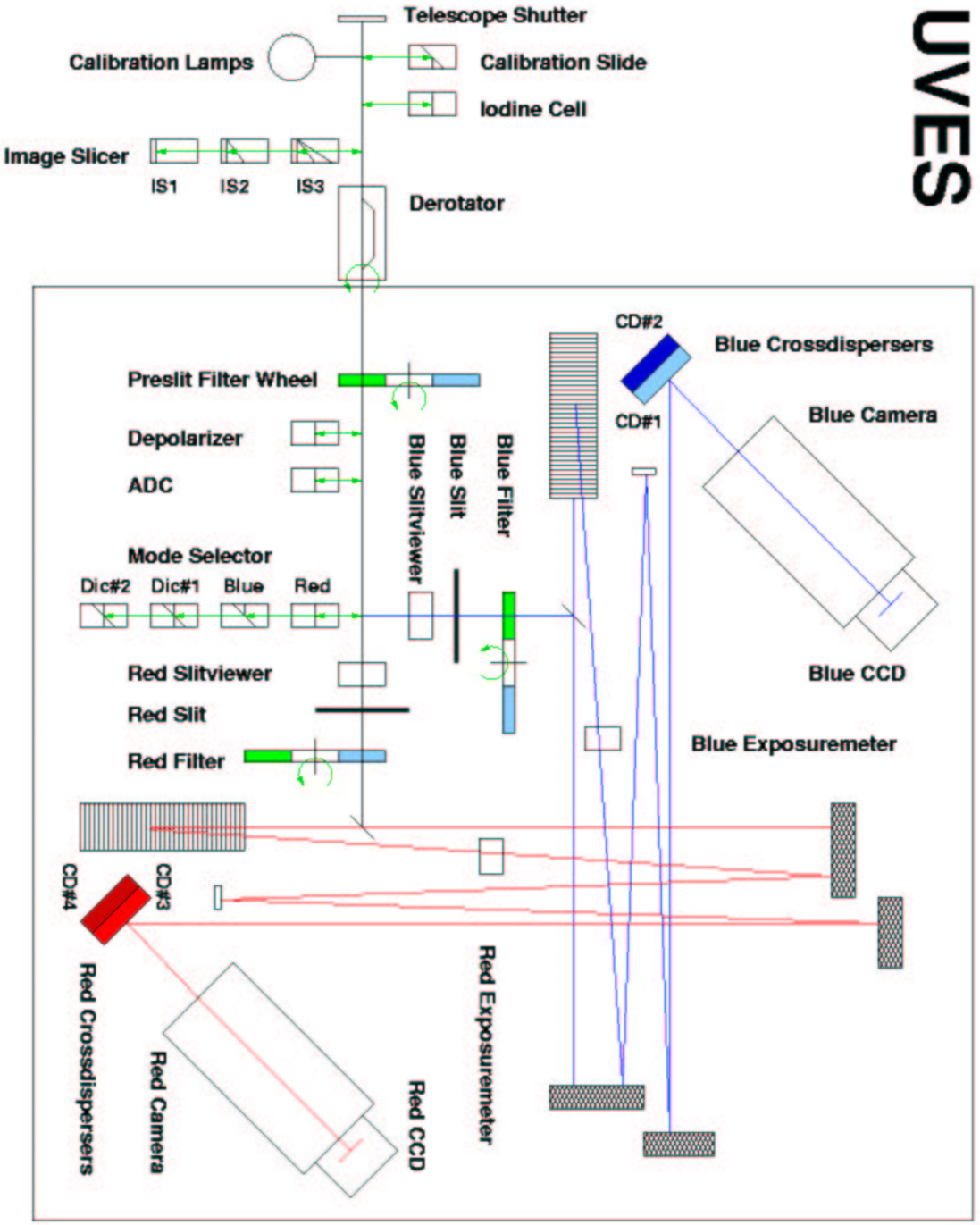

Figure 2.2: UVES setup (Mieske 2019)

2.2.2 Observational data

The spectra taken from the sample discussed in Sec. 2.1.1 were all recorded between May 2017 and April 2018 with exposure times between 300 s and 1100 s. The two-arm mode DICHR#2 was used which corresponds to a wavelength-coverage from 3755 Å to 4982 Å for the blue as well as 5692 - 7530 Å and 7658 - 9463 Å for the red arm. The resolution used in the blue and red arm was 40970 and 42310 set by the chosen slitwidth of 1 arcsec, respectively. The signal-to-noise ratio (SNR) was typically in a range of 200 or higher. Some spectra show a wobble-like structure, as can be seen in Fig. 2.3. These wobbles seem to decrease their period with increasing wavelength. Probably, these wobbles are caused by a miss-aligned flat-field. Due to the wobbles in the data an attempt was made to reduce the data and get rid of the wobbles, which will be discussed in the next section. The two sets of spectra of Feige 86 were obtained in 2006 using both DICHR#1 and DICHR#2, covering slightly different spectral ranges.
Four spectra of Feige 6 were recorded in October 2018 using DICHR#2. In order to obtain a higher SNR and to speed up the analysis, the spectra of the respective channels were all co-added which can be done since the individual spectra did not show radial velocity variations. Beforehand, the spectra were all corrected for barycentric movement and then divided by the median flux in order to roughly normalize the spectra. The SNRs of the individual spectra was taken as a weighing factor and the fluxes of the spectra were averaged. The resolution of the spectrum was used to obtain a common wavelength-scale for the spectra.

2.2.3 Data reduction

Spectrographs do not directly record spectra which can be scientifically analyzed. The raw-data recorded has to be reduced, using calibration data which also requires exact knowledge of how the instrument operates. The raw-data files and their corresponding calibration data files can be downloaded from the ESO raw-data archive. The data-reduction was performed using ESOs Recipe Flexible Execution Workbench REFLEX (Freudling et al. 2013). This interface can use all instrument pipelines and allows to adjust every sub-procedure individually and in real-time (Sterzik 2018). Therefore, it is very easy to adjust individual parameters and try different parameter-combinations to get rid of the wobbles.
The pipeline will create master calibration files in the first step. First, the detectors bias and dark currents have to be eliminated from the data. Therefore, a master bias frame is created from the raw bias frames. Using this master bias frame and the raw dark frames a master dark frame is created. Next, the single echelle orders have to be detected. This is performed using an order guess from a format check frame obtained using the ARC lamp. Using this guess the order position is determined with help of a continuum lamp. Flat field frames and other calibration frames are then used to create a master

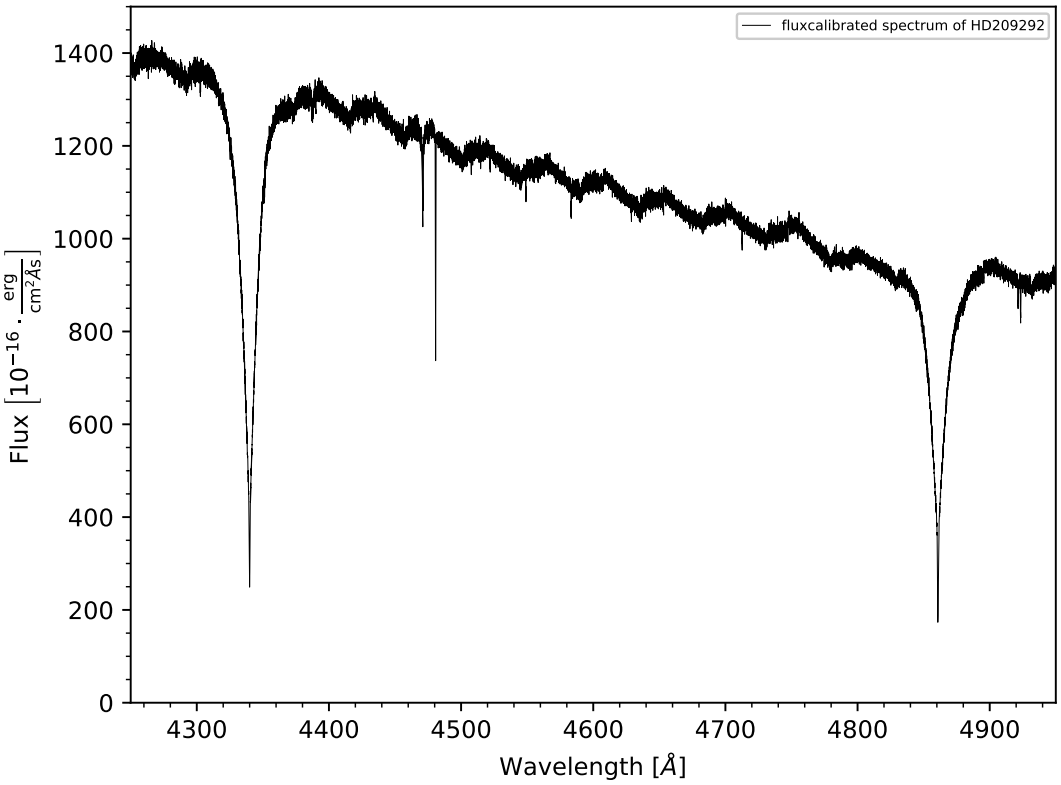

Figure 2.3: The wobbles in the UVES spectrum of HD 209292

flat field which allows corrections of pixel sensitivity variations and the blaze function. Then a wavelength-calibration can be performed and the response of UVES can be taken into account. It is performed using the ARC lamp and tracing the known lines of the lamp through the instrument. Using a standard star the response of the telescope and spectrograph can be determined. With all calibration files and the recorded spectrum of the star the final spectrum can be extracted and fully calibrated. By default, Reflex will produce the fluxun- as well as the flux-calibrated spectra (Sterzik 2018; Peron 2017). Various combinations of calibration parameters were tried, but unfortunately no way was found to reduce the wobbles in the spectra. Therefore, all the spectra were reduced using the default settings of Reflex in the end.

Table 2.2: Observational data of UVES spectra

star	date of observation [yyyy-mm-dd]	exposure time [s]
CD-38 8806	2017-05-06	938
CD-48 14233	2017-08-11	1153
HD 8269	2017-09-11	722
HD 12655	2017-08-11	300
HD 23342	2018-01-30	594
HD 156758	2018-04-03	882
HD 209292	2017-06-09	1109
TYC 1914-687-1	2018-02-03	1050
TYC 6036-1933-1	2018-01-17	1090
HD 110942	2017-05-03	800
Feige 86	2006-03-19	1400 and 1600
Feige 6	2018-10-01	1450

2.3 The FEROS spectrograph at ESO La Silla

2.3.1 The instrument

The Fiber-fed Extended Range Optical Spectrograph (FEROS)[2] (see Fig. 2.4) is currently mounted at the MPG/ESO-2.2m telescope at the ESO site in La Silla, after being first attached to the now decommissioned ESO 1.52m-telescope in November 1998. FEROS is a high efficiency and high resolution spectrograph with R $\sim$ 48,000 and covers a spectral range between 3,500 Å and 9,200 Å. The spectrograph is fed by two fibers, hence allowing observations and calibration measurements to be performed at the same time. The calibration fiber is either fed by a calibration lamp or by a region in the sky close to the target in order to monitor the sky background (Kaufer et al. 1999). Further attempts for data-reduction were not necessary, because the spectra did not show any problematic structures.

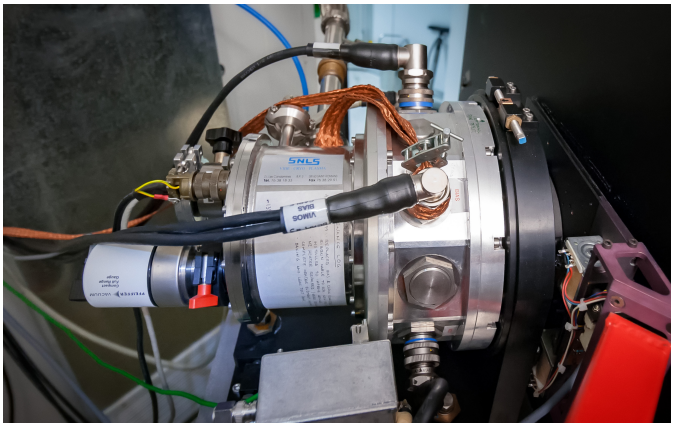

Figure 2.4: The FEROS spectrograph [3]

2.3.2 Observational data

The star PHL 382 was observed using FEROS. In total, seven spectra were obtained during September 2004 and October 2006. Exposure times between 600 s and 700 s were used. The spectra were co-added since they did not show any radial velocity variation, resulting in a SNR of $\sim$145 at $\lambda \sim 4936$Å. The individual spectra were radial velocity corrected and then co-added weighted by the SNR. The radial velocity for this star, which was adapted for the further analysis, was calculated as the average of all individual spectra (Edelmann and Heber, priv comm.). Co-addition was already performed by Schneider et al. (2018) using SPAS (Spectrum Plotting and Analysis Suite). Schneider et al. (2018) also analyzed the spectrum.

[2] https://www.eso.org/sci/facilities/lasilla/instruments/feros/overview.html (last accessed: 12/19/2019, 4:10pm)
[3] https://www.eso.org/public/images/AGIL1873-CC/ (last accessed: 12/19/2019, 4:04pm)

2.4 The HRS spectrograph at McDonald

2.4.1 The instrument

HRS (high resolution spectrograph) is a cross-dispersed echelle spectrograph. This instrument is mounted at the Hobby-Eberly Telescope, currently one of the five biggest telescopes worldwide, at the McDonald Observatory in Texas. The spectrograph is fiber-fed. The resolution can be varied from 30,000 up to 120,000 and a spectral range of 4,200 Å to 11,000 Å is covered (Tull 1998).

2.4.2 Observational data

PHL 25 was observed with HRS in January 2006. A total of two spectra were obtained, with a resolution of 60,000 and a SNR of up to 57 at $\lambda \sim 5466$Å. These spectra showed no radial velocity variations and, hence, were also co-added (Schneider et al. 2018). Again the radial velocity for sub-sequent analysis steps was determined by averaging the radial velocity shifts observed previously in the individual spectra (Edelmann and Heber, priv comm.).

2.5 The ESI spectrograph at Keck

2.5.1 The instrument

The Keck observatory located on Maunakea in Hawaii at 4.2 km altitude has two 10 m telescopes. Keck II is the host telescope of ESI. The Echellette Spectrograph and Imager (shown in Fig. 2.5) is an instrument which can be used for many different applications. It offers three modes, an echellette cross-dispersed mode with a resolving power of 13,000, a low-dispersion prismatic mode with resolving powers between 1,000 and 6,000, and an imaging mode. ESI uses prisms as dispersive elements. The spectral range covered is from 3,900 Å up to 11,000 Å (Sheinis et al. 2002).

2.5.2 Observational data

With ESI two spectra of Feige 6 were recorded in July 2018 using the 1 arcsecond slit, which then, since the 0.3 arcsec slit corresponds to R∼13,000, results in a resolving power of 3,900. The exposure time used was 180 s. These spectra were co-added in the same way as the UVES spectra, with the resulting SNR being ∼200 at 4000 Å.

Figure 2.5: The ESI spectrograph [4]

[4] https://www2.keck.hawaii.edu/inst/esi/ (last accessed: 12/21/2019, 11:44am)

2.6 Gaia

The spectroscopic analyses gives the radial velocities of all stars through the Doppler-formula, which will be discussed later on. Theses radial velocities are very accurate due to the high quality spectra used to derive them. However, since the radial velocity only quantifies the movement of a star in the line of sight, so towards or away from earth, additional information is needed to reconstruct the exact spatial movement of a star. Especially, the distance and the proper motions, the movement on the celestial sphere in direction of right ascension and declination, have to be known additionally to v_{rad}. Also, exact positions are needed. This kind of information can not be obtained by spectroscopy, hence, astrometry is needed. Since ground based astrometry is available for very few stars only, due to the position measurement-accuracy being limited by the atmosphere, space-based observations are crucial. The kinematic analyses, therefore, heavily relies on the space-mission Gaia. In the following, this space-observatory and the data used will be reviewed.

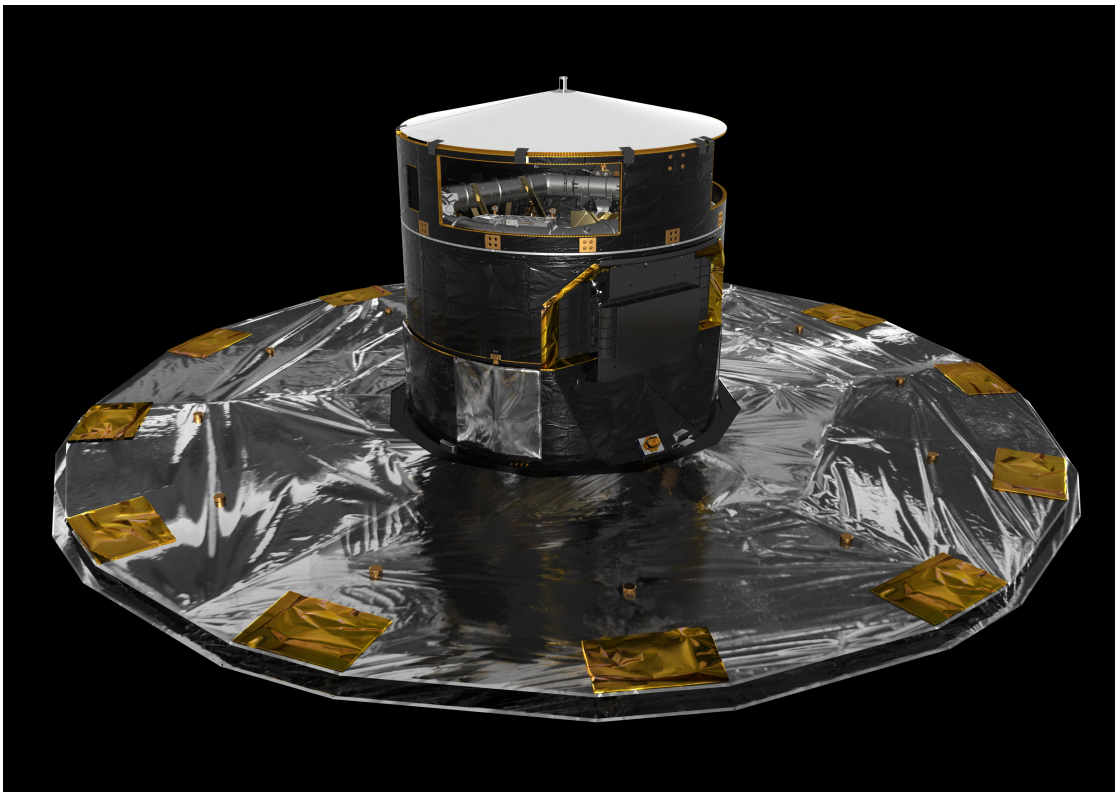

Figure 2.6: The Gaia spacecraft [5]

[5]ESA, ATG medialab, https://www.cosmos.esa.int/web/gaia/media-gallery/images/ig_spacecraft (last accessed: 12/27/2019, 11:50am)

2.6.1 The instrument

The Gaia spacecraft, which is shown in Fig. 2.6, was launched in December 2013 and reached its orbit around the L2-point a few weeks later. In summer 2014 science operations started. Gaia is an all-sky survey and scans the sky using two fields of view (FOV). The spacecraft slowly rotates around its own axis. Hence, objects observed by Gaia, which are all objects in the current field of view, will transit along the focal plane and be registered by the CCDs. Using two FOVs allows the relative measurements to be converted into absolute parameters. Gaia is mainly an astrometry mission and can measure accurate positions, parallaxes, and proper motions. However, Gaia also has spectrographs on board, hence, radial velocities of bright targets can be measured as well. Using the Gaia passband filters, additionally, photometric data of targets can be acquired. The second data release of Gaia (DR2) provides measurements for almost 1.7 billion targets and 5-parameter astrometry (right ascension, declination, parallax, and proper motions) for nearly 1.3 billion targets (Gaia Collaboration et al. 2016, 2018a,b).

2.6.2 Observational data

The positions in right ascension and declination, the proper motions in these two coordinates, denoted μ_α and μ_δ, the parallaxes ϖ, the respective uncertainties, and the correlation functions of the parallax and proper motions and the correlations function of the proper motions are taken from DR2 (Gaia Collaboration et al. 2018b) [6]. Proper motions and parallaxes are all given in milliarcseconds [mas]. The astrometric data used is listed in Tab. 2.3, the Gaia Id of each star and the correlation functions are listed in the appendix A1 in Tab.1.
Parallaxes are important because they give the distances of stars. Gaia has revolutionized the whole field in this context, Never before have so many distances been determined. The distance is derived from the parallax using the well known correlation:

$$d = \frac{1}{\varpi} \tag{2.1}$$

Since the parallaxes are all positive and have uncertainties below 20 % this approach can be used. For higher uncertainties and negative parallaxes statistical measures would be needed (Bailer-Jones 2015). The Renormalised Unit Weight Error (RUWE) is a statistical indicator for how trustworthy the astrometry of a source is. Values greater than 1.4 indicate a bad fit and, hence, data for these sources should not be used (Lindegren 2018). For all program stars the RUWE indicates that the Gaia data used here is reliable (RUWE for all stars is listed in Tab. 1 in App. A1).
Additionally, Gaia data is not only useful for the kinematic analyses. The apparent magnitudes of the program stars in the Gaia bands G (3300 Å - 10500 Å), G_{BP} (3300 Å - 6800 Å) and G_{RP} (6300 Å - 10500 Å) are used for the photometric analyses as well.

[6] data taken from Gaia archive https://gea.esac.esa.int/archive/

The parallaxes are employed to determine stellar parameters based on photometry and spectroscopy.

Table 2.3: Gaia astrometry data

	α	δ	ϖ	μ_α	μ_δ
star	[deg]	[deg]	[mas]	[mas]	[mas]
CD-38 8806	206.916511	-39.171863	1.47 ± 0.08	-38.66 ± 0.12	-43.52 ± 0.15
CD-48 14233	337.960970	-47.493969	0.97 ± 0.07	18.0 ± 0.1	-44.60 ± 0.09
HD 8269	20.448701	-15.051525	1.48 ± 0.06	-2.1 ± 0.1	-81.67 ± 0.09
HD 12655	30.909766	-18.622945	2.83 ± 0.06	90.85 ± 0.09	-128.92 ± 0.09
HD 23342	55.863859	-28.469729	1.31 ± 0.06	62.22 ± 0.07	-1.19 ± 0.09
HD 110942	191.495680	-43.089366	3.86 ± 0.08	-46.92 ± 0.12	7.73 ± 0.13
HD 156758	259.786523	5.649093	1.70 ± 0.08	-33.32 ± 0.13	-46.26 ± 0.09
HD 209292	330.660265	-19.385662	1.4 ± 0.1	26.79 ± 0.15	-62.38 ± 0.13
TYC 1914-687-1	112.897608	24.670204	0.88 ± 0.06	-50.1 ± 0.1	-40.69 ± 0.09
TYC 6036-1933-1	138.401952	-20.527876	1.06 ± 0.06	-48.68 ± 0.09	-12.5 ± 0.1
Feige 86	204.603119	29.365078	3.14 ± 0.08	-14.42 ± 0.15	-111.31 ± 0.09
PHL 25	322.983072	-17.325728	1.8 ± 0.1	12.31 ± 0.15	-72.21 ± 0.11
PHL 382	340.775153	-14.843825	1.07 ± 0.08	13.88 ± 0.17	-21.09 ± 0.19
Feige 6	10.760552	-8.775638	0.33 ± 0.06	-2.05 ± 0.15	-27.74 ± 0.07

3

Methods: overview

The analysis of every star is carried out in four steps. Thus a detailed picture of all program stars can be obtained using various available kinds of data. All these steps and relevant information will be presented in chapters 4 through 7.
1.) Atmospheric parameters and chemical abundances are determined by means of a quantitative spectral analysis using a hybrid LTE/NLTE approach which will be discussed in chapter 4.
2.) The angular diameter and interstellar reddening are derived from photometry. The photometric analysis is carried out adapting the atmospheric parameters determined in the first step through fitting the spectral energy distribution (SED). Additionally, the photometry of every program star is analyzed as a stand-alone dataset, hence, providing a consistency check for the spectroscopic analysis. The used data and the analyses will be described in chapter 5.
3.) Combining the atmospheric parameters derived in step 1, the angular diameters with the trigonometric parallaxes measured by the Gaia mission allows the stellar parameters mass, radius, and luminosity to be determined. How these parameters can be calculated will be summarized in chapter 6.
4.) Finally, the Galactic kinematics of the sample can be studied from the 6 dimensional phase information. The radial velocities from spectroscopy, Gaia parallaxes, proper motions, and positions are used to perform calculations of Galactic trajectories based on different Galactic mass models. Orbit calculation allows one to classify the stars kinematically. Chapter 7 will deal with the kinematic analyses.
Many parts of the analysis and information presented in these chapters are based on the work of Irrgang (2014) and Irrgang et al. (2014).

4

Quantitative spectral analysis

The high-quality spectra discussed in chapter 2 are analyzed by matching the observations to a pre-calculated grid of model-spectra. Therefore, the formation and identification of these lines will be the basis for the further discussion. The model spectra used were calculated using a hybrid LTE/NLTE approach. Since the computation of model-spectra requires the calculation of model atmospheres, the theoretical background of stellar atmospheres and assumptions going into the models will be reviewed shortly. Finally, this chapter will close describing the fitting method. Spectral fits of selected objects are show in appendix A6.

4.1 Spectral lines

Generally, the radiation field of stars, especially their interiors, is approximated as a black body. This approximation also gives the effective temperature $T_{\rm eff}$ of a star, as the black body has a continuous spectrum purely governed by its temperature. Therefore, the effective temperature of a star is defined as the temperature of a black body with the same radiative power as the observed star. However, stellar atmospheres can not be seen as black bodies. The continuum of a stellar spectrum arises from the hotter inner layers of the atmosphere, however, stellar spectra show several features such as spectral lines and continuum discontinuities.

4.1.1 Line formation

Spectral lines form in the cooler outer layers of the atmosphere and are either in absorption or in emission, meaning the flux at the wavelength of the line is either below or above continuum flux, respectively. Lines are associated with atoms and ions that are present in the atmosphere, hence, providing an access to analyze the composition of the stellar atmosphere. Spectral lines are due to interactions of emitted photons with the constitutes of the atmosphere. Photons are absorbed by atoms and ions through atomic

transitions, mostly through bound-bound transitions. For these specific transitions the energy of the absorbed photon matches an orbital transition of an electron. Therefore, lines of certain elements are observed at specific wavelengths in the spectrum, governed by the orbital transitions. The strength of the line is linked to the abundance of the element. The shape of the line depends on different properties, mainly the physical properties of the surrounding plasma. Lines are not infinitely sharp in the spectrum, but are broadened by a bunch of processes which can be divided into microscopic and macroscopic ones.
Microscopic processes: First of all, according to the Heisenberg uncertainty principal, the finite lifetime of an excited atomic level corresponds to a finite width of the level energy. Of course, all elements and ions will interact with each other via the Coulomb force, giving rise to changes in the atomic structure and the Stark effect. Therefore, the lines will be broadened scaling with the electron density. As the particles in the plasma move, the emitted and absorbed photons are subject to the Doppler effect, causing Gaussian-shaped broadening. The movement of particles are due to thermal movement and, possibly, additional terms, called microturbulence, accounting for movements on length scales below the photon-mean free path.
Macroscopic processes: Macroscopic movements of a star will introduce additional broadening terms. Stellar rotation leads to an ellipse shaped broadening profile. Macroturbulence, meaning macroscopic movements present in the stellar atmosphere, lead to a triangular shaped profile. Finally, the instrument also introduces an additional broadening since every spectrograph has a finite resolving power, hence, blurring spectral lines.

4.1.2 Line identification

The spectra presented in chapter 2 exhibit spectral lines from different atoms and ions. Due to existing atomic data these, lines can be identified as specific transitions of chemical elements in different stages of ionization. The ions and the neutral atoms of the same elements show different lines in the spectrum. The identification, therefore, also makes it possible to distinguish the different ionization stages of the elements from each other which also is a temperature indicator because the ratios of different ionization stages depend on the temperature. Lines are identified using the tabulated wavelength data of atomic transitions found in Moore (1959).
The most prominent lines in the spectra are those of hydrogen. In the covered spectral range two hydrogen-transition series are relevant. The Balmer-series is associated with transitions from the level with quantum number n=2 towards higher levels. The second series is the Paschen-series which are transitions originating from n=3.
Helium lines are visible in the spectra as well and can also be identified, providing additional sensitivity to the determination of temperature.
Additionally, lines of many different metals, mostly in singly ionized or neutral state, are found in the spectra, such as iron, magnesium, silicon, titanium, oxygen, etc.. Since identifying each of the hundreds of lines observed in the spectra is very time consuming,

not every line is identified in the beginning. As many lines are included in model atoms used, it is possible to classify most of the lines during the analysis, leaving only those lines unmatched in the fitting procedure which are not included in the respective model atoms or are caused by elements not included in the analysis.
The spectra also include lines not caused by processes associated with the star, because light emitted by the star passes through the interstellar medium (ISM). Therefore, also imprints of the ISM are seen in the spectra, such as the sodium I dublett at $\sim$ 5,890 Å or the CaIIűnd K lines at 3,934 Å and 3,968 Å. The interstellar lines have to be excluded from the analysis. The stellar light passes through the atmosphere, too, imprinting lines of water and ozone into the spectrum. These telluric bands have to be excluded as well.

4.2 Stellar atmospheres

To derive the emergent spectra detailed atmospheric models are required, therefore, the most basic theoretical background will be recapped in the following section. As assumptions about the state of the plasma have to be made beforehand, the differences between the two approaches typically used will be explained. Incorporating different models into the final synthetic spectra requires the availability of model atoms or lists of atomic data.

4.2.1 Theoretical background

The structure of a star is governed by the so called stellar structure equations. This set of differential equations assumes mass continuity, hydrostatic equilibrium, energy conservation, and energy transport by either convection or radiation. These equations hold in every layer of the star, including the most outer ones, the stellar atmosphere. This is the region of the star mainly responsible for the formation of the spectrum. Therefore, it is crucial to model the stellar atmosphere in order to understand how stellar spectra are formed. This also allows model spectra to be calculated, which then can be matched to the observed spectra, hence, making it possible to obtain the atmospheric parameters of the observed stars.
In order to model the atmosphere radiative transfer has to be considered. The basic quantity used is the specific intensity I_ν which is a function of frequency defined as the energy per frequency interval $\mathrm{d}\nu$ and time $\mathrm{d}t$ passing in the direction of the solid angle $\mathrm{d}\Omega$ through an area $\mathrm{d}A$ inclined by an angle θ towards the solid angle:

$$I_\nu = \frac{\mathrm{d}E}{\mathrm{d}A \cdot \mathrm{d}t \cdot \mathrm{d}\Omega \cdot \mathrm{d}\nu \cdot \cos(\theta)} \tag{4.1}$$

The specific intensity is linked to the total intensity I by integration over the entire frequency space and to the total flux F through integrating over the full solid angle and all frequencies:

$$F = \int_0^\infty \int_{4\pi} \mathrm{d}\nu \mathrm{d}\Omega \; I_\nu \cos(\theta) \tag{4.2}$$

The flux again can be connected to the luminosity of the star by integrating over its surface and making use of the Stefan-Boltzmann law ($F = \sigma_{\mathrm{SB}} \mathrm{T}_{\mathrm{eff}}$) where R denotes the stellar radius and σ_{SB} is the Stefan-Boltzmann constant:

$$L = \int_A \mathrm{d}A' \; F = 4\pi R^2 F = 4\pi R^2 \sigma_{\mathrm{SB}} \mathrm{T}_{\mathrm{eff}}^4 \tag{4.3}$$

The radiative transfer in the stellar atmosphere is described by the radiative transfer equation (RTE):

$$\mathrm{d}I_\nu = \kappa_\nu I_\nu \mathrm{d}s + \eta_\nu \mathrm{d}s \tag{4.4}$$

$\mathrm{d}s$ is the distance radiation has traveled in the direction of a solid angle, the opacity κ_ν is used to subsume all absorption-processes and the emissivity η_ν for all emission-processes. In order to simplify the RTE plane-parallelity can be assumed, with the advantage that photons travel in one direction only, outwards to the stellar surface $\mathrm{d}z = \mathrm{d}s \cos(\theta)$. The optical depth τ_ν

$$\tau_\nu = -\int_{z_0}^{z} \mathrm{d}z' \; \kappa_\nu \tag{4.5}$$

can be used to rewrite the RTE.
Therefore, the RTE can be expressed as:

$$\cos(\theta)\mathrm{d}I_\nu = I_\nu \mathrm{d}\tau_\nu - \frac{\eta_\nu}{\kappa_\nu}\mathrm{d}\tau_\nu \tag{4.6}$$

A formal solution for eq. 4.6 exists, considering the intensity between two different optical depths τ_1 and τ_2, which depend on ν. By defining the source function $S_\nu = \frac{\eta_\nu}{\kappa_\nu}$ the formal solution of eq. 4.6 can be expressed in the following way:

$$I_\nu(\tau_1, \cos(\theta)) = I_\nu(\tau_2, \cos(\theta)) \; \exp\left(-\frac{\tau_2 - \tau_1}{\cos(\theta)}\right) + \int_{\tau_1}^{\tau_2} \mathrm{d}\tau \; \frac{S_\nu(\tau)}{\cos(\theta)} \exp\left(-\frac{\tau - \tau_1}{\cos(\theta)}\right) \tag{4.7}$$

Equation 4.7 shows that the intensity drops exponentially from high optical depths outwards. However, eq. 4.7 can only be evaluated if the source function is independent from the intensity but this may not be the case, since the radiation field will influence the matter and vice-versa.
Assuming a plane-parallel geometry is justified since the thickness of the atmosphere is very small compared to the stellar radius. This, however, allows one to treat the

atmosphere in layers. The atmosphere is assumed to be chemically homogeneous, making the structure a function of z (z increases towards the surface) or of optical depth. The latter is also a function of wavelength. Therefore, an appropriate mean opacity has to be determined based on Rosselands prescription. The atmosphere is considered stationary, neglecting temporal changes in the structure such as pulsations. As in all the other layers of the star hydrostatic equilibrium is assumed to be established. The hydrostatic equation then reads:

$$\frac{\mathrm{d}P(z)}{\mathrm{d}z} = -G\frac{M}{R^2}\rho(z) = -g\rho(z) \tag{4.8}$$

Where G is the gravitational constant and g is the surface gravity. This equation links the pressure to the stellar parameters M and R and the depth-dependent density $\rho(z)$. The pressure is the sum of two terms, one due to the surrounding matter (plasma) and one due to radiation pressure. Assuming that the opacity and emissivity are isotropic, the radiation pressure term from eq. 4.8, which depends on the frequency, can be linked to the frequency dependent flux F_ν. Here, c denotes the speed of light:

$$\frac{\mathrm{d}P_{\mathrm{rad},\nu}(z)}{\mathrm{d}z} = \frac{1}{c}\int_{4\pi} \mathrm{d}\Omega\ \frac{\mathrm{d}I_\nu}{\mathrm{d}z}\cos^2(\theta) = -\frac{\kappa_\nu}{c}F_\nu \tag{4.9}$$

By integrating eq. 4.9 over the entire frequency space and introducing the radiative acceleration g_{rad}, the equation simplifies to:

$$\frac{\mathrm{d}P_{\mathrm{rad}}(z)}{\mathrm{d}z} = \int_0^\infty \mathrm{d}\nu\ \frac{\mathrm{d}P_{\mathrm{rad},\nu}(z)}{\mathrm{d}z} = -\frac{1}{\rho(z)c}\int_0^\infty \mathrm{d}\nu\ \kappa_\nu F_\nu \rho(z) = -g_{\mathrm{rad}}\rho(z) \tag{4.10}$$

Therefore, the pressure by the plasma can be described as:

$$\frac{\mathrm{d}P_{\mathrm{plasma}}(z)}{\mathrm{d}z} = -\rho(z)(g - g_{\mathrm{rad}}) \tag{4.11}$$

In the last step, radiative equilibrium is assumed. That means that emission and absorption are in equilibrium with each other which can be expressed as:

$$\int_0^\infty\int_{4\pi} \mathrm{d}\nu\mathrm{d}\Omega\ \kappa_\nu I_\nu = \int_0^\infty\int_{4\pi} \mathrm{d}\nu\mathrm{d}\Omega\ \eta_\nu \tag{4.12}$$

This can be rewritten using the RTE as:

$$\int_0^\infty\int_{4\pi} \mathrm{d}\nu\mathrm{d}\Omega\ (-\kappa_\nu I_\nu + \eta_\nu) = \int_0^\infty\int_{4\pi} \mathrm{d}\nu\mathrm{d}\Omega\ \left(\frac{\mathrm{d}I_\nu}{\mathrm{d}z}\cos(\theta)\right) \tag{4.13}$$

By pulling the derivative in front of the integrals eq. 4.12 can be expressed in terms of

flux using eq. 4.2.

$$\frac{\mathrm{d}}{\mathrm{d}z}\int_0^\infty\int_{4\pi}\mathrm{d}\nu\mathrm{d}\Omega\ I_\nu\cos(\theta)=\frac{\mathrm{d}F}{\mathrm{d}z}=0 \tag{4.14}$$

The flux is linked to the effective temperature, which means that the equations governing the structure of the atmosphere can now be written in terms of the atmospheric parameters $\mathrm{T_{eff}}$ and g. In order to obtain a model atmosphere, the following three equations have to be solved:

$$\frac{\mathrm{d}P_{\mathrm{plasma}}(z)}{\mathrm{d}z}=-\rho(z)\left(g-\frac{1}{\rho(z)c}\int_0^\infty\int_{4\pi}\mathrm{d}\nu\mathrm{d}\Omega\ I_\nu\kappa_\nu\cos(\theta)\right) \tag{4.15}$$

$$\int_0^\infty\int_{4\pi}\mathrm{d}\nu\mathrm{d}\Omega\ I_\nu\cos(\theta)=\sigma_{\mathrm{SB}}\mathrm{T_{eff}^4} \tag{4.16}$$

$$\cos(\theta)\frac{\mathrm{d}I_\nu}{\mathrm{d}\tau_\nu}=I_\nu-S_\nu \tag{4.17}$$

Solving eqs. 4.15 through 4.17 requires knowledge of the equation of state. The equation of state of an ideal gas gives the atmospheric structure. In order to solve the structure, the source function has to be further characterized which requires knowledge of the properties of the plasma. In particular, many atomic cross-sections have to be known.

4.2.2 LTE vs. NLTE

The thermodynamical properties of the plasma have a crucial influence on the source function and, therefore, have to be considered. This is done for each layer of the computed atmosphere. One assumption that is often made for those properties is the concept of thermodynamical equilibrium (TE). The system in TE can be characterized by the systems temperature. TE is assumed to be present in each individual layer of the atmosphere, so each layer can be described by the local layer temperature, implying local TE (LTE).

LTE: The particles in LTE are assumed to follow a Maxwell-Boltzmann velocity distribution (same applies for the later case of NLTE). The occupation number densities (n_i) are described by Boltzmann-excitation and depend on the energy of the levels E_i, the local temperature T and its statistical weight g_i,

$$\frac{n_i}{n_j}=\frac{g_j}{g_i}\exp\left(-\frac{E_j-E_i}{kT}\right) \tag{4.18}$$

where k is the Boltzmann-constant.

The number densities of the individual ionization stages N_I are given by the Saha-equation

$$\frac{N_{I+1}}{N_I} = \frac{2}{n_e}\frac{G_{I+1}}{G_I}\frac{(2\pi m_e kT)^{3/2}}{h^3}\exp\left(-\frac{\chi_I}{kT}\right) \tag{4.19}$$

where G_I denotes the partition function which depends on the statistical weights g_i, the level-energies, and the local temperature. n_e and m_e are the electron density and mass, respectively, and χ_I is the ionization potential.
These assumptions in combination with model atoms give the occupation numbers and, therefore, the source function, which then can be used to get the atmospheric structure. However, LTE assumes that the layers are independent and do not influence each other, but in stellar atmosphere the densities are low and the photon flux is high. Consequently, photons from one layer influence other layers, too. Hence, LTE is a valid approximation if collisional interaction dominates over radiative ones, which deteriorates especially with decreasing densities and increasing temperatures.
NLTE: In non-local TE (NLTE) the Boltzmann and Saha equations (eqs. 4.18 and 4.19) are replaced by statistical equilibria, which can be described by the rate-equations, assuming that the population of any atomic level is stationary with time. Hence, processes populating a level are balanced by the depopulating ones, where R_{ij} and C_{ij} denote radiative and collisional processes, respectively:

$$n_i \sum_{i\neq j}(R_{ij} + C_{ij}) = \sum_{j\neq i} n_j(R_{ji} + C_{ji}) \tag{4.20}$$

The rate-equations are coupled to the atmospheric structure equations (eqs. 4.15-4.17). Consequently, solving all these equations simultaneously is a numerically very complex procedure which requires extensive computing resources.

4.2.3 Model atoms

Atomic data are needed as an input for the atmospheric structure equations. In order to solve the atmosphere in NLTE, model atoms are constructed. These model atoms contain all kinds of atomic data, such as basic information on the energy levels, transition probabilities, cross-sections for the interaction with photons and particles, etc.. A list of model atoms used during the analysis can be found in Table 4.1. The model atoms do not contain all transitions of one specific element but are limited to certain ionization stages. The stages included are those one would expect to be present in B-type stars. If model atoms are not available, the level populations are calculated assuming LTE. Then, lists of atomic data containing the transition energies, statistical weights, and oscillator strengths are sufficient as input. LTE lists for the following elements are available: Na, P, Ca, Sc, Ti, V, Cr, Mn, Co, Ni, Sr, Y, Zr, Ba, La, Ce and Fe I.

Table 4.1: Available model atoms

element	ionization stages	reference
H		Przybilla and Butler (2004)
He	I, II	Przybilla (2005)
C	II, III	Nieva and Przybilla (2006, 2008)
N	II	Przybilla and Butler (2001); Nieva and Przybilla (2012)
O	I, II	Przybilla et al. (2000); Becker and Butler (1988)
		Nieva and Przybilla (2012)
Ne	I, II	Morel and Butler (2008); Nieva and Przybilla (2012)
Mg	II	Przybilla et al. (2001)
Al	II, III	Przybilla (in prep.), Irrgang et al. (2014)
Si	II, III, IV	Przybilla & Butler (in prep.), Irrgang et al. (2014)
S	II, II	Vrancken et al. (1996); Irrgang et al. (2014)
Ar	II	Butler (in prep.), Irrgang et al. (2014)
Fe	II, III	Becker (1998); Morel et al. (2006)
		Nieva and Przybilla (2012)

4.3 The ADS approach

4.3.1 Hybrid LTE/NLTE approach

NLTE model atmosphere calculations are very time consuming. While departures from LTE may be significant for some species, the temperature-density stratifications may be almost uneffected. In such a case, the stratification is calculated in LTE and subsequently the level population densities are derived from statistical equilibrium allowing for departures from LTE. A so called hybrid LTE/NLTE approach is chosen to calculate model spectra. This approach has first been described by Przybilla et al. (2006) and Nieva and Przybilla (2007) and has been improved subsequently by many other authors (Irrgang et al. 2014, 2018). Using a hybrid approach has been shown to be fully consistent with full-blown NLTE modeling for A and B-type stars (Przybilla et al. 2011).
The process of obtaining a LTE/NLTE-model spectrum has multiple steps using different model-codes. The atmosphere is divided into 72 layers. In the following the basic steps will be outlined, the approach is the same as chosen by Irrgang et al. (2018).
1) ATLAS9: Initially the atmospheric code ATLAS9 (Kurucz 1993) is used to obtain a initial guess of the atmospheric structure. The atmospheric structure equations are solved

for the LTE cases for a pre-set set of atmospheric parameters. In this code line opacity is treated with opacity distribution functions (ODFs). ODF are pre-calculated functions, assuming that the opacity can be treated as a smooth function within a sampled frequency interval of the spectrum. This first step is mainly used to speed up the calculation in the next step.
2) ATLAS12: The previously calculated ALTLAS9 atmosphere is passed on to ATLAS12 (Kurucz 1996; Irrgang et al. 2018). In contrast to ATLAS9 this code treats opacity through opacity sampling (OS). For OS, a sufficient number of frequency points is chosen and for each layer of the atmsophere the total opacity is calculated, hereby summing over the opacities of atoms, molecules, all bound-free and free-free transitions (Castelli 2005), hence reaching a higher accuracy in treating opacities at the price of much more frequency points and, therefore, more computation time. ATLAS12 will give back a line-blanketed, plane-parallel, homogeneous, and hydrostatic LTE atmosphere. Up until now everything has been considered in LTE.
3) DETAIL: The ATLAS12 atmosphere is passed on to the code DETAIL (Giddings 1981; Irrgang et al. 2018), which uses the atmosphere as a starting point to solve the radiative transfer and rate equations for hydrogen, helium and a number of other elements (only one of these elements at a time), which is done through accelerated lambda iteration, in NLTE using model atoms. This gives the radiation field and occupation numbers for the elements involved in NLTE, which then returns the source function. DETAIL calculates the source function on a rough frequency grid to speed up the calculation, which is not sufficient for reproducing line profiles in synthetic spectra. Now the radiative transfer is considered in NLTE, but not the atmospheric structure. By passing the NLTE occupation numbers for hydrogen and helium back to ATLAS12 before incorporating the other metals an iterative process between the two codes is started. The opacities of all other metals are treated as LTE background opacities. Now ATLAS12 again calculates the structure using the NLTE occupation numbers of H and He, this structure is passed on to DETAIL again to derive the occupation numbers. This is done until convergence is reached, which is defined as the moment when the changes in the temperature structure are less than 1 per mille or after 10 iterations. This is a step to approximately deal with NLTE effects on temperature stratification[1].
4) SURFACE: In order to extract a final synthetic spectrum for a set of parameters the level occupation densities of DETAIL are passed on to SURFACE (Giddings 1981; Irrgang et al. 2018). Here the formal solution of the RTE (eq. 4.7) is evaluated on a fine grid of frequencies and using the most detailed line broadening tables available. The emergent flux is obtained by integrating this solution over one hemisphere of the star.

$$F_\nu(0) = 2\pi \int_0^1 \mathrm{d}\cos(\theta) I_\nu(\tau_2, \cos(\theta)) \exp\left(-\frac{\tau_2}{\cos(\theta)}\right) + \int_0^{\tau_2} \mathrm{d}\tau \frac{S_\nu(\tau)}{\cos(\theta)} \exp\left(-\frac{\tau}{\cos(\theta)}\right) \quad (4.21)$$

The flux of every frequency point is divided by the continuum flux at that exact point in order to normalize the spectrum.

[1] This is mostly unimportant for late B and A stars

If a NLTE model atom is not available, the DETAIL part is skipped for the metal (not for hydrogen and helium) and everything is done in exactly the same way in LTE. The basic steps of the procedure are illustrated in Fig. 4.1. Since the codes employed are ATLAS, DETAIL and SURFACE the approach is also called ADS. This can now be used to calculate synthetic spectra for an appropriate parameter-range.

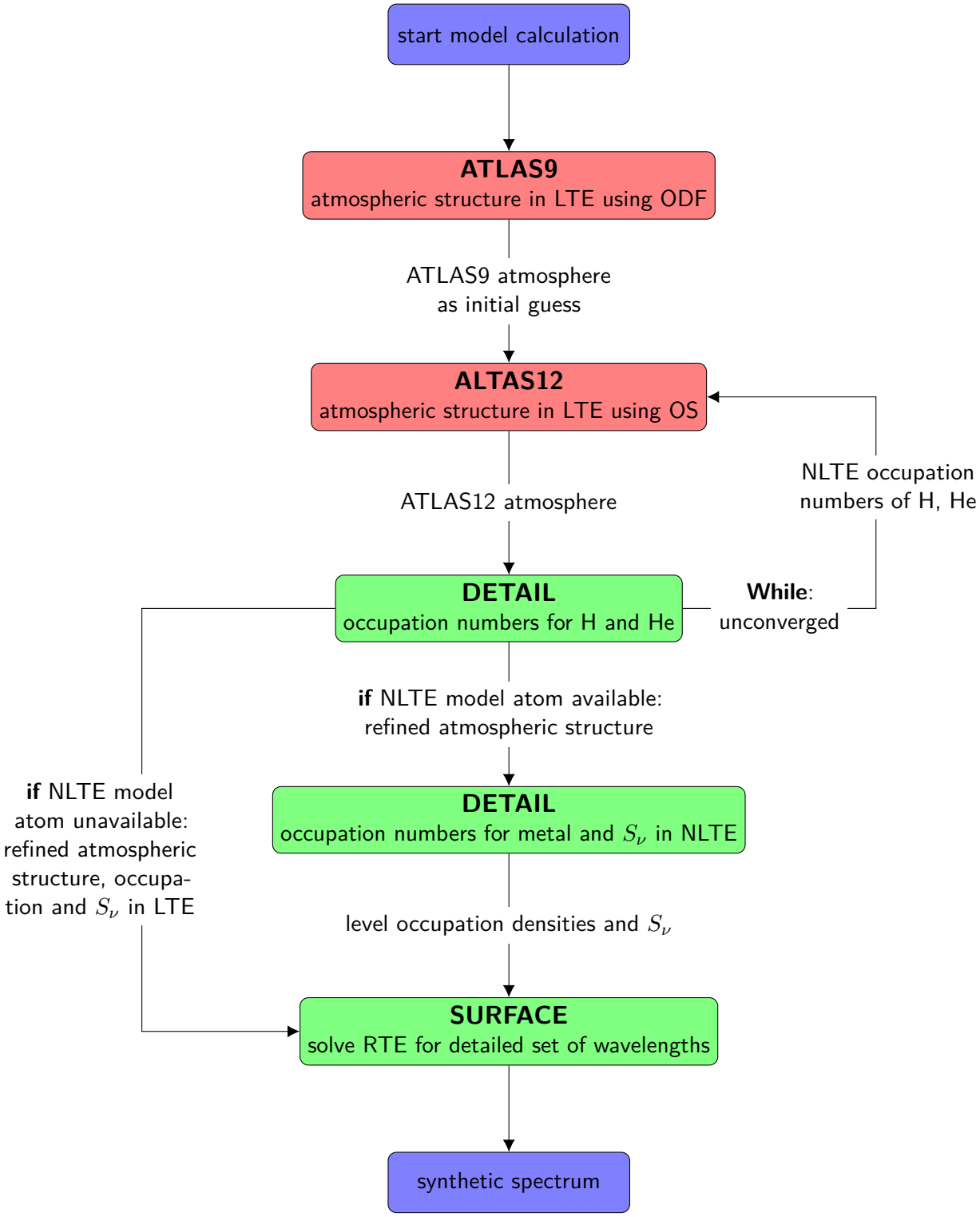

Figure 4.1: The ADS-approach for model spectra calculation. Atmospheric codes using LTE approximation are red, other codes used for NLTE-effects and spectrum-extraction are green

4.3.2 Model spectra

For spectral fitting grids of model spectra have to be pre-calculated. This is done using the ADS approach. Every parameter going into the calculation of the synthetic spectra is varied, resulting in a grid of synthetic spectra with as many dimensions as the number of input parameter. This is done separately for each metal included in the grid, meaning that every metal introduces another dimension to the grid. Abundances are treated as base-10 logarithm of the fractional particle number. The parameters going directly into the model calculations, therefore called primary parameters, and which therefore can be determined for each of the observations, are the following:
Z: the metallicity of the model spectra are varied. This metallicity parameter is a base-10 logarithmic scaling factor for the solar metallicity of Asplund et al. (2009) and is varied between -2 and 0.5 in steps of 0.5. During the fitting process Z is linked to the iron abundance.
$\boldsymbol{\xi}$: the microturbulence is considered for two values. The grids used offer X = 0 km/s and 2 km/s.
$\mathbf{T_{eff}}$: The effective temperature is usually spaced in 250 K steps for the A-type stars and in 1000 K steps for the B-type stars.
log(g): the surface gravity is varied in 0.2 steps in every grid.
The center point of each grid in temperature and surface gravity is different. Usually two parameter point below and above the central points are used for the individual grids in the adapted step-widths.
log(He): The logarithmic helium abundance with respect to all particles is also a very important parameter. The abundance is spaced in 0.25 dex steps.
For the B-BHBs the abundances of ^{3}He and ^{4}He are treated separately with the same spacing, the general helium abundance is then considered as the sum of the isotope-abundances. Both isotopes are incorporated as separate parameters into the models, which means they are both considered as two different primary parameters. This also means that the grids used for the B-BHBs have one additional dimension, hence, the grids are larger and more complex and the analysis also takes slightly longer, than when treating the total helium abundance as a single primary parameter.
metal-abundance: The abundance of the metals considered is also varied in 0.25 dex steps.
In order to save calculation time later a coarse grid considering hydrogen and helium was calculated in the beginning. The fit results of this first fit were used as the central point of the grids used later. Around these parameter combinations very detailed grids with the previously described step-sizes and incorporating all the metals were calculated covering a range big enough to avoid running into the grid limits when fitting, usually spanning the spanning ± 1000 K and ± 0.2 dex in log(g) for the A-BHB-stars and ± 2000 K for the B-BHB-stars. Usually four different helium abundances were used. The metal abundances in every gird were varied according to the Z-values, normally covering the values given by: $\log(n_\odot(\mathrm{X}))$ + Z, except for the cases where metals were clearly more abundant (here the term in the logarithm denotes the solar abundance of a metal).
The model spectra are calculated considering only hydrogen, helium and one metal at a

time. The full spectrum is later produced by multiplying the individual metal spectra, therefore, creating a model with all metals (Irrgang et al. 2014). This is a very efficient approach, which, however, does not allow to treat line blends. Hence the method can not be applied to the crowded spectra of cool stars, but is perfectly suited for those of A and B-type stars.

4.4 Fitting method

The entire fitting process, as well as the model calculations, are all carried out using the ISIS package (Houck and Denicola 2000). The fitting procedure follows an updated version of the approach presented in Irrgang et al. (2014). Using this approach makes it possible to simultaneously fit multiple spectra of the same star, if available, and obtain the best global fit, by employing the condition that the stellar parameters must have the same values in all observations used for the fit.

4.4.1 Preparing the observations

Before the spectra can be fitted using the pre-calculated girds of model spectra the observations have to be prepared. First artifacts (emission spikes a.k.a. cosmics), which are produced by cosmic particles hitting the detector, are removed from the spectra. The whole spectrum is searched for cosmics by comparing every data-points or pixels flux value with the flux of the environment around it. Pixels with values deviating by 3 standard deviations from the continuum flux are defined as cosmics and replaced by the median value of the environmental flux. Since the model spectra are all normalized the observations have to be normalized as well, which can be done later during the fitting procedure, but in order to start off with a good guess the a procedure was applied following the approach of Przybilla et al. (2008). This was applied to the blue parts of the spectra of the stars taken from the first sample (Sec. 2.1.1). The blue spectra were all divided by the spectrum of the WD WD0123−262, since this spectrum shows no lines it represents the instrument response of UVES quite well, leaving a roughly normalized spectrum. The WD spectrum had to be smoothed first using Savitzky-Golay filtering. The spectrum is then re-binned to an optimal wave-grid according to the spectral resolution and taking into account that an echelle spectrograph is used. The observations are also corrected for barycentric motion.
The spectrum is normalized using a spline with anchor points spread over the entire spectral range. Now the spectrum can be fitted. The fit-parameters are grouped into three distinct categories, the pre-defined wavelength-positioned spline anchor points, the telluric spectrum, which is included using a pre-calculated grid of spectra varying airmass and water-vapor, and the stellar parameters, which in addition to the primary parameters incorporated in the models also include the secondary parameters marcoturbulence ζ, the projected rotational velocity $v \cdot \sin(i)$ and the radial velocity v_{rad}.

4.4.2 Spectral fitting

The observations are compared to the model grids to obtain the parameters. In order to take all the primary parameters into account the model spectra have to be multiplied with each other. A spectrum only including one trace metal is produced by dividing the model spectrum containing the metal, hydrogen and helium by a spectrum with the

same parameters but only including hydrogen and helium. All these single-metal spectra and the hydrogen-helium spectrum can be multiplied again to get a model including all the primary parameters. Additionally the model is convolved with the instrumental profile. The different parameter combinations can be produced by linear interpolation within the model grid. The secondary parameters, which were not considered in the model calculations are treated somewhat differently. The radial velocity is determined by shifting the spectrum using the Doppler formula. Macroturbulence and rotational velocity are derived by convolving the model with a combined profile function.
Since the parameters are derived by comparing the observations to the models, it is important to know how parameters influence the spectrum and its features. To illustrate the effect, Fig. 4.2 shows synthetic spectra computed with ADS for different parameter combinations. All panels show the region around H_β. The top left one shows a spectrum computed for solar metallicity, $T_{\rm eff}$ = 10,000 K, log(g) = 4.0, log(He)= -1 dex, ξ= 0 km/s and log($n_{\rm Fe}$) = -6 dex. The same spectrum is shown in all other panels in red. The effective temperature has an influence on the shape and depth of the hydrogen lines, as can be seen in the upper right panel, as these lines become less deep for higher temperatures. However, the helium lines also become stronger with increasing temperature and there is also an influence on the metal lines, especially on the ratio of different ionization stages. The surface gravity is derived mainly from the wings of the hydrogen lines, a lower log(g) will make the lines less broad and the wings steeper. A higher helium abundance will make the helium lines stronger and will also slightly influence the shape of the hydrogen lines. A higher metal abundance, although making the corresponding lines stronger and even causing more lines to appear, will not influence the hydrogen lines as much as that of helium. A higher macroturbulence and faster rotation will broaden all lines.
The best fit within the grid is determined by χ^2-minimization. To derive the χ^2 the observed flux F, the model flux $F_{\rm model}$ and the uncertainty of the observed flux δf are considered for every pixel i.

$$\chi^2 = \sum_i \left(\frac{F_i - F_{{\rm model},i}}{\delta f_i} \right)^2 \tag{4.22}$$

Including the entire spectrum in the analysis has advantages, compared to selective fitting routines, because one uses all available lines to get the parameters. However, some regions have to be excluded. Besides interstellar and telluric features, lines with incorrect atomic data or missing in the model atoms have to be avoided. Also the lines of metals for which no model atoms or LTE-line lists are available, which therefore can not be modeled, are excluded.
The χ^2 is minimized using the minimization algorithms implemented in ISIS. Mainly the two algorithms mpfit and powell are used. Mpfit (Bevington and Robinson 1992) is a Levenberg-Marquardt algorithm and is used as default. Powell (Powell 1964; Zangwill 1967) is a non-gradient method to find the minimum of a function. During the analysis both methods are used to minimize the χ^2 and the method resulting in a better fit is used.
After regions which can not be modeled have been excluded from the fit, the current best

fit has been found and a list of visible lines has been created, a continuum correction is applied locally. Regions having no spectral lines or which are marked as continuum by eye are set to be the normalized continuum by smoothing these regions using a local filter. Now the observations are completely normalized and the best fit is found. Since a good fit is defined by the reduced χ^2 being close to unity and the χ^2-statistics can be used for the error calculation, systematics are added in order to achieve a reduced χ^2 of unity. For this it is assumed that the deviations between the model and the observation are due to systematic errors and appropriate values are added in quadrature to the statistical ones.

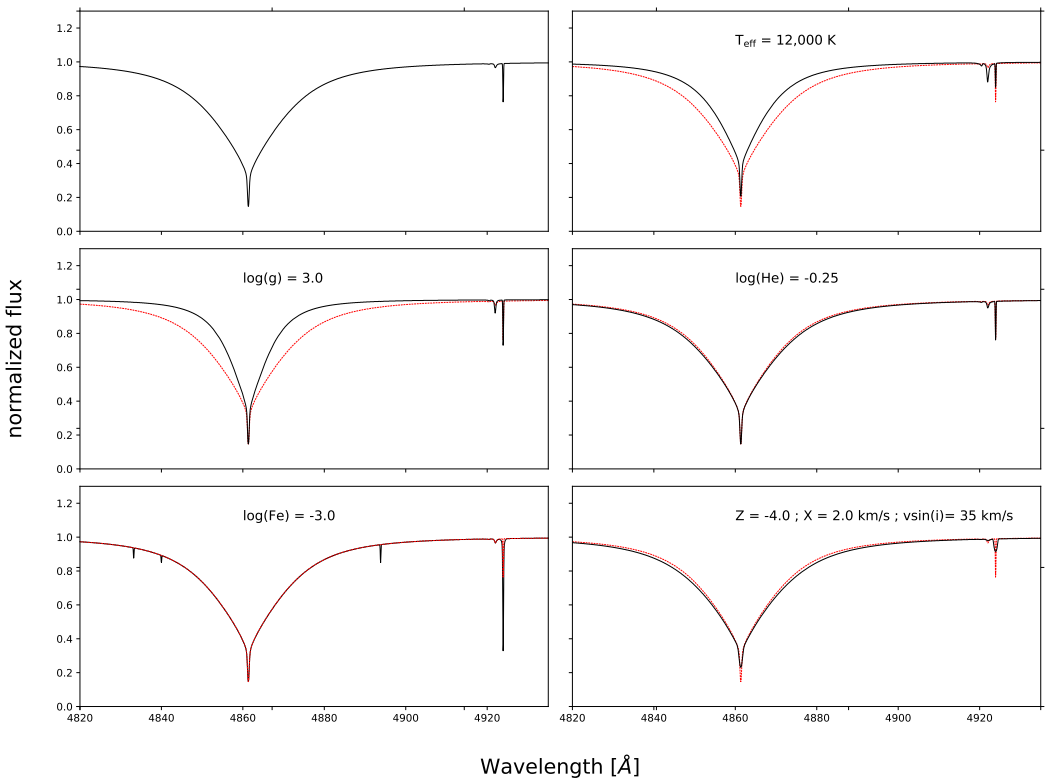

Figure 4.2: Influence of different primary and secondary parameters on the spectrum covering H_β, He I (4922 Å) and iron lines. The upper left panel shows a spectrum computed for solar metallicity, $T_{\rm eff}$ = 10,000 K, log(g) = 4.0, log(He)= -1 dex, ξ= 0 km/s and log($n_{\rm Fe}$) = -6 dex, the same spectrum is shown in all other panels (red dashed line), the other panels show a spectrum differing in one or more parameters

4.4.3 Error calculation

The uncertainties of all the parameters have to be calculated as well. Errors presented are all 1 σ-errors corresponding to a confidence level of 68%. The errors are separated into statistical and systematic errors. The total errors given throughout the errors are the errors resulting from combining the statistical and systematic errors through quadratic addition.

Statistical errors: Statistical errors occur due to the noise in the spectra and can be determined using the χ^2 statistics. Staring from the best fit and a reduced χ^2 of about 1 the confidence levels of all the parameters are determined. The parameter for which the uncertainty is estimated at the moment is stepped through by increasing and decreasing the value, while all the other parameters are fitted. This process for a single parameter is stopped once a specified deviation of the reduced χ^2 is reached. Then the next parameters error is estimated, until confidence levels have been calculated for all parameters. This can be done in a serial or a parallel way. If during this process an improved fit (within a reasonable level of change of the χ^2) is found the whole procedure is started all over again.

Systematic errors: Throughout the entire analysis systematic errors are introduced. The atomic data is an important source of systematic errors, since the model atoms are not complete and may contain errors. Also the continuum correction, especially the regions chosen as continuum by eye, the fitting methods and any procedure applied to the observations, introduce some kind of systematics. In order to perform a full systematic error estimation all sources would have to be taken into account as well as correlations between them, which, however, is not feasible. Since the entire available spectral range is used the parameters are derived using multiple features in the spectrum, hence, the systematics should be considerably low. Assuming that the systematics are mainly dominated by those resulting from temperature and surface gravity, allows the systematic uncertainties to be estimated by varying these two parameters. Because of the excellent quality of the spectra, a systematic uncertainty as low as 1% for $T_{\rm eff}$ and 0.04 for log(g) can be assumed. These two parameters are stepped through according to their systematics and statistics by taking the best fit values as the center and increasing and decreasing them by the quadratic addition of the errors, using 7×7 different parameter combinations. For each of these configurations effective temperature and surface gravity are fixed and all the other parameters are fitted, yielding a confidence map. The regions of this confidence map, an example is shown in Fig. 4.4, which do not agree with the observations in comparison with the other regions of the map, are excluded. The minimum and maximum values of a parameter derived for the other regions are used to estimate the systematic uncertainties.

For high-quality spectra, the statistical errors are usually small, therefore, the total uncertainties, derived by quadratically summing both, are dominated by the systematics. Inspection of the final spectral fits revealed that for some elements no spectral line can be distinguished from noise. Hence those resulting abundances are spurious and, therefore, excluded. In case the abundance derived corresponded to the lower limit of the grid, but lines of the respective element were somewhat visible the abundance is kept, but,

however, is merely an upper limit.
An example fit is shown in Fig. 4.3, the black line is the observed normalized spectrum and the red line is the best fitting model, this is the case in all subsequently shown fits.

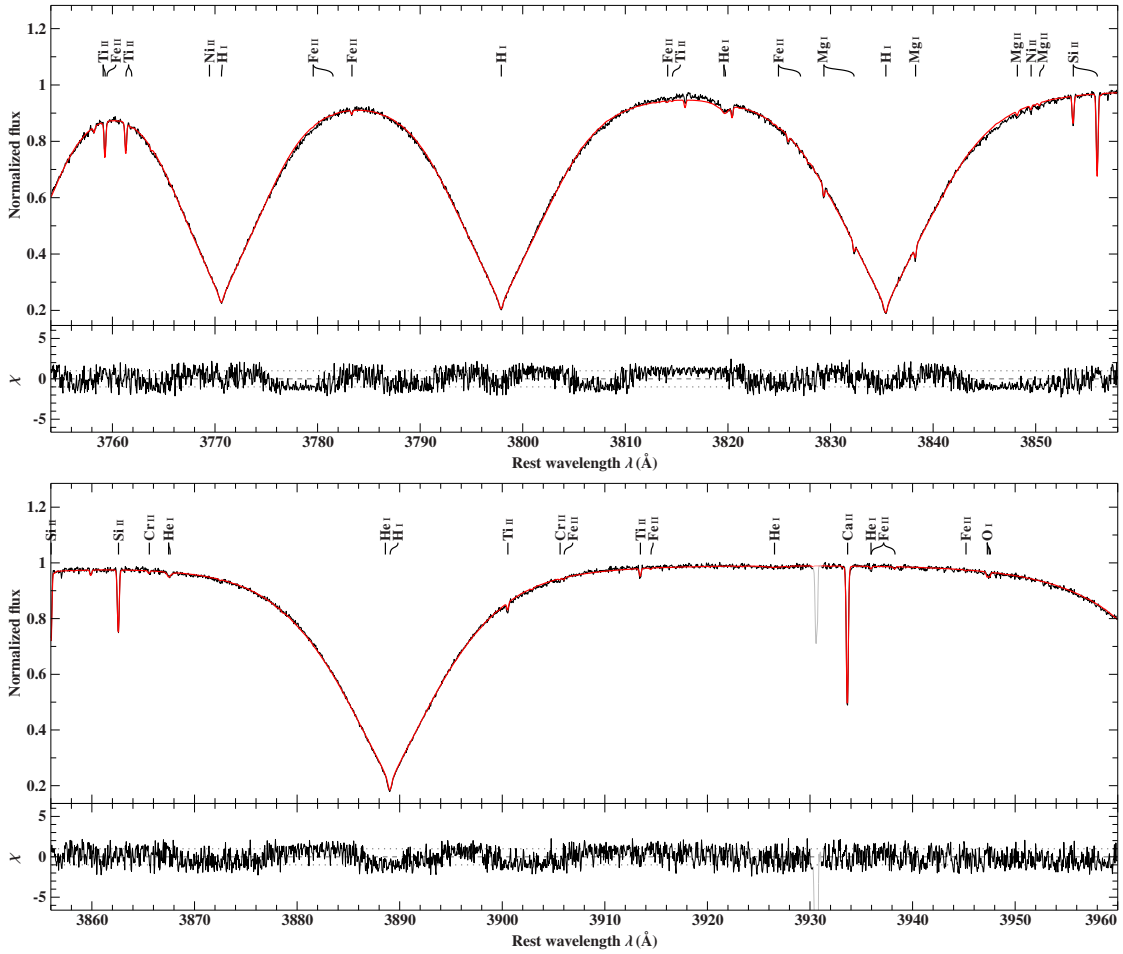

Figure 4.3: Example fit to a part of the blue spectral range to the observation of CD-38 8806

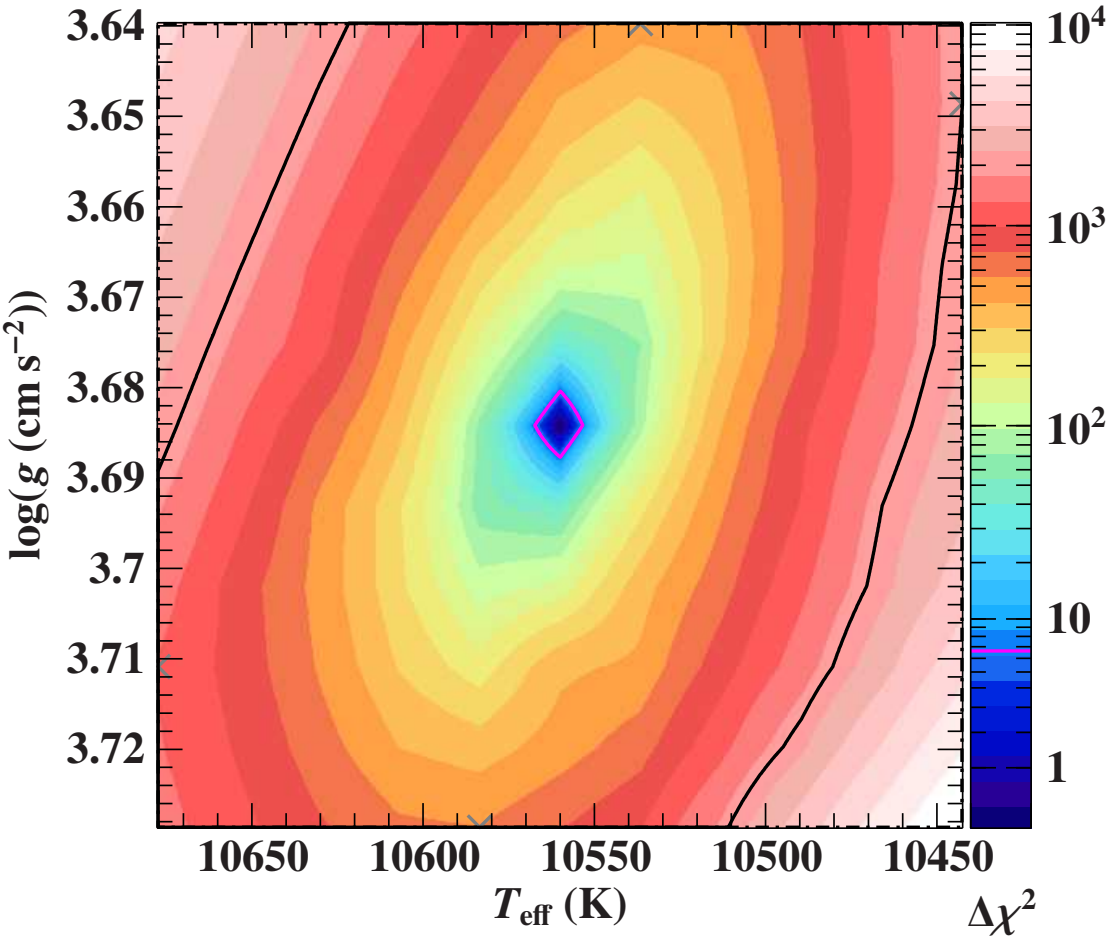

Figure 4.4: Confidence map calculated for CD-38 8806

5

Photometric analysis

5.1 Photometric data

Photometry (magnitudes in different wavelength filters) is compiled from many catalogs, by querying the star in various catalogs. False data is excluded based on missing uncertainties and when magnitudes clearly belong to nearby sources other than the target stars. After omitting obviously flawed magnitudes and colors, only data from the following sources remains:
Gaia: Gaia gives magnitudes in the three available passbands.
Tycho: data collected with the Tycho instrument which operated aboard of Hipparcos is used (Høg et al. 2000). This catalog provides two magnitudes B_T and V_T.
Hipparcos: Hipparcos (van Leeuwen 2007) provides Johnson system V magnitudes.
2MASS: The two micron all sky survey (2MASS) was operated in the infra-red using telescopes in Arizona and Chile (Skrutskie et al. 2006). This survey used three different filters: J (1.25 μm), H (1.65 μm), and K (2.16 μm).
WISE: The Wide-field Infrared Survey Explorer (WISE) spacecraft was an all-sky survey (Wright et al. 2010). WISE provides magnitudes for filters with central wavelengths of: 3.4 μm, 4.6 μm, 12 μm, and 22 μm.
SDSS: The Solan digital sky survey (SDSS) provides photometry and spectroscopy (Ahn et al. 2012; Blanton et al. 2017). The SDSS filters are spread over a wide spectral range with five filters: u (3543 Å), g (4770 Å), r (6231 Å), i (7625 Å) and z (9134 Å).
Mermilliod catalog: the catalog compiled by Mermilliod (1992) contains a collection of U, V, B magnitudes and colors from multiple sources.
Sky Mapper: Sky Mapper (Wolf et al. 2018) is an Australian survey and provides u, v, g, r, i and z filters, quite similar to SDSS. The v filter is an additional filter in the blue (3840 Å). DR1 is used for the analyses.
PAN-STARRS1 The Panoramic Survey Telescope and Rapid Response System (PAN-STARRS1) is a wide-filed imaging survey located in Hawaii (Chambers et al. 2016). g, r, i and z filters similar to SDSS are available. PAN-STARRS1 (PS1) also offers a y filter at 9644 Å.

Stroemgren: Stroemgren photometry is taken from the Stroemgren-Crawford uvbyβ photometry catalog by Paunzen (2015).
IUE-box filters: International Ultraviolet Explorer (IUE) spectra (Wamsteker 2000) for observed targets are used to calculate the magnitudes in the box-filters in the UV range of the spectrum.
VST: The VLT survey telescope (VST) is operated by ESO (Arnaboldi et al. 1998; Kuijken et al. 2002; Kuijken 2011). The ATLAS VST survey uses passbands similar to SDSS (Shanks et al. 2015).
VISTA: The Visible and Infrared Survey Telescope for Astronomy (VISTA) at Paranal also operated by ESO is the largest survey telescope ever build (Emerson et al. 2006; Dalton et al. 2006). It operates in the near-infrared. Data used is taken from the VISTA Hemisphere Survey DR4.
The response of every filter used depending on the wavelength is shown in Fig. 5.1. This shows at which wavelength the filters operate but also how well the different ranges are sampled by the used photometry. Tables containing all the photometric data used can be found in A1.2.

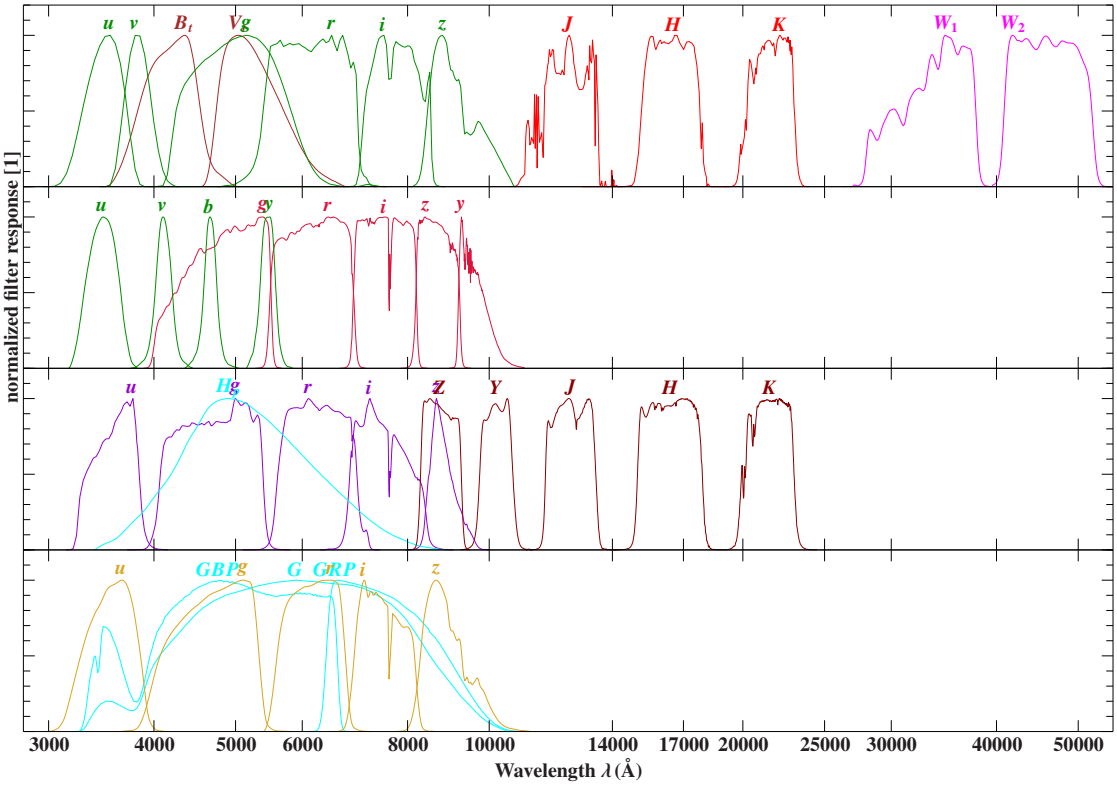

Figure 5.1: The normalized filter response as a function of wavelength (top: Sky Mapper, Tycho, 2MASS, WISE; top-middle: Stroemgren, PS1; lower-middle: VISTA, Hipparcos, VST; lower: SDSS, Gaia)

5.2 SEDs based only on photometry

The model grids used for the spectroscopic analyses also contain synthetic SEDs, hence, they can be used to fit the compiled photometric data using the hydrogen-helium components of the girds. Using a χ^2 minimization the observations can be fitted. For this purpose the minimization algorithms implemented in ISIS are used. Uncertainties are again derived using the χ^2-statistics, with the same approach as for the statistical uncertainties during the spectroscopic analysis (Heber et al. 2018).
Therefore, the primary atmospheric parameters can be determined. Since observed magnitudes are a function of distance, the SED has to be scaled to the observed magnitudes. This can be expressed through the angular diameter of the star on the celestial sphere Θ. Additional parameters which can be determined through SED fitting are the color excess $E(B-V)$ and the interstellar extinction R_V, which is fixed to 3.1 throughout the analyses.
Using the girds used to determine the first guess for the spectroscopic analysis (see Sec. 4.3.2), the SEDs were fitted and, therefore, the effective temperature, surface gravity, and relative metal abundance are determined, whereas the helium abundance was fixed to solar and the microturbulence to zero, because the SED is not sensitive to these parameters at all. However, the uncertainties for surface gravity and metallicity span over significant fractions of the entire parameter range covered by the grid. Also, the uncertainties derived for the effective temperatures are significantly higher than those from spectroscopy. Since the parameters are not well constrained by pure photometry, this part merely services as a consistency check.
Figure 5.2 shows the SED fit of CD-38 8806. The upper panel shows the synthetic spectrum for the derived atmospheric parameters, which is over-plotted with the computed fluxes based on the magnitudes. The lower panel is, however, more important since it indicates the goodness of fit. This panel shows the difference between the observed and synthetic magnitudes.

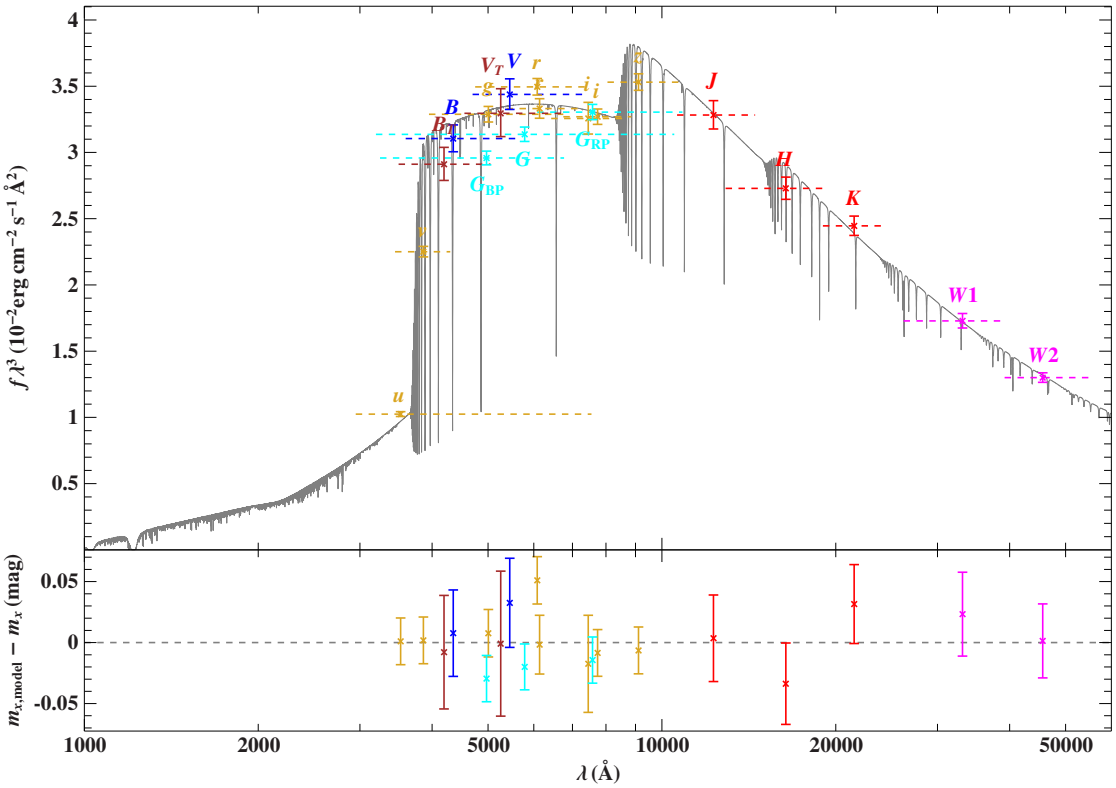

Figure 5.2: SED of CD-38 8806 based on photometry only

5.3 SEDs in combination with spectroscopy

The atmospheric parameters are very well constrained by spectroscopy, far better than it would be possible from pure photometry, hence, they can also be plugged into the SED fit. The atmospheric parameters are set to the ones derived from spectroscopy and the photometric data is fitted with Θ and $E(B-V)$ being the only fitparameters. Therefore, the angular diameter can be constrained even better.

The fits are performed using the same fitting routine as for the pure photometry fit, but different girds are used. Like for the spectroscopic fits, the individual small refined grids are used.

The resulting SED of CD-38 8806 is shown in Fig. 5.3, as can be seen from the residuals, there is a difference compared with the pure photometry SED, which is not too surprising since the fits use different parameters and grids.

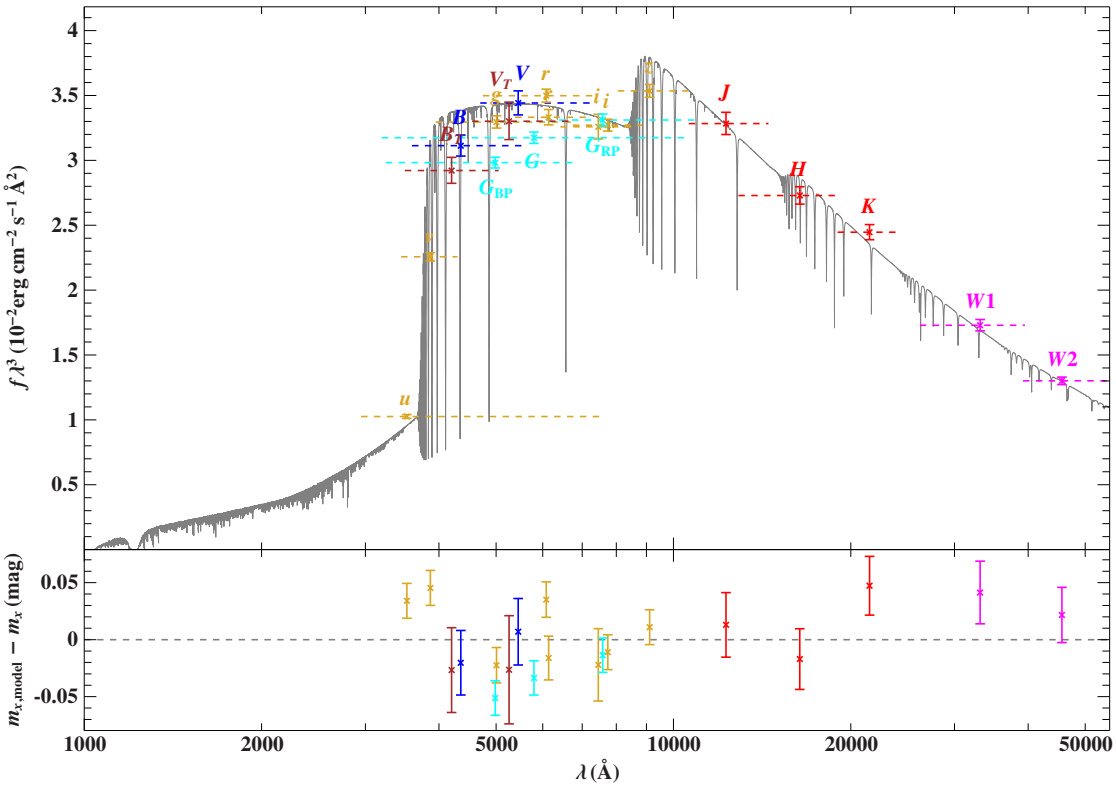

Figure 5.3: SED of CD-38 8806 based on spectroscopy

6

Fundamental stellar parameters: radius, mass, and luminosity

The spectro-photometric analysis gives the angular diameter Θ in addition to the atmospheric parameters $T_{\rm eff}$ and log(g) from spectroscopy. When these parameters are combined with the distances, the stellar parameters radius, mass and luminosity can be calculated (Heber et al. 2018; Schindewolf et al. 2018). Gaia gives the parallax, thus, the distance d is known, when using eq. 2.1. Θ and the distance are used first to derive the radius. Due to the large distance the small-angle approximation can be used.

$$R_* = \Theta \frac{d}{2} = \Theta \frac{1}{2\varpi} \tag{6.1}$$

Using the definition of the surface gravity g, the mass can be expressed as:

$$M_* = g \frac{R_*^2}{G} = \frac{10^{\log(g)} \Theta^2}{4G\varpi^2} \tag{6.2}$$

Finally the radius and effective temperature can be used to calculate the luminosity:

$$L_* = 4\pi\sigma R_*^2 T_{\rm eff}^4 = \frac{\pi\sigma\Theta^2 T_{\rm eff}^4}{\varpi^2} \tag{6.3}$$

All needed parameters are available and trustworthy for the program stars. Equations 6.1-6.3 are used to calculate the stellar parameters. Errors of the stellar parameters are derived using Gaussian error-propagation for the errors of ϖ, log(g), $T_{\rm eff}$ and Θ.

7

Kinematic analysis

7.1 Milky Way mass models

Calculating the orbits of stars, GCs or satellite galaxies in and around the Galaxy, requires knowledge about the mass distribution within the Milky Way. The gravitational potential has to be known in order to solve the equations of motion. To obtain the orbits and kinematic parameters of the stars three different Milky Way potentials were used. To keep numerical calculations as simple as possible these potentials can all be expressed as analytical equations. The form of each potential is taken from literature, but the parameters governing these equations have been calibrated by Irrgang et al. (2013). This calibration was performed using a few simple constrains: the solar movement, the observed rotation curve, the local mass and surface density of the solar neighborhood, the proper motion of Sgr A*, the observed velocity dispersion in Baade's window and requiring that the halo HB star J1539+0239 be bound, are used as constraints and the parameters of the potentials are obtained by least χ^2-fitting.
All potentials are expressed in cylindric coordinates (r,ϕ,z), the spherical radius is defined as R(r,z)= $\sqrt{r^2 + z^2}$. Potentials are all expressed as the sum of a spherical bulge, an axis-symmetric disk and a spherical dark matter halo.

$$\Phi(r,z) = \Phi_b(R) + \Phi_d(r,z) + \Phi_h(R) \tag{7.1}$$

All the used potentials are time-independent, hence, features such as spiral arms are not taken into account.
Allen and Santillan potential: The first potential is the one proposed by Allen and Santillan (1991) (AS). The bulge and disk components used in the AS-potential are those used by Miyamoto and Nagai (1975). The halo potential is slightly modified. In the following M always denotes a mass-weighting factor and a and b are scale-lengths.

$$\Phi_b(\mathrm{R}) = -\frac{M_b}{\sqrt{\mathrm{R}^2 + b_b^2}} \tag{7.2}$$

$$\Phi_d(\mathrm{r,z}) = -\frac{M_d}{\sqrt{\mathrm{r}^2 + \left(a_d + \sqrt{\mathrm{z}^2 + b_d^2}\right)^2}} \tag{7.3}$$

The AS-halo potential is expressed as:

$$\Phi(\mathrm{R}) = \begin{cases} \frac{M_h}{a_h}\left(\frac{1}{\gamma-1}\ln\left(\frac{1+\left(\frac{\mathrm{R}}{a_h}\right)^{\gamma-1}}{1+\left(\frac{\Lambda}{a_h}\right)^{\gamma-1}}\right) - \frac{\left(\frac{\Lambda}{a_h}\right)^{\gamma-1}}{1+\left(\frac{\Lambda}{a_h}\right)^{\gamma-1}}\right) & \text{if } \mathrm{R} < \Lambda \\ -\frac{M_h}{\mathrm{r}}\frac{\left(\frac{\Lambda}{a_h}\right)^{\gamma}}{1+\left(\frac{\Lambda}{a_h}\right)^{\gamma-1}} & \text{otherwise} \end{cases} \tag{7.4}$$

Truncated and flat halo: The second potential uses the same bulge and disk potentials as the AS-potential. However, a truncated and flat totation curve halo (TF) is used, as suggested by Wilkinson and Evans (1999).

$$\Phi_h(\mathrm{R}) = -\frac{M_h}{a_h}\ln\left(\frac{\sqrt{\mathrm{R}^2 + a_h^2} + a_h}{\mathrm{R}}\right) \tag{7.5}$$

Navarro-Frenk-White halo: The last potential used for orbit calculations uses a Navarro, Frenk, and White (NFW) halo potential (Navarro et al. 1997). The bulge and disk components remain the same as before.

$$\Phi_h(\mathrm{R}) = -\frac{M_h}{\mathrm{R}}\ln\left(1 + \frac{\mathrm{R}}{a_h}\right) \tag{7.6}$$

The parameters in equations 7.2 throughout 7.6 were alls determined by Irrgang et al. (2013) and used during the orbit calculation, these parameters are listed in Tab. 7.1.

Table 7.1: Potential parameters (Irrgang et al. 2013)

potential	AS	TF	NFW
parameter			
M_b $[M_{\mathrm{gal}}]$	409 ± 63	175 ± 28	439 ± 28
M_d $[M_{\mathrm{gal}}]$	2856^{+376}_{-202}	2829 ± 192	3096 ± 197
M_h $[M_{\mathrm{gal}}]$	1018^{+27933}_{-603}	69725^{+5790}_{-20931}	$142200^{+137900}_{-75500}$
b_b [kpc]	0.23 ± 0.03	0.184 ± 0.040	0.236 ± 0.021
a_d [kpc]	$4.22^{+0.53}_{-0.99}$	$4.85^{+0.41}_{-0.33}$	$3.262^{+0.144}_{-0.121}$
b_d [kpc]	$0.292^{+0.020}_{-0.025}$	0.305 ± 0.020	0.289 ± 0.022
a_h [kpc]	$2.562^{+25.963}_{-1.419}$	200^{+0}_{-60}	$45.02^{+22.56}_{-16.78}$
Λ [kpc]	200^{+0}_{-83}	-	-
γ [1]	2	-	-

7.2 Analysis method

The orbit of a star in the Milky Way can be expressed using one of the potentials in cylindric coordinates by the Lagrangian $\mathcal{L}$.

$$\mathcal{L}(\mathrm{r},\mathrm{z},\dot{\mathrm{r}},\dot{\phi},\dot{\mathrm{z}}) = \frac{1}{2}(\dot{\mathrm{r}}^2 + (\mathrm{r}\dot{\phi})^2 + \dot{\mathrm{z}}^2) - \Phi(\mathrm{r},\mathrm{z}) \tag{7.7}$$

Equation 7.7 can be used to derive a system of differential equations, the equations of motion, which are expressed in terms of momenta p (Irrgang et al. 2013).

$$p_{\mathrm{r}} = \dot{\mathrm{r}} = \partial_{\dot{\mathrm{r}}}\mathcal{L} \tag{7.8}$$

$$p_{\phi} = \dot{\phi}\mathrm{r}^2 = \partial_{\dot{\phi}}\mathcal{L} \tag{7.9}$$

$$p_{\mathrm{z}} = \dot{\mathrm{z}} = \partial_{\dot{\mathrm{z}}}\mathcal{L} \tag{7.10}$$

$$\dot{p_{\mathrm{r}}} = \frac{p_{\phi}^2}{\mathrm{r}^3} - \frac{GM_b\mathrm{r}}{\left(\mathrm{r}^2+\mathrm{z}^2+b_b^2\right)^{1.5}} - \frac{GM_d\mathrm{r}}{\left(\mathrm{r}^2+\left(a_d+\sqrt{\mathrm{z}^2+b_d^2}\right)^2\right)^{1.5}} - \partial_{\mathrm{R}}\Phi_h\frac{\mathrm{r}}{\sqrt{\mathrm{r}^2+\mathrm{z}^2}} \tag{7.11}$$

$$\dot{p_{\phi}} = 0 \tag{7.12}$$

$$\dot{p_{\mathrm{z}}} = -\frac{GM_b\mathrm{z}}{\left(\mathrm{r}^2+\mathrm{z}^2+b_b^2\right)^{1.5}} - \frac{GM_d\mathrm{z}\left(\frac{a_d}{\sqrt{\mathrm{z}^2+b_d^2}}+1\right)}{\left(\mathrm{r}^2+\left(a_d+\sqrt{\mathrm{z}^2+b_d^2}\right)^2\right)^{1.5}} - \partial_{\mathrm{R}}\Phi_h\frac{\mathrm{z}}{\sqrt{\mathrm{r}^2+\mathrm{z}^2}} \tag{7.13}$$

This system of differential equations (eq.7.8-7.13) can be solved by integrating them using an adaptive Runge-Kutta method when plugging in the potentials and present position and movement information from astrometry and spectroscopy. The orbits are calculated for 10 Gyrs and uncertainties are estimated through Monte-Carlo simulations, in this case 10,000 runs are performed. The correlations-functions are also considered. This will give the orbit of a star, in means of positions (x,y,z), respective velocity components, angular momentum in z-direction L_{z} and current kinetic energy for each time step. Further this allows the mean L_{z}, the eccentricity e, and the velocity components U and V, towards the Galactic center and in direction of Galactic rotation, to be determined. The orbit of every program is calculated in every potential.

7.3 Kinematic classification scheme

Based on the kinematic parameters stars can be classified into being part of the thin disk, thick disk or halo. Since not one set of parameters on its own is sufficient for the classification, multiple parameters have to be taken into account. The U and V velocity components, the eccentricity e, the angular momentum L_{z} and the shape of the orbits are used for this purpose. The adapted classification scheme has been proposed by Pauli et al. (2003) and Pauli et al. (2006).
A few orbits are shown in Fig. 1.16. The halo-orbits are those which deviate from the galactic plane quite significantly. The thick-disk orbits are slightly more extended over and below the Galactic disk than the thin disk orbits. The U-V diagram is another instrument to classify stars. As shown in Fig. 7.1 two ellipses (Pauli-ellipses) can be defined in the U-V plane. Stars within those ellipses belong to the disk. The inner ellipse marks the thin-disk area. Although very helpful, the fact that the ellipses of the thin and thick disk overlap, clearly indicates the need of additional criteria. The eccentricity

and the angular momentum are additional parameters that have to be considered. In the $L_z - e$ plane the Pauli-box can be defined, as seen in Fig. 7.2. Stars within this box are most likely thick disk members, those to the left thin disk and those on the right side of the box halo stars. Only based on all the criteria stars can be classified.

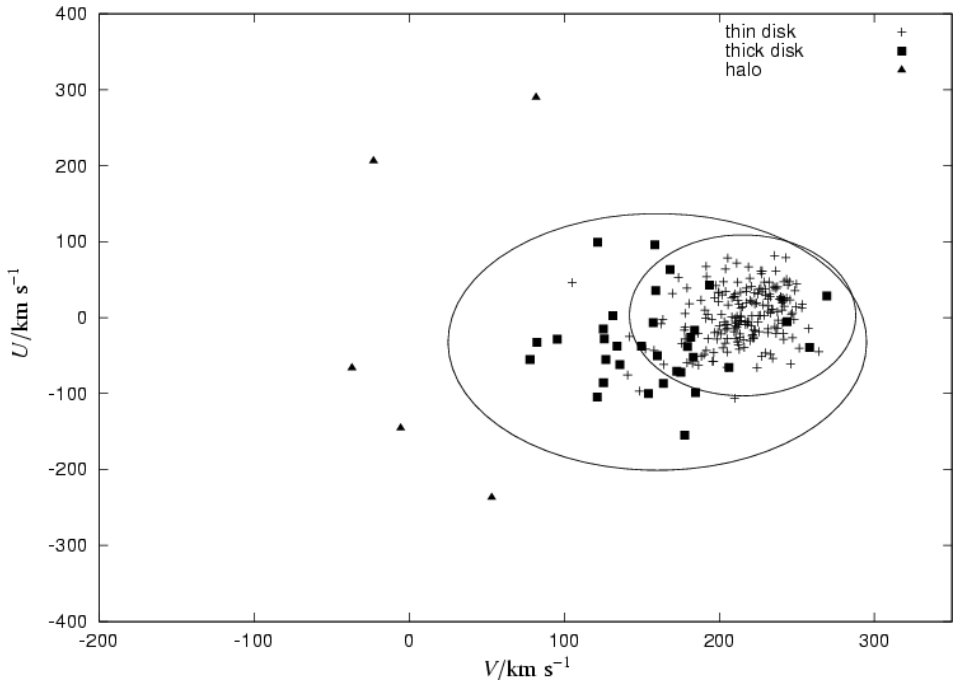

Figure 7.1: The U-V diagram showing the Pauli-ellipses (Pauli et al. 2006)

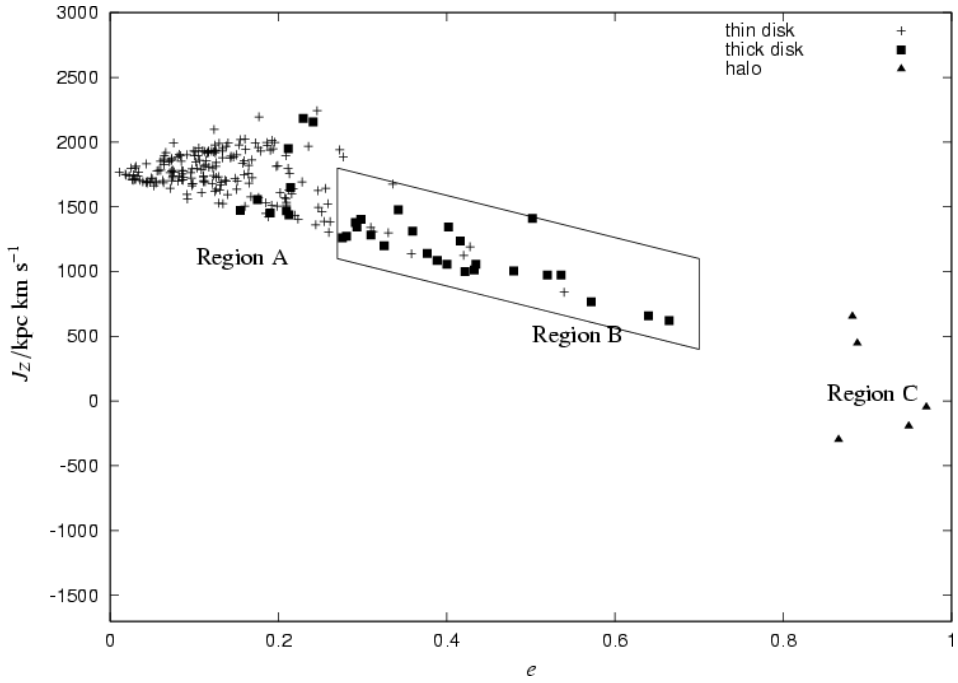

Figure 7.2: The L_z-e diagram with the Pauli-box (Pauli et al. 2006)

8

Results

The methods and data presented in the previous chapters are used for all the program stars. During the first steps of the analyses, especially for spectroscopy, it is important to test how well the chosen approach works and which specifications are appropriate. Furthermore, it is important to quantify systematics uncertainties of the derived parameters. By testing different specifications for the analysis using either mock or real data of a few program stars the best approach can be found. The results of this testing-phase and the implications for the further analyses will be presented first. The spectra are analyzed with the wobbles discussed in Sec. 2.2.2. This, however, is not a problem, since they can be eliminated using the local normalization. Additionally, tests revealed that the impact of the wobbles is negligible (see appendix A2).
After establishing a standard approach the results of the individual objects will be summarized, starting with the derived abundances patterns and the kinematic results. The results of stars taken directly from the literature will then also be compared to previous ones.
Thereafter, the results will be presented in the context of the entire sample. The results will be presented focusing on the distribution of the overall atmospheric parameters, abundances, and stellar parameters. Additionally, the kinematic characteristics of the entire sample will be presented.
Tables summarizing the results can be found in the appendices A3 through A5. Appendix A7 shows additional plots to illustrate the results in this chapter as well as in the following.

8.1 Spectral analysis: method-specifications

8.1.1 Why use a hybrid LTE/NLTE approach?

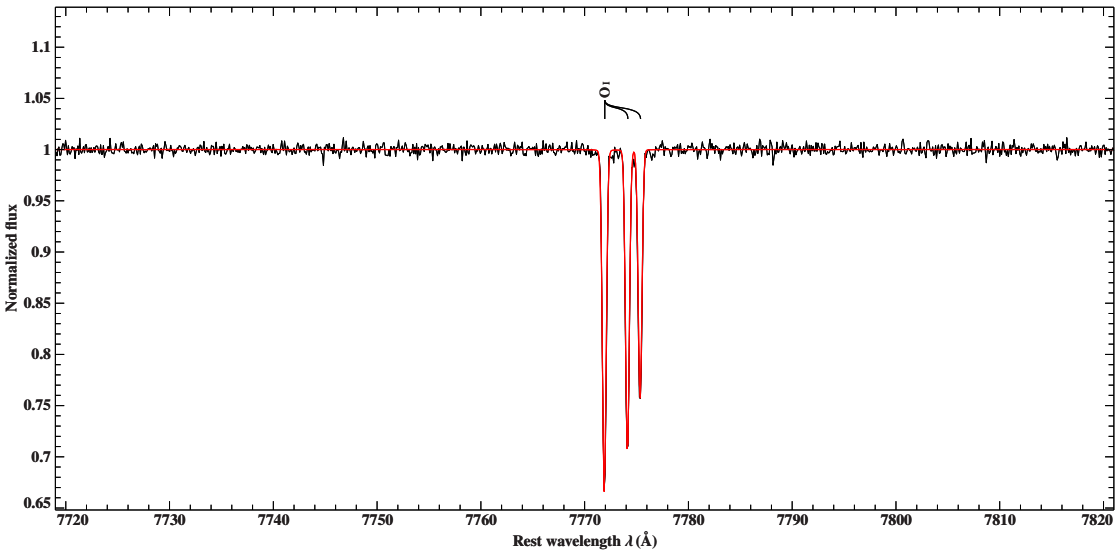

Figure 8.1: Oxygen triplet in the spectrum of CD-38 8806

Compared to full NLTE-calculations the hybrid approach is faster, but on the other hand an approach fully using LTE would be even faster. Also some studies find that a full LTE-description is sufficient to model A-type and late-B type stars (Przybilla et al. 2011). However, the data-quality of the analyzed spectra is significantly higher than in other studies. The excellent data-quality and the high resolution used allow even tiny NLTE-effects to be detectable. Structures such as the oxygen triplet (Fig. 8.1) are very sensitive to NLTE-effects, hence, incorporating NLTE-effects into the models to a certain extend will lead to better reproducing such sensitive structures or they are even needed to reproduce the observations. Using the hybrid approach leads to an excellent reproduction of NLTE-sensitive structures such as the oxygen triplet. This means a hybrid approach is very reasonable, since a full NLTE-approach would be way more complicated and time intensive and, in the studied temperature range, has been shown to be fully consistent with the hybrid approach (Przybilla et al. 2011).

8.1.2 Spectral ranges

It is crucial to know how different regions of the spectrum influence the analysis and the results. Previously published spectral analyses rely on the blue part of the visual spectrum. The UVES date allows a much wider wavelength range to be exploited. Therefore, it is crucial to explore the influence of different regions and to find out if the entire spectrum or only specific regions should be used, initial fits were performed for four program stars using different regions of the spectrum. The fit was performed with different spectral configurations: 1.) using the whole spectrum (3755 - 9463 Å), 2.) excluding only the red region with the Paschen lines (3755 - 7530 Å), 3.) using only the Paschen lines (7658 - 9463 Å), and 4.) using the spectral range of the integral field spectrograph MUSE (4650 - 9300 Å). For all these configurations, the fit was also performed a second time while excluding the Balmer-line cores, which might possibly show NLTE-effects.
In particular, the effects on the atmospheric parameters are found to be small and observed deviations were well within the assumed systematic errors for effective temperature (1%) and surface gravities (0.04 dex). However, the influence on some of the derived abundances was obvious, in particular if no spectral lines of a certain species are present in the selected wavelength range. For example, the helium abundances derived using the Paschen-region only are not reliable, since this region lacks helium lines. Elements showing a sufficient amount of spectral lines spread over the entire spectral range only showed differences within the errors. The blue region is especially important, because this region exhibits a lot of metal lines and is not contaminated with telluric lines. Nevertheless, the other regions are important. For example, the Paschen-region is also essential to derive reliable calcium abundances, because it covers the important CaII triplet (8498 Å, 8542Å, 8662Å). In the blue region only the calcium resonance doublet is present, but the ISM shows these two lines also, therefore, the stellar lines can only be modeled, if the ISM and stellar lines are well separated by radial velocity. The Paschen-region provides additional calcium lines, which are not contaminated by ISM lines and, hence, allow the calcium abundance to be determined.
In the temperature range of A-type stars, at effective temperatures of about 9,000 K, the Balmer-lines reach a maximum in strength (Mihalas 1966). Consequently, around this maximum the Balmer-line profiles can be reproduced by two T_{eff}-log(g) solutions, one at a temperature above and one below the maximum. This means that other temperature indicators are needed in order to investigate which of the solutions is the right one. Because the Balmer lines cover a wide region in the spectrum, hence, having a high weight in the fit, due to the high amount of pixels, other very sensitive indicators besides the Balmer-lines are needed. Tests with different regions showed that using the Paschen-lines as indicator is essential to distinguish between both solutions. The reason is that Balmer and Paschen-lines arise from different atomic levels, principal quatum number n=2 and n=3, respectively, the relative line strength then depends on the population density ratio $(\frac{n_3}{n_2})$ which depends on the temperature via the Boltzmann and Saha equations. For example, the star TYC 1914-687-1 is located in the discussed temperature region. The Balmer-lines can be reproduced by the high temperature solution: $T_{eff} = 9248 \pm 100$ K and log(g)=3.52 ± 0.05 and a low temperature solution with $T_{eff} = 8679 \pm 90$ K and

log(g)=3.34 ± 0.05 equally well. The Balmer-lines are perfectly reproduced in both cases, however, the same does not apply for the Paschen-series. Using the high temperature solution the Paschen-cores can not be reproduced, the lines are not deep enough, which can also be seen in the residuals. The Paschen-regions for both solutions are shown in Figs. 8.2 and 8.3.
Based on these results and on the goal to keep the systematics as low as possible by including as many spectral parameter indicators as possible, it can be concluded that the entire spectral range should be used, in order to obtain the most accurate results possible. Hence, the entire spectrum was used in the analysis, only excluding the regions contaminated with telluric lines, ISM lines, lines with known shortcomings due to atomic data and lines produced by metals not included in the models. Due to NLTE-effects becoming stronger with increasing effective temperature and, hence, effecting the Balmer-line cores more, the Balmer-line cores were excluded from the fit for temperates above the NG1.

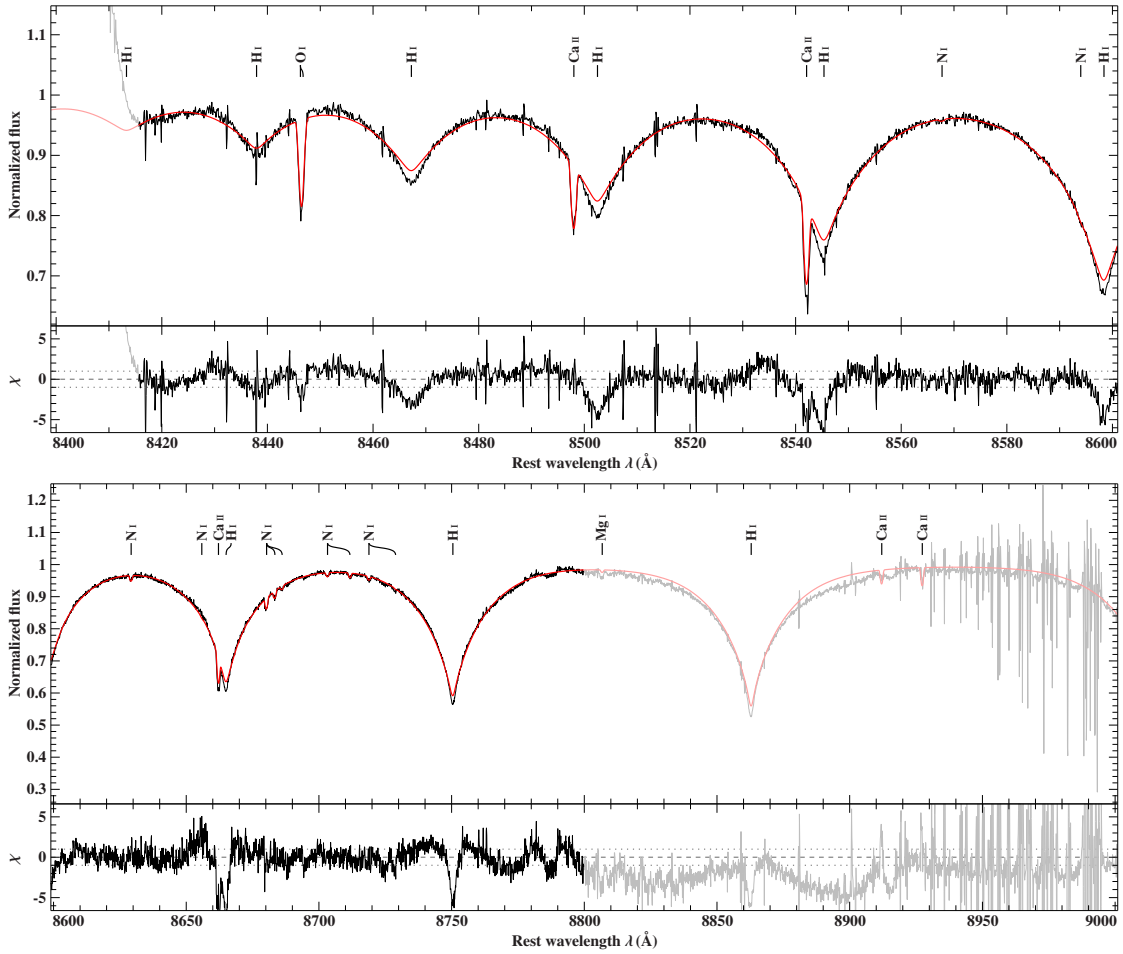

Figure 8.2: Paschen-lines in the spectrum of TYC 1914-687-1, the red line is the model of the high temperature solution

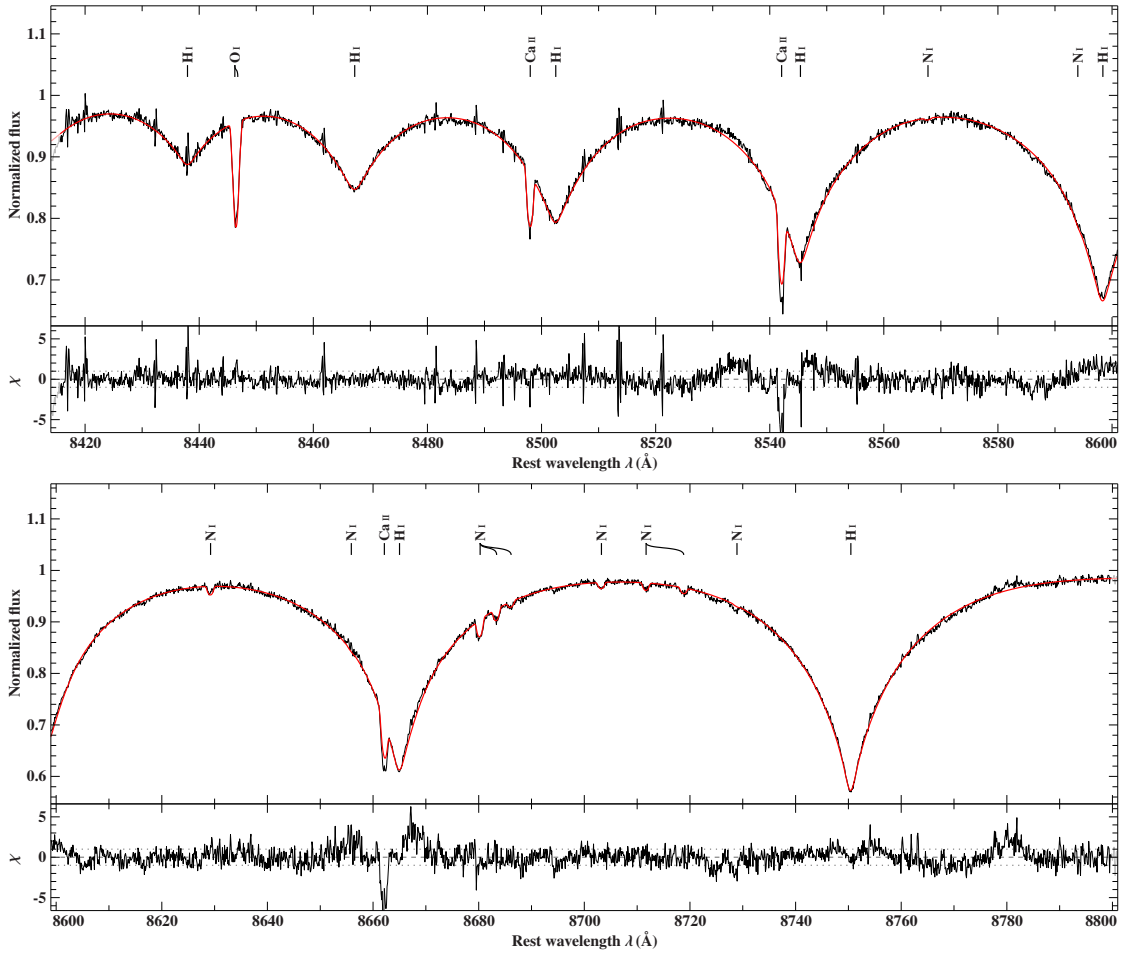

Figure 8.3: Paschen-lines in the spectrum of TYC 1914-687-1, the red line is the model of the low temperature solution

8.1.3 flux-calibrated vs. flux-uncalibrated

The UVES pipeline produces flux- and flux-un-calibrated spectra. The flux-calibration, of course, also contains some additional information, but at the same time systematics are introduced through the flux-calibration, since the calibration is performed using standard stars. Also, the spectra are normalized during the fitting process. Thus, it is necessary to investigate how strong the influence of the flux-calibration is on the derived parameters, in order to decide which output of the pipeline should be used. The full fit is performed for the stars CD-38 8806 and CD-48 14233 once using the calibrated and once the un-calibrated spectra. Within the errors, the results for both approaches were identical. The temperature difference between both spectra was at most 43 K and 0.02 for the log(g), which is well below the adopted systematic uncertainties. Also the differences in derived abundances were well within the errors.
Therefore, both types of spectra will lead to the same results and can be used. Because the continuum of the un-calibrated spectra was slightly easier to normalize the flux-uncalibrated spectra were used throughout the analysis.

8.2 Individual objects

In this section the results of the spectral and kinematic analysis of the individual objects will be presented. The abundances will be shown in terms of logarithmic total number fraction, denoted $\log_{10}\left(\frac{\mathrm{X(Z)}}{\mathrm{N_{tot}}}\right)$, which are the values resulting from the analysis for each chemical element X, which depends on the atomic number Z. For reference the solar abundances (Asplund et al. 2009) are shown in every abundance plot. The markers in these plots all have different colors, one for each star. The same color coding is used in the figures concerning the sample, to identify individual objects.
Since the iron abundances can be derived for all stars, also the ratios of the elements to iron can be calculated. In the literature, the abundances are often given with respect to iron, in this section, however, the abundances with respect to all particles will be discussed. Nevertheless, it is also interesting to check element-to-iron-ratios, which will be done for the entire sample in the next section.
Accordingly, the abundance patterns are shown in the following subsections (Fig. 8.4, 8.6, etc.) and compared to the solar pattern. Additionally a figure summarizing the kinematic properties of each star will be shown (Fig. 8.5, 8.7, etc.).
Values not explicitly listed in this section can be found in the appendices A3 through A5.

8.2.1 TYC 6036-1933-1

TYC 6036-1933-1 is the coolest star in the sample. The atmospheric parameters (T_{eff}=8642 ± 90 K and log(g)=3.33 ± 0.05) are those of an A-BHB-star. As can be seen in Fig. 8.4, the abundances are all below solar. The uncertainty on the helium abundance is quite large, since the helium lines are barely present, due to the low temperature. The orbit of TYC 6036-1933-1 (shown in Fig. 8.5) have the shape of a halo orbit, as it extends quite a bit over and below the Galactic disk and the orbit is highly eccentric. In the U-V diagram this star is located outside of the Pauli-ellipses, as would be expected of a halo-star. Finally, the angular momentum and eccentricity show halo-characteristics. Based on the kinematic properties, this star is part of the halo.

8.2.2 TYC 1914-687-1

Besides TYC 6036-1933-1, this is the only other star below 9,000 K. The atmospheric parameters agree with it potentially being a A-BHB-star (T_{eff}=8679±90 K and log(g)=3.34± 0.05). The same can be said about the abundances (Fig. 8.6), as all abundances are below solar. Again, due to the low temperature the helium abundance has a high uncertainty. According to the U-V diagram, this star could be a disk star, but this does not agree with the other kinematic indicators (see Fig. 8.7). The orbit has the highest extension below and above the Galactic disk in the entire sample. The position in the $L_z - e$-diagram would be consistent with the star being a thick disk or halo member. Nevertheless, this star most likely is also a halo-member.

8.2.3 HD 23342

The temperature of HD 23342 places it at the lower temperature-end of the A-type sample (T_{eff}=9107 ± 100 K and log(g)=3.43 ± 0.05). All abundances are below solar and helium is at solar level (Fig. 8.8). The orbit has the typical shape of a halo-orbit and in the U-V and $L_z - e$ diagrams this star again falls into the regions typical for halo-stars. Consequently, based on its kinematics (Fig. 8.9) this star belongs to the halo.

8.2.4 HD 156758

According to its atmospheric parameters, HD 156758 could be a A-BHB-star (T_{eff}=9349 ± 100 K and log(g)=3.45 ± 0.05). As in all previously discussed targets again all elements are underabundant and helium is solar (Fig. 8.10). This star is the only A-type star in the sample where the abundance of Mn could be constrained. Although the position in the U-V diagram could make this star part of the thick-disk population, the orbit as well as the position in the eccentricity-angular momentum digram are those of a halo-star. So, HD 156758 is a member of the halo (Fig. 8.11).

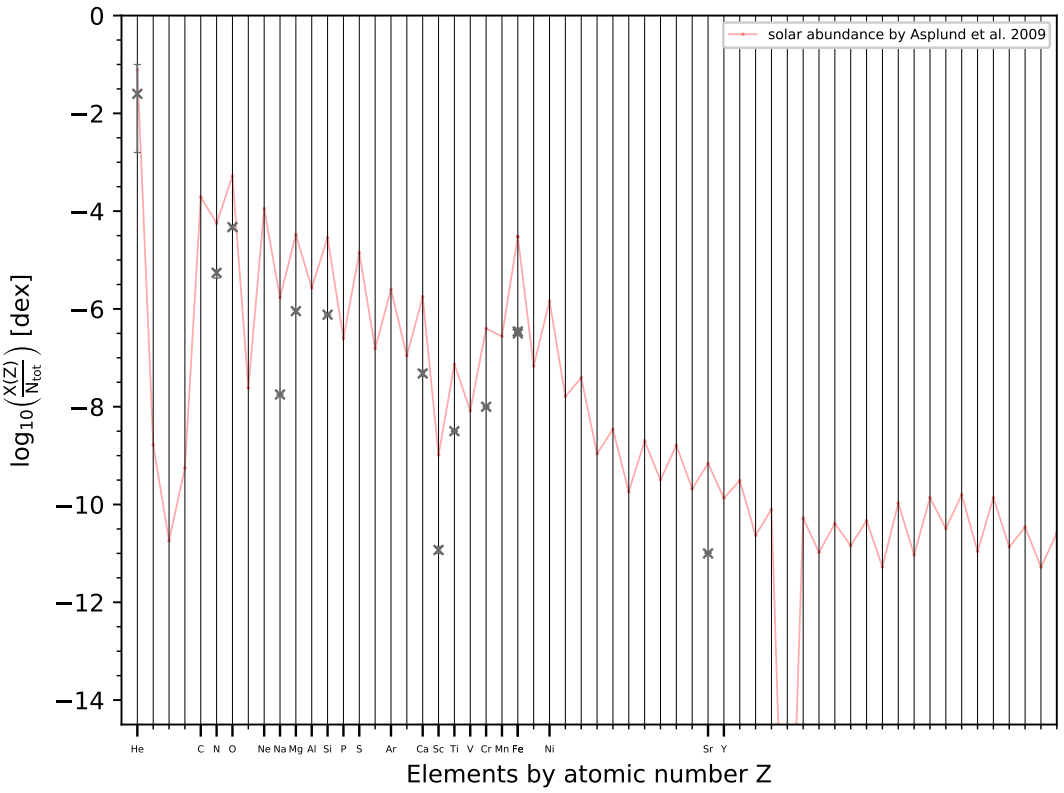

Figure 8.4: Abundances pattern of TYC 6036-1933-1 in logarithmic total number fraction, the red line shows the solar abundances pattern (Asplund et al. 2009)

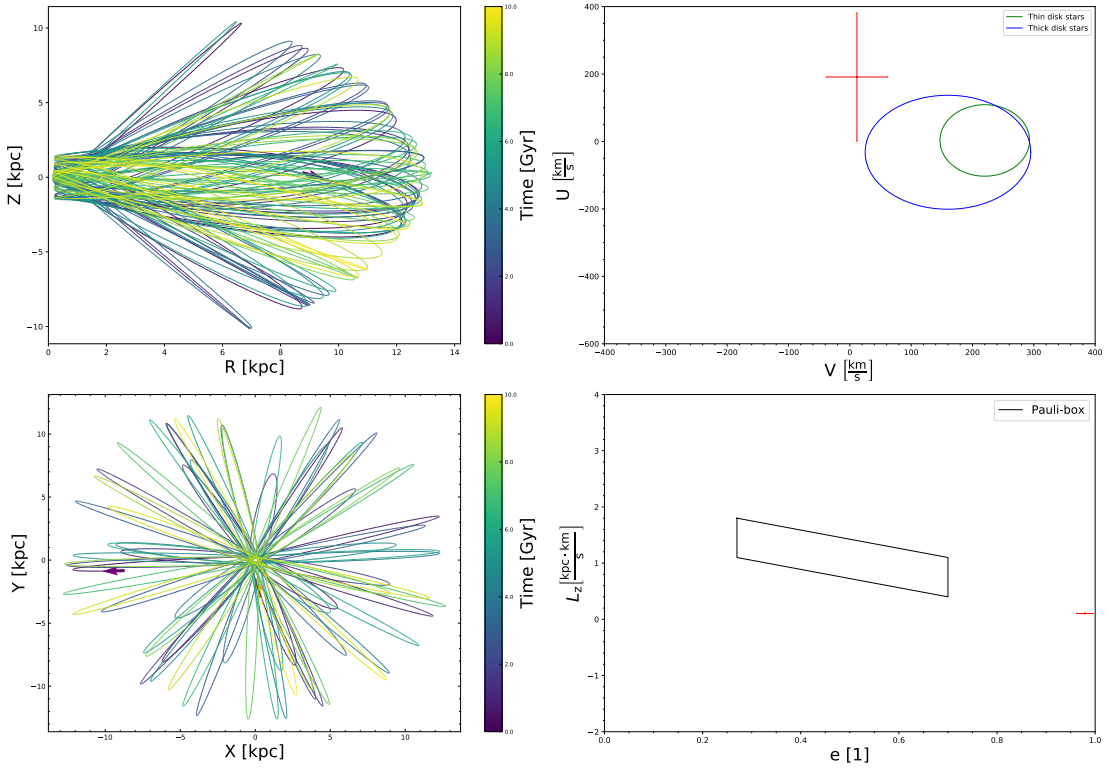

Figure 8.5: Kinematics of TYC 6036-1933-1 using the AS-potential
Panels on the left hand side show the orbits, the top panel shows the projection of the orbit in the R-Z plane, so this perspective shows how stars move relative to the disk, whereas the lower panel shows the X-Y plane, which is the projection one would see from the Galactic pole from atop. The time is color coded and the arrows indicate the initial and final (in terms of the calculation) direction of the star, using the same color-coding. The panels to the right show the same as Figures 7.1 and 7.2, and where the star is placed with respect to the Pauli-ellipses and box. The U-V diagram is shown in the right top panel and the angular momentum-eccentricity plot in the right lower one.

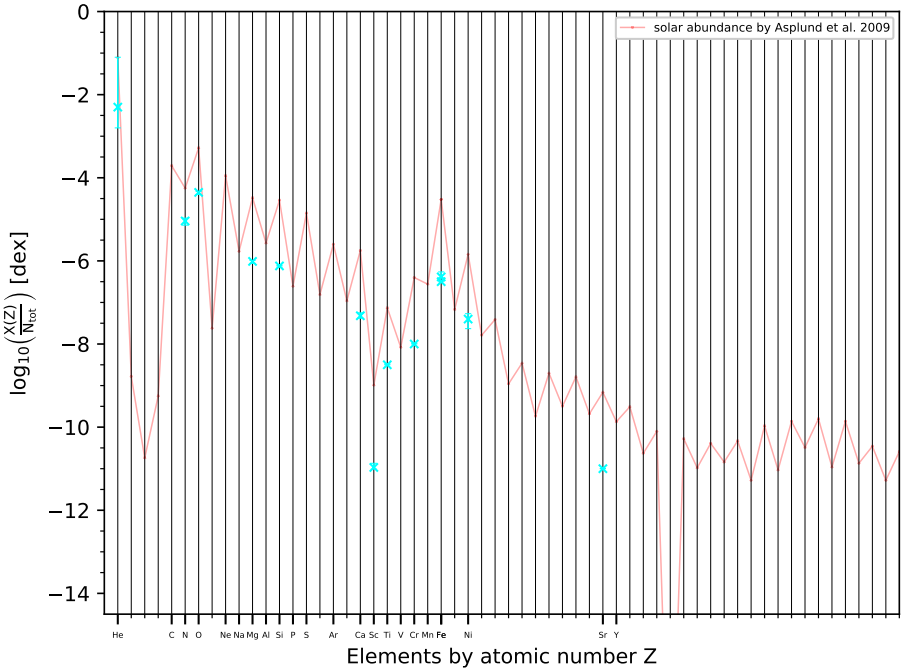

Figure 8.6: Same as Fig. 8.4 for TYC 1914-687-1

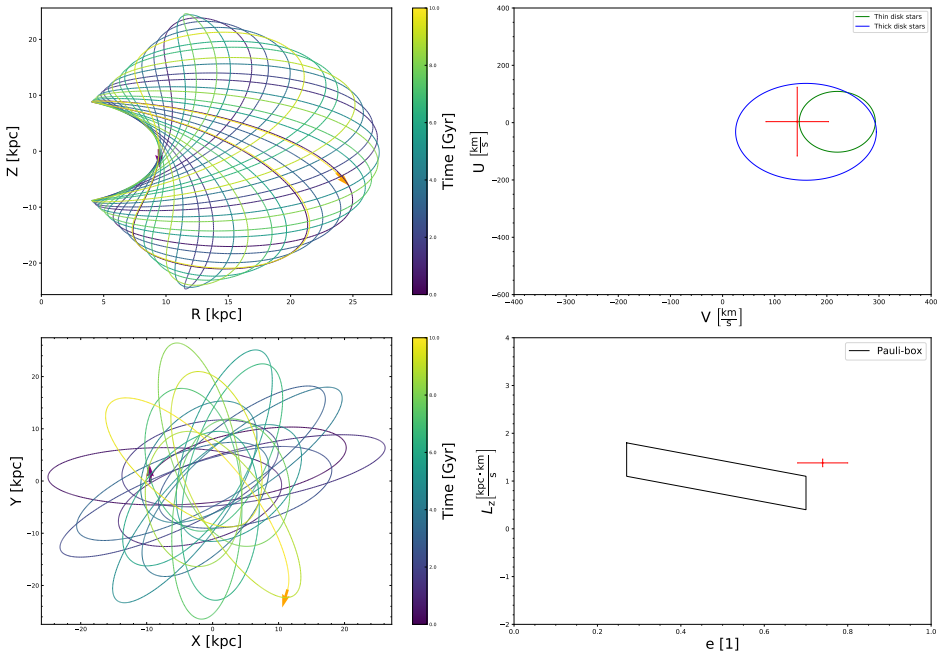

Figure 8.7: Same as Fig. 8.5 but for TYC 1914-687-1

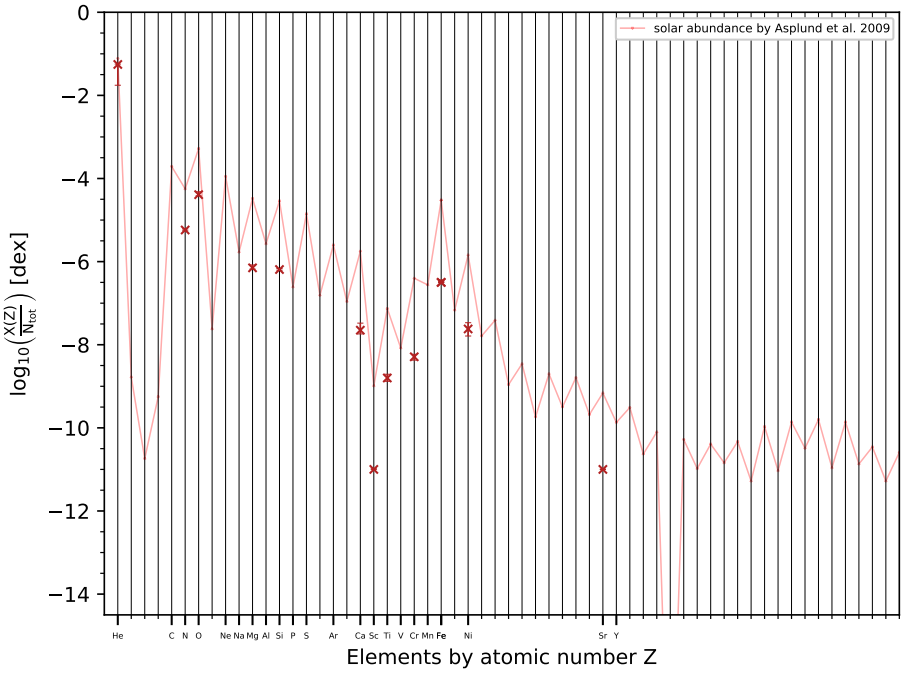

Figure 8.8: Same as Fig. 8.4 but for HD 23342

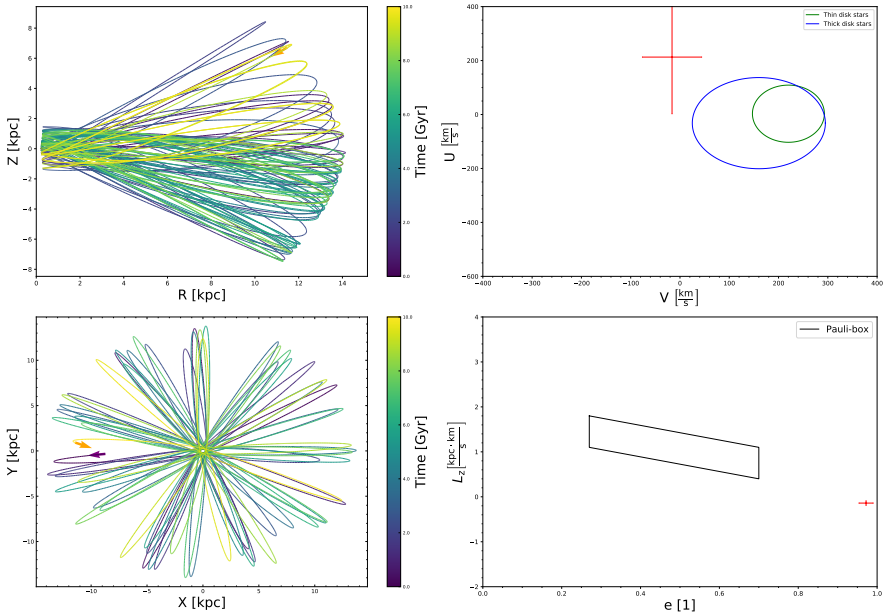

Figure 8.9: Same as Fig. 8.5 but for HD 23342

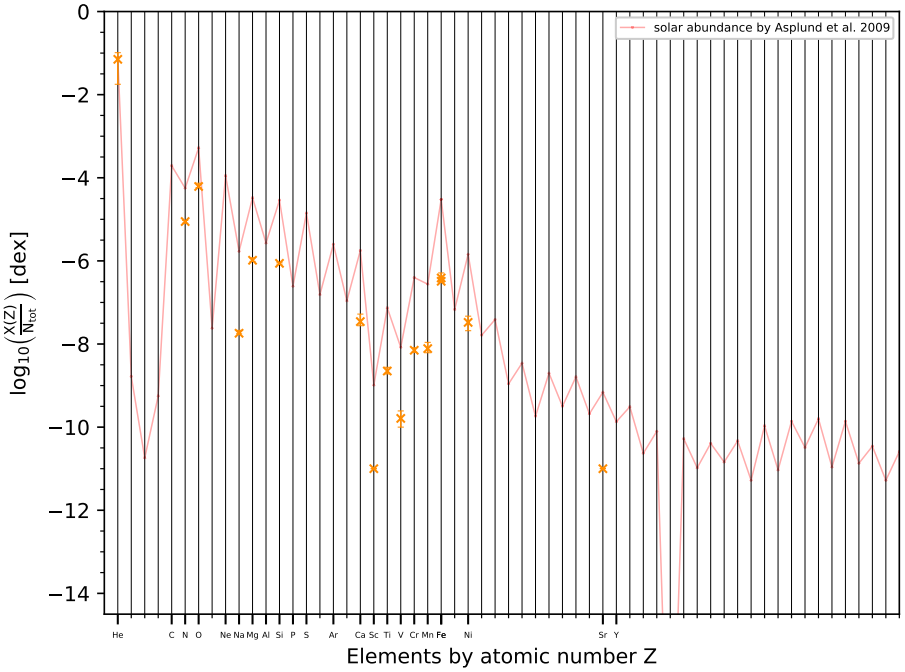

Figure 8.10: Same as Fig. 8.4 but for HD 156758

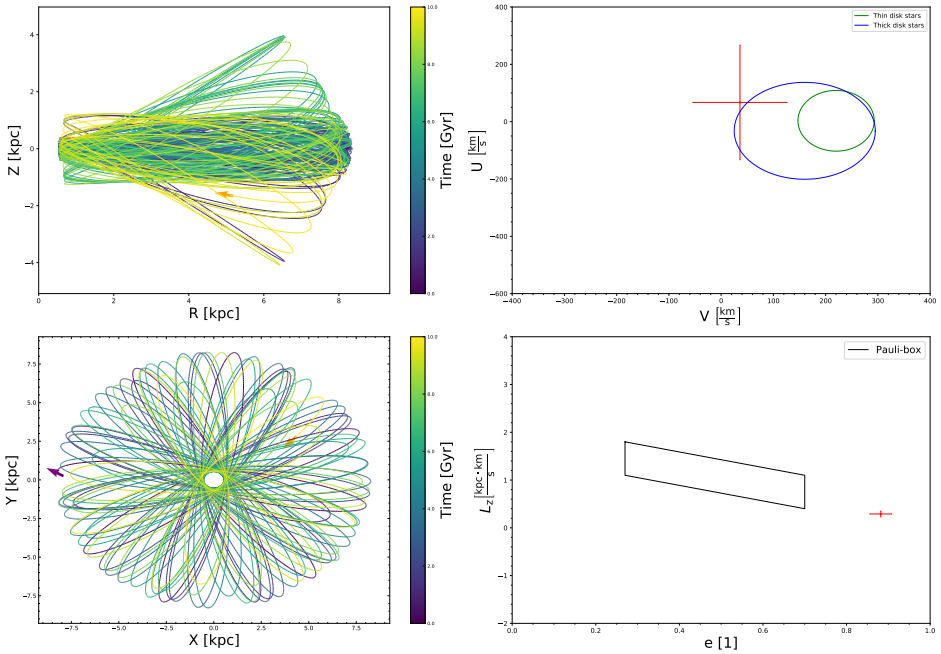

Figure 8.11: Same as Fig. 8.5 but for HD 156758

8.2.5 CD-48 14233

CD-48 14233 exhibits atmospheric parameters consistent with a HB-nature (T_{eff}=9583 ± 100 K and log(g)=3.55 ± 0.05). According to its temperature, it clearly is of spectral type A. As expected all elements, besides helium which is solar, are under-abundant with respect to solar (see Fig. 8.12). The kinematic properties of this star (Fig. 8.13) make it a halo-member, especially based on the shape of the orbit and the eccentricity and angular momentum. However, the position in the U-V diagram could also be consistent with a thick-disk membership.

8.2.6 HD 12655

Again, the stellar and atmospheric parameters agree with a A-BHB-nature for HD 12655 (T_{eff}=9613 ± 100 K and log(g)=3.53 ± 0.05). Also, all elements are underabundant with respect to solar, except for helium (Fig. 8.14). The shape and extent of the orbit of HD 12655 are consistent with a halo-membership (Fig. 8.15). Also, the position in the U-V and $L_z - e$ diagrams agrees with the orbital shape. Therefore, this star is again a halo object.

8.2.7 HD 8269

The atmospheric parameters of HD 8269 (T_{eff}=9695 ± 100 K and log(g)=3.53 ± 0.05) are in agreement with what is expected for A-BHB-stars. Again, except for helium, all elements are below solar level (Fig. 8.16). The kinematic analysis, shown in Fig. 8.17, clearly shows that this star exhibits halo characteristics. The orbit, eccentricity and angular momentum are those of a halo-star. The position in the U-V diagram, however, could also put this star in the thick-disk.

8.2.8 CD-38 8806

CD-38 8806 is one of the hotter potential A-BHB-stars in the sample (T_{eff}=10560 ± 110 K and log(g)=3.68 ± 0.05). Relative to all particles the abundances of all elements are below the solar values, as can be seen in Fig. 8.18, which is expected for A-BHBs, since they should not be subject to diffusion. Helium is around the solar value. According to the shape of the orbit and the kinematic properties, visualized by the position in the diagrams on the right-hand side, this star can be classified as a halo-member.

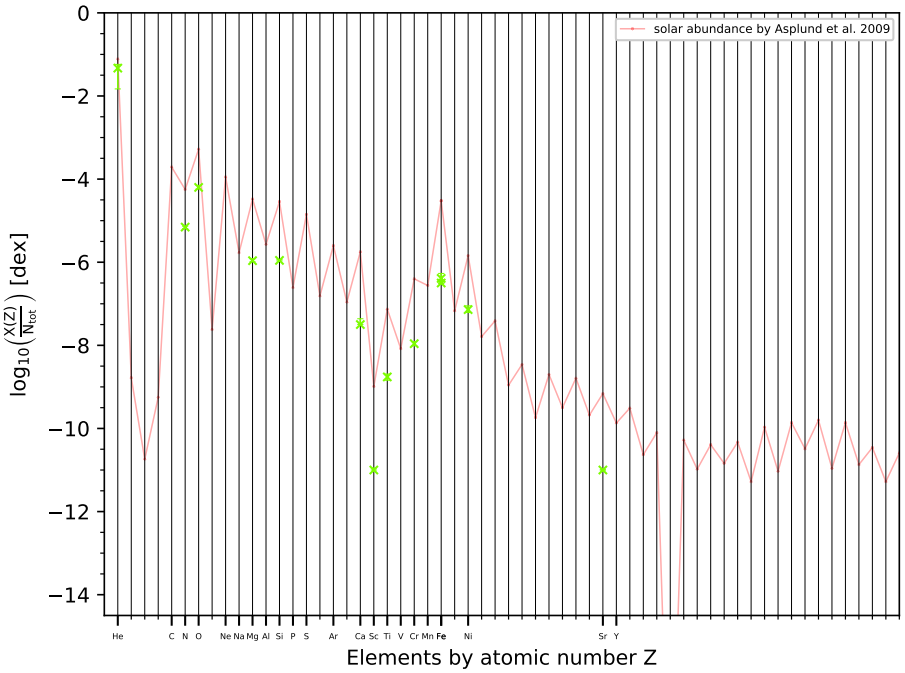

Figure 8.12: Same as Fig. 8.4 but for CD-48 14233

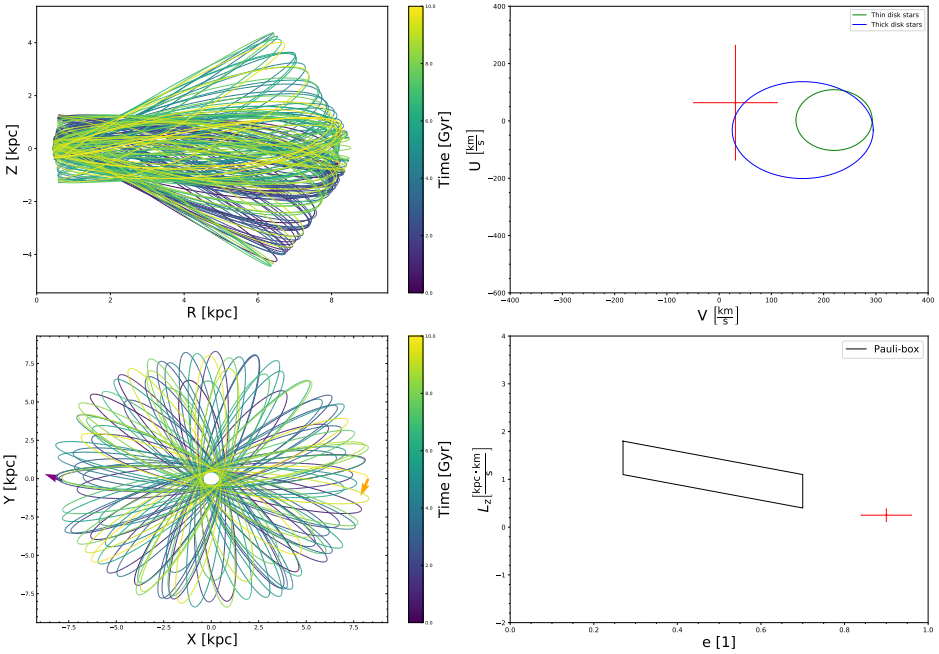

Figure 8.13: Same as Fig. 8.5 but for CD-48 14233

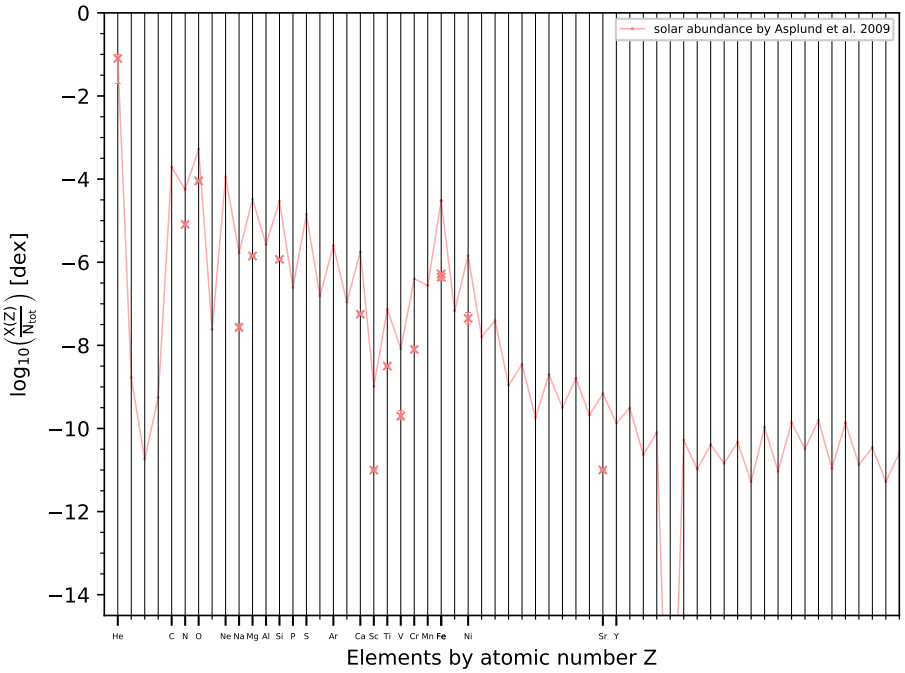

Figure 8.14: Same as Fig. 8.4 but for HD 12655

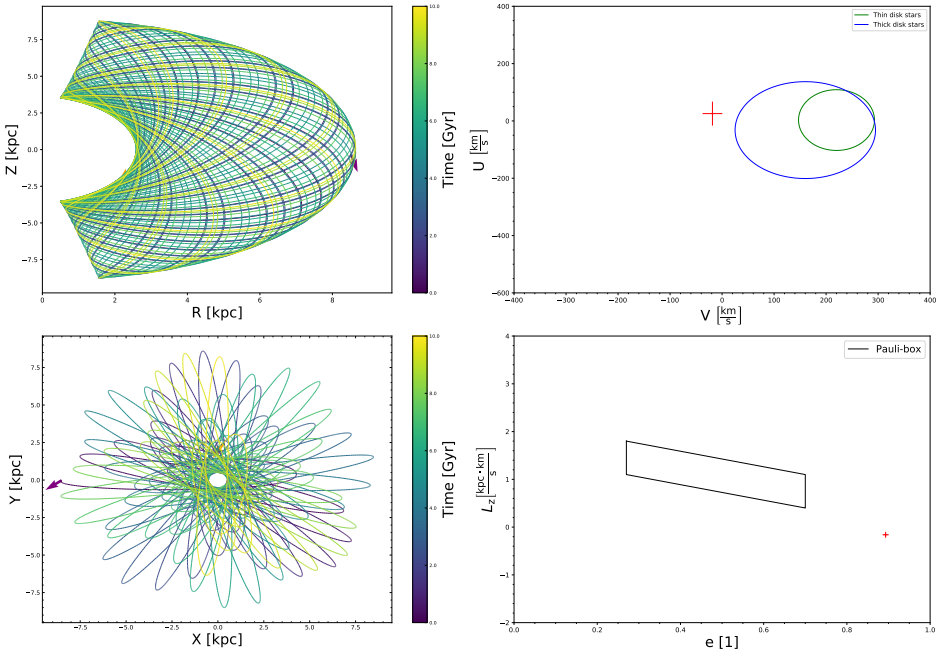

Figure 8.15: Same as Fig. 8.5 but for HD 12655

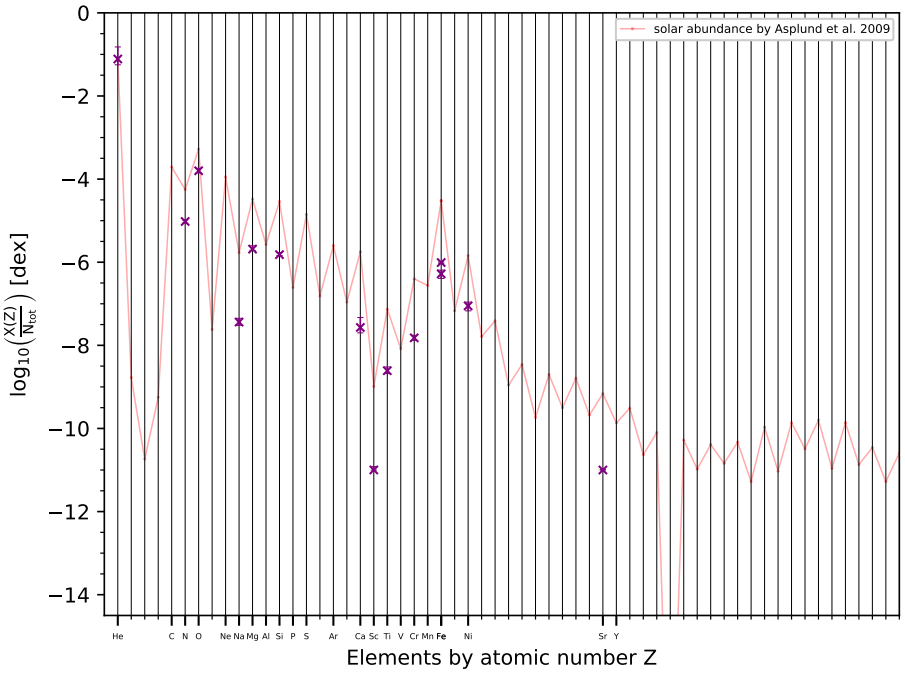

Figure 8.16: Same as Fig. 8.4 but for HD 8269

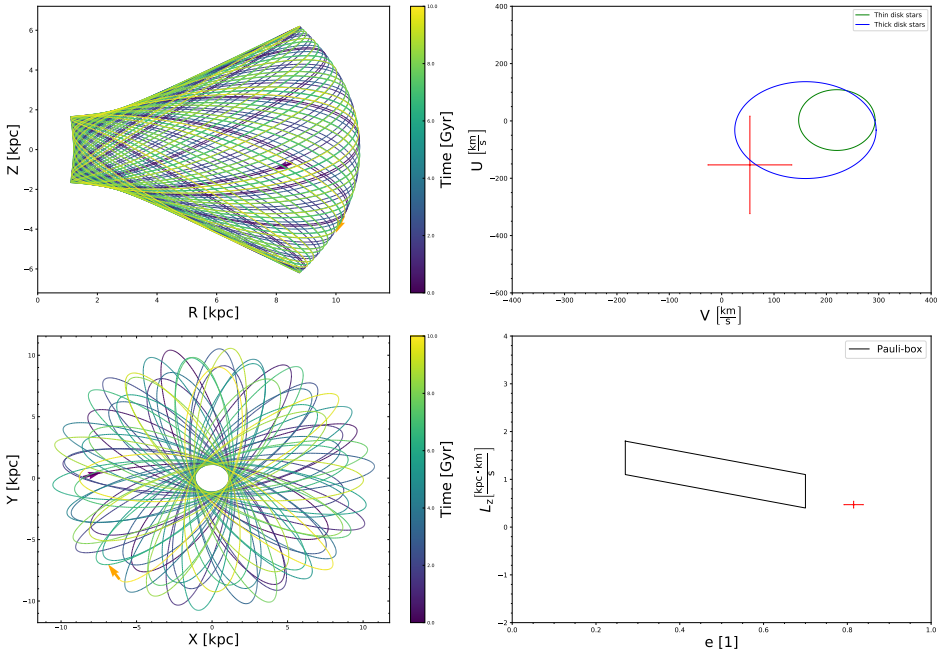

Figure 8.17: Same as Fig. 8.5 but for HD 8269

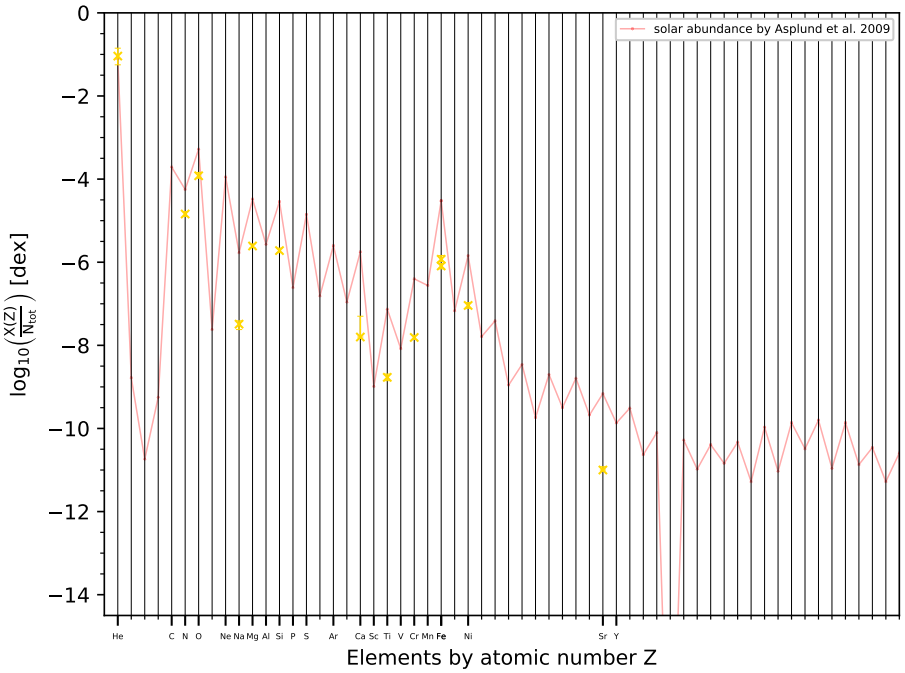

Figure 8.18: Same as Fig. 8.4 but for CD-38 8806

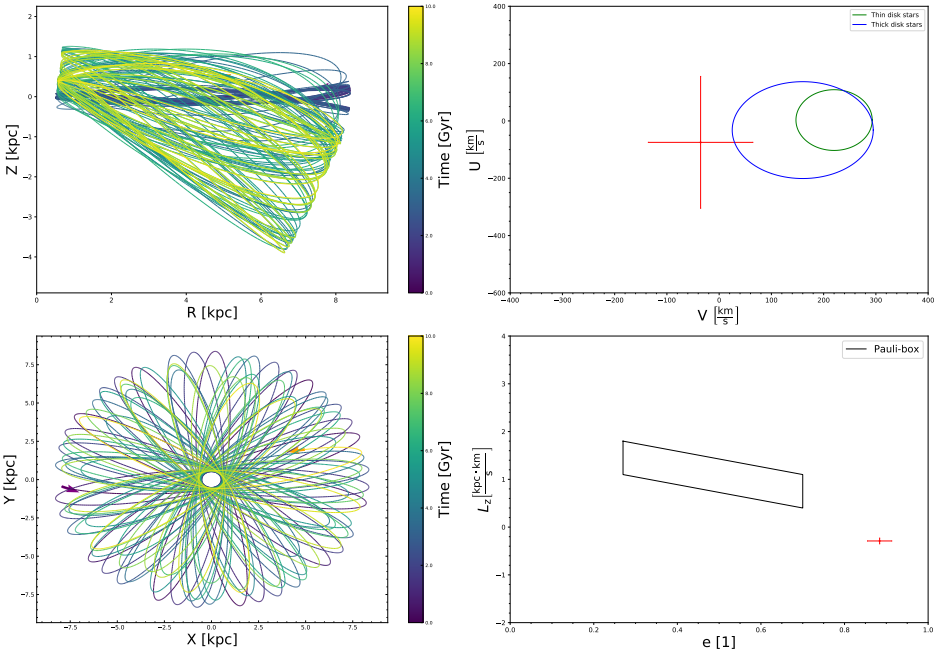

Figure 8.19: Same as Fig. 8.5 but for CD-38 8806

8.2.9 HD 209292

HD 209292 is the hottest A-type star in the sample (T_{eff}=11079±120 K and log(g)=3.77± 0.05). As typical for the other A-type stars in the sample all elements except for helium are below the solar value, as can be seen in Fig. 8.20. It is safe to say that this star belongs to the halo (see Fig. 8.21) , as this is indicated by the shape of the orbit, its eccentricity and the angular momentum. The U-V parameters, however, could also make the case for HD 209292 to be a thick disk star.

8.2.10 Feige 6

Crossing the NG1, Feige 6 is the coolest B-type-star in the sample. The atmospheric parameters of Feige 6 could place it on the HB (T_{eff}=14544±150 K and log(g)=4.16±0.05). The abundance of helium is well below solar. The abundances of P and iron are above solar, same applies to Y, with Feige 6 being the only star in the sample with clear Y-lines. All the other metals are below solar level, as can be seen in the abundance pattern shown in Fig. 8.22. Except for Fe and Y, for which this star yield the highest abundances among stars hotter than the NG1, the abundances of all other elements are the lowest ones observed amongst the B-type stars. However, the spectrum show quite a high number of unidentified lines, probably associated with elements not incorporated in the models. In contrast to all the other B-type stars, Feige 6 is the only member of these showing the kinematic characteristics of a halo-star, as indicated by the shape of the orbit and all the derived kinematic parameters (Fig. 8.23).

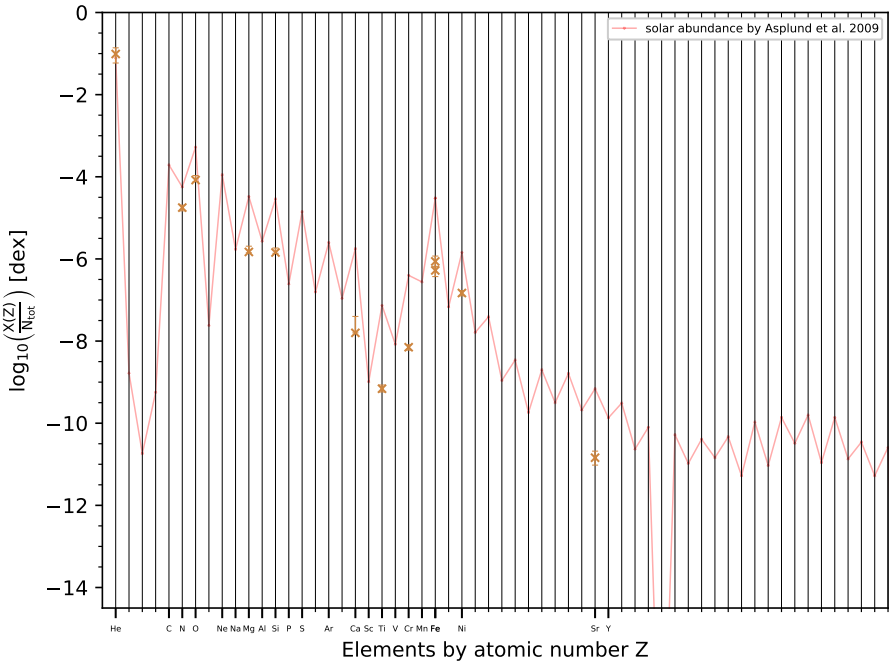

Figure 8.20: Same as Fig. 8.4 but for HD 209292

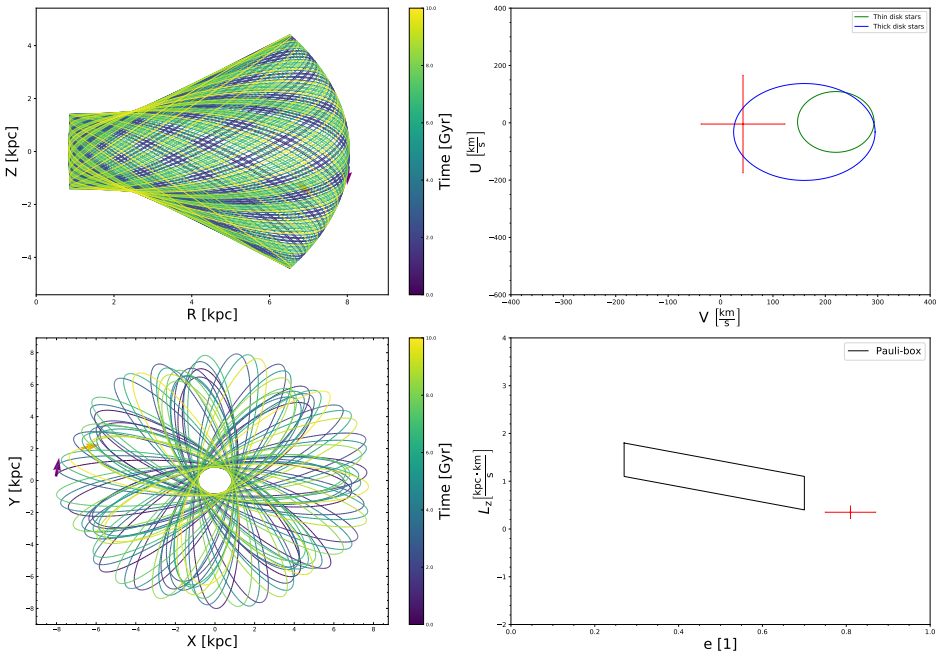

Figure 8.21: Same as Fig. 8.5 but for HD 209292

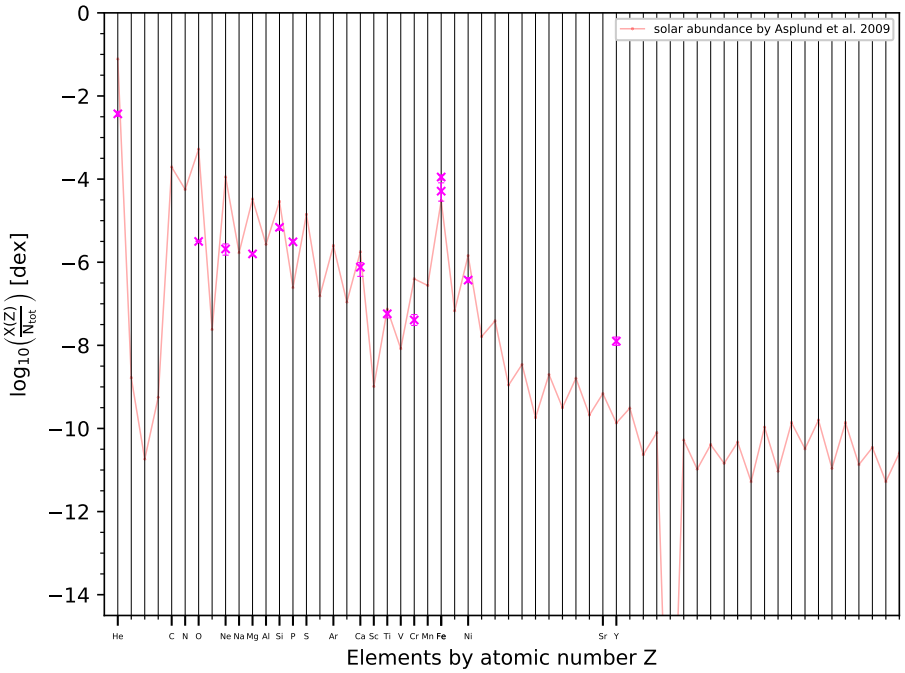

Figure 8.22: Same as Fig. 8.4 but for Feige 6

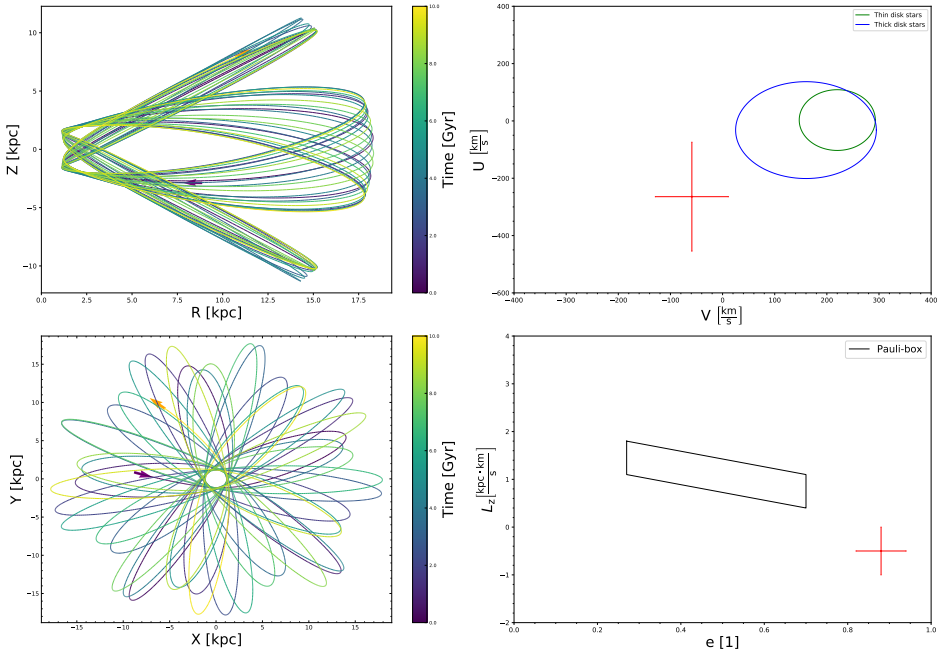

Figure 8.23: Same as Fig. 8.5 but for Feige 6

8.2.11 Feige 86

Feige 86 is the prototype B-BHB-star, therefore, it is not surprising that the atmospheric parameters agree with Feige 86 being a B-BHB-star (T_{eff}=15393±160 K and log(g)=4.43± 0.05), a more detailed comparison with the literature will be made later on. Clear overabundances of P, Ca, Ti, Mn and Fe are observed (Fig. 8.24), as well as a low helium abundance. Feige 86 is the only B-type star in which Mn lines are visible. The orbit of this star, shown in Fig. 8.25, looks like a disk-orbit, but based on the relatively high eccentricity and the position within the U-V diagram, it is probably a member of the thick disk.

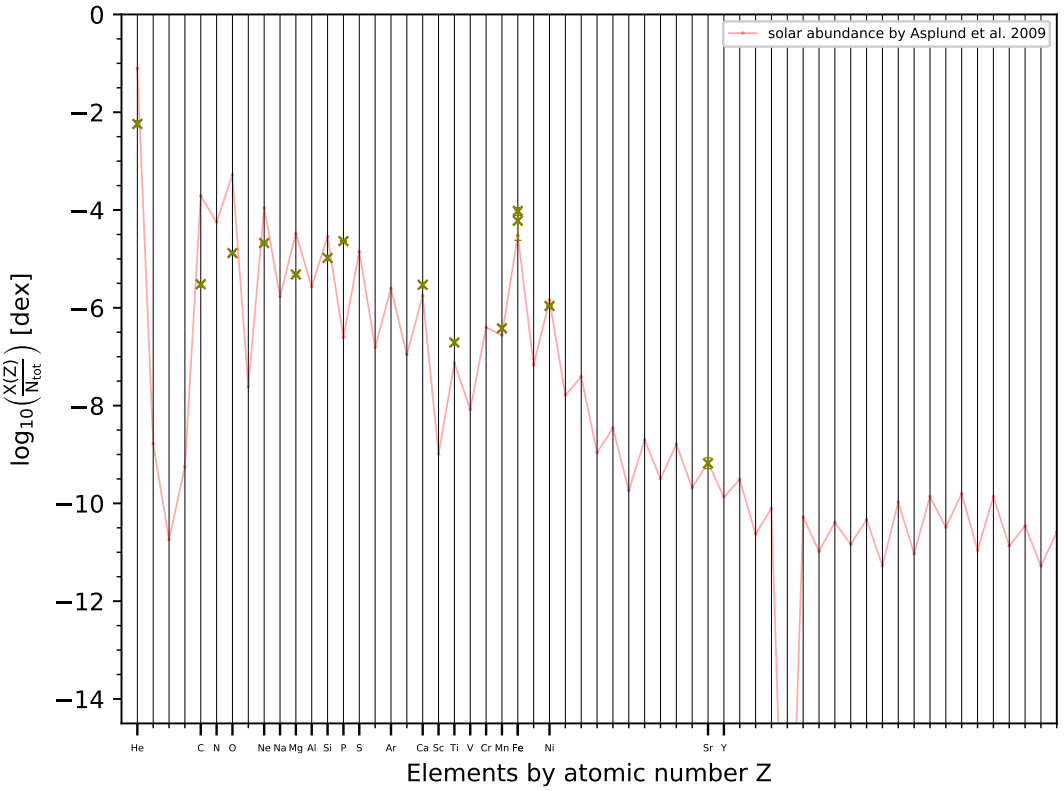

Figure 8.24: Same as Fig. 8.4 but for Feige 86

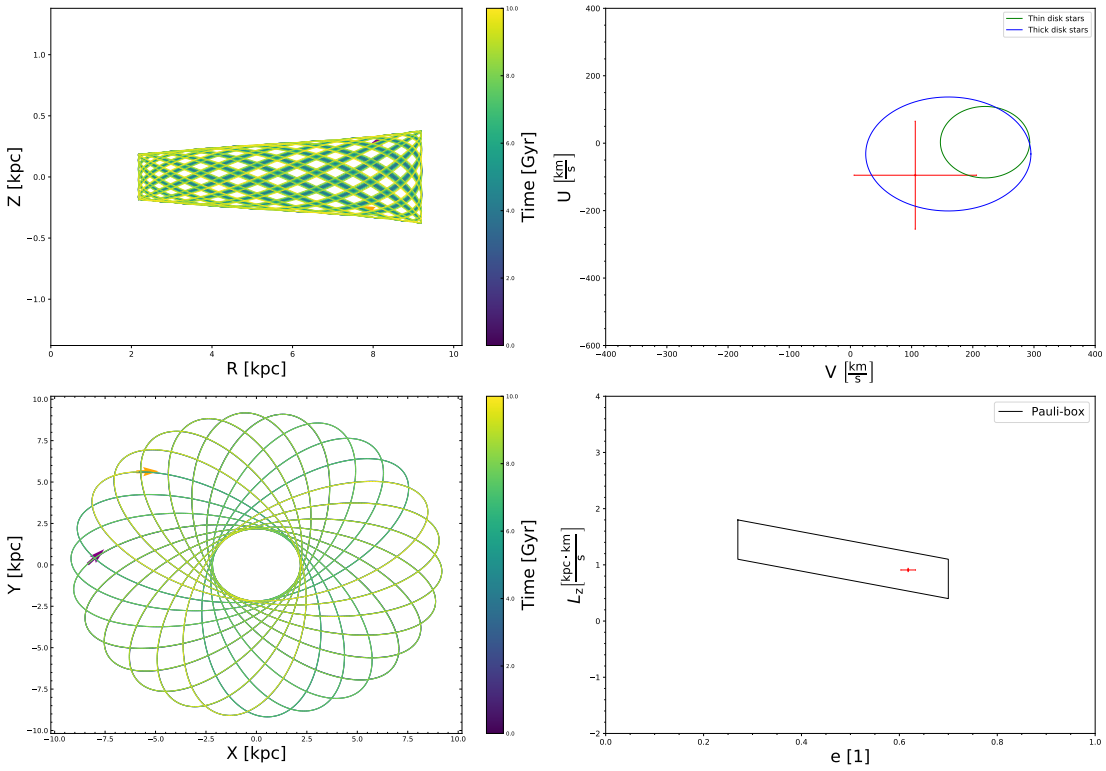

Figure 8.25: Same as Fig. 8.5 but for Feige 86

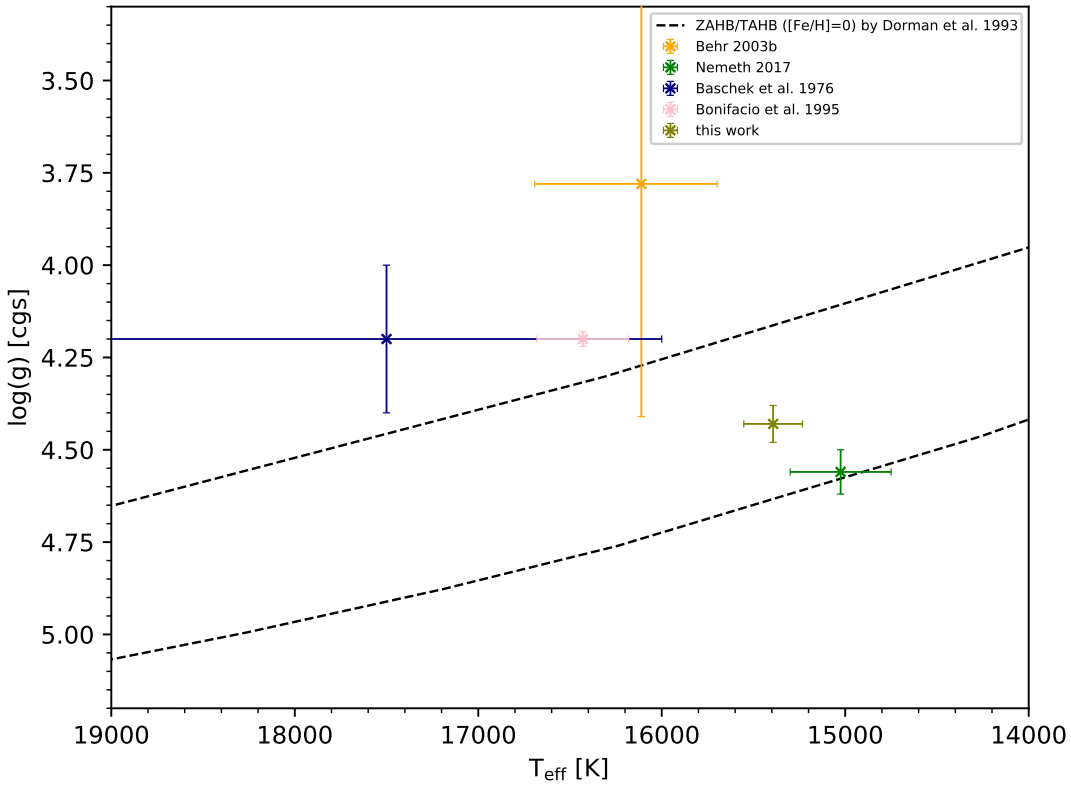

Figure 8.26: Kiel digram summarizing previous literature results for the atmospheric parameters found for Feige 86

Compared to the previous results which can be found in the literature the derived temperature using the ADS-approach is lower than found in previous studies which did not rely on the UVES spectra used. A higher surface gravity is derived, as indicated by the positions within the Kiel diagram shown in Fig. 8.26 for the different parameter combinations of Feige 86. However, the older results did not have high quality data available and did not use the entire visible spectral range in those cases where spectroscopy was used to derive the parameters. The uncertainties of the parameters adapted or found in older studies are quite large. Therefore, the values derived for Feige 86 agree with the older results. The analysis by Németh (2017) used NLTE model atmospheres to find the atmospheric parameters. They find a slightly lower temperature as well as a higher log(g), but again, within the uncertainties the results almost agree with each other. The parameters are much better constrained by the ADS-analysis than when compared to other approaches, as indicated by the size of the error-bars, which are quite small compared to the other literature values.
However, the comparison is not limited to the atmospheric parameters only, since many others have studied the abundances of Feige 86. The derived abundance pattern of Feige 86 (shown in Fig 8.24) looks very similar to the one found by Németh (2017) which is

shown in Fig. 1.17. Therefore, yielding a good agreement with this study. However, the overabundances for some elements can not be confirmed here as the performed analysis of Feige 86 did not make use of UV spectra but focused on the optical, in which some elements clearly overabundant in Feige 86 do not show any strong lines. Fig. 8.27 compares the derived abundances for elements in common with Kafando et al. (2016). This analysis as well used the UVES spectra, however, the abundances were all derived adopting the atmospheric parameters found by Behr (2003b). Nevertheless, the abundances agree well with each other. The orbit calculated for Feige 86 (shown in Fig. 8.25) looks very similar to the one found by (Altmann and de Boer 2000) (Fig. 1.16), again yielding a good agreement with the literature. Since basically every analysis step gives results consistent with the literature, the validity of the approach used can be confirmed. Based on Feige 86, the results are trustworthy.

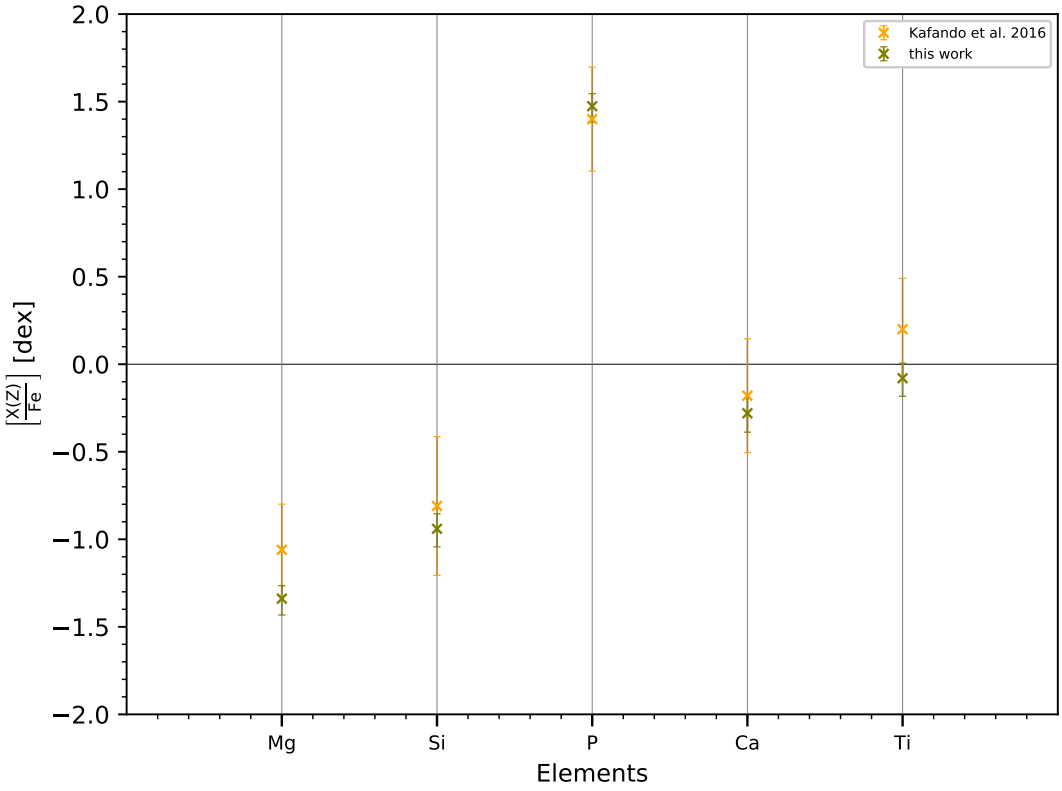

Figure 8.27: Abundances as element-to-iron ratios relative to solar derived by Kafando et al. (2016) and in the performed analysis

8.2.12 HD 110942

HD 110942 is the only B-type star selected from the Altmann-Catelan sample. According to its atmospheric parameters this star could be a HB-star (T_{eff}=17046 ± 180 K and log(g)=4.74 ± 0.05). The helium abundance is low, as expected if HD 110942 is a HB-star. Enrichment compared to solar is found for a number of elements such as N, P, Ti or Fe (see Fig. 8.28). The orbit is contained within a very distinct narrow region, hinting at this star being a disk member. In the U-V diagram this star is located in the inner Pauli-ellipse, which would indicate that HD 110942 is a thin-disk star. Also, the position in the $L_z - e$ diagram is that of a thin-disk star. The kinematic analysis (see Fig. 8.29) of HD 110942 clearly shows that it is a disk star, very likely even a thin-disk member.

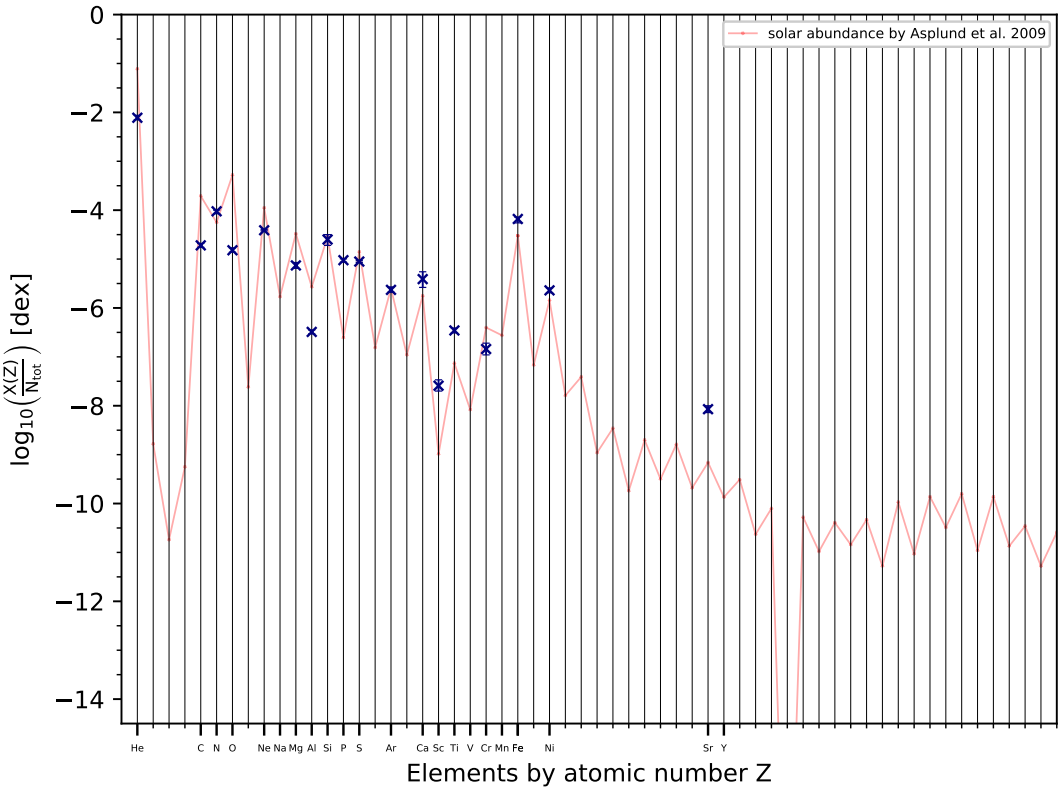

Figure 8.28: Same as Fig. 8.4 but for HD 110942

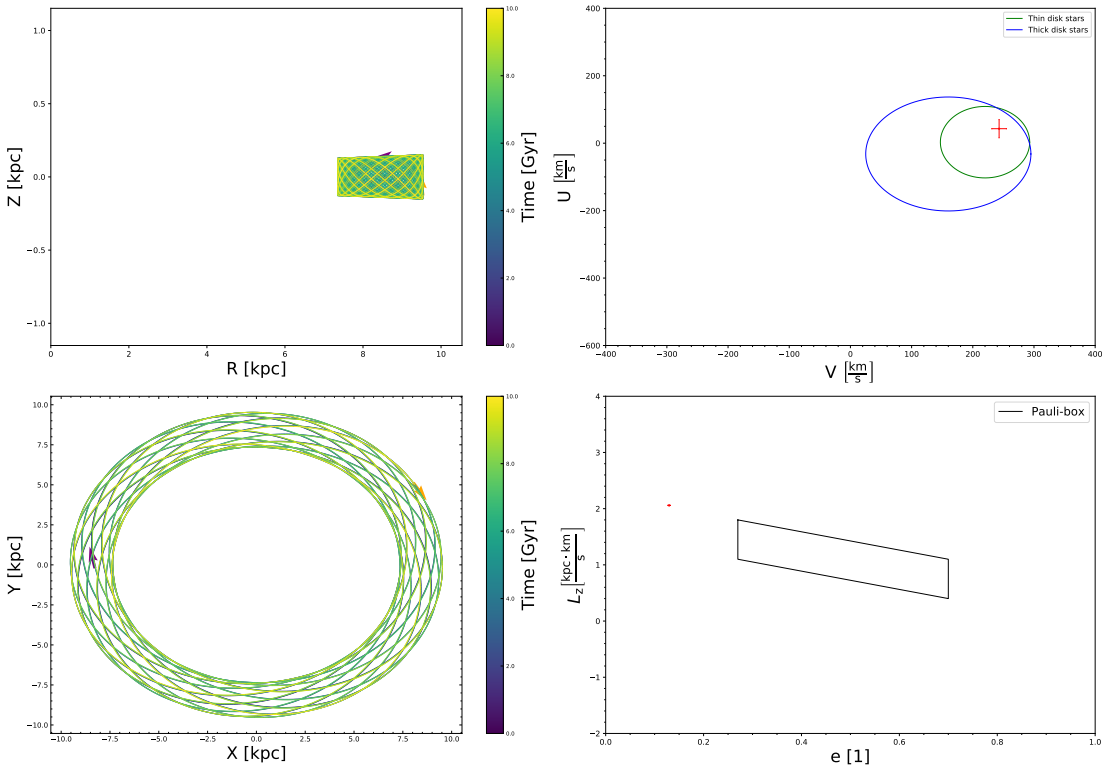

Figure 8.29: Same as Fig. 8.5 but for HD 110942

8.2.13 PHL 25

The atmospheric parameters of PHL 25 place it on the HB-band (T_{eff}=17585 ± 200 K and log(g)=4.57 ± 0.05). Again helium is depleted. Overabundances are detected for Si, P and Ar (Fig. 8.30). Although the orbit is contained in regions quite close to the disk, the shape looks somewhat chaotic when compared to the e.g. Feige 86 or HD 110942. However, the positions in the U-V and $L_z - e$ diagrams are consistent with those of a thick-disk star. Therefore, the kinematics of PHL 25 show the characteristics of a thick-disk star (Fig. 8.31). As this star was taken from the literature, the results will be compared to previous as well.

PHL 25 has been studied previously, especially under the aspect of helium isotope

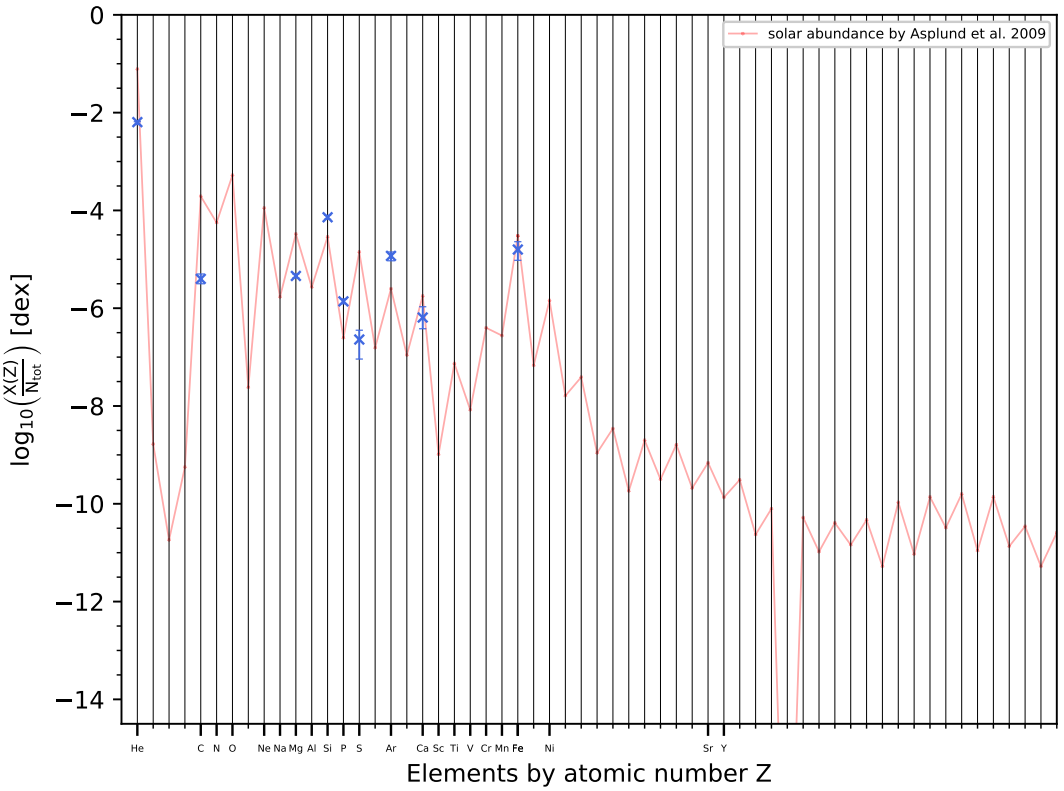

Figure 8.30: Same as Fig. 8.4 but for PHL 25

anomalies. Heber (1987) found an effective temperature of 19000 K and a log(g) of 5.0, hence this star was classified as a BHB-star due to its atmospheric parameters. Additionally, they found an isotope ratio smaller than unity. Later on, this star was studied by Schneider et al. (2018) in the context of investigating the helium isotope anomaly as well. This analysis utilized a similar approach chosen. Just like Heber (1987) the effective temperature (19500 ± 100 K) is higher than the one found here. The log(g) ($4.77^{+0.01}_{-0.02}$) on the other hand is found to be lower than in the analysis by Heber (1987) but

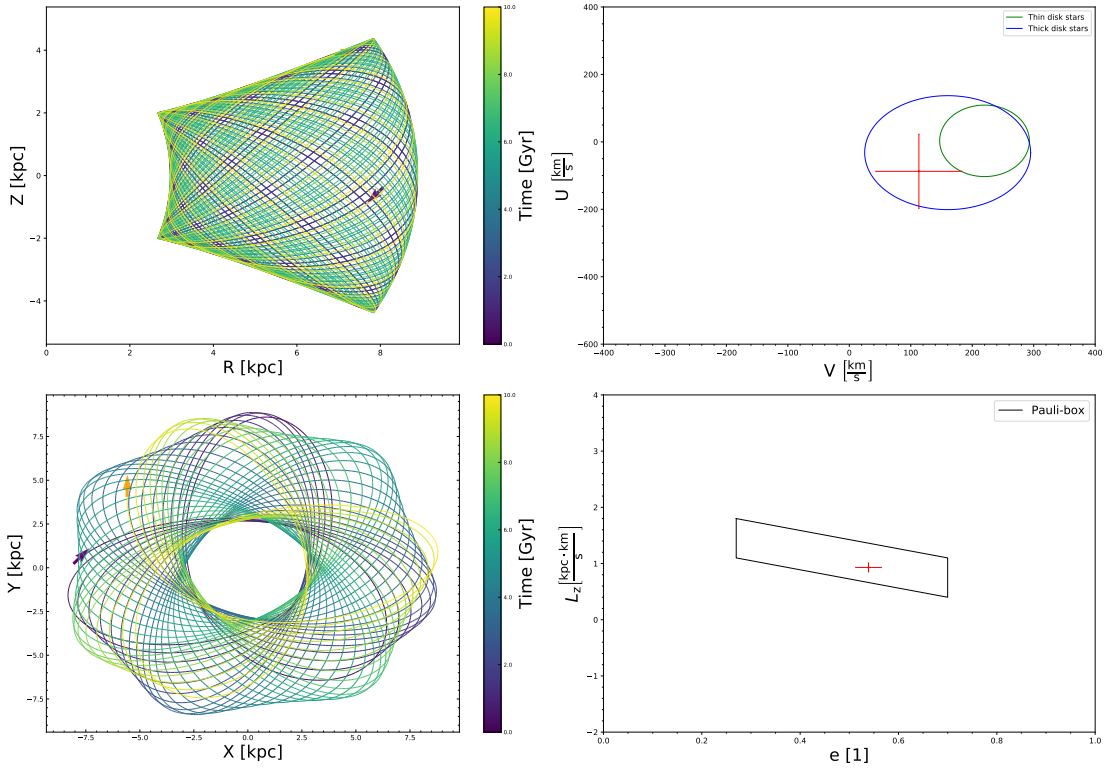

Figure 8.31: Same as Fig. 8.5 but for PHL 25

still higher than the newly derived one. In contrast to Schneider et al. (2018) the helium abundances is found to be slightly higher, which could be linked to the temperature being lower. Generally the findings for the helium lines agree with the literature, a clear enhancement of ^{3}He is detected and the overall helium abundance is below solar. The metal abundances derived by Schneider (2017) are similar to the ones found and mostly agree within the errors although towards heavier elements the abundances are found to be slightly higher than previously. However, the atmospheric parameters are different. For the comparison with Heber (1987), the discrepancies could be explained by the fact that better data is used, the analysis is more advanced in terms of spectral range, and models. Surprisingly, although the same spectrum and a similar approach was used, the results are quite different, as PHL 25 is found to be slightly cooler than previously thought. This either indicates that the analysis is actually not valid for the spectrum analyzed which is not expected to be the case, or that the small improvements and differences implemented into the models and analysis-procedures since the analysis by Schneider et al. (2018); Schneider (2017), for example the local normalization procedure or the updated model spectra codes, have a bigger impact on the results than thought, or that just like in the case of TYC 1914-687-1 two solutions exist, based on the available spectral data. However, it might be noteworthy that the photometrically derived temperature is lower, hence, agrees with the spectroscopic value found here and is even further away from the

parameters found previously.
Therefore, the results deviate from those found in the literature, however, no analysis of this star has been as extensive before.

8.2.14 PHL 382

PHL 382 could be a quite peculiar object, as it is the only star with atmospheric parameters not agreeing with the solar metallicity canonical HB, the surface gravity is too low (T_{eff}=17903 ± 190 K and log(g)=4.08 ± 0.05). Helium is underabundant. Overabundances (see Fig. 8.32) are found for N, Si, Ar and Ti. The calculated orbit, which can be seen in Fig. 8.33, has the shape of a disk orbit. The position within the Pauli-ellipses additionally indicates a disk membership, however, this position is consistent with the thin and the thick disk. Furthermore, the star is placed within the Pauli-box, henceforth, indicating a thick-disk characteristic. Therefore, PHL 382 is most likely a thick-disk star. Since, just like PHL 25, PHL 382 is a known literature star, a more extensive comparison with previous studies will be made later on.
PHL 382 has also been studied on multiple occasions, even resulting in different classifica-

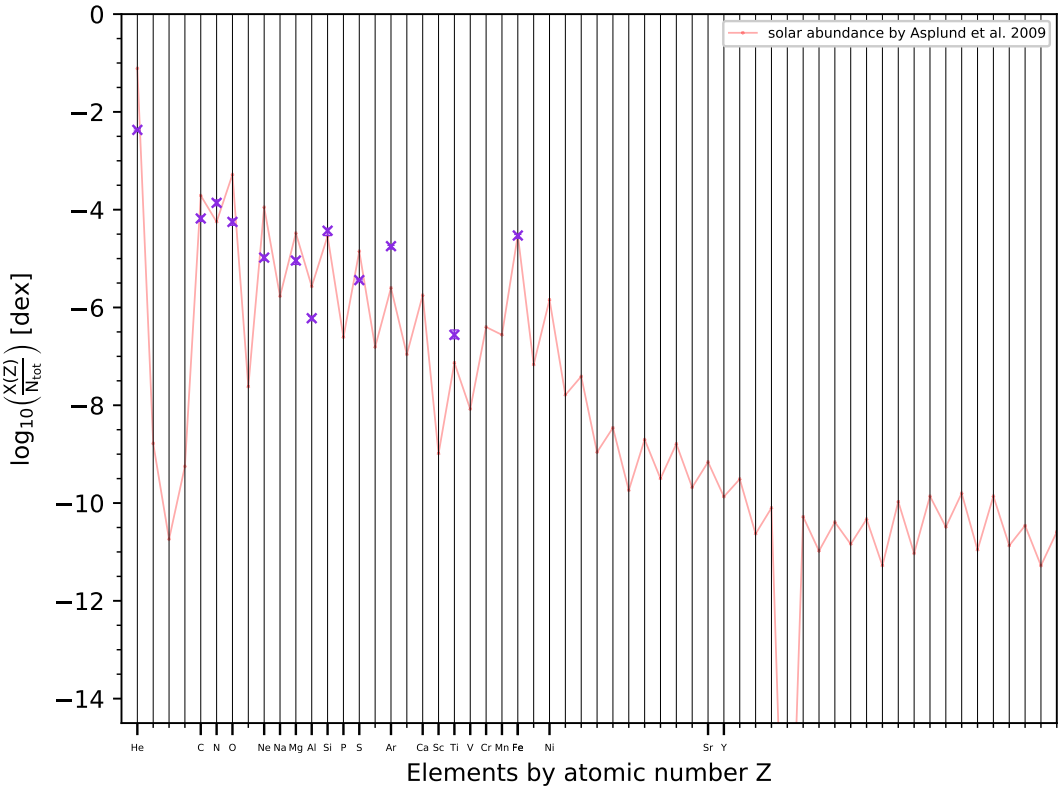

Figure 8.32: Same as Fig. 8.4 but for PHL 382

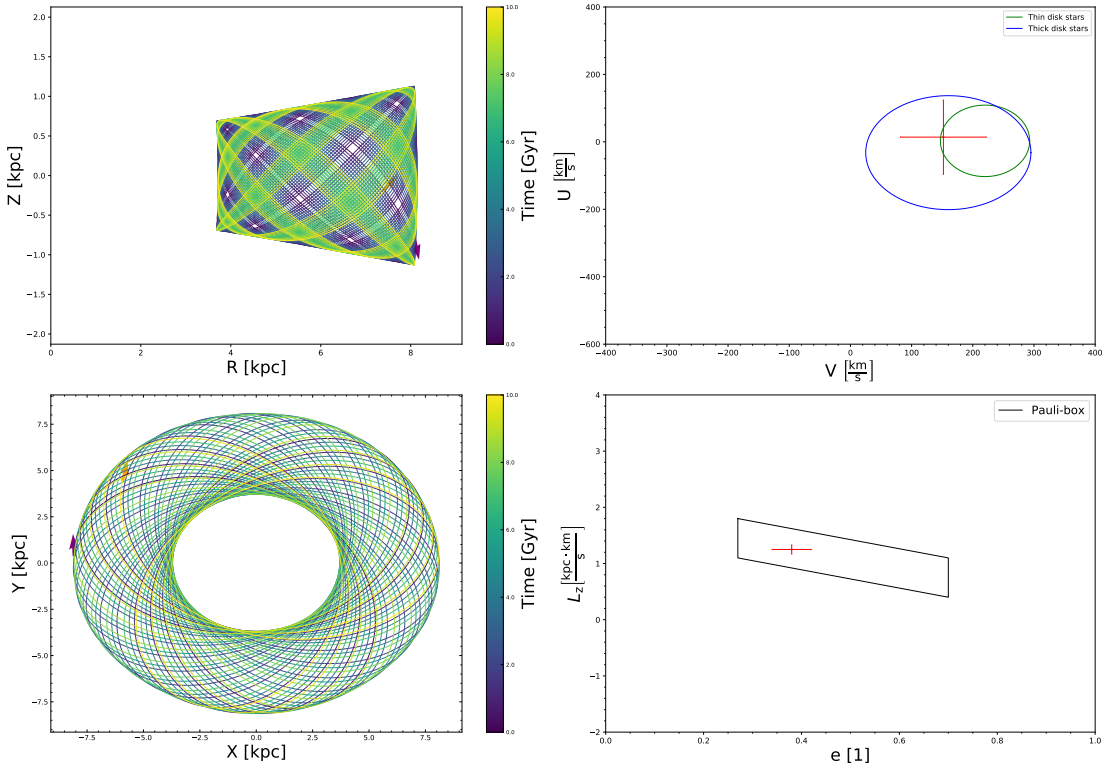

Figure 8.33: Same as Fig. 8.5 but for PHL 382

tions. According to Heber (1987) this star has an effective temperature of about 18200 K and a surface gravity of about 4.1, plus showing a clear enrichment in ^{3}He, too, while still being underabundant in helium. Hence, PHL 382 was classified as a BHB-star. Within the uncertainties, the results are consistent with each other. Kilkenny and van Wyk (1990) found similar parameters through fitting the profiles of H_γ and H_β ($T_{\rm eff} = 18000 \pm 1000$K and log(g)=3.75 $\pm$ 0.25), these parameters are reasonable close to the once obtained. Later on Dufton et al. (1993) found similar atmospheric parameters. Due to the low surface gravity, PHL 382 was classified as MS star. Additionally, PHL 382 was found to have a low helium abundance, agreeing with the results, and underabundances for Mg which is observed as well, and Si which in the new analysis is found to be slightingly higher than the solar value have been reported. Dufton et al. (1993) classified PHL 382 as a halo-star, which is not confirmed by high precision Gaia data. Schneider et al. (2018); Schneider (2017) find atmospheric parameters agreeing well with the results (17600 $\pm$ 100 K and log(g)=3.92 $\pm$ 0.01). Although, the helium abundance is found to be slightly higher. The abundances found by Schneider (2017) are similar to the newly derived ones. Based on the low surface gravity Schneider et al. (2018) classified PHL 382 as a post-HB star.

Generally, the results of PHL 382 are in good agreement with the literature. As this is the case for PHL 382 and Feige 86 this again clarifies the validity of the analysis approach.

8.3 The sample

8.3.1 Kiel diagram

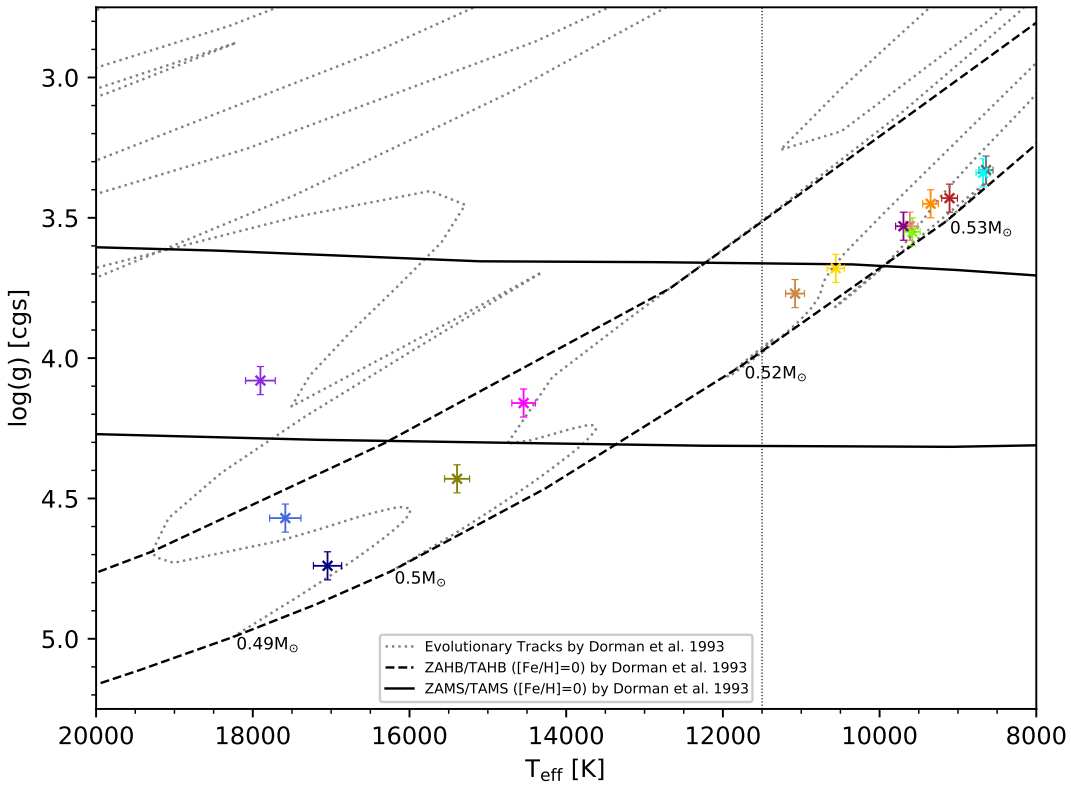

Figure 8.34: Atmospheric parameters of the program stars, compared to evolutionary tracks of different ZAHB masses, computed for solar metallicity (dotted lines). The dashed curves show the theoretical HB-band and the full drawn lines the MS. The vertical dotted line indicates the position of the NG1

Figure 8.34 shows the derived surface gravities (in logarithmic values of the surface gravity in cgs units) and effective temperatures in Kelvin of all program stars. Additionally theoretical sequences and evolutionary tracks computed by Dorman et al. (1993) are shown as well (if not otherwise specified Dorman-tracks shown are taken for solar metallicity), as these tracks indicate stars will move towards lower surface gravities after being born on the ZAHB. Stars on the HB-band could be HB-stars based on their atmospheric parameters. The atmospheric parameters of all program stars except for PHL 382, which lie above the HB-band, are consistent with the stars being part on the HB, at least when

solar metalicity is assumed. Generally the hotter stars seem to have evolved more than the cool ones, as those are closer to the ZAHB. Generally the atmospheric parameters agree well with the expectations if the stars are all on the HB, except for PHL 382.
Figure 8.35 also shows the Kiel diagram, but also includes a HB-bands for metallicitiy below solar. The lower metallicity considered corresponds to the iron abundances found in the A-type stars. However, in the metal-poor case the A-BHBs seem to systematically have gravities that are too high, even though the metallicity of the red HB-band in Fig. 8.35 should be appropriate for theses stars. The fact that these stars are halo stars, hence, should be metal-poor, but do not fall onto the theoretical metal-poor HB-band seems puzzling. This either implies that the models especially for lower metallicities are not appropriate to describe these stars, as factors having significant impact on the position of the HB might have been missed by theory so far. Another possible explanation could be that the iron abundances found in the A-type stars actually do not represent the initial ones which is not expected or that only taking iron as a proxy for metallicity is not sufficient. The HB-band shifts towards higher gravities and lower temperatures for a higher metallicity, therefore, the B-BHBs would be more evolved, if they belong to a metal-rich population. Feige 6 and PHL 25 would then be very close to the TAHB. When considering metal-richer case the A-type stars would be more evolved.
In any case the atmospheric parameters of all program stars are close to those expected for HB-stars. However, these parameters alone are not sufficient to verify that the stars in fact are on the HB. Based on the atmospheric parameters alone CD-38 8806, HD 209292, Feige 6 and PHL 382 could also be MS stars.

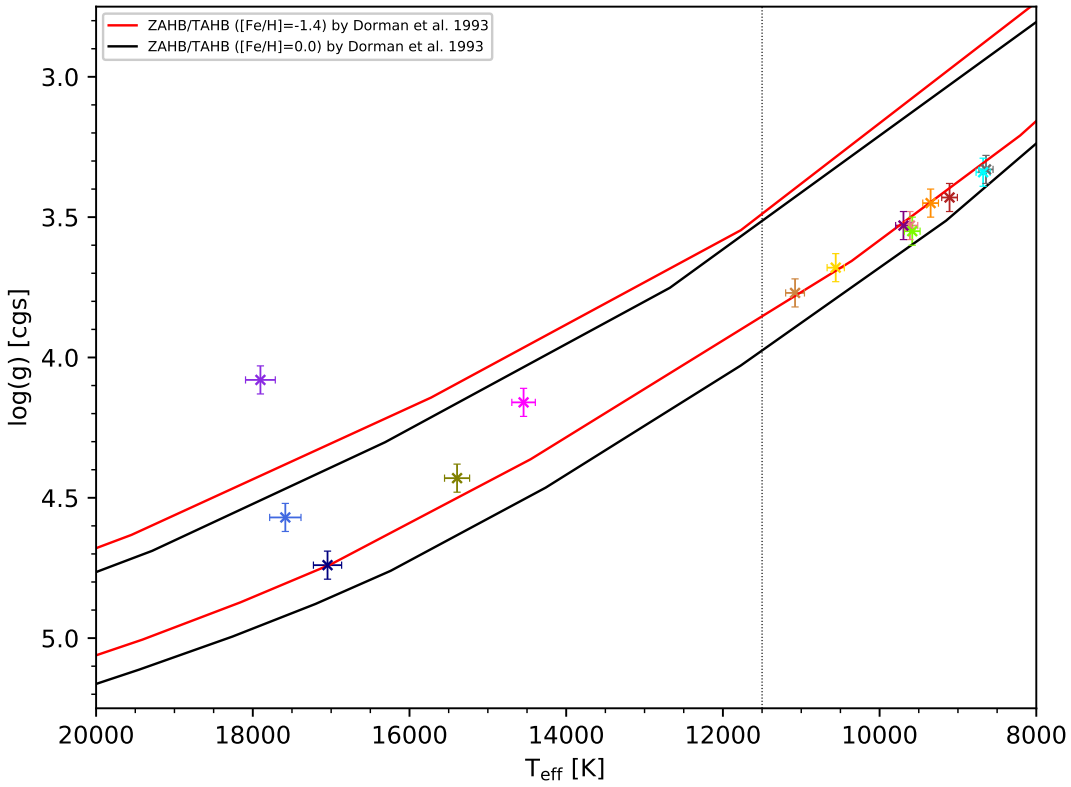

Figure 8.35: Atmospheric parameters of the program stars, compared to HB-bands computed for different metallicities

8.3.2 Stellar rotation

The stellar rotation, expressed by the projected rotational velocity is expected to drop significantly at temperatures above the NG1. The A-type stars show quite a wide spread of rotational velocities, as can be seen in Fig. 8.36, with TYC 1914-687-1 having the highest projected rotational velocity in the sample. Stars hotter than the NG1 are expected to have rotational velocities below $\sim 10\ \frac{\mathrm{km}}{\mathrm{s}}$, this is also observed as all these stars show a slower rotation than the cooler stars. PHL 382 has a quite high v·sin(i) value, above the expected value if PHL 382 is a HB-star.

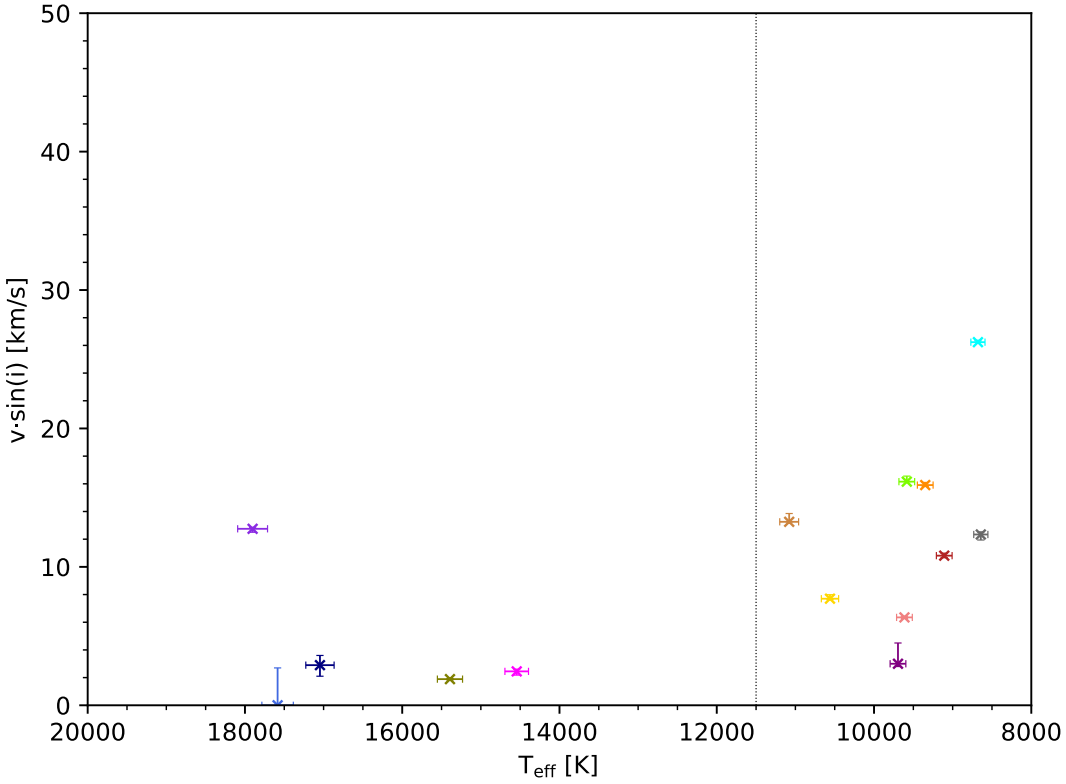

Figure 8.36: The derived projected rotational velocity as a function of effective temperature, the solid black line marks the position of the NG1

8.3.3 Helium abundances

Figure 8.37 shows the helium abundance depending on the effective temperature. At the low temperature end of the A-stars the uncertainties are quite large, which is not surprising, since the helium lines are barely visible below 9,000 K. As temperature increases the helium lines become stronger, hence yielding smaller uncertainties. Helium is similar to the solar value in this temperature range. For temperatures higher than the NG1 the overall helium abundance is expected to drop due to diffusion. This is indeed observed, as the helium abundance drops significantly with respect to the A-type stars. The lowest helium abundance is found in Feige 6 (-2.43 ± 0.06 dex), towards higher temperatures a slight increase in helium abundance is evident among the B-stars.

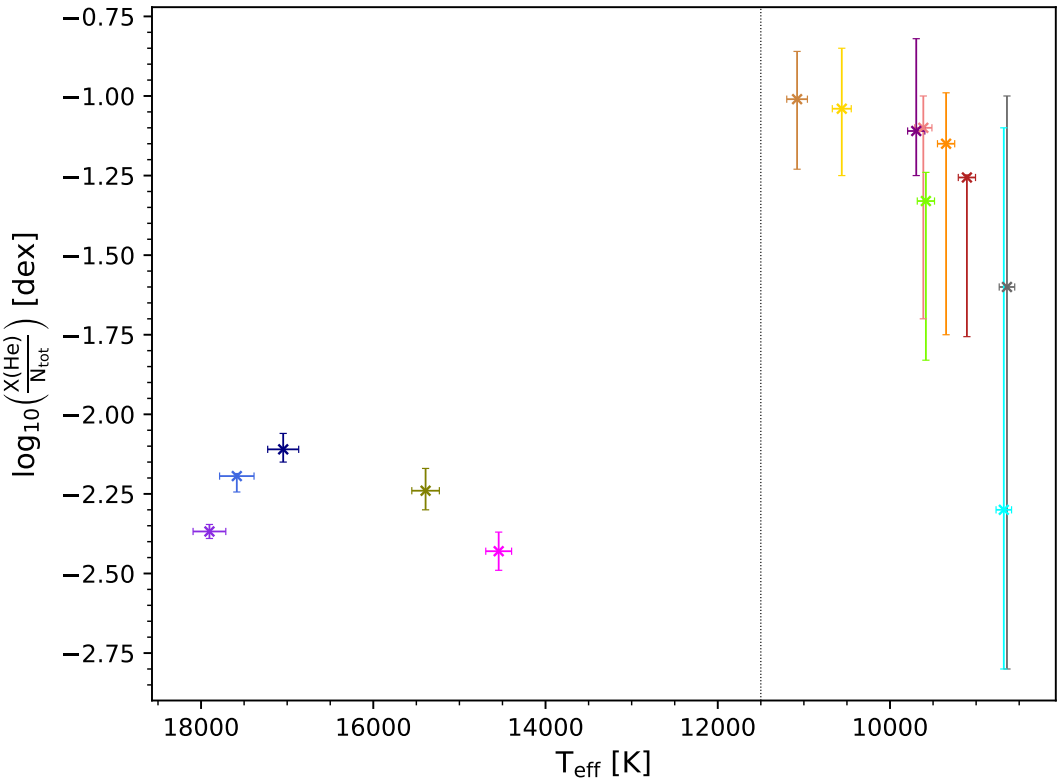

Figure 8.37: The derived total helium abundance as a function of effective temperature

8.3.4 Helium isotope ratios in B-BHBs

For all potential B-BHB-stars the abundances of the isotopes ^{3}He and ^{4}He were treated separately, since these stars are known to show helium lines for which the shape indicates a clear contribution of the lighter isotope to the lines. In general, the ratio of both isotopes is different from the solar one and a clear enrichment of ^{3}He is found. Table 8.1 summarizes the derived ratios of ^{4}He to ^{3}He, and they clearly indicate a strong enrichment for the lighter helium isotope. The solar particle-number ratio is very high $\sim 6,000$. This indicates an enrichment of up to three or four orders of magnitude compared to solar. In PHL 382, the ^{3}He isotope is even more abundant than ^{4}He. This enrichment is probably due to diffusion and consistent with previous results.

Table 8.1: Helium isotope ratios

star	Feige 86	PHL 25	HD 110942	PHL 382	Feige 6
$\frac{n(^4\mathrm{He})}{n(^3\mathrm{He})}$	$4.7^{+1.1}_{-0.9}$	$1.10^{+0.17}_{-0.22}$	$6.8^{+0.9}_{-1.0}$	$0.177^{+0.030}_{-0.027}$	$2.7^{+0.7}_{-0.6}$

8.3.5 Helium stratification in B-BHBs

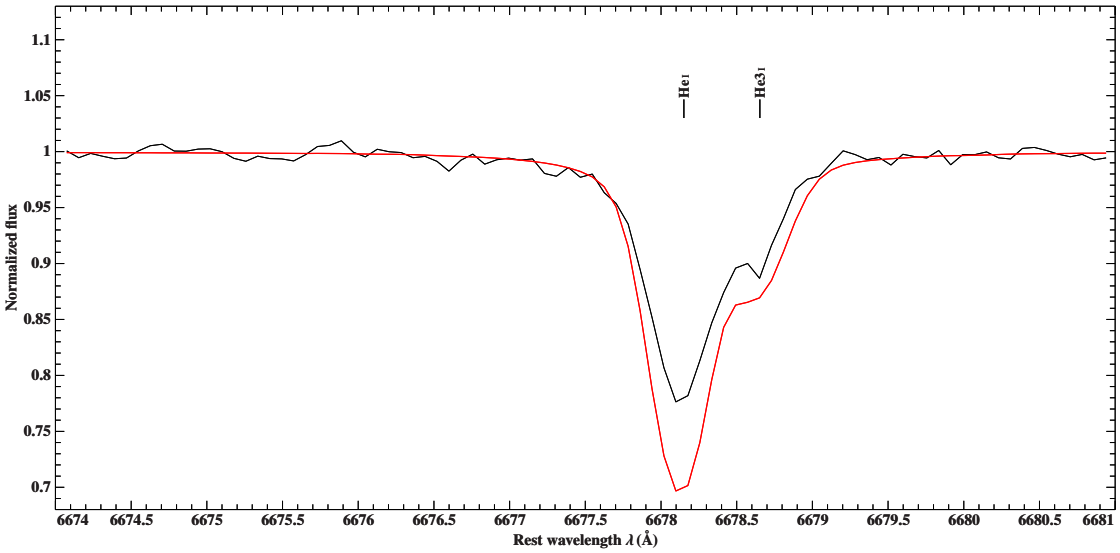

Figure 8.38: Spectral fit of HD 110942 showing the 6678 Å helium line

For the B-type stars, the helium lines can generally not be matched very well compared to the lines of other elements, especially for the lines showing the highest shifts in wavelength between the isotopes, however, the overall abundances are reliable (Schneider et al. 2018). The clear separation between the lines caused by the different isotopes can be seen in Fig. 8.38, which shows a part of the spectral fit for HD 110942. The line is not matched in depth, however, the overall shape seems to be quite similar. The fact that the lines are not matched perfectly could be explained by helium being vertically stratified in the atmospheres of B-BHB-stars, which means that the helium abundance is not homogeneous throughout the atmosphere but changes with depth.

8.3.6 Abundances of A-BHBs

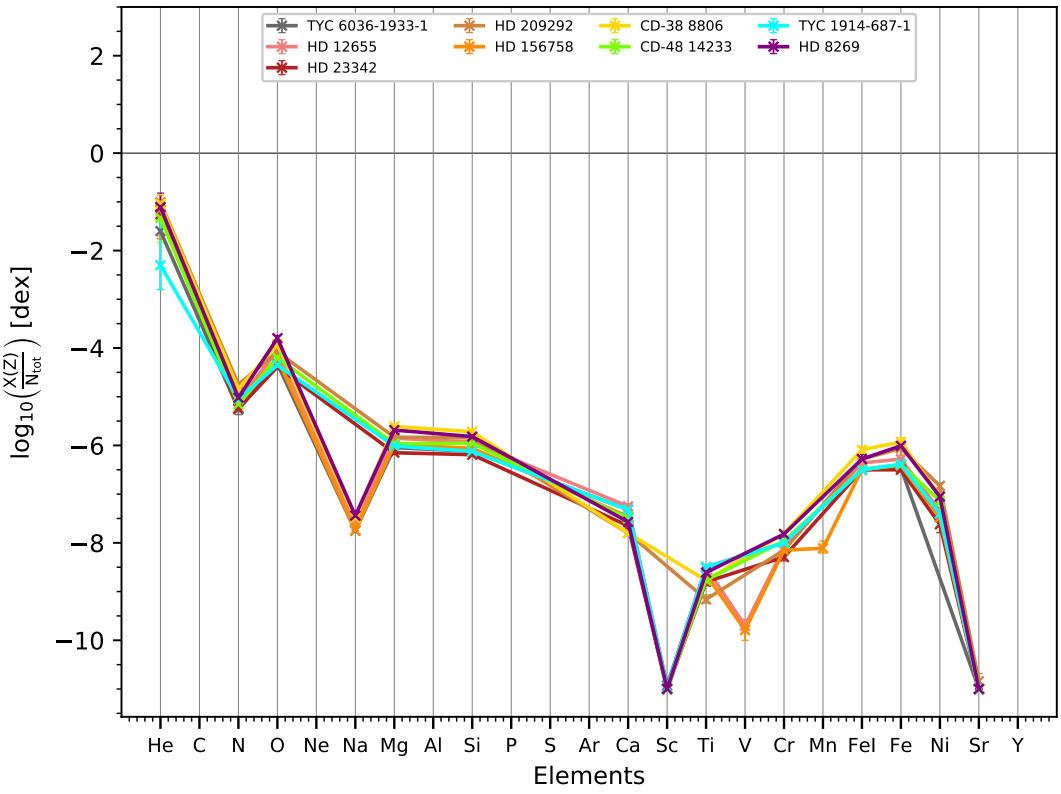

Figure 8.39: Derived total abundances for A-stars

The helium abundances are consistent with the solar value and all other metals are underabundant, compared to the solar values, which can be seen in Fig.8.40. Nitrogen and oxygen are clearly more abundant than other metals. When not scaled to solar, the nitrogen abundance is lower than the abundance of oxygen, therefore, no signatures of CNO-burning are observed in among the A-BHB-stars (see Fig. 8.39). The α-elements Mg and Si are less abundant than N and O, but enhanced compared to heavier elements and they show similar total abundances. Some heavier elements show wide spreads such as Ca or Ni. Compared to solar heavier elements exhibit similar abundances, however, the total abundance shows a clear peak towards iron.

When abundances are considered as ratios to iron, a similar overall pattern as the

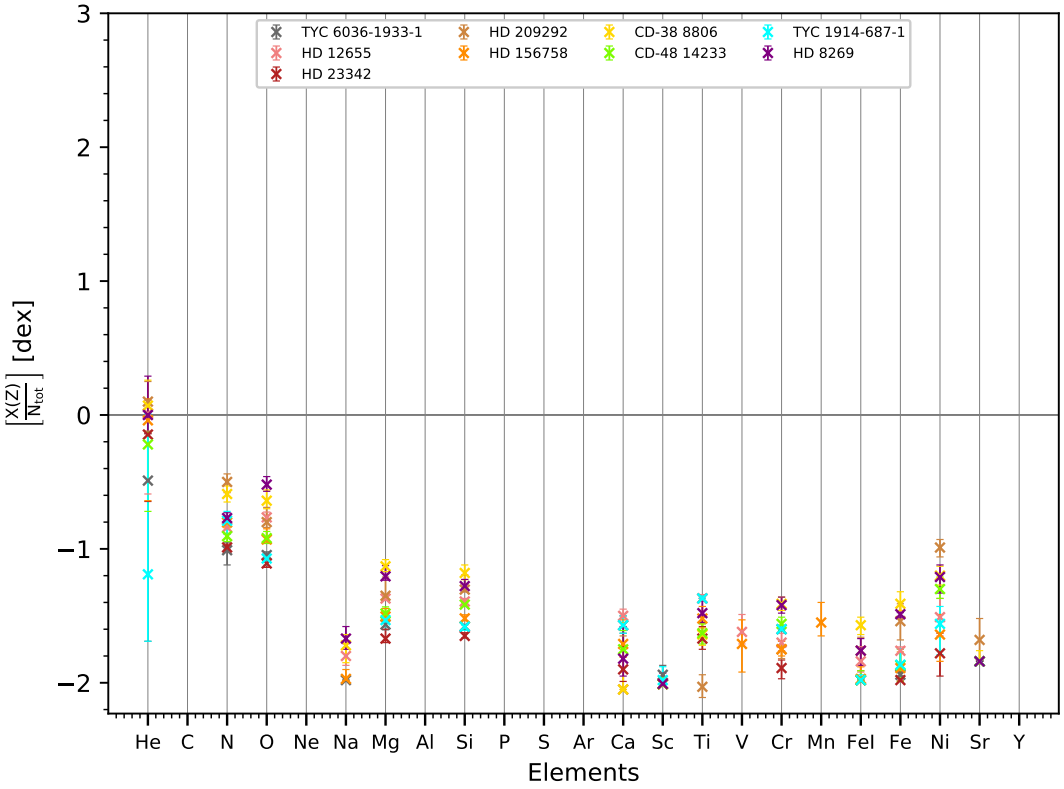

Figure 8.40: Derived abundances for A-BHB-stars relative to solar

one shown in Fig. 8.39 is observed, which means that the abundances of the different elements scale with the iron abundance. Compared to the solar element-iron ratios, N and O show overabundances of about 1 dex, and Mg and Si show the expected 0.3 dex enhancement for α-elements. Abundances of the heavier elements scatter around the solar value, with Ca, Ti, Cr and Ni being, on average, more abundant than the other elements. The deviation from the solar ratio, however, does not correlate with the star, which also means that the abundances of the different elements do not actually scale

or correlate with the solar abundance pattern. In order to show this effect, the dots in Fig. 8.41, have been connected. Clearly the lines cross each other all the time, especially beyond Si. Based on these findings it can be concluded that in A-BHB-stars the iron abundance is a good proxy for overall metallicity, as the other elements scale with iron. Additionally the scatter effect indicated that compared to the solar ratios the elemental composition behaves differently in these stars. Therefore, the potential A-type BHB-stars show an own abundance pattern different from that observed in the sun.

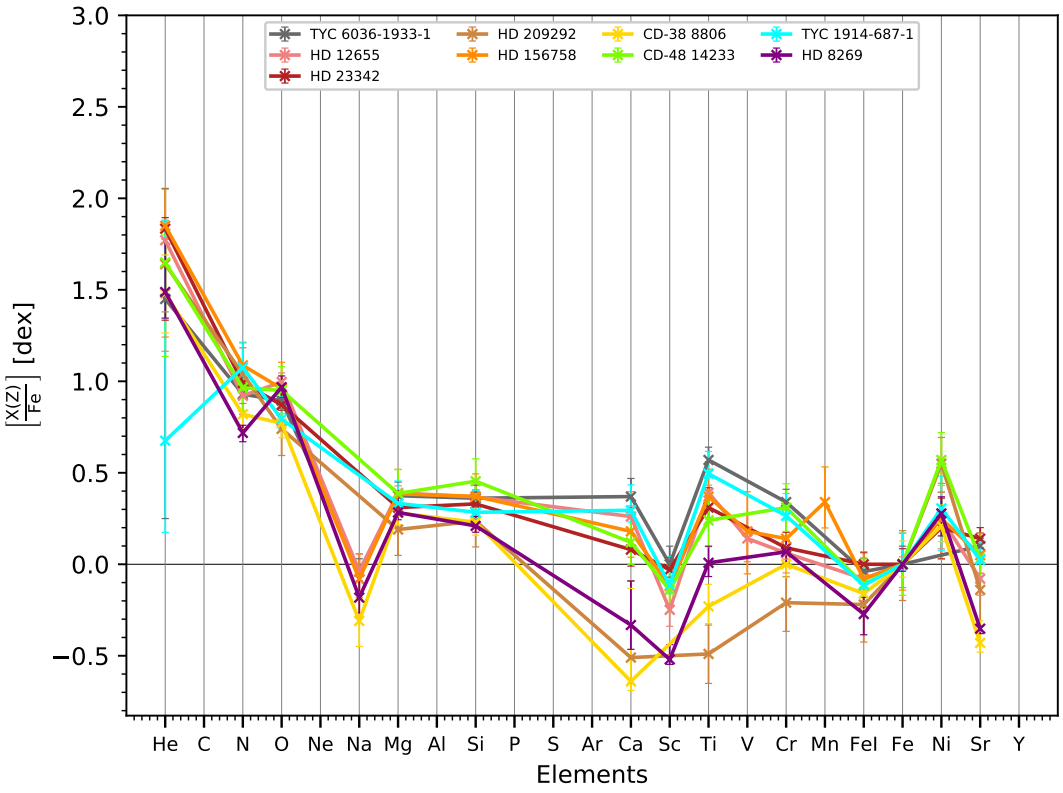

Figure 8.41: Derived abundances relative to iron for A-BHB-stars relative to solar

8.3.7 Abundances of B-BHBs

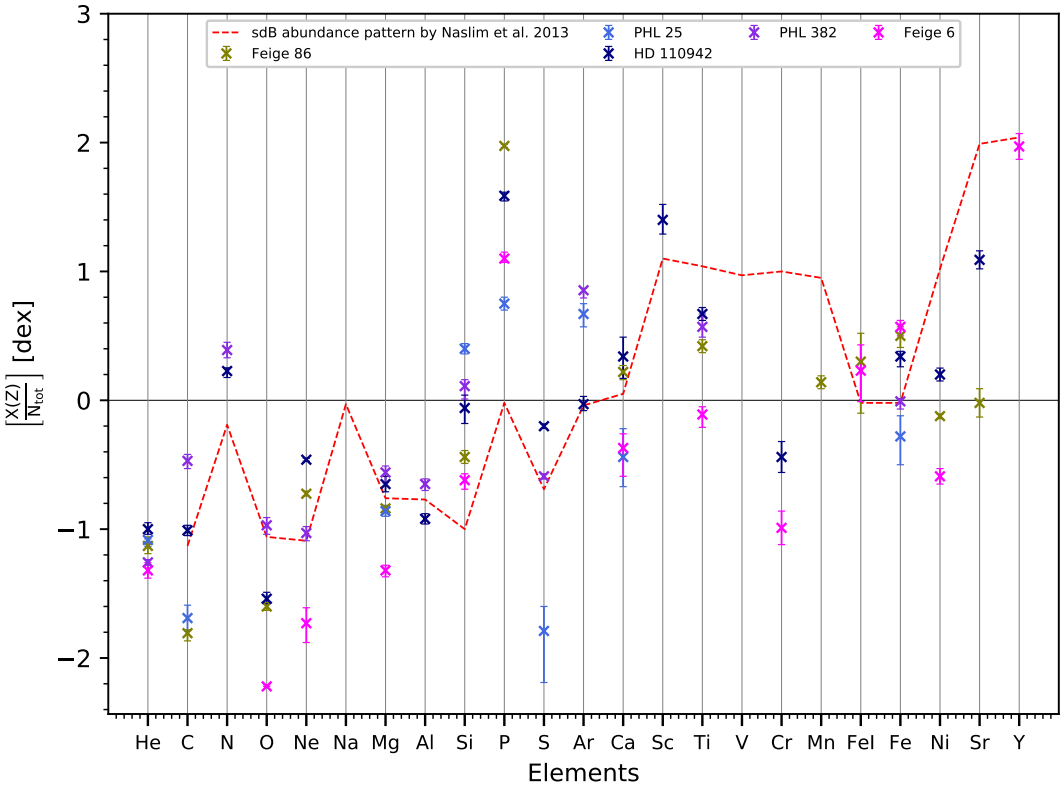

Figure 8.42: Derived abundances for B-BHB-stars relative to solar

The abundances in B-BHB-stars are expected to be subject to diffusion, causing underabundances in helium, isotopic anomalies and overabundances for heavier elements. This general behavior is in fact observed in the hot stars of the sample. Isotopic shifts for helium are observed in the B-type stars and the overall helium abundance is below solar. Also overabundances for heavier elements are observed, with the general trend that abundances increase with atomic number. Figure 8.42 shows the derived abundances scaled to solar. Additionally, the mean sdB abundance pattern (Naslim et al. 2013) is shown. The general trend in sdBs agrees quite well with the B-BHB-abundances. When scaled to iron the pattern seems to shift towards lower abundances, but the overall shape seems to follow the sdBs, which can be seen in Fig. 8.43.
Although the B-BHB stars seem to be general quite similar to the sdBs, differences are observed. The most striking feature is a strong enhancement in phosphorus, which is not observed in sdBs. Also a slight enhancement in Si could be present. Overall sdBs and B-BHB-stars seem to have similar abundance-patterns, therefore, indicating that diffusion, if present in both, is similar on both sides of the NG2. Since the NG2 separates the sdBs and BHBs from each other and manifests itself as a gap in the HB-sequence

there must be a physical explanation for the occurrence of the gap. Hence, the similarities in terms of abundances patterns found among both groups, indicate that the NG2 is not caused by diffusion processes or a detectable change in those.

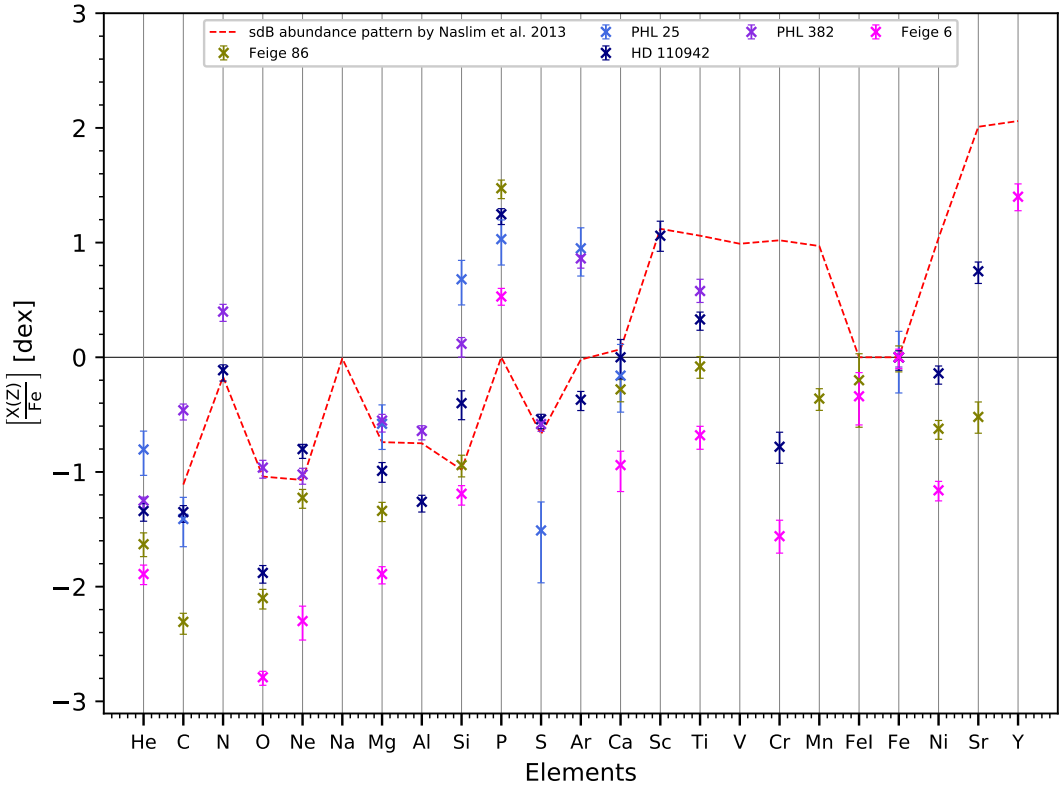

Figure 8.43: Derived abundances for B-BHB-stars scaled to iron relative to solar

8.3.8 Abundance-trends

Combing both sub-samples allows for the investigation of trends of abundances with other parameters, such as atmospheric parameters and other abundances, on both sides of the NG1. Generally the abundances of metals are expected to increase with temperature, due to diffusion setting in around the NG1. Overall the abundances of many elements increase with temperature, a few examples for elements found in a significant number of stars are shown in Fig. 8.44. Beyond NG1 the abundances increase significantly, among A-type stars the abundance seems to increase slightly for some elements while others seem to scatter or decrease, hence showing no clear trend. As mentioned previously, diffusion is expected to be dominant in stable atmospheric configurations and higher stellar rotations are thought to, therefore, suppress diffusion. In the sample, a trend with projected rotational velocity can be observed with stars having lower rotations exhibiting

higher abundances, hence, indicating the atmospheric stability giving rise to diffusion.

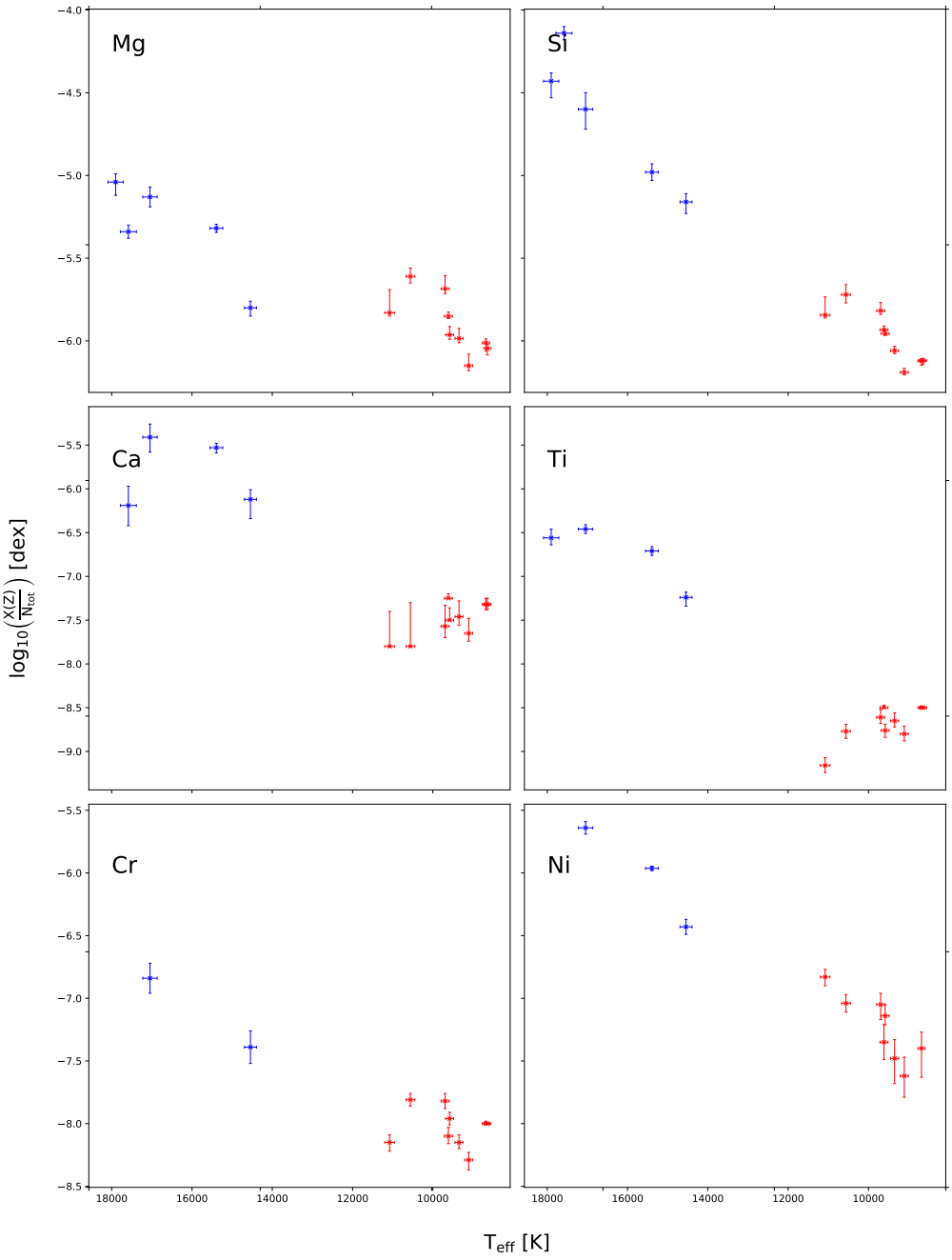

Figure 8.44: Abundances selected elements vs. effective temperature, A-BHBs in red and B-BHBs in blue

Also correlations between abundances of different chemical elements could be present in the sample. Figure shows the correlation of the selected elements as in Fig. 8.45 and the iron abundance. As already indicated by the presented abundance-patterns the abundances in A-BHBs scale with iron, confirming that iron is a proxy for overall metallicity in these stars. In B-BHB-stars it seems that a few elements (e.g. Mg and Si) peak at some point in total iron abundance and drop again towards higher iron abundances.

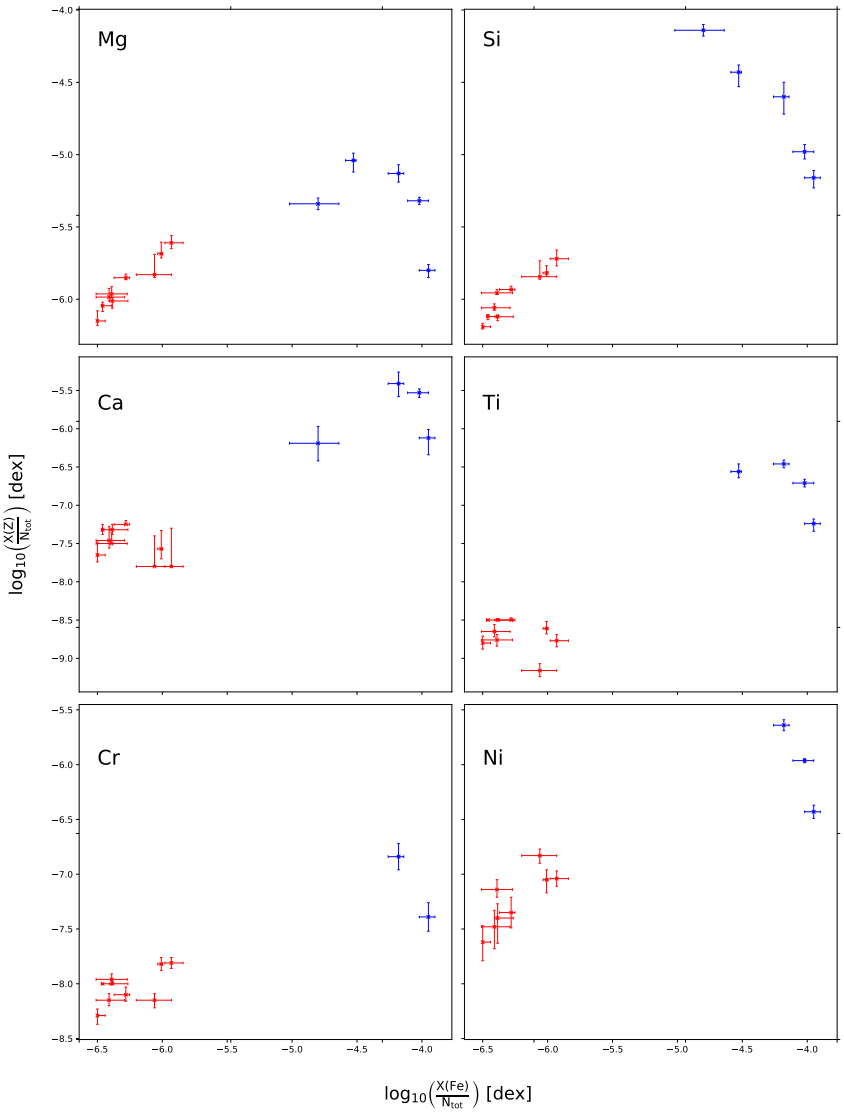

Figure 8.45: Abundances of selected elements vs. iron abundance, A-BHBs in red and B-BHBs in blue

8.3.9 Photometric results

The photometric analyses have two different aims. On the one hand it allows for a consistency check, by determining the atmospheric parameters from the spectral energy distribution. On the other hand, the stellar angular diameter Θ and interstellar reddening $E(B-V)$ can be determined.

8.3.9.1 Consistency check

The analyses based purely on photometry merely services as a consistency check, especially for the spectroscopically derived effective temperatures. Photometric temperatures are constrained well enough to compare them to the spectroscopic results. The surface gravities are not constrained very well, as indicated by the fact that the uncertainties are quite large, covering significant ranges of the grid. Also the other free parameters are not suitable and far better constrainable by spectroscopic means. However, the photometric and spectroscopic results are consistent with each other. Fig. 8.46 shows that the derived effective temperatures agree well with each other. The uncertainties are higher for the photometric approach, especially when comparing them to the spectroscopic results. Nevertheless, the photometric results back up the spectroscopic ones, indicating that the determined atmospheric parameters are robust.

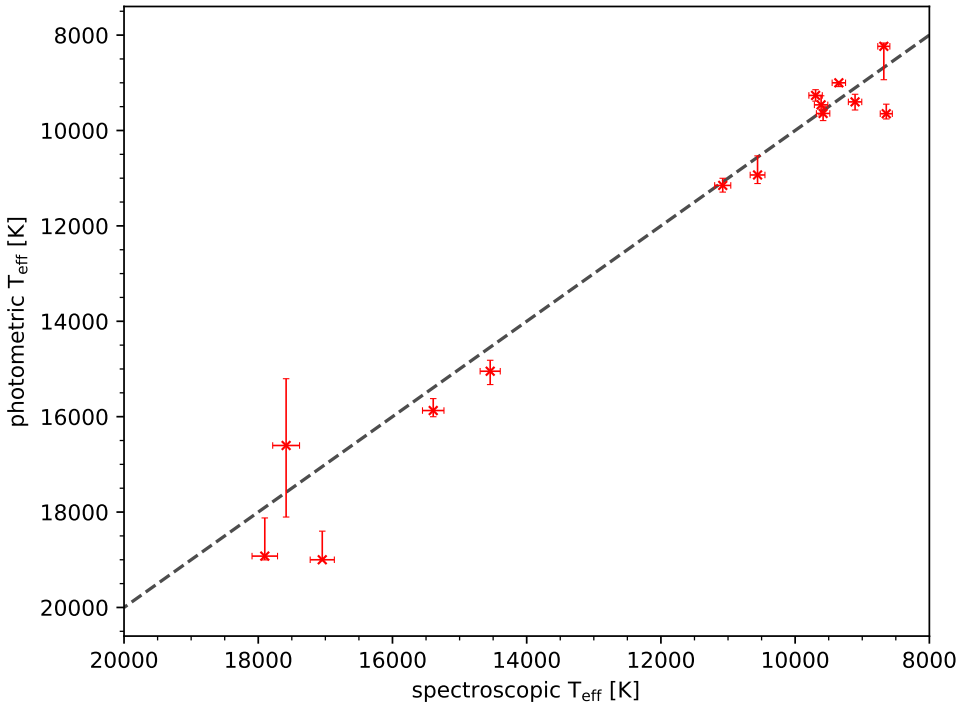

Figure 8.46: Spectroscopically vs. photometrically derived effective temperature

8.3.9.2 Stellar angular diameters and interstellar reddening

The atmospheric parameters derived from spectroscopy are plugged into the photometric analyses as well, this will yield the interstellar reddening and the angular diameter of each star. Since the atmospheric parameters are well constrained also these parameters are now more accurate and better constrained than when ignoring the spectroscopic result as an input. The results are listed in Tab. 8.2. Generally, the interstellar reddening is small. The angular diameter of B-type stars is lower than for the A-stars. The angular diameter can now be used to derive the stellar parameters.

Table 8.2: results of photometry based on spectroscopicly derived atmospheric parameters

	$E(B-V)$	Θ
star	[mag]	[rad]
TYC 6036-1933-1	0.058 ± 0.004	$(1.457 \pm 0.008) \times 10^{-10}$
HD 12655	0.030 ± 0.004	$(2.678 \pm 0.013) \times 10^{-10}$
HD 23342	$0.0004^{+0.0040}_{-0.0005}$	$\left(1.631^{+0.008}_{-0.005}\right) \times 10^{-10}$
HD 209292	0.019 ± 0.004	$(9.57 \pm 0.05) \times 10^{-11}$
HD 156758	0.179 ± 0.005	$(1.844 \pm 0.011) \times 10^{-10}$
CD-38 8806	0.020 ± 0.004	$\left(1.139^{+0.006}_{-0.005}\right) \times 10^{-10}$
Feige 86	0.016 ± 0.004	$(9.89 \pm 0.05) \times 10^{-11}$
CD-48 14233	0.004 ± 0.004	$\left(1.040^{+0.005}_{-0.006}\right) \times 10^{-10}$
TYC 1914-687-1	0.040 ± 0.005	$(1.425 \pm 0.008) \times 10^{-10}$
PHL 25	$0.026^{+0.004}_{-0.003}$	$\left(3.537^{+0.015}_{-0.014}\right) \times 10^{-11}$
HD 110942	0.044 ± 0.004	$(7.77 \pm 0.04) \times 10^{-11}$
PHL 382	0.020 ± 0.004	$\left(5.029^{+0.028}_{-0.027}\right) \times 10^{-11}$
HD 8269	0.032 ± 0.004	$(1.409 \pm 0.007) \times 10^{-10}$
Feige 6	0.044 ± 0.006	$(1.781 \pm 0.013) \times 10^{-11}$

8.3.10 Stellar parameters

The stellar parameters of a star give valuable insight into the evolutionary status and the nature of a star. For example, as seen in Fig. 8.34, the MS and the HB cross each other. Stars in these loci will show the same atmospheric parameters, hence, based on these alone it can not be distinguished whether a star in the crossing region is on the MS or the HB. This is not the only region along the horizontal branch occupied by different groups of stars. The stellar parameters, however, will be tale telling to unravel the nature of a star and its evolutionary status. The stellar parameters are calculated for all stars based on the atmospheric parameters and the angular diameter, and the Gaia parallaxes. The parallax-uncertainties and the RUWE of all stars indicate that the parallax can be used for this part of the analyses. Derived stellar parameters are listed in Tab. 8.3.
Figure 8.47 shows the three fundamental stellar parameters as a function of effective temperature. Additionally, the values for ZAHBs and TAHBs are shown for solar and sub-solar metallicity. The radii exhibit a steep decrease. From the cooler to the hotter end of the A-BHB-stars the radius decreases quite steadily by almost a factor of two. Once the NG1 is crossed a further decrease in radius is expected, for the majority of B-BHBs this behavior is indeed observed. However, objects are found to have radii not matching the theoretical expectations. Some A-BHBs have radii smaller than expected based on the models with an appropriate metallicity which is also observed in the Kiel diagram. Amongst the B-BHB-stars the coolest and hottest stars have higher radii. Feige 6 has a radius slightly above a solar radius, however, radii should drop quite significantly once the temperature is higher than the NG1. The observed radius would put Feige 6 close to the TAHB. PHL 382 is found to have a radius over a solar radius as well, which is too high for this temperature regime, as indicated by its position relative to the TAHBs. Masses among the HB are expected to be around half a solar mass, with a slight decrease among the HB due to decreasing envelope mass. The middle panel of Fig. 8.47 shows the mass along different Dorman ZAHBs. Most of the derived masses are consistent with the theoretical predictions. The metal-poor model yields a better agreement for the masses of A-BHBs than the solar one. Nevertheless, again three objects seem to have peculiar masses. TYC 1914-687-1 in fact also has the highest mass of any sample star at around a solar mass. The uncertainties for Feige 6 are quite large, and within the errors, consistent with the HB, but also with one solar mass. The mass of PHL 25 is significantly below the HB and is the lowest mass in the sample.
Also the luminosity, just like the radius, is expected to drop with increasing effective temperature. This again is observed in the sample, therefore, the observations agree with the model calculations. The luminosities of stars exhibiting increased radii are the highest ones in the sample. The luminosity of TYC 1914-687-1 is higher than those of the other A-stars, but within the errors quite similar. Feige 6 clearly shows an increased luminosity compared to the B-type objects in the sample, although also in this case the uncertainties are quite high and consistent with the models for solar and sub-solar metallicity. PHL 382 has a very high luminosity at about 100 solar luminosities. Generally, the fundamental parameters show the expected trends with temperature.

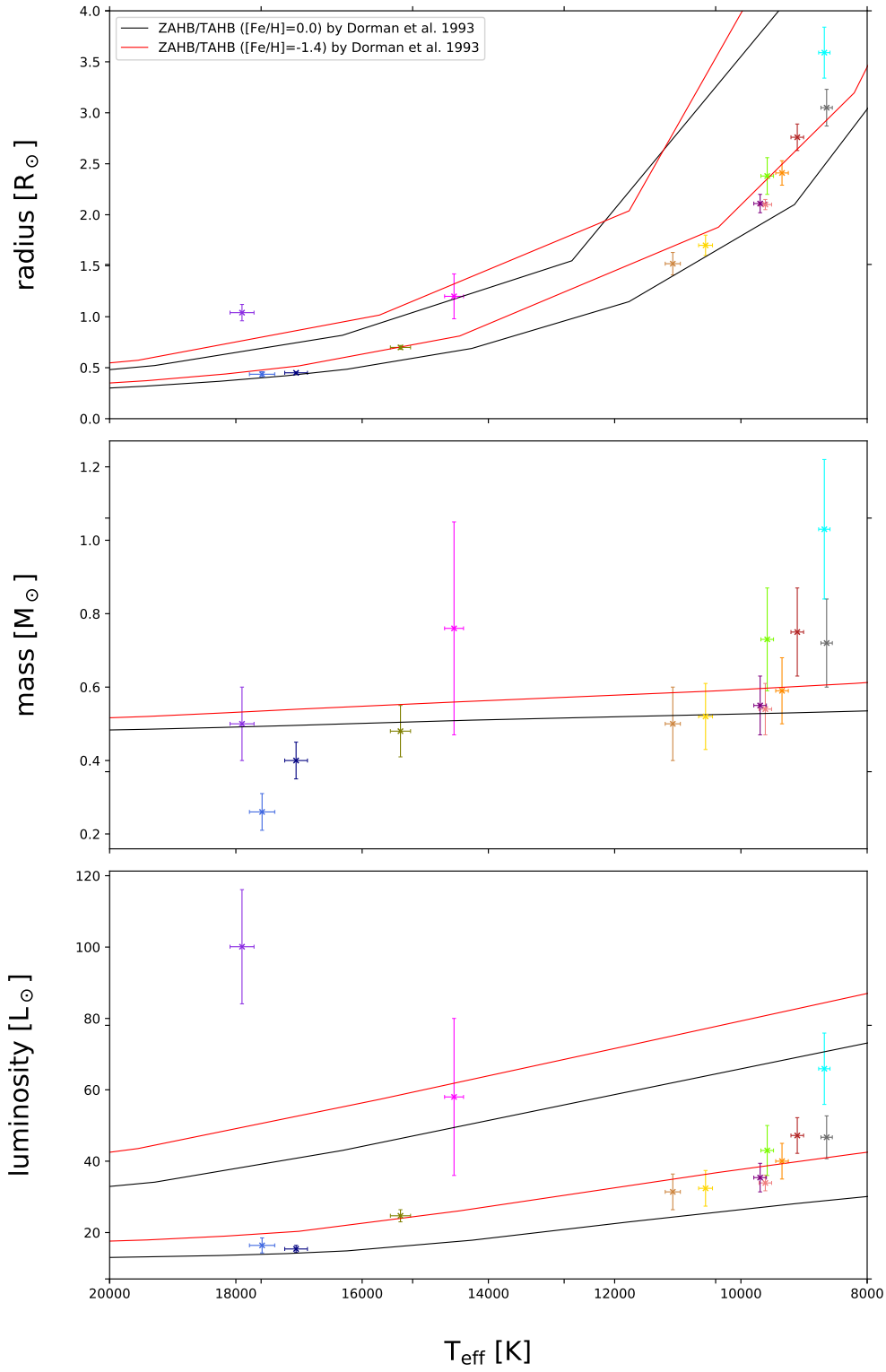

Figure 8.47: The fundamental stellar parameters as a function of effective temperature

Table 8.3: Derived stellar parameters

	R_*	M_*	L_*
star	$[R_\odot]$	$[M_\odot]$	$[L_\odot]$
TYC 6036-1933-1	3.05 ± 0.18	0.72 ± 0.12	46.7 ± 6.0
HD 12655	2.10 ± 0.05	0.54 ± 0.07	33.9 ± 2.2
HD 23342	2.76 ± 0.13	0.75 ± 0.12	47.2 ± 5.0
HD 209292	1.52 ± 0.11	0.5 ± 0.1	31.4 ± 5.0
HD 156758	2.41 ± 0.12	0.59 ± 0.09	40.0 ± 5.0
CD-38 8806	1.7 ± 0.1	0.52 ± 0.09	32.4 ± 5.0
Feige 86	0.699 ± 0.019	0.48 ± 0.07	24.7 ± 1.7
CD-48 14233	2.38 ± 0.18	0.73 ± 0.14	43.0 ± 7.0
TYC 1914-687-1	3.59 ± 0.25	1.03 ± 0.19	65.9 ± 10.0
PHL 25	0.436 ± 0.025	0.26 ± 0.05	16.4 ± 2.1
HD 110942	0.45 ± 0.01	0.40 ± 0.05	15.4 ± 1.0
PHL 382	1.04 ± 0.08	0.5 ± 0.1	100.1 ± 16.0
HD 8269	2.11 ± 0.09	0.55 ± 0.08	35.4 ± 4.0
Feige 6	1.20 ± 0.22	0.76 ± 0.29	58.0 ± 22.0

8.3.11 Population membership

Three indicators were used to determine population membership: the U-V, the $L_z - e$ diagram, and the morphology of the Galactic orbit.
Because of the selection criteria applied by Altmann and Catelan, the A-BHBs are expected to belong to the halo. This, indeed is the case. The B-BHB stars are expected to have disk characteristics. The majority of the hot sub-sample is found to belong to the disk, which can clearly be seen in Figs. 8.48 and 8.49. However, the B-star Feige 6, the most distant object studied, clearly exhibits halo kinematics contrary to theoretical expectations.
The results for the different Milky Way potentials are very similar and the values derived for U, V, e and L_z agree quite well with each other within the uncertainties. Also the orbits look very similar. This shows that, at least for the stars studied, the Milky Way mass models, yield similar results and can all be used for the calculation of the orbits.

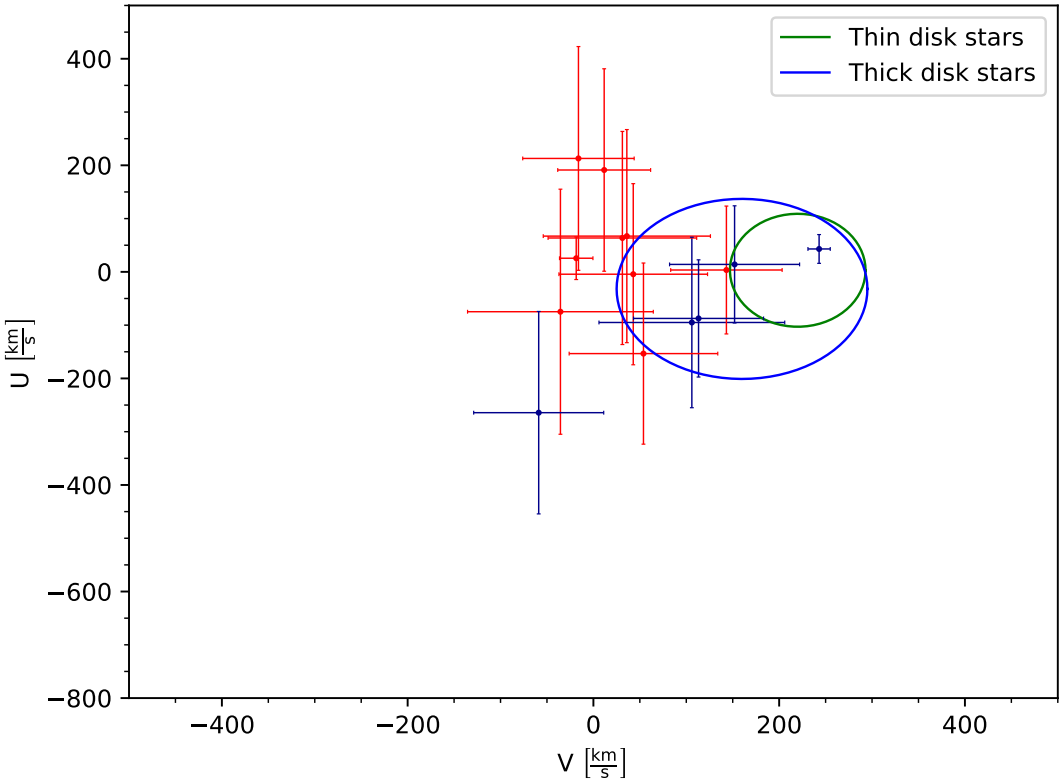

Figure 8.48: The $U - V$ diagram with the Pauli-ellipses and the results of the sample stars using the AS-potential. A-BHBs are shown in red and B-BHBs in blue.

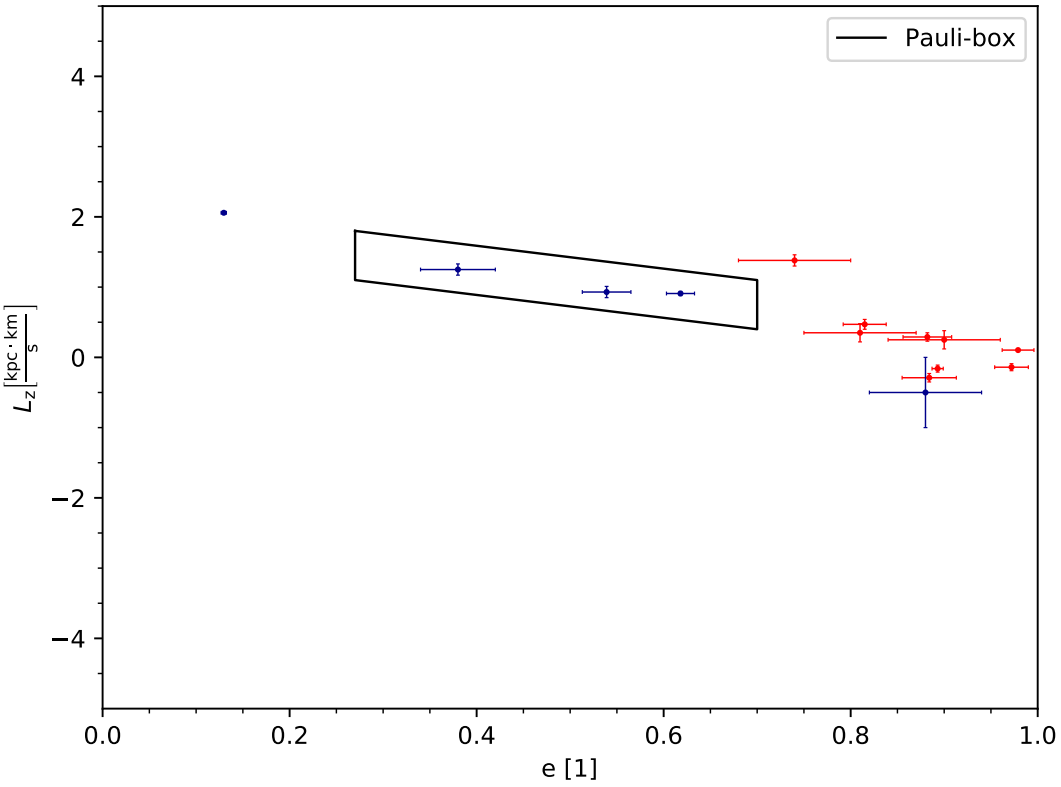

Figure 8.49: The L_z-e diagram with the Pauli-box and the results of the sample stars using the AS potential, colorcoding as in Fig. 8.48

9

Evolutionary status

The target selection by Altmann and Catelan anticipated that all stars in their sample are BHB-stars of the Galactic halo, and based on the analyses this is indeed the case for all A-BHBs selected from this sample. HD 110942 is the only star from this sample that has disk kinematics. Based on the atmospheric and stellar parameters, the abundances and the kinematics, most stars can be unambiguously classified as either A-BHBs or B-BHBs. Still, a few stars, TYC 1914-687-1, PHL 25, PHL 382, and Feige 6, are not straightforward to classify. Possible, evolutionary scenarios will be presented in sections 9.3 throughout 9.6 separately for every remaining unclassified star. In the Kiel diagrams used to discus some of these peculiar objects the position of the star is marked with a circle.

9.1 A-BHB-stars

TYC 6036-1933-1: This star's mass is higher than found for the other A-stars, however, still consistent with the others. The same applies for the other stellar parameters. The atmospheric parameters, put it on the HB and the abundances are similar to the other potential A-BHB-stars. As TYC 6036-1933-1 also shows halo kinematics, it can be classified as A-BHB-star.
HD 23342: is quite similar to TYC 6036-1933-1 in terms of stellar parameters. The atmospheric parameters, abundances, and the kinematics agree with HD 23342 being a A-BHB-star.
HD 156758: The atmospheric and stellar parameters, in combination with the kinematic results and derived abundances make HD 156758 a A-BHB-star.
CD-48 14233: Based on all the performed analysis steps CD-48 14233 is a A-BHB-star.
HD 12655: Taking all aspects and parameters into account HD 12655 is a A-BHB-star.
HD 8269: As for the other previously decribed stars HD 8269 can straightforwardly be classified as one of the A-BHBs.
CD-38 8806: The atmospheric parameters could place this star either on the MS or on the HB. The mass, however, is too low for a MS-star, and since all other parameters agree with the other A-BHBs, this star is also a A-BHB-star.
HD 209292: Just like CD-38 8806, HD 209292 could also be on the MS according to the atmospheric parameters. However, all other parameters point towards this star being on the HB and being similar to the other A-stars. Therefore, this star is classified as a A-BHB-star.

9.2 B-BHB-stars

Feige 86: The results for Feige 86 are fully consistent with it being a B-BHB-star which has been found by other studies as well.
HD 110942: The properties of HD 110942 are remarkably similar to those of Feige 86. Again the different indicators, stellar and atmospheric parameters, the abundances and the kinematic properties, clearly show the B-BHB nature of HD 110942.

9.3 TYC 1914-687-1 - too massive?

The atmospheric parameters and the kinematic analysis would be consistent with TYC 1914-687-1 being an A-BHB-star. The observed abundances are not peculiar with respect to the other safely classified A-BHBs. However, this A-type star has a mass of (1.03 ± 0.19) $M_\odot$ considerably larger than the expected mass range on the A-BHBs with models predicting masses of up to 0.75 $M_\odot$ at most. The radius and the luminosity are also higher than expected, which could be explained by the star being subject to post-HB evolution which, however, does not explain the high mass. At first glance, a MS and BS nature of TYC 1914-687-1 can be excluded, since it is located above the MS in the Kiel diagram (see Fig. 8.34). Stars with such atmospheric parameters might be in the post-MS phase. But as can be seen in Fig. 9.1, in order to explain the atmospheric parameters by means of post-MS evolution the mass would have to exceed 2 $M_\odot$. The tracks shown in Fig. 9.1 were computed for low metallicity and increasing metallicity would just mean that higher masses would be needed to make TYC 1914-687-1 a post-MS star. Hence, also the post-MS scenario can be excluded.
The spectral fit is not peculiar in any way and the spectrum is fitted just as well as any other in the sample, same applies to the photometric fit. The fact that TYC 1914-687-1 is located within the region in which the Balmer-lines reach their maximum strength and a model with higher temperature could match the blue part just as well as the low temperature solution can not explain the peculiar mass. First of all the high temperature solution fails to match the Paschen-line. Hence, this solution is discarded, and secondly, adapting the high temperature solution would result in an even higher mass of (1.48 ± 0.27) $M_\odot$ which would be even harder to explain because the same line of argumentation applies in the high temperature case, therefore, excluding the MS, post-MS and BS-sequence as a possible explanation for this star. Since possible mistakes in most of the analysis-steps can be excluded the only possible explanation rooted in the analysis is that the Gaia parallax is wrong and does not represent the actual distance of this system. However, this is not indicated by the Gaia parameters as the uncertainty of the parallax is below 10 % and several quality flags, including the RUWE do not give rise to the suspicion that the Gaia data might be in error but the Gaia parallax is derived assuming the star to be single. In the spectrum contributions of a possible companion are not observed, same can be said about the photometric data. Therefore, if TYC 1914-687-1 were to be a binary system it would most likely be a SB1 system because the companion is not visible in the spectrum at least not kinematically in the form of being double lined. In the binary scenario, either the spectrum or the photometry give wrong results due to the double system nature. Alternatively, the companion could also not influence the spectrum and photometry but mess up the Gaia data. Further observations are needed to confirm or disprove TYC 1914-687-1 being a binary system, in particular, further spectroscopic observations are needed to search for radial velocity variations. Also, lightcurves might be helpful to clarify the nature of TYC 1914-687-1.
The final option considered to explain the observed parameters is that TYC 1914-687-1 is in fact a A-BHB-star with an anomalously high mass which currently is not considered in theory.

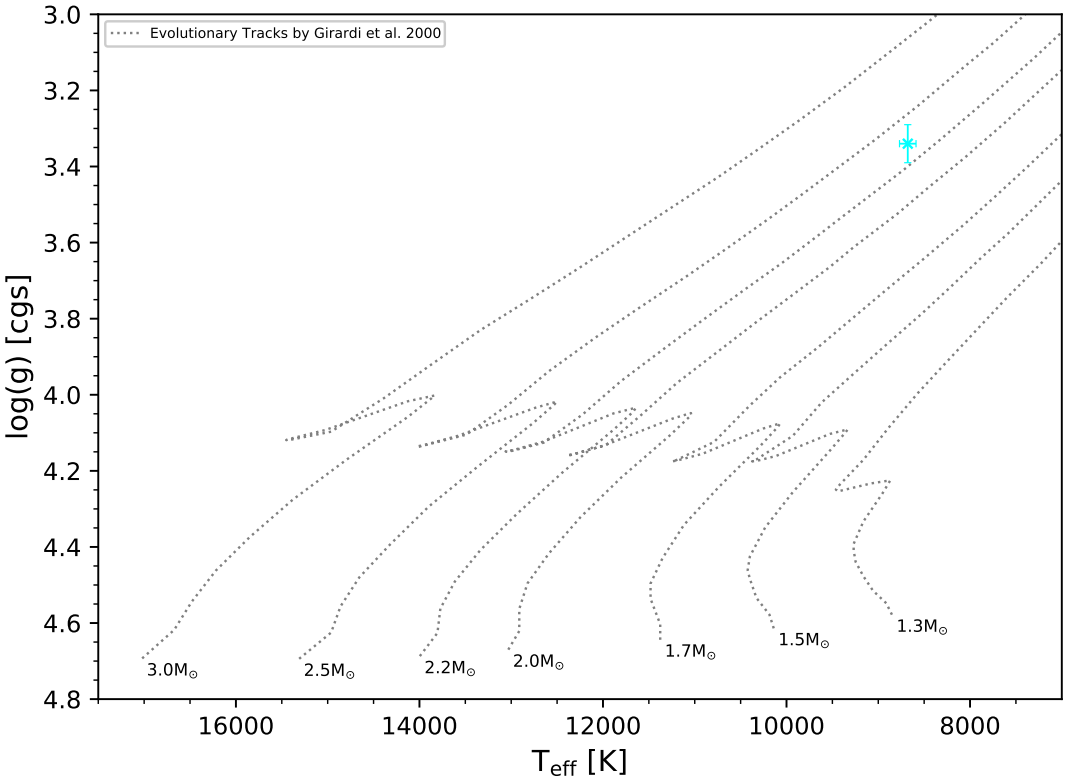

Figure 9.1: The atmospheric parameters of TYC 1914-687-1 and TYC 6036-1933-1 plotted with evolutionary MS-tracks for low metallicity (Girardi et al. 2000)

9.4 Feige 6 - a halo object

Feige 6 is peculiar in a few aspects. The atmospheric parameters are consistent with this star being on the HB. The abundance pattern is similar to the other B-BHBs in the sample, however, except for iron and yttrium where it shows the highest total abundances in the sample and phosphorus, all the other elements have the lowest abundances among the B-type stars. The mass is higher than expected but still consistent with Feige 6 being on the HB and too low to make it a MS-star or BS. The radius and the luminosity on the other hand, although also having high uncertainties, put Feige 6 close to the TAHB which is not the case in the Kiel diagram. The Gaia data should be reliable, as indicated by quality flags and the RUWE. As Feige 6 is the most distant star in the sample, the parallax also has the highest uncertainty, hence, making the stellar parameters more uncertain as well. However, since the uncertainty is below 20 %, the parallax should still be good enough to derive the distance. The spectral and photometric fits are unsuspicious,

as well. In contrast to all other B-type stars in the sample its kinematics shows halo characteristics.
The halo is generally thought to be metal poor. Using metal-poor HB-models would place Feige 6 towards the middle of the HB-band (see Fig. 9.2) in terms of atmospheric parameters. This would also be able to explain the higher radius and luminosity. Contradicting the assumption that Feige 6 belongs to a low metal population as indicated by the kinematics, if its membership in a metal-rich population (similar to the level of iron abundance in Feige 6 itself) is assumed, Feige 6 would be closer to the TAHB which could mean that it is currently or about to evolve off the HB which would be able to explain the high radius and luminosity as well. Using models close to the iron abundance found in Feige 6, however, does not seem appropriate because diffusion is active in stars beyond the NG1 and, hence, the iron abundance at the surface most likely would not represent the initial metallicity which is used as an input for the model calculations. Hence, using the same iron abundance as the one derived from the spectroscopic analysis might not be representative for the metallicity. Additionally, the kinematics seem to imply Feige 6 belonging to a metal-poor population. However, simply implying that the halo is metal-poor does not seem to always hold, as sub-populations are found in the halo, especially in GCs, which are not as metal-poor as the rest of the halo. Consequently, despite being a halo-star, Feige 6 could still originate from a metal rich sub-population, although unlikely given the fact that for the metal poor models a better match in atmospheric and stellar parameters is achieved. Alternatively, the Feige 6 could also have been born in a metal-rich environment not associated with the halo but could have become a member of it later on through dynamical interactions or other processes. In any case, Feige 6 is on the HB-band.
Nevertheless, Feige 6, whether it belongs to a metal-rich or poor population or is more evolved or not, is the only known halo B-BHB star. Further analysis, especially more advanced kinematic studies and more accurate astrometry, probably provided by Gaia DR3, will help to investigate the curious case of Feige 6 further. Additionally, other stars may be searched for in the future to find more halo B-BHBs.

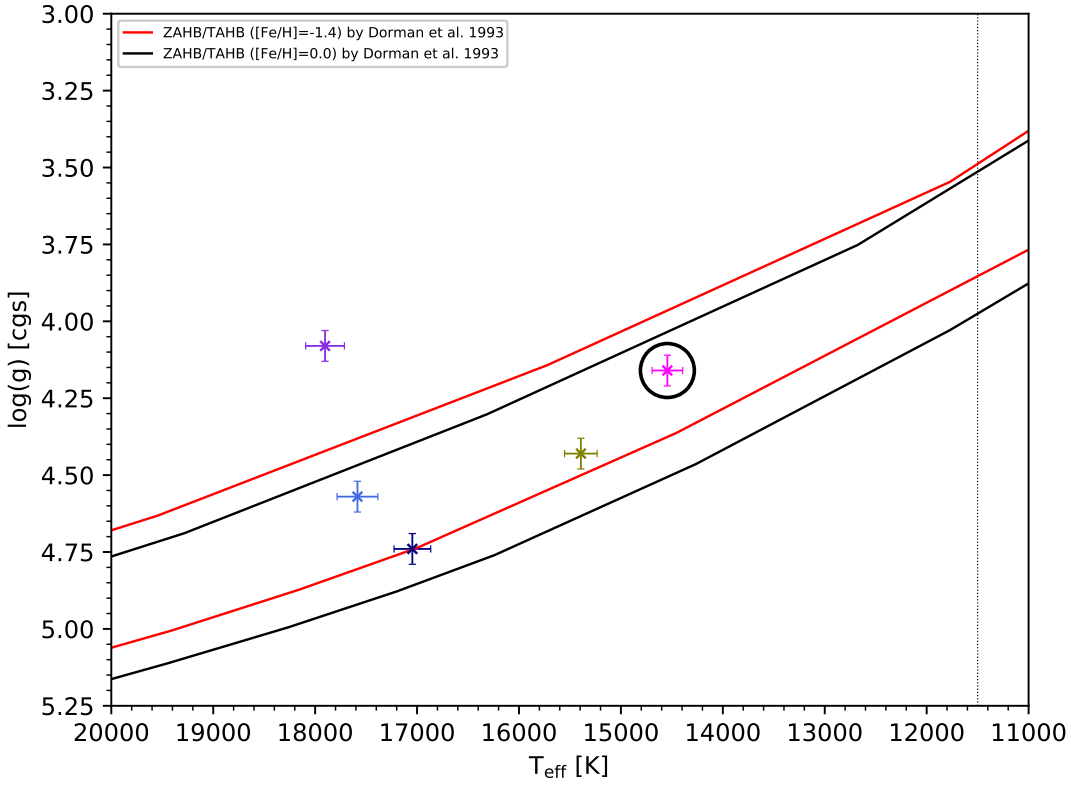

Figure 9.2: Kiel diagram showing the B-type stars and two sets of ZAHB and TAHBs

9.5 PHL 25 - a pre-ELM?

The kinematics, abundances, and also the atmospheric parameters derived for PHL 25 would be in agreement with this star being on the HB. Same can be said about radius and luminosity which are close to those found for HD 110942. However, this does not apply to the mass derived which is as low as (0.26 ± 0.05) $M_{\odot}$. Previously, this star has always been classified as a BHB-star. The derived mass seriously challenges this classification as the mass is significantly lower than expected if it were a HB-stars. The HB-sequence is defined by stars burning helium in their cores. In order to maintain the helium burning process stellar masses around the canonical sub-dwarf mass are needed. Under non-degenerate conditions RGB stars are able to ignite helium while having core masses as low as 0.33 $M_{\odot}$ (Heber 2016). Even within the uncertainties this mass is larger than the mass of PHL 25. Consequently, PHL 25 most likely is not burning helium and, hence, could be a helium core object. PHL 25 could therefore be an extremely low mass WD (ELM) or a pre-ELM, the possible remnant of a stripped red giant star. The Kiel diagram in Fig. 9.3 also shows the tracks of pre-ELMs computed for masses similar to the mass of PHL 25. The star is within the region of the Kiel diagram where pre-ELMs within a similar mass range are predicted to be located, solidifying the assumption that PHL 25 might be a pre-ELM. The abundance pattern derived for PHL 25 is similar to the other B-type stars. Comparing the abundances to those found in ELMs does not prove or disprove PHL 25 as a (pre-)ELM. In agreement with Latour et al. (2016) C, N, and O are found to be underabundant with respect to solar. For heavier elements the results are not conclusive, after all extensive abundance studies in ELMs are essentially limited to a handful of objects. ELMs with temperatures close to the temperature of PHL 25 have been studied as well. In agreement with the findings of Hermes et al. (2014) carbon is found to be underabundant, while N and O are barely detected. Underabundances for Mg, S and Fe are detected in PHL 25 as well. Just like in the analysis by Kaplan et al. (2013), Si is found to be enriched in PHL 25 and Ca lines are observed which is also the case in ELMs (Gianninas et al. 2014). One feature not observed in ELMs is the P overabundances. Due to the low sample, the abundances could be consistent with PHL 25 being an ELM or an HB-star as some studies find overabundances in some elements (Gianninas et al. 2014) while others find underabundances (Shimanskii 2002) (HZ22 as studied by Shimanskii (2002) is thought to be more massive than the other ELMs studied but very close to the ELM mass range). However, if PHL 25 is a pre-ELM or ELM and the abundance pattern still agrees with the one for B-BHB-stars, this could also mean that diffusion is similar in B-BHBs, sdBs and ELMs, therefore, indicating that diffusion effects depends predominantly on the atmospheric parameters and not on the actual type of the star. Due to the low number of ELMs as well as B-BHB-stars studied in detail, a sure conclusion can not be made at this point. One way to possibly confirm PHL 25 as a pre-ELM would be to search for pulsations via analyzing the lightcurve as some ELMs pulsate (Hermes et al. 2012), whereas this is not expected from other star types occupying similar regions in the Kiel diagram.
Based on the results, PHL 25 is most likely not a B-BHB-star but a pre-ELM.

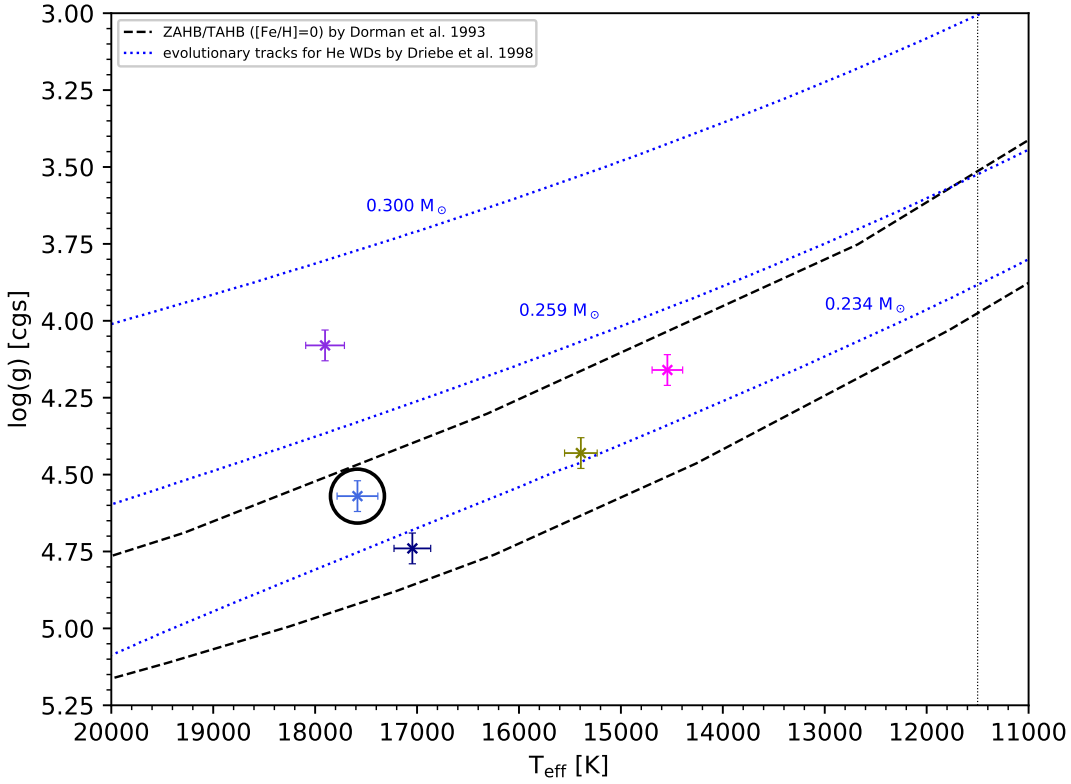

Figure 9.3: Kiel diagram showing the B-type stars and pre-ELM tracks (Driebe et al. 1998)

9.6 PHL 382 - post-HB vs. enhanced helium scenario

The abundances and kinematics of PHL 382 are those expected from B-BHB-stars. The atmospheric and stellar parameters on the other hand are peculiar. The low log(g) determined for PHL 382 puts it over the HB-band (when considering solar metallicity). In combination with the enhanced luminosity and radius, this could mean that PHL 382 is a post-BHB star currently evolving away from the HB. A possible MS and BS origin can be excluded since the mass is consistent with the HB and therefore, too low for these possibilities to be true. As can be seen in Fig. 8.34, PHL 382 is quite close to the parameter combinations expected for evolved HB-objects within a similar mass range. PHL 382 has been classified as a post-BHB before (Schneider et al. 2018). A post-HB nature is, however, not the only possible explanation for the observed parameters. This star could still be a helium burning HB star and therefore a B-BHB-star which can be seen in Fig. 9.4. The position in the Kiel diagram is consistent with PHL 382 belonging to a helium enriched population. The same applies for the mass because its in the appropriate range. Scenarios like this are also used to explain the parameters found in

GCs. Multiple and possibly helium enhanced populations are found in GCs, although it is not completely clear how these populations formed (compare with section 1.1.4.1). It is possible that helium enhanced populations might also be present in the disk, to which PHL 382 belongs. The helium enhanced population-membership could also explain the stellar parameters, as stars formed with higher helium content are expected to be more luminous and have larger radii. Unfortunately, spectroscopy can not be used to test this hypothesis because due to diffusion the abundances do not represent the initial ones. Helium is especially depleted in the atmospheres of B-BHBs and hence the measured helium abundance can not be used to confirm if PHL 382 in fact belongs to a helium enhanced population.
If diffusion depends mainly on the atmospheric configuration, abundances can not be used at all to distinguish the nature of a star and consequently stars belonging to the respective populations would still show similar abundances. The abundances in post-HB-stars are not expected to be different from those observed on the HB.
Based on the findings PHL 382 could be a post-BHB-star or a B-BHB-star if belonging to a helium enhanced population.

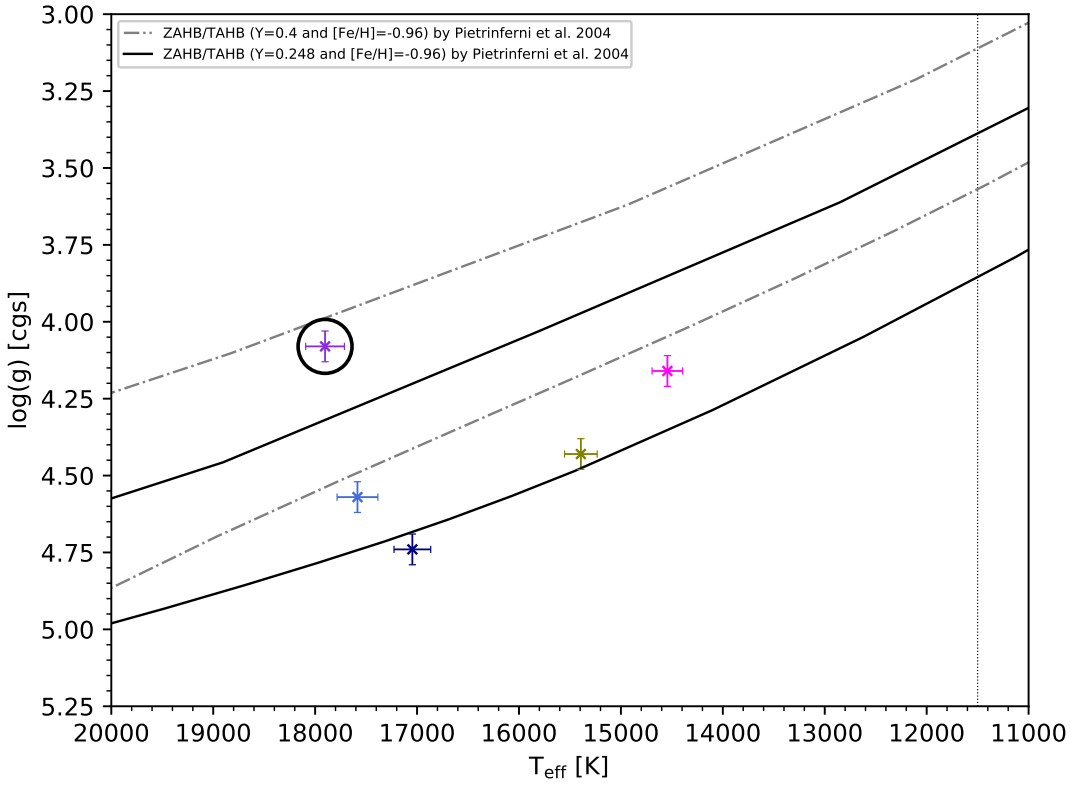

Figure 9.4: Kiel diagram showing the B-type stars and HB-sets for normal and enhanced helium (Pietrinferni et al. 2004)

Another aspect making PHL 382 very interesting is the possible detection of a supposed Si-emission line, as can be seen in Fig.9.5. The model predicts an absorption line at the position which is not observed in the data. The overall reliable Si-abundance is quite high compared to other B-type stars in the sample. Si-emission lines have been recently reported in B-type MS-stars (Sadakane and Nishimura 2017, 2019). It is speculated that the emission arises from outermost layer of the stellar atmosphere (Sadakane and Nishimura 2017). However, it is also possible that the emission is caused by NLTE-effects. Since similar findings have not yet been reported in HB-stars PHL 382 is an interesting target for further observations in from spectroscopy as spectra with higher quality and better spectral coverage would be needed in order to decide if the supposed emission line is real or not.

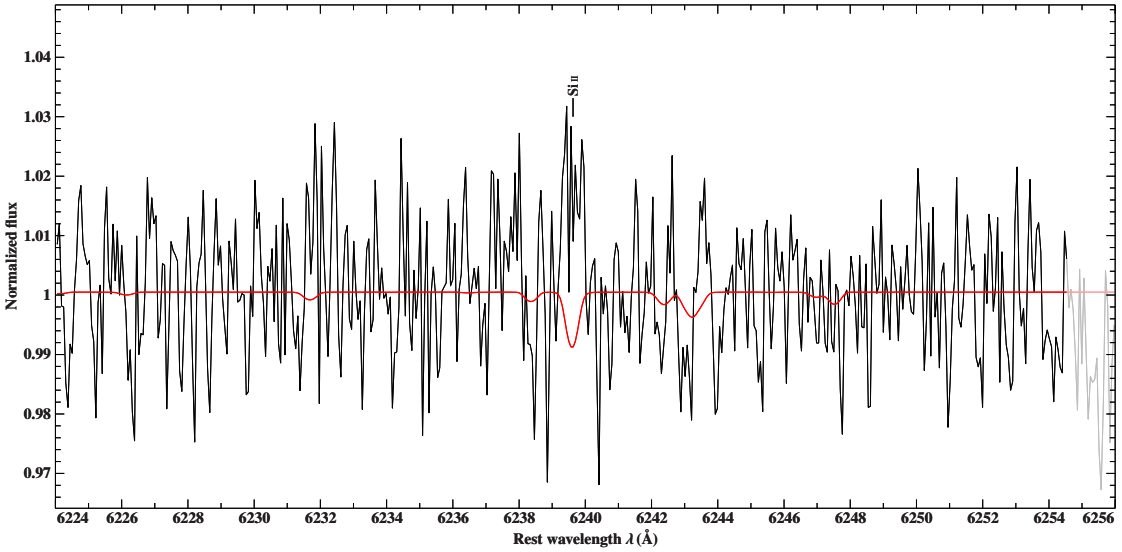

Figure 9.5: Possible Si-emission line in PHL 382

10

Discussion

The results presented in the previous chapters revealed some very interesting findings, also the results should be trustworthy considering single stars in common with previous studies. The results for the field stars studied can be compared to the literature values for other field stars which is done in the first section.
Most studies conducted studied BHBs in GCs. Although, due to the low number of stars studied, a detailed comparison between the field and GC population is still not possible in full detail but one can check for general trends and search for systematic differences. Hence, the results will be compared to those of a few GCs.

10.1 Comparison with field stars from the literature

Previous studies analyzed other possible field BHB-stars which are not part of the sample. In order to see if the results agree with other previous studies focused on the field, the atmospheric parameters and available abundances will be compared to literature values. This also allows to check for systematic differences among the different approaches. However, the literature on field A-BHB and B-BHB stars is not very extensive in contrast to other stars on the HB.

10.1.1 Atmospheric parameters

Comparing the effective temperatures and surface gravities found in the literature and the results it can be concluded that they agree with each other. In the Kiel diagram, which is shown in Fig. 10.1, the atmospheric parameters of a few studies are shown in addition to the program stars. Generally, the stars occupy the same loci in the diagram along the HB-band. The stars studied by Kinman et al. (2000) are restricted to the A-BHB and are found at similar parameter combinations. The values derived by Behr (2003b) exhibit a wider spread than the other studies, also the uncertainties are significantly larger which again stresses the higher data-quality in comparison with previous studies used here again indicating the validity of the analysis approach. Whereas most stars studied in other programs are consistent with being on the HB, the stars in the Behr-sample scatter more and are probably not all HB-stars. The stars located above the HB-band in Fig. 10.1 are either within the high uncertainties HB-stars, MS, BS, or post-HB stars. There also is a quite obvious group of stars below the HB-band which could also contain MS-stars and BS. The atmospheric parameters by Kafando et al. (2016) have higher uncertainties as they have all been adapted from the literature, still they agree with the stars being on the HB. As expected, the program stars agree with literature results in terms of effective temperatures and surface gravities.
Since Behr (2003b) and Kafando et al. (2016) also derived projected rotational velocities these can be compared as well. For the A-BHB stars the results agree well with the literature because they show the typically expected spread. A good agreement could also be present at temperatures above the NG1, however the number of stars studied is small and especially Behr (2003b) found quite a few stars in this temperature range with higher rotations. This could be due to possible contamination of his sample by other star-types, but generally no deviations compared to the literature are found for the stellar rotation, indicating a reasonably well agreement.

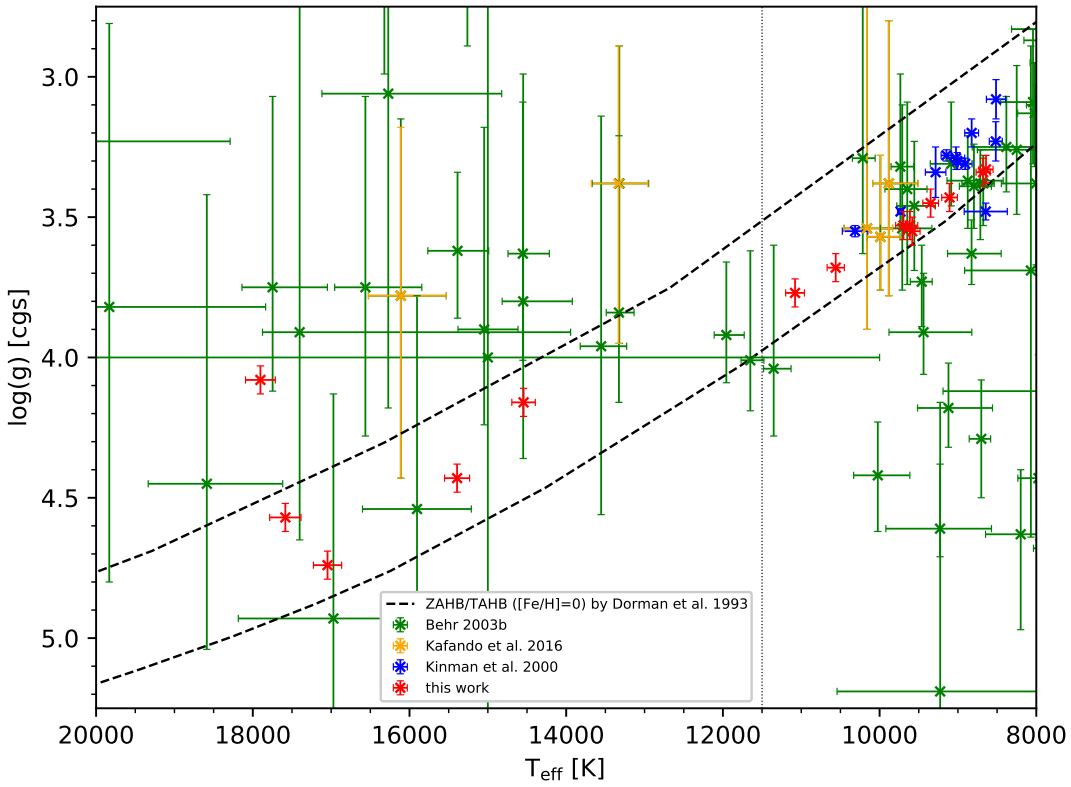

Figure 10.1: Kiel diagram showing the stars studied plus the stars from Kinman et al. (2000); Behr (2003b); Kafando et al. (2016)

10.1.2 Abundances

Until now not a lot of information on abundances in field BHB-stars has been available. The derived abundances are limited to very few elements only. Abundances of Mg and Ti have been studied for larger samples than the abundances of other elements. Kinman et al. (2000) derived abundances for Ti in A-BHBs, whereas Ti-abundances for B-BHB-stars are available for single stars only. The abundances of Mg were all derived by Behr (2003b) and span the entire temperature range. For other elements abundances are only found for very few stars in the literature. Therefore, the derived abundances are compared to the small sample studied by Kafando et al. (2016). Fig. 10.2 shows the element-to-iron ratios of O, Mg, Si, P, Ca and Ti. Again the results are in agreement with the abundances from the literature, as indicated by the same positions in the diagram and by the same general trends being observed for the different elements, e.g. the decrease of Ca abundance with temperature towards the NG1. When available, the mean abundances of slightly cooler field A-BHB-stars and halo-RGBs are shown as well. As expected these two groups should have similar abundances. For the A-BHB program stars and those from the literature, abundances are found to be very close to these mean abundances which is predicted

by theory. The high abundances of P found among most of potential B-BHB-stars are also observed by Kafando et al. (2016) in other field stars. This indicates that the overabundances of P are a real effect, unique to these stars because similar abundances are not observed in sdBs, possibly linked to diffusion. Diffusion, although similar in sdBs as hinted at by the observed abundance patterns, seems to be a bit different in B-BHBs at least for P. The Mg abundances for the A-BHB-stars agree well with the literature values. However, the abundances in the program B-type stars and those investigated by Kafando et al. (2016) are lower than those of Behr (2003b). The Ti abundance seems to drop towards the NG1-region and then increase again towards higher temperatures which is also obvious for the stars studied in the literature.
Therefore, it can be concluded that also the derived abundances agree with the literature.

10.1.3 Kinematics

According to the literature, the A-type stars are expected to have halo kinematics and the B-type stars are found to belong to the disk (Altmann and de Boer 2000). This is in fact observed among the program stars with the exception of Feige 6 which is part of the B-type sub-sample but shows the kinematics of a halo star.
The findings obtained using spectroscopy, photometry and kinematic data for the filed stars studied agree well with the field BHB-stars from the literature. Not only the general agreement with the literature and, hence, with the expectation, but also how well constrained most parameters are compared to older studies shows how well the hybrid NLTE/LTE models and performed analysis is suited for the spectral analyses of BHB-stars.

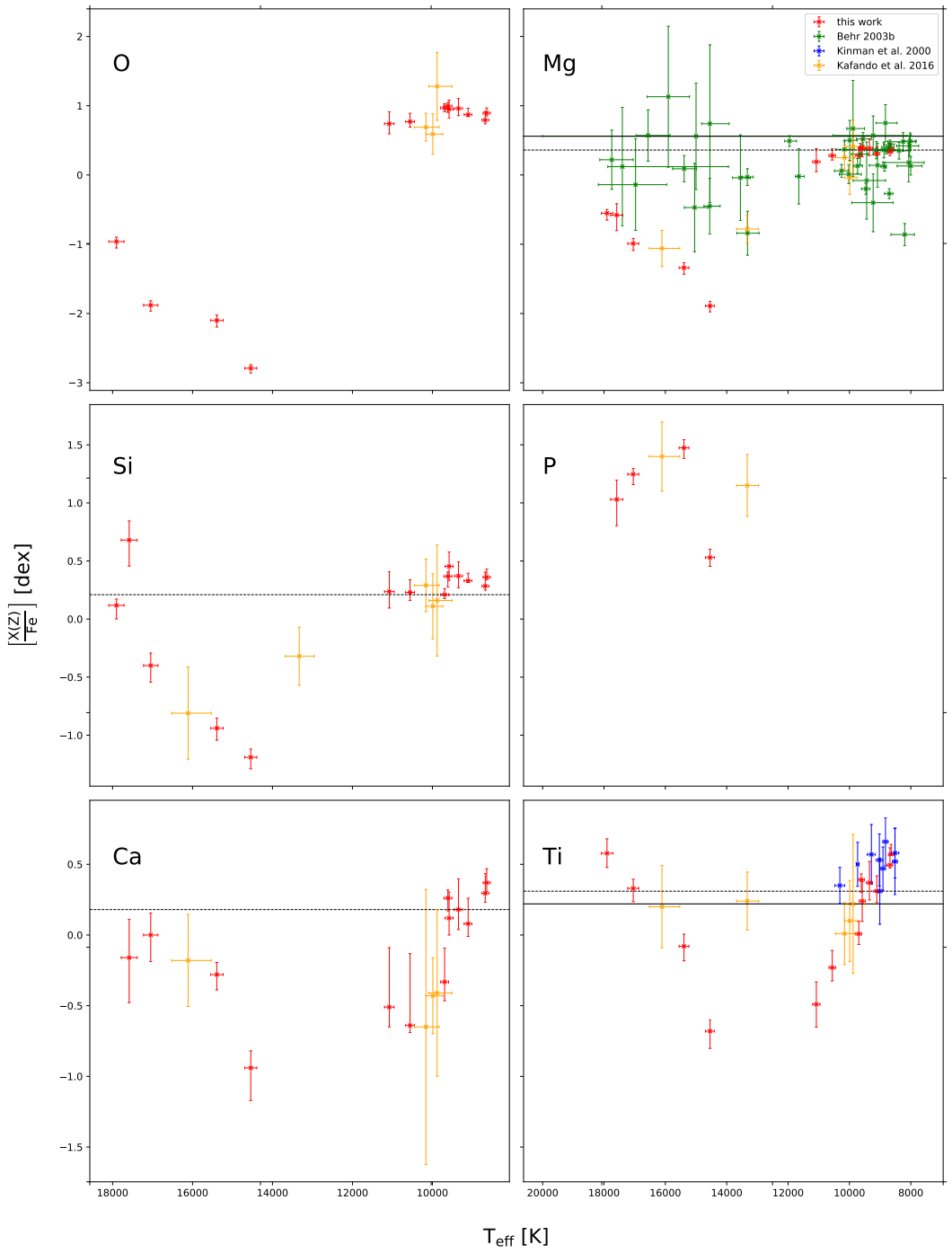

Figure 10.2: Abundances as element-to-iron ratios relative to solar for different metals in depends of the effective temperature derived by Kinman et al. (2000); Behr (2003b); Kafando et al. (2016), the drawn and dotted lines represent the mean abundances found in A-BHBs and halo giants, respectively (For and Sneden 2010; Hollek et al. 2011)

10.2 Comparison with the globular cluster population

An interesting question that still remains unanswered is if the field and GC BHB-populations are different from each other in general physical terms, as well as if they are in principal the same but subject to environmental parameters such as e.g. metallicity, stellar densities etc.. The results of the program stars are not sufficient enough to answer these questions, however, both populations can be compared based on the available information and general trends can be investigated, especially since the number of studied BHB-stars is increased significantly through the analysis. The atmospheric parameters are compared to those found by Behr (2003a). These stars have been taken from six different GCs. Stars from the GC ω Cen are taken from Moehler (2001) and Moni Bidin et al. (2012) and stars located in NGC 6752 are chosen from Moehler et al. (1996); Moni Bidin et al. (2007) and Hubrig et al. (2009). The sample from the GC NGC 6397 analyzed by Hubrig et al. (2009) is taken into account as well. Abundances are compared as well to those determined by Behr (2003a) and Hubrig et al. (2009).

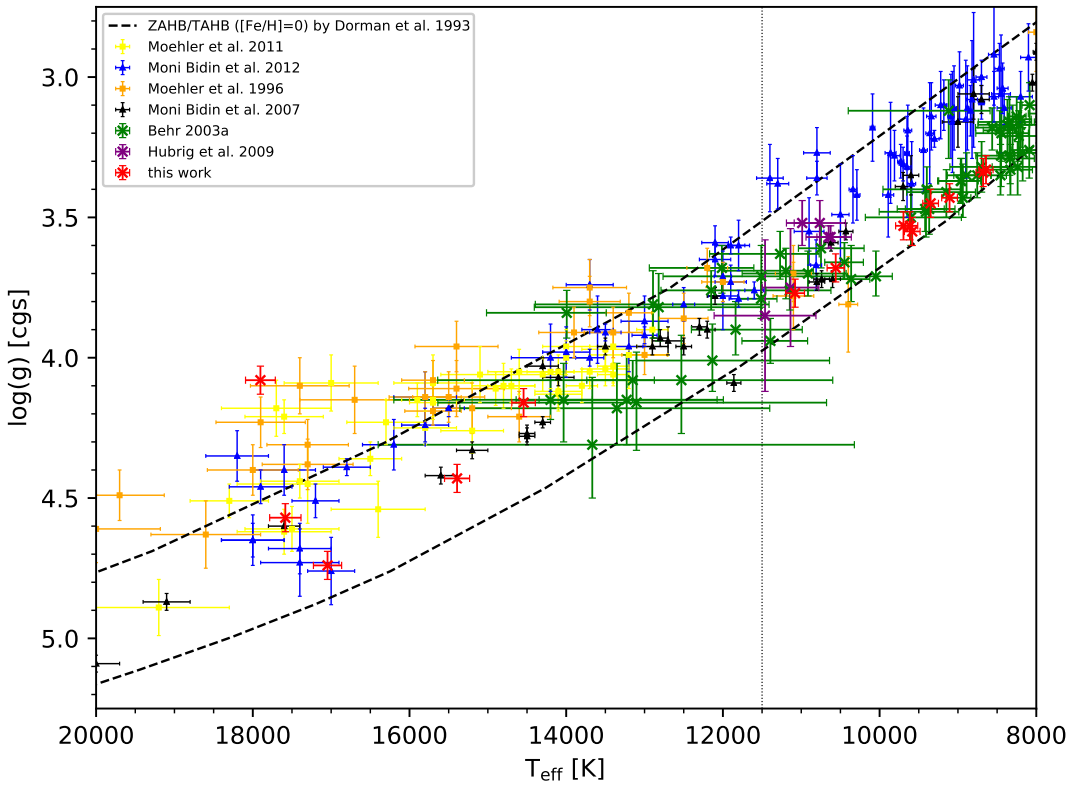

Figure 10.3: Kiel diagram showing the stars studied plus the stars from Behr (2003a); Moehler et al. (1996); Moehler (2001); Moni Bidin et al. (2007, 2012); Hubrig et al. (2009)

10.2.1 Atmospheric parameters

As already seen in the field comparison, and as indicated by the fact that up until now no systematic difference between the two populations has been found, the atmospheric parameters of the program stars agree with those of their GC counterparts. In the Kiel diagram (shown in Fig. 10.3), the GC stars from different GCs and the studied stars fall into similar positions. For the cooler A-BHBs the results are in excellent agreement with those from Behr (2003a). When comparing the results by Behr (2003a) with those of the GC ω Cen it seems that the ω Cen sequence is shifted towards lower surface gravities compared to others. The same behavior can be observed in the older results by Moehler et al. (1996). This so called low-gravity problem has been discussed in literature, and is thought to arise from the models not considering the right metallicities and, hence, the opacity in these models not being treated correctly. Using models with different metallicities yield a better agreement (Moehler 2001). However, GC are known to host multiple populations, especially peculiar clusters such as ω Cen. A population born with higher initial helium content would exhibit lower gravities, therefore, the shift might also be due to these stars actually belonging to a helium-enriched sub-population of the respective GCs.
The rotational velocities of BHB-stars in GCs and the studied field stars agree very well with each other. A significant drop in rotational velocity is observed in the GC sample which means the rotational results are consistent with those found for GC-stars.

10.2.2 Abundances

The abundances of elements in common with Behr (2003a) and Hubrig et al. (2009) are shown in Fig. 10.4 in terms of element-to-iron ratios as a function of effective temperature. The abundances of the GC BHB-stars agree well with those of the program stars. The helium abundances are found to be higher in the A-type stars across both populations, also the predicted drop in helium abundance for temperatures higher than the NG1 is present within both populations. The observed increase of helium abundance with temperature above the NG1 is in agreement with the results for stars in the GC ω Cen, by Moni Bidin et al. (2012). They find a minimum helium-abundances at around 15,000 K and a slight increase towards higher temperatures. This trend can be seen in Fig. 1.13 and the results (Fig. 8.37). Within the B-BHB-population of GC overabundances of phosphorus are found at quite similar levels as in the field stars. This means that the process responsible for the P overabundance could be universal and not linked to environmental properties. A similar trend for the Ti abundance among field stars is observed, with the titan abundance decreasing with increasing temperature, however, an increase towards the sdB temperature range can not be verified nor excluded, due to non-existing data. The observed Mg abundance agrees with the analysis as well, even agreeing better than for the field stars (compare with Fig. 10.2) since within the GC-population a decrease of Mg abundances is observed with temperature, which is consistent with the studied field BHB-stars. The GC-population lacks the MG-rich stars

found by Behr (2003b). This could be due to the low number of stars studied or due to contamination with other non-HB-stars in the sample studied by Behr (2003b).
Since no differences between the program stars, other field stars, and the GC-stars are observed. Based on the currently available data the field and the GC population of BHB-stars seem to be similar to each other. More analyses is needed to settle this issue.

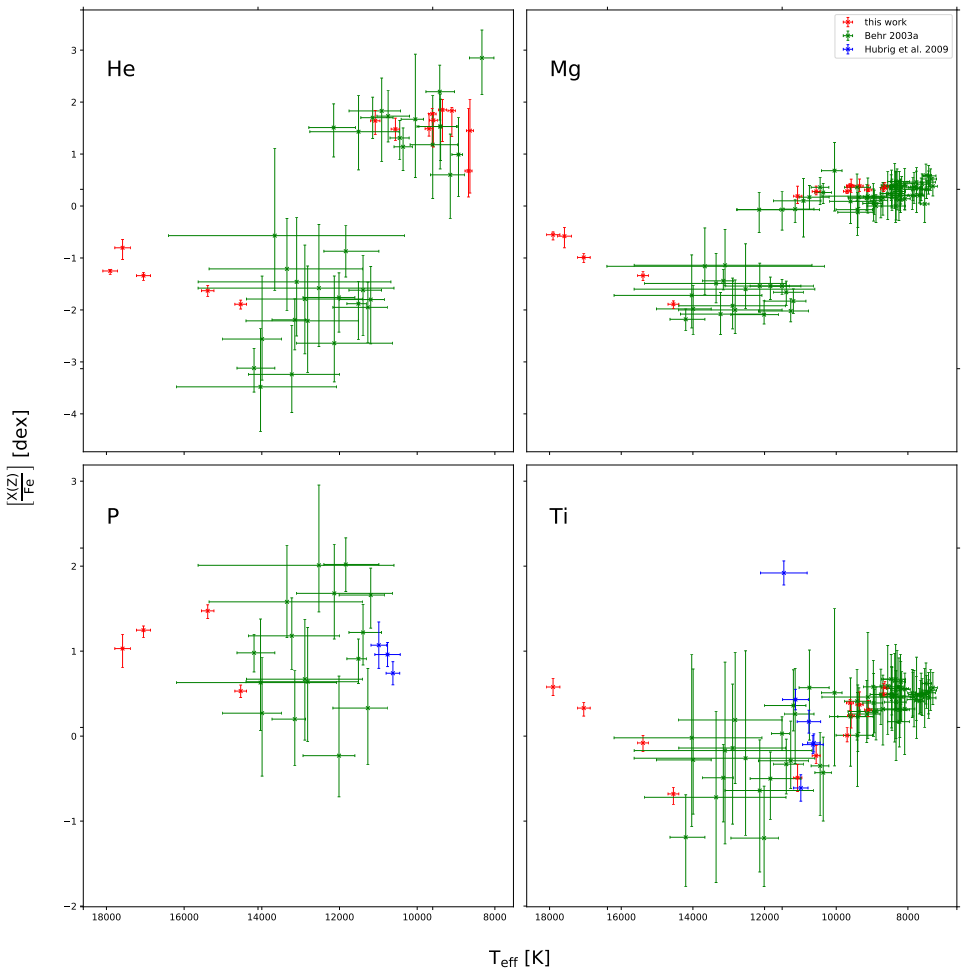

Figure 10.4: Element-to-iron ratios in dependence of the effective temperatures for the program stars and those studied by Behr (2003a); Hubrig et al. (2009)

11

Summary and outlook

The horizontal branch (HB) consists of stars that burn helium in their cores. Unlike the main sequence the horizontal branch band is a structure showing gaps which separate HB-subtypes. The HB clearly is a sequence of temperature and envelope mass with low temperatures and high envelope masses found at the red end of the branch and higher temperatures and lower masses found towards the blue. Stars on the HB which correspond to spectral types A and B are part of the blue horizontal branch (BHB) and named A-BHB and B-BHB, respectively. These stars are less massive and hotter than their red horizontal branch siblings but compared to even hotter objects, the subluminous B (sdB) stars which are part of the extreme horizontal branch (EHB), they have hydrogen envelopes massive enough to sustain hydrogen shell burning. Most prominent are the two gaps discovered by Newell and Graham (1976) which occur at $T_{\rm eff} = 11500$ K (Newell gap 1, NG1) and $T_{\rm eff} = 20000$ K (Newell gap 2, NG2), respectively. The transition from A- to B-type BHB-stars is associated with changes in the atmospheric structure as the A-BHBs have convective envelopes. Convection breaks down close to 11500 K at the NG1, hence, the atmospheres of B-BHBs are radiation dominated. With the atmospheres of the B-type stars being more stable than those of A-types, the changes in the atmospheric structures at the NG1 might give rise to atomic diffusion caused by the interplay of gravitational settling and radiative levitation. Therefore, the two groups show very different abundance patterns. In the A-type stars helium is expected to be close to solar and all other elements should be underabundant because the stars belong to the metal poor halo population. In B-BHBs, however, the abundances are different. While helium is depleted via gravitational settling, heavier elements can be enriched in the outer layer due to radiative levitation. For metals radiative acceleration is larger because they have more transition lines, especially in the ultra violet where the radiative flux of BHBs peaks. In terms of abundances the published studies were mostly limited to iron, magnesium and titanium. Detailed abundance studies are needed to first of all characterize differences and similarities between the field BHBs and those found among other populations. Additionally, abundances in B-BHBs can be used to further investigate the phenomenon of diffusion. In the past claims have been made

that some field BHBs might originate from other populations such as globular clusters (GCs) and abundance-studies may help to further investigate this possibility. Globular clusters are an ideal laboratory to study stellar evolution, therefore, they have attracted great interest in the past. Hence, GC-BHBs are much better studied than their probable field counterparts, which have mostly been ignored so far. Further detailed analyses of BHB-stars can also be used to gain further insight into the complex HB-morphology. In addition results could also have implications for stellar evolution theory and the composition and structure of the Galaxy. Hence, it is crucial to carry out spectroscopic analyses in great detail. The Gaia mission recently provided trigonometric parallaxes allowing us for the first time to convert spectroscopically derived atmospheric parameters into the fundamental stellar parameters, that is mass, radius, and luminosity.
High quality optical spectra are analyzed using a hybrid LTE/NLTE approach. Model spectra calculated with the codes ATLAS, DETAIL, and SURFACE containing 22 different elements, ranging from helium up to yttrium, either incorporated via NLTE model atoms or LTE line lists are matched to the entire available spectral range after excluding features associated with the ISM, the atmosphere of Earth or which have not been considered in the models, e.g. missing lines in the model atoms, by treating all the elements as trace-elements. This approach is valid for A- and B-type stars because the number of metal-lines in their spectra is small compared to other spectral types. The quantitative spectral analyses made use of the high resolution spectra taken with UVES and FEROS from the European Southern Observatory (ESO), HRS, at the McDonald Observatory in Texas, and ESI located at the Keck observatory. All A-BHB spectra were obtained by Martin Altmann and Marcio Catelan and taken from their kinematically selected sample of BHB-stars. Spectra for most B-BHBs were available in the ESO data archive. The atmospheric parameters and abundances of various elements were determined. As indicated by the derived effective temperatures the sample contains stars on both sides of the NG1, hence, covering the spectral types A and B. This, however, is only the first step of the performed analysis. The atmospheric parameters are used as an input for fitting synthetic spectral energy distributions to photometric data from multiple surveys in order to derive the angular diameter and the interstellar reddening and provide consistency checks. Due to high precession astrometry being available for more stars than ever before thanks to the Gaia space mission, astrometric data for the program stars can be used as well. Combining the previous analysis steps with the Gaia parallaxes gives access the stellar parameters radius, mass, and luminosity. Additionally, the Gaia proper motions can be combined with the radial velocity derived from spectroscopy to calculate the orbits of the program stars in three different Milky Way mass models.
The results from all these steps can be used to confine the properties of the stars and their evolutionary status. The derived atmospheric parameters are consistent with the stars being on the HB, with the exception of PHL 382 which shows a surface gravity lower than expected. It may belong to a helium rich HB-population, similar to those observed in GCs. The deduced rotational velocities agree with previous findings for other stars in the Galactic field as well as in GCs. As the other steps clearly show, the atmospheric parameters alone are not sufficient to classify a star as being on the HB. The abundance patterns derived are different for the A- and B-type stars. Helium is

found to be near the solar level in A-stars, while it clearly is deficient in the B-type stars. Additionally, the B-type stars show a strong enrichment of the ^{3}He isotope, which could be due to diffusion acting differently on the helium isotopes. As the helium lines are often not matched satisfactorily in the B-type sample this hints at helium being vertically stratified in their atmospheres. The abundances of all metals in the A-type stars are below the solar abundance in agreement with their halo membership which is also backed up by our kinematic analyses. The abundance pattern of all A-stars appear to be the same when scaling all the abundances with iron, indicating that iron is a good proxy for the overall metallicity. When comparing the element-to-iron ratios to the solar ratios they do not scale with the stars among the sample A-stars, therefore indicating that the composition and, hence, also the abundance patterns of A-BHB-stars are very different from the solar standard. It seems that three element groups can be distinguished. N and O are more abundant than the other elements, show similar abundances relative to solar, and no signatures of CNO-burning are observed. α-elements are less abundant than N and O but seem slightly enhanced compared to the even heavier elements. Metals from Ca up to Sr are less abundant than the previously mentioned groups but seem to exhibit a peak at iron. With respect to solar abundances are at similar levels among these metals. Amongst the B-stars overabundances of several metals are found, with a slight increase in abundances towards heavier elements. The overall abundance pattern is in good agreement with the sdB abundance pattern. This hints at diffusion, if in fact present, being similar in B-BHBs and sdBs. However, a very prominent difference to the sdBs is an enrichment in phosphorus, which is not observed in sdBs.

The stellar parameters (mass, radius, and luminosity) are mostly in agreement with the sample stars being on the HB, however, a few peculiarities are found as some masses are higher or lower than predicted by stellar evolution theory. The kinematic analyses using the three different Galactic mass models agree well with each other, showing that the results do not depend on the mass model chosen.

The evolutionary status of the majority of stars in the sample is consistent with the helium burning model HB-sequences. Four interesting objects include a potentially high mass HB-star, a halo B-BHB, and a post-HB-star or helium enriched population HB-star. PHL 25 may even be unrelated to the BHB. It may be a stripped red giant star evolving into an extremely low mass (ELM) helium white dwarf of (0.26 ± 0.05) $M_\odot$.

Comparing the previous results from the literature with those obtained here matches the coarse information available for the Galactic field as well as for the GC-population. Based on the currently available data no differences between the field and the GC population are detected.

In order to further investigate the nature of the peculiar objects more extensive observations are needed, also in order to exclude or find out if the classified stars could be binaries. Lightcurves are required to search for pulsation. This is particularly interesting for the potential ELM. Ground based projects such as Evryscope or space based missions such as TESS could be used for this purpose. Analyzing the lightcurves would mean that the stars then would be analyzed using every kind of observation common in stellar astrophysics.

Many more stars that are thought to be A-type BHBs from the Altmann and Catelan

sample are left to analyze (∼100). The approach and results presented here could guide the analysis of the entire sample using many different data sources and, therefore, gaining a clearer picture of theses stars than from spectroscopy alone. Extending the analysis of this sample could make it possible to derive a mean abundance pattern for A-BHBs. The results based on the Altmann and Catelan sample imply that selecting BHBs based on their kinematic properties works reasonably well. With Gaia data available and further data releases coming up in the future more A-BHBs and B-BHBs could be selected for spectroscopic observations, hence making the sample of field BHBs studied even larger. The same applies for the GC-counterparts which can be studied with the MUSE integral field spectrograph from ESO. Ultimately, having large samples from different populations is essential to answer the open questions in GC HB morphology.
As some chemical elements do not show lines in the optical which is especially the case for many heavier elements, other spectral ranges, in particular the ultra violet should be investigated, requiring observations with the Hubble space telescope.
Much data are already available, in particular from the MUSE instrument, and many more will be collected. Therefore, many interesting results concerning BHB-stars can be expected in the future.

References

(2001). SciPy: Open source scientific tools for python.

Adelman, S. J. and Philip, A. G. D. (1996). Elemental abundances of field horizontal branch stars - IV. HD 74721, 86986 and 93329. *MNRAS*, 280(1):285–290.

Ahn, C. P., Alexandroff, R., Allende Prieto, C., Anderson, S. F., Anderton, T., Andrews, B. H., and et al. (2012). The Ninth Data Release of the Sloan Digital Sky Survey: First Spectroscopic Data from the SDSS-III Baryon Oscillation Spectroscopic Survey. *APJS*, 203(2):21.

Allen, C. and Santillan, A. (1991). An improved model of the galactic mass distribution for orbit computations. *RMXAA*, 22:255.

Altmann, M., Catelan, M., and Zoccali, M. (2005). Searching for merger debris in the Galactic halo: chemodynamical evidence based on local blue HB stars. *AAP*, 439(2):L5–L8.

Altmann, M. and de Boer, K. S. (2000). Kinematical trends among the field horizontal branch stars. *AAP*, 353:135–146.

Altmann, M., Edelmann, H., and de Boer, K. S. (2004). Studying the populations of our Galaxy using the kinematics of sdB stars. *AAP*, 414:181–201.

Arnaboldi, M., Capaccioli, M., Mancini, D., Rafanelli, P., Scaramella, R., Sedmak, G., and Vettolani, G. P. (1998). VST: VLT Survey Telescope. *The Messenger*, 93:30–35.

Asplund, M., Grevesse, N., Sauval, A. J., and Scott, P. (2009). The Chemical Composition of the Sun. *ARAA*, 47(1):481–522.

Astropy Collaboration, Robitaille, T. P., Tollerud, E. J., Greenfield, P., Droettboom, M., Bray, E., Aldcroft, T., Davis, M., Ginsburg, A., Price-Whelan, A. M., Kerzendorf, W. E., Conley, A., Crighton, N., Barbary, K., Muna, D., Ferguson, H., Grollier, F., Parikh, M. M., Nair, P. H., Unther, H. M., Deil, C., Woillez, J., Conseil, S., Kramer, R., Turner, J. E. H., Singer, L., Fox, R., Weaver, B. A., Zabalza, V., Edwards, Z. I., Azalee Bostroem, K., Burke, D. J., Casey, A. R., Crawford, S. M., Dencheva, N., Ely, J., Jenness, T., Labrie, K., Lim, P. L., Pierfederici, F., Pontzen, A., Ptak, A., Refsdal, B., Servillat, M., and Streicher, O. (2013). Astropy: A community Python package for astronomy. *AAP*, 558:A33.

Bailer-Jones, C. A. L. (2015). Estimating Distances from Parallaxes. *PASP*, 127(956):994.

Baschek, B. and Sargent, A. I. (1976). The chemical composition of the horizontal-branch star Feige 86. *AAP*, 53:47–52.

Becker, S. R. (1998). *Non-LTE Line Formation for Iron-Group Elements in A Supergiants*, volume 131 of *Astronomical Society of the Pacific Conference Series*, page 137.

Becker, S. R. and Butler, K. (1988). Non-LTE line formation in early B and late O stars. I. Singly ionizedoxygen. *AAP*, 201:232–246.

Beers, T. C., Almeida, T., Rossi, S., Wilhelm, R., and Marsteller, B. (2007). A Catalog of Candidate Field Horizontal-Branch and A-Type Stars. III. A 2MASS-Cleaned Version. *APJS*, 168(2):277–288.

Behr, B. B. (2003a). Chemical Abundances and Rotation Velocities of Blue Horizontal-Branch Stars in Six Globular Clusters. *APJS*, 149(1):67–99.

Behr, B. B. (2003b). Rotation Velocities of Red and Blue Field Horizontal-Branch Stars. *APJS*, 149(1):101–121.

Bevington, P. R. and Robinson, D. K. (1992). *Data reduction and error analysis for the physical sciences*.

Blanton, M. R., Bershady, M. A., Abolfathi, B., Albareti, F. D., Allende Prieto, C., Almeida, A., Alonso-García, J., Anders, F., Anderson, S. F., Andrews, B., and et al. (2017). Sloan Digital Sky Survey IV: Mapping the Milky Way, Nearby Galaxies, and the Distant Universe. *AJ*, 154:28.

Boer, K. S. d. and Seggewiss, W. (2008). *Stars and Stellar Evolution*. EDP Sciences.

Bonifacio, P., Castelli, F., and Hack, M. (1995). The field horizontal-branch B-type star Feige 86. *AAPS*, 110:441.

References

Brown, D., Salaris, M., Cassisi, S., and Pietrinferni, A. (2008). Impact of rotation on the evolution of low-mass stars. *MEMSAI*, 79:579.

Brown, T. M., Cassisi, S., D'Antona, F., Salaris, M., Milone, A. P., Dalessandro, E., Piotto, G., Renzini, A., Sweigart, A. V., Bellini, A., Ortolani, S., Sarajedini, A., Aparicio, A., Bedin, L. R., Anderson, J., Pietrinferni, A., and Nardiello, D. (2016). The Hubble Space Telescope UV Legacy Survey of Galactic Globular Clusters. VII. Implications from the Nearly Universal Nature of Horizontal Branch Discontinuities. *APJ*, 822(1):44.

Brown, T. M., Lanz, T., Sweigart, A. V., Cracraft, M., Hubeny, I., and Landsman, W. B. (2012). New observational evidence of flash mixing on the white dwarf cooling curve. *arXiv preprint arXiv:1201.4204*.

Brown, T. M., Sweigart, A. V., Lanz, T., Landsman, W. B., and Hubeny, I. (2001). Flash mixing on the white dwarf cooling curve: understanding hot horizontal branch anomalies in ngc 2808. *The Astrophysical Journal*, 562(1):368.

Brown, T. M., Taylor, J. M., Cassisi, S., Sweigart, A. V., Bellini, A., Bedin, L. R., Salaris, M., Renzini, A., and Dalessandro, E. (2017). A Universal Transition in Atmospheric Diffusion for Hot Subdwarfs Near 18,000 K. *APJ*, 851(2):118.

Caloi, V. (1999). On the gap in horizontal branches at B - V about zero. *AAP*, 343:904–908.

Castelli, F. (2005). ATLAS12: how to use it. *Memorie della Societa Astronomica Italiana Supplementi*, 8:25.

Catelan, M. (2009). Horizontal branch stars: the interplay between observations and theory, and insights into the formation of the Galaxy. *APSS*, 320:261–309.

Chambers, K. C., Magnier, E. A., Metcalfe, N., Flewelling, H. A., Huber, M. E., and et al. (2016). The Pan-STARRS1 Surveys. *arXiv e-prints*, page arXiv:1612.05560.

Dalton, G. B., Caldwell, M., Ward, A. K., Whalley, M. S., Woodhouse, G., Edeson, R. L., Clark, P., Beard, S. M., Gallie, A. M., Todd, S. P., Strachan, J. M. D., Bezawada, N. N., Sutherland, W. J., and Emerson, J. P. (2006). *The VISTA infrared camera*, volume 6269 of *Society of Photo-Optical Instrumentation Engineers (SPIE) Conference Series*, page 62690X.

De Marco, O., Shara, M. M., Zurek, D., Ouellette, J. A., Lanz, T., Saffer, R. A., and Sepinsky, J. F. (2005). A Spectroscopic Analysis of Blue Stragglers, Horizontal Branch Stars, and Turnoff Stars in Four Globular Clusters. *APJ*, 632(2):894–919.

Dekker, H., D'Odorico, S., Kaufer, A., Delabre, B., and Kotzlowski, H. (2000). *Design, construction, and performance of UVES, the echelle spectrograph for the UT2 Kueyen Telescope at the ESO Paranal Observatory*, volume 4008 of *Society of Photo-Optical Instrumentation Engineers (SPIE) Conference Series*, pages 534–545.

Dorman, B. (1992). The Structure of Horizontal-Branch Models. I. The Zero-Age Horizontal Branch. *APJS*, 80:701.

Dorman, B., Rood, R. T., and O'Connell, R. W. (1993). Ultraviolet Radiation from Evolved Stellar Populations. I. Models. *APJ*, 419:596.

Dotter, A., Sarajedini, A., Anderson, J., Aparicio, A., Bedin, L. R., Chaboyer, B., Majewski, S., Marín-Franch, A., Milone, A., Paust, N., Piotto, G., Reid, I. N., Rosenberg, A., and Siegel, M. (2010). The ACS Survey of Galactic Globular Clusters. IX. Horizontal Branch Morphology and the Second Parameter Phenomenon. *APJ*, 708(1):698–716.

Driebe, T., Schoenberner, D., Bloeckera, T., and Herwig, F. (1998). VizieR Online Data Catalog: PSR J1012+5307 evolutionary tracks (Driebe+ 1998). *VizieR Online Data Catalog*, pages J/A+A/339/123.

Dufton, P. L., Conlon, E. S., Keenan, F. P., McCausland , R. J. H., and Holmgren, D. E. (1993). Three stars at high galactic latitudes with peculiar helium abundances. *AAP*, 269:201–208.

Edelmann, H., Heber, U., Hagen, H. J., Lemke, M., Dreizler, S., Napiwotzki, R., and Engels, D. (2003). Spectral analysis of sdB stars from the Hamburg Quasar Survey. *AAP*, 400:939–950.

Emerson, J., McPherson, A., and Sutherland, W. (2006). Visible and Infrared Survey Telescope for Astronomy: Progress Report. *The Messenger*, 126:41–42.

Faulkner, J. (1966). On the Nature of the Horizontal Branch. I. *APJ*, 144:978.

Fontaine, G., Brassard, P., Charpinet, S., Green, E. M., Randall, S. K., and Van Grootel, V. (2012). A preliminary look at the empirical mass distribution of hot B subdwarf stars. *AAP*, 539:A12.

For, B.-Q. and Sneden, C. (2010). The Chemical Compositions of Non-variable Red and Blue Field Horizontal Branch Stars. *AJ*, 140(6):1694–1718.

Freeman, K. C. and Norris, J. (1981). The chemical composition, structure, and dynamics of globular clusters. *araa*, 19:319–356.

Freudling, W., Romaniello, M., Bramich, D. M., Ballester, P., Forchi, V., García-Dabló, C. E., Moehler, S., and Neeser, M. J. (2013). Automated data reduction workflows for astronomy. The ESO Reflex environment. *AAP*, 559:A96.

Gaia Collaboration, Babusiaux, C., van Leeuwen, F., Barstow, M. A., Jordi, C., Vallenari, A., Bossini, D., and et al. (2018a). Gaia Data Release 2. Observational Hertzsprung-Russell diagrams. *AAP*, 616:A10.

Gaia Collaboration, Brown, A. G. A., Vallenari, A., Prusti, T., de Bruijne, J. H. J., Babusiaux, C., Bailer-Jones, C. A. L., and et al. (2018b). Gaia Data Release 2. Summary of the contents and survey properties. *AAP*, 616:A1.

Gaia Collaboration, Prusti, T., de Bruijne, J. H. J., Brown, A. G. A., Vallenari, A., Babusiaux, C., and et al. (2016). The Gaia mission. *AAP*, 595:A1.

Geier, S. and Heber, U. (2012). Hot subdwarf stars in close-up view. II. Rotational properties of single and wide binary subdwarf B stars. *AAP*, 543:A149.

Geier, S., Heber, U., Edelmann, H., Morales-Rueda, L., and Napiwotzki, R. (2010). Metal abundances of subdwarf B stars—the extended sample. *APSS*, 329(1-2):127–131.

Gianninas, A., Hermes, J. J., Brown, W. R., Dufour, P., Barber, S. D., Kilic, M., Kenyon, S. J., and Harrold, S. T. (2014). SDSS J074511.56+194926.5: Discovery of a Metal-rich and Tidally Distorted Extremely Low Mass White Dwarf. *APJ*, 781(2):104.

Giddings, J. R. (1981). PhD thesis, -.

Giesers, B., Dreizler, S., Husser, T.-O., Kamann, S., Anglada Escudé, G., Brinchmann, J., Carollo, C. M., Roth, M. M., Weilbacher, P. M., and Wisotzki, L. (2018). A detached stellar-mass black hole candidate in the globular cluster NGC 3201. *MNRAS*, 475(1):L15–L19.

Giesers, B. D. (2019). *Spectroscopy of Binaries in Globular Clusters* . PhD thesis, Georg-August-Universität Göttingen.

Girardi, L., Bressan, A., Bertelli, G., and Chiosi, C. (2000). Evolutionary tracks and isochrones for low- and intermediate-mass stars: From 0.15 to 7 M_{sun}, and from Z=0.0004 to 0.03. *AAPS*, 141:371–383.

Gratton, R., Bragaglia, A., Carretta, E., D'Orazi, V., Lucatello, S., and Sollima, A. (2019). What is a globular cluster? An observational perspective. *AAPR*, 27(1):8.

Gratton, R., Sneden, C., and Carretta, E. (2004). Abundance variations within globular clusters. *araa*, 42:385–440.

Gratton, R. G., Carretta, E., Bragaglia, A., Lucatello, S., and D'Orazi, V. (2010). The second and third parameters of the horizontal branch in globular clusters. *AAP*, 517:A81.

Gratton, R. G., Lucatello, S., Sollima, A., Carretta, E., Bragaglia, A., Momany, Y., D'Orazi, V., Salaris, M., Cassisi, S., and Stetson, P. B. (2015). The Na-O anticorrelation in horizontal branch stars. V. NGC 6723. *aap*, 573:A92.

Grundahl, F., Catelan, M., Landsman, W. B., Stetson, P. B., and Andersen, M. I. (1999). Hot Horizontal-Branch Stars: The Ubiquitous Nature of the "Jump" in Strömgren u, Low Gravities, and the Role of Radiative Levitation of Metals. *APJ*, 524(1):242–261.

Harris, W. E. (1996). A Catalog of Parameters for Globular Clusters in the Milky Way. *aj*, 112:1487.

Harris, W. E. and Racine, R. (1979). Globular clusters in galaxies. *araa*, 17:241–274.

Hartoog, M. R. (1979). Helium-3 in the horizontal-branch star Feige 86. *APJ*, 231:161–163.

Heber, U. (1987). Spectral analysis of hot subdwarfs (fieldversus globular cluster population). *Mitteilungen der Astronomischen Gesellschaft Hamburg*, 70:79.

Heber, U. (2016). Hot subluminous stars. *pasp*, 128(8):082001.

Heber, U., Irrgang, A., and Schaffenroth, J. (2018). Spectral energy distributions and colours of hot subluminous stars. *Open Astronomy*, 27(1):35–43.

Hermes, J. J., Gänsicke, B. T., Koester, D., Bours, M. C. P., Townsley, D. M., Farihi, J., Marsh, T. R., Littlefair, S., Dhillon, V. S., Gianninas, A., Breedt, E., and Raddi, R. (2014). Heavy metals in a light white dwarf: abundances of the metal-rich, extremely low-mass GALEX J1717+6757. *MNRAS*, 444(2):1674–1682.

Hermes, J. J., Montgomery, M. H., Winget, D. E., Brown, W. R., Kilic, M., and Kenyon, S. J. (2012). SDSS J184037.78+642312.3: The First Pulsating Extremely Low Mass White Dwarf. *APJL*, 750(2):L28.

Høg, E., Fabricius, C., Makarov, V. V., Urban, S., Corbin, T., Wycoff, G., Bastian, U., Schwekendiek, P., and Wicenec, A. (2000). The Tycho-2 catalogue of the 2.5 million brightest stars. *AAP*, 355:L27–L30.

Hollek, J. K., Frebel, A., Roederer, I. U., Sneden, C., Shetrone, M., Beers, T. C., Kang, S.-j., and Thom, C. (2011). The Chemical Abundances of Stars in the Halo (CASH) Project. II. A Sample of 14 Extremely Metal-poor Stars. *APJ*, 742(1):54.

Houck, J. C. and Denicola, L. A. (2000). *ISIS: An Interactive Spectral Interpretation System for High Resolution X-Ray Spectroscopy*, volume 216 of *Astronomical Society of the Pacific Conference Series*, page 591.

Hoyle, F. and Schwarzschild, M. (1955). On the Evolution of Type II Stars. *APJS*, 2:1.

Hubrig, S., Castelli, F., de Silva, G., González, J. F., Momany, Y., Netopil, M., and Moehler, S. (2009). A high-resolution study of isotopic composition and chemical abundances of blue horizontal branch stars in the globular clusters NGC 6397 and NGC 6752. *AAP*, 499(3):865–878.

Hui-Bon-Hoa, A., LeBlanc, F., and Hauschildt, P. H. (2000). Diffusion in the Atmospheres of Blue Horizontal-Branch Stars. *APJL*, 535(1):L43–L45.

Hunter, J. D. (2007). Matplotlib: A 2d graphics environment. *Computing In Science & Engineering*, 9(3):90–95.

References

Irrgang, A. (2014). *Origin of runaway OB stars*. PhD thesis, Friedrich-Alexander-Universität Erlangen-Nürnberg.

Irrgang, A., Kreuzer, S., Heber, U., and Brown, W. (2018). A quantitative spectral analysis of 14 hypervelocity stars from the MMT survey. *AAP*, 615:L5.

Irrgang, A., Przybilla, N., Heber, U., Böck, M., Hanke, M., Nieva, M. F., and Butler, K. (2014). A new method for an objective, χ^2-based spectroscopic analysis of early-type stars. First results from its application to single and binary B- and late O-type stars. *AAP*, 565:A63.

Irrgang, A., Wilcox, B., Tucker, E., and Schiefelbein, L. (2013). Milky Way mass models for orbit calculations. *AAP*, 549:A137.

Ivanova, N., Belczynski, K., Fregeau, J. M., and Rasio, F. A. (2005). The evolution of binary fractions in globular clusters. *Monthly Notices of the Royal Astronomical Society*, 358(2):572–584.

Kafando, I., LeBlanc, F., and Robert, C. (2016). Detailed abundance analysis of five field blue horizontal-branch stars. *MNRAS*, 459(1):871–879.

Kamann, S., Husser, T. O., Dreizler, S., Emsellem, E., Weilbacher, P. M., Martens, S., Bacon, R., den Brok, M., Giesers, B., Krajnović, D., Roth, M. M., Wendt, M., and Wisotzki, L. (2018). A stellar census in globular clusters with MUSE: The contribution of rotation to cluster dynamics studied with 200 000 stars. *MNRAS*, 473(4):5591–5616.

Kaplan, D. L., Bhalerao, V. B., van Kerkwijk, M. H., Koester, D., Kulkarni, S. R., and Stovall, K. (2013). A Metal-rich Low-gravity Companion to a Massive Millisecond Pulsar. *APJ*, 765(2):158.

Kaufer, A., Stahl, O., Tubbesing, S., Nørregaard, P., Avila, G., Francois, P., Pasquini, L., and Pizzella, A. (1999). Commissioning FEROS, the new high-resolution spectrograph at La-Silla. *The Messenger*, 95:8–12.

Kilkenny, D. and van Wyk, F. (1990). The high-latitude blue variable PHL 346 and helium-weak star PHL 382. *MNRAS*, 244:727.

Kinman, T., Castelli, F., Cacciari, C., Bragaglia, A., Harmer, D., and Valdes, F. (2000). A spectroscopic study of field BHB star candidates. *AAP*, 364:102–136.

Kinman, T. D., Morrison, H. L., and Brown, W. R. (2009). Do the Nearby Blue Horizontal Branch Stars Belong to the Thick Disk or the Halo? *AJ*, 137(2):3198–3209.

Knies, J. (2020). Remeis meme wall contribution.

Krauss, L. M. and Chaboyer, B. (2003). Age estimates of globular clusters in the milky way: Constraints on cosmology. *Science*, 299(5603):65–69.

Kuijken, K. (2011). OmegaCAM: ESO's Newest Imager. *The Messenger*, 146:8–11.

Kuijken, K., Bender, R., Cappellaro, E., Muschielok, B., Baruffolo, A., Cascone, E., Iwert, O., Mitsch, W., Nicklas, H., Valentijn, E. A., Baade, D., Begeman, K. G., Bortolussi, A., Boxhoorn, D., Christen, F., Deul, E. R., Geimer, C., Greggio, L., Harke, R., Häfner, R., Hess, G., Hess, H. J., Hopp, U., Ilijevski, I., Klink, G., Kravcar, H., Lizon, J. L., Magagna, C. E., Müller, P., Niemeczek, R., de Pizzol, L., Poschmann, H., Reif, K., Rengelink, R., Reyes, J., Silber, A., and Wellem, W. (2002). OmegaCAM: the 16k×16k CCD camera for the VLT survey telescope. *The Messenger*, 110:15–18.

Kurucz, R. (1993). ATLAS9 Stellar Atmosphere Programs and 2 km/s grid. *ATLAS9 Stellar Atmosphere Programs and 2 km/s grid. Kurucz CD-ROM No. 13. Cambridge*, 13.

Kurucz, R. L. (1996). *Status of the ATLAS 12 Opacity Sampling Program and of New Programs for Rosseland and for Distribution Function Opacity*, volume 108 of *Astronomical Society of the Pacific Conference Series*, page 160.

Latour, M., Heber, U., Irrgang, A., Schaffenroth, V., Geier, S., Hillebrandt, W., Röpke, F. K., Taubenberger, S., Kromer, M., and Fink, M. (2016). Quantitative spectral analysis of the sdB star HD 188112: A helium-core white dwarf progenitor. *AAP*, 585:A115.

LeBlanc, F., Hui-Bon-Hoa, A., and Khalack, V. R. (2010). Stratification of the elements in the atmospheres of blue horizontal-branch stars. *MNRAS*, 409(4):1606–1610.

Lindegren, L. (2018). Re-normalising the astrometric chi-square in Gaia DR2. GAIA-C3-TN-LU-LL-124.

Magurno, D., Sneden, C., Bono, G., Braga, V. F., Mateo, M., Persson, S. E., Preston, G., Thévenin, F., da Silva, R., Dall'Ora, M., Fabrizio, M., Ferraro, I., Fiorentino, G., Iannicola, G., Inno, L., Marengo, M., Marinoni, S., Marrese, P. M., Martínez-Vázquez, C. E., Matsunaga, N., Monelli, M., Neeley, J. R., Nonino, M., and Walker, A. R. (2019). Chemical Compositions of Field and Globular Cluster RR Lyrae Stars. II. ω Centauri. *APJ*, 881(2):104.

Massari, D., Koppelman, H. H., and Helmi, A. (2019). Origin of the system of globular clusters in the Milky Way. *AAP*, 630:L4.

McKinney, W. (2010). Data structures for statistical computing in python. In van der Walt, S. and Millman, J., editors, *Proceedings of the 9th Python in Science Conference*, pages 51 – 56.

Mermilliod, J. C. (1992). Archives of photometric data. *Highlights of Astronomy*, 9:725.

Meylan, G. and Heggie, D. C. (1997). Internal dynamics of globular clusters. *AAPR*, 8:1–143.

Michaud, G., Richer, J., and Richard, O. (2011). Horizontal branch evolution, metallicity, and sdB stars. *AAP*, 529:A60.

References

Mieske, S. (2019). UV-Visual Echelle Spectrograph User manual. *European southern observatory*, VLT-MAN-ESO-13200-1825.

Mihalas, D. (1966). Balmer-Line Model Atmospheres for A-Type Stars. *APJS*, 13:1.

Miyamoto, M. and Nagai, R. (1975). Three-dimensional models for the distribution of mass in galaxies. *PASJ*, 27:533–543.

Moehler, S. (2001). Hot stars in globular clusters: A spectroscopist's view. *Publications of the Astronomical Society of the Pacific*, 113(788):1162.

Moehler, S., Dreizler, S., LeBlanc, F., Khalack, V., Michaud, G., Richer, J., Sweigart, A. V., and Grundahl, F. (2014). Hot horizontal branch stars in NGC 288 - effects of diffusion and stratification on their atmospheric parameters. *AAP*, 565:A100.

Moehler, S., Heber, U., and Rupprecht, G. (1996). Hot hb stars in globular clusters-physical parameters and consequences for theory. iii. ngc 6752 and its long blue vertical branch. *arXiv preprint astro-ph/9607151*.

Momany, Y., Piotto, G., Recio-Blanco, A., Bedin, L. R., Cassisi, S., and Bono, G. (2002). A New Feature along the Extended Blue Horizontal Branch of NGC 6752. *apjl*, 576:L65–L68.

Moni Bidin, C., Moehler, S., Piotto, G., Momany, Y., and Recio-Blanco, A. (2007). Spectroscopy of horizontal branch stars in ngc 6752-anomalous results on atmospheric parameters and masses. *Astronomy & Astrophysics*, 474(2):505–514.

Moni Bidin, C., Villanova, S., Piotto, G., Moehler, S., Cassisi, S., and Momany, Y. (2012). Spectroscopy of horizontal branch stars in ω centauri. *Astronomy & Astrophysics*, 547:A109.

Moore, C. E. (1959). *A multiplet table of astrophysical interest. Part 1*.

Morel, T. and Butler, K. (2008). The neon content of nearby B-type stars and its implications for the solar model problem. *AAP*, 487(1):307–315.

Morel, T., Butler, K., Aerts, C., Neiner, C., and Briquet, M. (2006). Abundance analysis of prime B-type targets for asteroseismology. I. Nitrogen excess in slowly-rotating β Cephei stars. *AAP*, 457(2):651–663.

Naslim, N., Jeffery, C. S., Hibbert, A., and Behara, N. T. (2013). Discovery of extremely lead-rich subdwarfs: does heavy metal signal the formation of subdwarf B stars? *MNRAS*, 434(3):1920–1929.

Navarro, J. F., Frenk, C. S., and White, S. D. M. (1997). A Universal Density Profile from Hierarchical Clustering. *APJ*, 490(2):493–508.

Németh, P. (2017). Atomic diffusion in the atmosphere of Feige 86. *Open Astronomy*, 26(1):280–284.

Newell, B. and Graham, J. A. (1976). Gaps in the blue horizontal branch. *APJ*, 204:804–809.

Newell, E. B. (1973). The evolutionary status of the blue halo stars. *APJS*, 26:37–82.

Nieva, M. F. and Przybilla, N. (2006). C II Abundances in Early-Type Stars: Solution to a Notorious Non-LTE Problem. *APJL*, 639(1):L39–L42.

Nieva, M. F. and Przybilla, N. (2007). Hydrogen and helium line formation in OB dwarfs and giants. A hybrid non-LTE approach. *AAP*, 467(1):295–309.

Nieva, M. F. and Przybilla, N. (2008). Carbon abundances of early B-type stars in the solar vicinity. Non-LTE line-formation for C II/III/IV and self-consistent atmospheric parameters. *AAP*, 481(1):199–216.

Nieva, M. F. and Przybilla, N. (2012). Present-day cosmic abundances. A comprehensive study of nearby early B-type stars and implications for stellar and Galactic evolution and interstellar dust models. *AAP*, 539:A143.

Pauli, E. M., Napiwotzki, R., Altmann, M., Heber, U., Odenkirchen, M., and Kerber, F. (2003). 3D kinematics of white dwarfs from the SPY project. *AAP*, 400:877–890.

Pauli, E. M., Napiwotzki, R., Heber, U., Altmann, M., and Odenkirchen, M. (2006). 3D kinematics of white dwarfs from the SPY project. II. *AAP*, 447(1):173–184.

Paunzen, E. (2015). A new catalogue of Strömgren-Crawford uvbyβ photometry. *AAP*, 580:A23.

Peron, M. (2017). UVES Pipeline User manual. *European southern observatory*, VLT-MAN-ESO-19500-2965.

Pietrinferni, A., Cassisi, S., Salaris, M., and Castelli, F. (2004). A Large Stellar Evolution Database for Population Synthesis Studies. I. Scaled Solar Models and Isochrones. *APJ*, 612(1):168–190.

Powell, M. J. D. (1964). An efficient method for finding the minimum of a function of several variables without calculating derivatives. *The Computer Journal*, 7(2):155–162.

Prialnik, D. (2000). *An Introduction to the Theory of Stellar Structure and Evolution*.

Price-Whelan, A. M., Sipőcz, B. M., Günther, H. M., Lim, P. L., Crawford, S. M., Conseil, S., Shupe, D. L., Craig, M. W., Dencheva, N., Ginsburg, A., VanderPlas, J. T., Bradley, L. D., Pérez-Suárez, D., de Val-Borro, M., Paper Contributors, P., Aldcroft, T. L., Cruz, K. L., Robitaille, T. P., Tollerud, E. J., Coordination Committee, A., Ardelean, C., Babej, T., Bach, Y. P., Bachetti, M., Bakanov, A. V., Bamford, S. P., Barentsen, G., Barmby, P., Baumbach, A., Berry, K. L., Biscani, F., Boquien, M., Bostroem, K. A., Bouma, L. G., Brammer, G. B., Bray, E. M., Breytenbach, H., Buddelmeijer, H., Burke, D. J., Calderone, G., Cano Rodríguez, J. L., Cara, M., Cardoso, J. V. M., Cheedella, S., Copin, Y., Corrales, L., Crichton, D., D'Avella, D., Deil, C., Depagne, É., Dietrich, J. P., Donath, A., Droettboom, M., Earl, N., Erben, T., Fabbro, S., Ferreira, L. A., Finethy, T., Fox, R. T., Garrison, L. H., Gibbons, S. L. J., Goldstein, D. A., Gommers, R., Greco, J. P., Greenfield, P., Groener, A. M., Grollier, F., Hagen, A., Hirst, P., Homeier, D., Horton, A. J., Hosseinzadeh, G., Hu, L., Hunkeler, J. S., Ivezić, Ž., Jain, A., Jenness, T., Kanarek, G., Kendrew, S., Kern, N. S., Kerzendorf, W. E., Khvalko, A., King, J., Kirkby, D., Kulkarni, A. M., Kumar, A., Lee, A., Lenz, D., Littlefair, S. P., Ma, Z., Macleod, D. M., Mastropietro, M., McCully, C., Montagnac, S., Morris, B. M., Mueller, M., Mumford, S. J., Muna, D., Murphy, N. A., Nelson, S., Nguyen, G. H., Ninan, J. P., Nöthe, M., Ogaz, S., Oh, S., Parejko, J. K., Parley, N., Pascual, S., Patil, R., Patil, A. A., Plunkett, A. L., Prochaska, J. X., Rastogi, T., Reddy Janga, V., Sabater, J., Sakurikar, P., Seifert, M., Sherbert, L. E., Sherwood-Taylor, H., Shih, A. Y., Sick, J., Silbiger, M. T., Singanamalla, S., Singer, L. P., Sladen, P. H., Sooley, K. A., Sornarajah, S., Streicher, O., Teuben, P., Thomas, S. W., Tremblay, G. R., Turner, J. E. H., Terrón, V., van Kerkwijk, M. H., de la Vega, A., Watkins, L. L., Weaver, B. A., Whitmore, J. B., Woillez, J., Zabalza, V., and Contributors, A. (2018). The Astropy Project: Building an Open-science Project and Status of the v2.0 Core Package. *AJ*, 156:123.

Przybilla, N. (2005). Non-LTE modelling of the He I 10830 Å line in early-type main sequence stars. *AAP*, 443(1):293–296.

Przybilla, N. and Butler, K. (2001). Non-LTE line formation for N: Abundances and stellar parameters. Model atom and first results on BA-type stars. *AAP*, 379:955–975.

Przybilla, N. and Butler, K. (2004). Non-LTE Line Formation for Hydrogen Revisited. *APJ*, 609(2):1181–1191.

Przybilla, N., Butler, K., Becker, S. R., and Kudritzki, R. P. (2001). Non-LTE line formation for {Mg}{I/II}: Abundances and stellar parameters. Model atom and first results on A-type stars. *AAP*, 369:1009–1026.

Przybilla, N., Butler, K., Becker, S. R., and Kudritzki, R. P. (2006). Quantitative spectroscopy of BA-type supergiants. *AAP*, 445(3):1099–1126.

Przybilla, N., Butler, K., Becker, S. R., Kudritzki, R. P., and Venn, K. A. (2000). Non-LTE line formation for neutral oxygen. Model atom and first results on A-type stars. *AAP*, 359:1085–1106.

Przybilla, N., Nieva, M.-F., and Butler, K. (2011). Testing common classical LTE and NLTE model atmosphere and line-formation codes for quantitative spectroscopy of early-type stars. In *Journal of Physics Conference Series*, volume 328 of *Journal of Physics Conference Series*, page 012015.

Przybilla, N., Nieva, M. F., Heber, U., Firnstein, M., Butler, K., Napiwotzki, R., and Edelmann, H. (2008). LMC origin of the hyper-velocity star HE 0437-5439. Beyond the supermassive black hole paradigm. *AAP*, 480(3):L37–L40.

Quievy, D., Charbonneau, P., Michaud, G., and Richer, J. (2009). Abundances anomalies and meridional circulation in horizontal branch stars. *AAP*, 500(3):1163–1171.

Sadakane, K. and Nishimura, M. (2017). Weak metallic emission lines in early B-type stars. *PASJ*, 69(3):48.

Sadakane, K. and Nishimura, M. (2019). A spectroscopic study of weak metallic emission lines in a B3 V star Herculis. *PASJ*, 71(2):45.

Sarajedini, A., Bedin, L. R., Chaboyer, B., Dotter, A., Siegel, M., Anderson, J., Aparicio, A., King, I., Majewski, S., Marín-Franch, A., Piotto, G., Reid, I. N., and Rosenberg, A. (2007). The ACS Survey of Galactic Globular Clusters. I. Overview and Clusters without Previous Hubble Space Telescope Photometry. *AJ*, 133(4):1658–1672.

Schindewolf, M., Németh, P., Heber, U., Battich, T., Miller Bertolami, M. M., Irrgang, A., and Latour, M. (2018). A quantitative NLTE analysis of visual and ultraviolet spectra of four helium-rich subdwarf O stars. *AAP*, 620:A36.

Schneider, D. (2017). Spectroscopic analysis of the 3he anomaly in b-type stars.

Schneider, D., Irrgang, A., Heber, U., Nieva, M. F., and Przybilla, N. (2018). NLTE spectroscopic analysis of the ^{3}He anomaly in subluminous B-type stars. *AAP*, 618:A86.

Shanks, T., Metcalfe, N., Chehade, B., Findlay, J. R., Irwin, M. J., Gonzalez-Solares, E., Lewis, J. R., Yoldas, A. K., Mann, R. G., Read, M. A., Sutorius, E. T. W., and Voutsinas, S. (2015). The VLT Survey Telescope ATLAS. *MNRAS*, 451(4):4238–4252.

Sheinis, A. I., Bolte, M., Epps, H. W., Kibrick, R. I., Miller, J. S., Radovan, M. V., Bigelow, B. C., and Sutin, B. M. (2002). ESI, a New Keck Observatory Echellette Spectrograph and Imager. *PASP*, 114(798):851–865.

Shi, X. (1995). The Uncertainties in the Age of Globular Clusters from Their Helium Abundance and Mass Loss. *APJ*, 446:637.

Shimanskii, V. V. (2002). Parameters of UX CVn. *Astronomy Reports*, 46(2):127–138.

Skrutskie, M. F., Cutri, R. M., Stiening, R., Weinberg, M. D., Schneider, S., Carpenter, J. M., Beichman, C., Capps, R., Chester, T., Elias, J., Huchra, J., Liebert, J., Lonsdale, C., Monet, D. G., Price, S., Seitzer, P., Jarrett, T., Kirkpatrick, J. D., Gizis, J. E., Howard, E., Evans, T., Fowler, J., Fullmer, L., Hurt, R., Light, R., Kopan, E. L., Marsh, K. A., McCallon, H. L., Tam, R., Van Dyk, S., and Wheelock, S. (2006). The Two Micron All Sky Survey (2MASS). *AJ*, 131(2):1163–1183.

Snoop Dogg (2018). *Walk of fame acceptance speech*.

Spruit, H. C. (2015). The growth of helium-burning cores. *AAP*, 582:L2.

Sterzik, M. (2018). Refelex UVES Tutorial. *European southern observatory*, VLT-MAN-ESO-19540-5296.

Sweigart, A. V. (1987). Evolutionary Sequences for Horizontal-Branch Stars. *APJS*, 65:95.

Sweigart, A. V. (1997). Effects of Helium Mixing on the Evolution of Globular Cluster Stars. *APJL*, 474(1):L23–L26.

Sweigart, A. V. (2002). Horizontal branch models as a test of mixing on the RGB. *Highlights of Astronomy*, 12:292–294.

Tull, R. G. (1998). *High-resolution fiber-coupled spectrograph of the Hobby-Eberly Telescope*, volume 3355 of *Society of Photo-Optical Instrumentation Engineers (SPIE) Conference Series*, pages 387–398.

Van Der Walt, S., Colbert, S. C., and Varoquaux, G. (2011). The numpy array: a structure for efficient numerical computation. *Computing in Science & Engineering*, 13(2):22–30.

van Leeuwen, F. (2007). Validation of the new Hipparcos reduction. *AAP*, 474(2):653–664.

Villanova, S., Piotto, G., King, I. R., Anderson, J., Bedin, L. R., Gratton, R. G., Cassisi, S., Momany, Y., Bellini, A., Cool, A. M., Recio-Blanco, A., and Renzini, A. (2007). The Multiplicity of the Subgiant Branch of ω Centauri: Evidence for Prolonged Star Formation. *apj*, 663:296–314.

Vrancken, M., Butler, K., and Becker, S. R. (1996). Non-LTE line formation for SII and SIII. I. Model atoms and first results. *AAP*, 311:661–668.

Wallerstein, G., Greenstein, J. L., Parker, R., Helfer, H. L., and Aller, L. H. (1963). Red Giants with Extreme Metal Deficiencies. *APJ*, 137:280.

Wamsteker, W. (2000). *The IUE newly extracted spectra system.*

Wilkinson, M. I. and Evans, N. W. (1999). The present and future mass of the Milky Way halo. *MNRAS*, 310(3):645–662.

Wolf, C., Onken, C. A., Luvaul, L. C., Schmidt, B. P., Bessell, M. S., Chang, S.-W., Da Costa, G. S., Mackey, D., Martin-Jones, T., Murphy, S. J., Preston, T., Scalzo, R. A., Shao, L., Smillie, J., Tisserand, P., White, M. C., and Yuan, F. (2018). SkyMapper Southern Survey: First Data Release (DR1). *PASA*, 35:e010.

Wright, E. L., Eisenhardt, P. R. M., Mainzer, A. K., Ressler, M. E., Cutri, R. M., Jarrett, T., Kirkpatrick, J. D., Padgett, D., McMillan, R. S., Skrutskie, M., Stanford, S. A., Cohen, M., Walker, R. G., Mather, J. C., Leisawitz, D., Gautier, Thomas N., I., McLean, I., Benford, D., Lonsdale, C. J., Blain, A., Mendez, B., Irace, W. R., Duval, V., Liu, F., Royer, D., Heinrichsen, I., Howard, J., Shannon, M., Kendall, M., Walsh, A. L., Larsen, M., Cardon, J. G., Schick, S., Schwalm, M., Abid, M., Fabinsky, B., Naes, L., and Tsai, C.-W. (2010). The Wide-field Infrared Survey Explorer (WISE): Mission Description and Initial On-orbit Performance. *AJ*, 140(6):1868–1881.

Yi, S. K. (2008). *The Current Understanding on the UV Upturn*, volume 392 of *Astronomical Society of the Pacific Conference Series*, page 3.

Zangwill, W. I. (1967). Minimizing a function without calculating derivatives. *The Computer Journal*, 10(3):293–296.

Acknowledgments

1 Used data, software and services

Based on observations collected at the European Southern Observatory under ESO programmes 073.D-0495(A), 076.D-0169(A), 078.D-0098(A), 099.B-0042(A), 0100.B-0223(A), 0101.B-0342(A), 0102.D-0388(A), 177.A-3011, 179.A-2010. Some of the data presented herein were obtained at the W. M. Keck Observatory, which is operated as a scientific partnership among the California Institute of Technology, the University of California and the National Aeronautics and Space Administration. The Observatory was made possible by the generous financial support of the W. M. Keck Foundation. The author wishes to recognize and acknowledge the very significant cultural role and reverence that the summit of Maunakea has always had within the indigenous Hawaiian community. We are most fortunate to have the opportunity to conduct observations from this mountain. This paper includes data taken at The McDonald Observatory of The University of Texas at Austin. This work has made use of data from the European Space Agency (ESA) mission *Gaia* (https://www.cosmos.esa.int/gaia), processed by the *Gaia* Data Processing and Analysis Consortium (DPAC, https://www.cosmos.esa.int/web/gaia/dpac/consortium). Funding for the DPAC has been provided by national institutions, in particular the institutions participating in the *Gaia* Multilateral Agreement. This publication makes use of data products from the Two Micron All Sky Survey, which is a joint project of the University of Massachusetts and the Infrared Processing and Analysis Center/California Institute of Technology, funded by the National Aeronautics and Space Administration and the National Science Foundation. This publication makes use of data products from the Wide-field Infrared Survey Explorer, which is a joint project of the University of California, Los Angeles, and the Jet Propulsion Laboratory/California Institute of Technology, funded by the National Aeronautics and Space Administration. Funding for SDSS-III has been provided by the Alfred P. Sloan Foundation, the Participating Institutions, the National Science Foundation, and the U.S. Department of Energy Office of Science. The SDSS-III web site is http://www.sdss3.org/. SDSS-III is managed by the Astrophysical Research Consortium for the Participating Institutions of the SDSS-III Collaboration including the University of Arizona, the Brazilian Participation Group, Brookhaven National Laboratory, Carnegie Mellon University, University of Florida, the French Participation Group, the German Participation Group, Harvard University, the Instituto de Astrofisica de Canarias, the Michigan State/Notre Dame/JINA Participation Group, Johns Hopkins University, Lawrence Berkeley National Laboratory, Max Planck Institute for Astrophysics, Max Planck Institute for Extraterrestrial Physics, New Mexico State University, New York University, Ohio State University, Pennsylvania State University, University of Portsmouth, Princeton University, the Spanish Participation Group, University of Tokyo, University of Utah, Vanderbilt University, University of Virginia, University of Washington, and Yale University. The national facility capability for SkyMapper has been funded through ARC LIEF grant LE130100104 from the Australian Research Council, awarded to the University of Sydney, the Australian National University, Swinburne University of Technology, the University of Queens-

land, the University of Western Australia, the University of Melbourne, Curtin University of Technology, Monash University and the Australian Astronomical Observatory. SkyMapper is owned and operated by The Australian National University's Research School of Astronomy and Astrophysics. The survey data were processed and provided by the SkyMapper Team at ANU. The SkyMapper node of the All-Sky Virtual Observatory (ASVO) is hosted at the National Computational Infrastructure (NCI). Development and support the SkyMapper node of the ASVO has been funded in part by Astronomy Australia Limited (AAL) and the Australian Government through the Commonwealth's Education Investment Fund (EIF) and National Collaborative Research Infrastructure Strategy (NCRIS), particularly the National eResearch Collaboration Tools and Resources (NeCTAR) and the Australian National Data Service Projects (ANDS). The Pan-STARRS1 Surveys (PS1) and the PS1 public science archive have been made possible through contributions by the Institute for Astronomy, the University of Hawaii, the Pan-STARRS Project Office, the Max-Planck Society and its participating institutes, the Max Planck Institute for Astronomy, Heidelberg and the Max Planck Institute for Extraterrestrial Physics, Garching, The Johns Hopkins University, Durham University, the University of Edinburgh, the Queen's University Belfast, the Harvard-Smithsonian Center for Astrophysics, the Las Cumbres Observatory Global Telescope Network Incorporated, the National Central University of Taiwan, the Space Telescope Science Institute, the National Aeronautics and Space Administration under Grant No. NNX08AR22G issued through the Planetary Science Division of the NASA Science Mission Directorate, the National Science Foundation Grant No. AST-1238877, the University of Maryland, Eotvos Lorand University (ELTE), the Los Alamos National Laboratory, and the Gordon and Betty Moore Foundation. Based on data from the IUE satellite obtained under program IDs: FC027, BSJLG and MHD02. I thank John E. Davis for the development of the slx-fig module used to prepare some of the figures in this thesis. This research has made use of ISIS functions (ISISscripts) provided by ECAP/Remeis observatory and MIT (http://www.sternwarte.uni-erlangen.de/isis/). This research has made use of NASA's Astrophysics Data System, the VizieR catalogue access tool, CDS, Strasbourg, France. Some parts of the acknowledgments were compiled using the Astronomy Acknowledgment Generator. Some of the data presented in this thesis were obtained from the Mikulski Archive for Space Telescopes (MAST). STScI is operated by the Association of Universities for Research in Astronomy, Inc., under NASA contract NAS5-26555. Support for MAST for non-HST data is provided by the NASA Office of Space Science via grant NNX13AC07G and by other grants and contracts. This research has made use of the SIMBAD database, operated at CDS, Strasbourg, France, SciPy (jon 2001), NumPy (Van Der Walt et al. 2011), matplotlib, a Python library for publication quality graphics (Hunter 2007), Scikit-learn (McKinney 2010) (Pandas), Astropy (http://www.astropy.org) a community-developed core Python package for Astronomy (Astropy Collaboration et al. 2013; Price-Whelan et al. 2018).

2 The real acknowledgments

First things first I want to thank my supervisor Uli Heber for the unique opportunity to also write my master's thesis at the Remeis-Observatory and providing me with this interesting topic. Also I want to thank him for the useful discussions going into this research, as well as for always having an open door to ask questions. Of course also thank you for answering all those questions, even the really really stupid ones and for always being patient with me. I am also thankful for all the opportunities that arose while working on this topic and at the observatory.
Also I want to thank Martin Altmann for providing the spectra, answering my questions, the interesting information on Gaia and involving me in his project.
A big thank you to Andreas Irrgang for explaining his ISIS-scripts to me and for constantly improving them. Thanks for answering all my questions and always finding time to help me and teach me further things about spectral analysis.
I also want to thank Roberto Raddi and Thomas Kupfer (also for the football conversations Who Dey!) for providing the Feige 6 spectra and David Schneider for the PHL spectra.
Also I have to mention Ingo Kreykenbohm, Philipp Weber, Simon Kreuzer and the other admins for keeping the Remeis cluster and the machines running. Thank you to Philipp and Simon for helping me out with SLURM-stuff big time and making sure I was able to finish my calculations on time.
I am also thankful to David, Simon and Matti Dorsch for helping me with all kinds of computer stuff and questions concerning analysis-programs. I also thank Roberto and David for useful astrophysical discussions.
Furthermore, I want to mention how thankful I am to have had the opportunity to present a part of my results at the sdOB9 meeting in Hendaye. I had a great week there, learning about astrophysics within a vacation-like environment and getting to know a lot of new people. It was a fun week with David, Matti, Alex, Tiara, Thomas, Fluffy, Conor, Marilyn, Barbara and the kids and the rest of the participants. Also, I had the opportunity to chair a session at the conference, even though that kind of took me by surprise. Thank you to the FRANCI committee for the opportunity to present my results there as well and for organizing the FRANCI-ball tournament, which of course we won. Thank you to Marilyn and the MUSE team in Göttingen for having me there, I learned a lot during that week.
I want to thank my fellow open day OC-members Dominic Bernreuther, Melanie Lang and Eva von Gemünden for organizing the open day together. It was really stressful, but working with you guys made things much better.
I am also thankful for being part of the social media (SM) team. Thank you to my SM-buddy Dominic for working together on all kinds of ideas, including the silly ones. I want to thank the SM-newbie Andrea Gokus "Gokus Fidibus" for joining the SM-team later on, it was always so much fun coming up with new ideas with you guys.
Furthermore, I want to thank the whole observatory team and the institute board, Manami, Jörn and Uli, for the great working atmosphere! Thank you to every single one of you for organizing stuff and making this place so special! Thank you to the people taking

care of the coffee machine, I was really happy when I passed the 1000 coffee milestone! Thank you to Edith Day for keeping the organizational stuff running and reminding me to hand in my time-sheets for my HIWI, something I am also really thankful for as well! At this point I want to apologize for laughing extremely loud and sometimes annoying people. Thank you to every single Remeis-member for enduring my shenanigans. Thank you for the cake, an essential part of the Remeis-life, and interesting conversation.
I had the rare opportunity to join the best office in the history of offices, maybe ever, the Drechsel room (see Fig. 1)! Big thank you to all my office mates David, Jonathan Knies, Roberto, Lars Möller and Katrin Reisdorf for always making the time at the observatory so much fun, even during the "jetzt komm ich hier hoch jetzt guck dir die ... an"-moments! Thanks to you guys, this is the best office ever, we have a meme-wall and its going to be huge! Aber wen juckts halt! Thank you not just for all the fun (ich mag euren Humor!) but also the emotional support. Möge all dies bewahrt werden und das großartige Drechsel-Zimmer niemals untergehen!
Thank you for the motivating and uplifting serious conversations to David, Philipp, Dominic, Eva, Melanie, Katrin, Sara Saeedi and Katya Sokolova-Lapa. Also I always had great lunch-times with the crew! Shoutout to the Cafe Esspress at this point! Thank you to Roberto for teaching me many life-lessons and about Italian culture and to Sara for making the observatory even more fun than it already is!
Now this turned out to me far more than I thought, but I still have to mentioned a few more personal things. Many parts of the analysis and the writing, especially the final weeks, have felt like needing a TD but getting the ball on the own 10, with two minutes left and no timeouts. However, many different things and people helped me, probably more than many would know! I had great observing nights at the observatory as well which all resulted in very nice memories and/or pictures. Thank you to Tamara Eisenblätter for the awesome moon pictures, for my dog Sirius and, also to Tammy Hämmerich, for the interesting observational runs. Thank you to all my friends who showed up at the observatory. At this point I also want to highlight my fellow students Sebastian Spiegel, Leon Schiller and Katrin, as we spent a lot of time in lectures and during coffee together. My studies would not have been the same without you guys! I want to thank my friends for their support and help, in no particular order: Dominik Stahl, Tamara, Max and Marcel Bergemann, Yonatan Tzuriel, Jonah Cerrotta, Chiara Keuth, Andreas and Anja Trötscher, Elizabeth Friedrich, and everyone else I forgot to mention! I especially want to thank my family, my mom, Tammy and Jesse for their support and help and for dealing with me throughout my studies, I could not have done it without you! Thank you to "Papa" Domi for organizing the last fun day before submitting this thesis with my sisters Delia and Mary and for inviting "Oma" Anja and "Opa" Andreas as well. I am very thankful for all the comments, tips and spell-checking concerning this thesis by Ela Sigurani, Natalie Morbitzer, Tamara, Katrin and Eva. Sorry for making you guys read this much! General thank you and apologies to everyone who had to deal with me during the final days of the writing process! Finally, I also have to thank the team at the Starbucks at the Hauptmarkt in Nürnberg for the excellent coffee, without which I would not have survived! Also thank you to whoever invented coffee!!!

Sorry to everyone I forgot, but I somehow have to end the credits at some point. Like in the marvel movies if you made it this far you are probably just waiting for the post-credit goodie, so here we go:

Figure 1: The Drechsel room in a nutshell (Knies 2020)

”Last but not least, I want to thank me for believing in me. I want to thank me for doing all this hard work, I want to thank me for having no days off, I want to thank me for never quitting, I want to thank me for always being a giver and trying to give more than I receive. I want to thank me for trying to do more rights than wrong, I want to thank me for just being me at all times.” (Snoop Dogg 2018)
”That was!”

Appendices

Appendix A1

Observational data

A1.1 Gaia

Table 1: Gaia source Ids, correlation functions and RUWE (RUWE taken from http://gaia.ari.uni-heidelberg.de/index.html)

star	source Id	ϖ-μ_α-corr.	ϖ-μ_δ-corr.	μ_α-μ_δ-corr.	RUWE
CD-38 8806	6114877567905306496	-0.004256	0.142720	-0.370346	1.27
CD-48 14233	6517692040812640128	-0.342458	-0.424362	0.025000	1.14
HD 8269	2455119103008073600	-0.104335	0.010560	0.447591	1.14
HD 12655	5138157513229675776	0.072215	0.011799	0.077799	0.76
HD 23342	5080408585559380608	0.133620	0.026329	-0.450017	1.21
HD 110942	6133549684824797440	0.000627	-0.155049	-0.047095	1.18
HD 156758	4390411334860750080	-0.207446	-0.012392	0.123546	1.28
HD 209292	6823752612916615296	-0.179667	-0.401340	0.046763	1.35
TYC 1914-687-1	868447614227967744	0.302950	0.035667	-0.275182	1.18
TYC 6036-1933-1	5679291850286256640	0.140887	-0.307808	-0.006969	1.27
Feige 86	1455929729357283840	-0.243452	0.194182	-0.116888	1.20
PHL 25	6834927185812261632	-0.563386	-0.493390	0.221242	1.24
PHL 382	2597188787138939520	0.121027	-0.003545	0.461110	1.16
Feige 6	2522306719528527488	0.381534	0.022878	0.370330	1.11

A1.2 Photometric data

Table 2: Photometric data used for CD-38 8806

system	passband	value [mag]	type
Tycho	Bt	10.59 ± 0.04	magnitude
Tycho	Vt	10.63 ± 0.05	magnitude
Gaia	G	10.6084 ± 0.0006	magnitude
Gaia	GRP	10.6128 ± 0.0017	magnitude
Gaia	GBP	10.6111 ± 0.0021	magnitude
2MASS	J	10.627 ± 0.025	magnitude
2MASS	H	10.667 ± 0.023	magnitude
2MASS	K	10.611 ± 0.022	magnitude
WISE	W1	10.621 ± 0.024	magnitude
WISE	W2	10.64 ± 0.02	magnitude
SDSS	r	10.743 ± 0.013	magnitude
SDSS	i	10.969 ± 0.029	magnitude
Johnson	B	10.589 ± 0.025	magnitude
Johnson	V	10.605 ± 0.026	magnitude
SkyMapper	u	11.510 ± 0.004	magnitude
SkyMapper	v	10.750 ± 0.004	magnitude
SkyMapper	g	10.533 ± 0.005	magnitude
SkyMapper	r	10.685 ± 0.005	magnitude
SkyMapper	i	10.999 ± 0.004	magnitude
SkyMapper	z	11.128 ± 0.004	magnitude

Table 3: Photometric data used for CD-48 14233

system	passband	value [mag]	type
Tycho	Bt	10.92 ± 0.05	magnitude
Gaia	G	10.9836 ± 0.0006	magnitude
Gaia	GRP	10.976 ± 0.001	magnitude
Gaia	GBP	10.974 ± 0.004	magnitude
WISE	W1	10.935 ± 0.024	magnitude
WISE	W2	10.963 ± 0.022	magnitude
2MASS	H	10.933 ± 0.022	magnitude
2MASS	K	10.936 ± 0.022	magnitude
SDSS	g	10.853 ± 0.029	magnitude
SDSS	i	11.33 ± 0.04	magnitude
Johnson	B	10.92 ± 0.04	magnitude
Johnson	V	10.961 ± 0.026	magnitude
SkyMapper	u	12.119 ± 0.012	magnitude
SkyMapper	v	11.208 ± 0.014	magnitude
SkyMapper	g	10.903 ± 0.009	magnitude
SkyMapper	r	11.080 ± 0.007	magnitude
SkyMapper	i	11.366 ± 0.007	magnitude
SkyMapper	z	11.488 ± 0.004	magnitude

Table 4: Photometric data used for HD 8269

system	passband	value [mag]	type
Tycho	Bt	10.338 ± 0.029	magnitude
Tycho	Vt	10.35 ± 0.04	magnitude
Gaia	G	10.3357 ± 0.0005	magnitude
Gaia	GRP	10.3343 ± 0.0007	magnitude
Gaia	GBP	10.3314 ± 0.0007	magnitude
WISE	W1	10.255 ± 0.024	magnitude
WISE	W2	10.330 ± 0.021	magnitude
2MASS	J	10.299 ± 0.024	magnitude
2MASS	H	10.324 ± 0.028	magnitude
2MASS	K	10.290 ± 0.024	magnitude
SDSS	g	10.25 ± 0.05	magnitude
SDSS	r	10.5 ± 0.1	magnitude
PS1	g	10.320 ± 0.017	magnitude
VST	g	10.27120 ± 0.00021	magnitude
Stroemgren	bmy	-0.011	color
Stroemgren	m1	0.125	color
Stroemgren	c1	1.12	color
SkyMapper	u	11.560 ± 0.004	magnitude
SkyMapper	v	10.693 ± 0.011	magnitude
SkyMapper	r	10.445 ± 0.018	magnitude
SkyMapper	z	10.848 ± 0.004	magnitude

Table 5: Photometric data used for HD 12655

system	passband	value [mag]	type
Tycho	Bt	9.019 ± 0.018	magnitude
Tycho	Vt	8.978 ± 0.017	magnitude
Hipparcos	Hp	9.0063 ± 0.0016	magnitude
Gaia	G	8.9758 ± 0.0005	magnitude
Gaia	GRP	8.9479 ± 0.0018	magnitude
Gaia	GBP	8.9970 ± 0.0015	magnitude
Johnson	BmV	0.0	color
Johnson	UmB	0.01	color
2MASS	J	8.88 ± 0.02	magnitude
2MASS	H	8.927 ± 0.025	magnitude
2MASS	K	8.859 ± 0.022	magnitude
WISE	W1	8.846 ± 0.024	magnitude
WISE	W2	8.866 ± 0.021	magnitude
VST	i	9.38580 ± 0.00021	magnitude
SkyMapper	u	10.193 ± 0.014	magnitude
SkyMapper	v	9.238 ± 0.011	magnitude
SkyMapper	i	9.427 ± 0.024	magnitude
SkyMapper	z	9.48 ± 0.04	magnitude

Table 6: Photometric data used for HD 23342

system	passband	value [mag]	type
Tycho	Bt	10.156 ± 0.021	magnitude
Tycho	Vt	10.144 ± 0.023	magnitude
Gaia	G	10.1497 ± 0.0005	magnitude
Gaia	GRP	10.1194 ± 0.0007	magnitude
Gaia	GBP	10.1685 ± 0.0007	magnitude
WISE	W1	10.003 ± 0.024	magnitude
WISE	W2	10.030 ± 0.021	magnitude
2MASS	J	10.070 ± 0.025	magnitude
2MASS	H	10.047 ± 0.023	magnitude
2MASS	K	10.016 ± 0.022	magnitude
SDSS	r	10.27 ± 0.04	magnitude
Johnson	B	10.168 ± 0.027	magnitude
Johnson	V	10.162 ± 0.021	magnitude
PS1	z	10.514 ± 0.007	magnitude
VST	u	11.0028 ± 0.0005	magnitude
VST	i	10.41260 ± 0.00021	magnitude
SkyMapper	u	11.382 ± 0.006	magnitude
SkyMapper	v	10.394 ± 0.015	magnitude
SkyMapper	g	10.068 ± 0.009	magnitude
SkyMapper	r	10.260 ± 0.004	magnitude

Table 7: Photometric data used for HD 156758

system	passband	value [mag]	type
Tycho	Bt	10.51 ± 0.04	magnitude
Tycho	Vt	10.37 ± 0.04	magnitude
Gaia	G	10.2914 ± 0.0006	magnitude
Gaia	GRP	10.1097 ± 0.0011	magnitude
Gaia	GBP	10.3982 ± 0.0007	magnitude
WISE	W1	9.755 ± 0.025	magnitude
WISE	W2	9.780 ± 0.021	magnitude
2MASS	J	9.848 ± 0.023	magnitude
2MASS	H	9.812 ± 0.028	magnitude
2MASS	K	9.857 ± 0.025	magnitude
SDSS	r	10.36 ± 0.04	magnitude
Johnson	B	10.491 ± 0.019	magnitude
Johnson	V	10.319 ± 0.029	magnitude

Table 8: Photometric data used for HD 209292

system	passband	value [mag]	type
Gaia	G	10.8809 ± 0.0007	magnitude
Gaia	GRP	10.9199 ± 0.0016	magnitude
Gaia	GBP	10.8636 ± 0.0023	magnitude
WISE	W1	10.976 ± 0.023	magnitude
WISE	W2	11.015 ± 0.021	magnitude
2MASS	J	10.947 ± 0.025	magnitude
2MASS	H	10.955 ± 0.022	magnitude
2MASS	K	10.97 ± 0.02	magnitude
SDSS	g	10.755 ± 0.028	magnitude
SDSS	r	11.02 ± 0.06	magnitude
SDSS	i	11.23 ± 0.06	magnitude
Johnson	B	10.83 ± 0.06	magnitude
Johnson	V	10.86 ± 0.04	magnitude
SkyMapper	u	11.704 ± 0.005	magnitude
SkyMapper	v	10.991 ± 0.004	magnitude
SkyMapper	g	10.799 ± 0.006	magnitude
SkyMapper	r	11.003 ± 0.004	magnitude
SkyMapper	i	11.287 ± 0.004	magnitude
SkyMapper	z	11.424 ± 0.004	magnitude

Table 9: Photometric data used for TYC 1914-687-1

system	passband	value [mag]	type
Tycho	Vt	10.75 ± 0.08	magnitude
Gaia	G	10.6655 ± 0.0005	magnitude
Gaia	GRP	10.5879 ± 0.0015	magnitude
Gaia	GBP	10.7089 ± 0.0013	magnitude
WISE	W1	10.380 ± 0.024	magnitude
WISE	W2	10.400 ± 0.022	magnitude
2MASS	J	10.445 ± 0.023	magnitude
2MASS	H	10.417 ± 0.023	magnitude
2MASS	K	10.416 ± 0.021	magnitude
SDSS	r	10.769 ± 0.028	magnitude
SDSS	i	10.87 ± 0.02	magnitude
Johnson	V	10.654 ± 0.019	magnitude
SDSS	u	11.833 ± 0.016	magnitude

Table 10: Photometric data used for TYC 6036-1933-1

system	passband	value [mag]	type
Tycho	Bt	10.86 ± 0.04	magnitude
Tycho	Vt	10.79 ± 0.06	magnitude
Gaia	G	10.6972 ± 0.0005	magnitude
Gaia	GRP	10.582 ± 0.001	magnitude
Gaia	GBP	10.763 ± 0.001	magnitude
WISE	W1	10.280 ± 0.024	magnitude
WISE	W2	10.297 ± 0.022	magnitude
2MASS	J	10.420 ± 0.027	magnitude
2MASS	H	10.373 ± 0.025	magnitude
2MASS	K	10.316 ± 0.024	magnitude
SDSS	g	10.679 ± 0.022	magnitude
Johnson	B	10.83 ± 0.05	magnitude
Johnson	V	10.72 ± 0.04	magnitude
SkyMapper	u	12.080 ± 0.024	magnitude
SkyMapper	v	11.071 ± 0.016	magnitude
SkyMapper	g	10.672 ± 0.009	magnitude
SkyMapper	r	10.7770 ± 0.0021	magnitude
SkyMapper	i	10.967 ± 0.004	magnitude

Table 11: Photometric data used for HD 110942

system	passband	value [mag]	type
Tycho	Bt	10.35 ± 0.04	magnitude
Gaia	G	10.5026 ± 0.0007	magnitude
Gaia	GRP	10.6229 ± 0.0011	magnitude
Gaia	GBP	10.4341 ± 0.0021	magnitude
WISE	W1	10.875 ± 0.024	magnitude
WISE	W2	10.931 ± 0.021	magnitude
2MASS	J	10.783 ± 0.029	magnitude
2MASS	H	10.87 ± 0.03	magnitude
2MASS	K	10.92 ± 0.03	magnitude
SDSS	r	10.64 ± 0.05	magnitude
Johnson	V	10.50 ± 0.06	magnitude
SkyMapper	u	10.526 ± 0.004	magnitude
SkyMapper	v	10.376 ± 0.005	magnitude
SkyMapper	g	10.396 ± 0.011	magnitude
SkyMapper	r	10.646 ± 0.012	magnitude
SkyMapper	i	10.986 ± 0.011	magnitude
SkyMapper	z	11.214 ± 0.007	magnitude

Table 12: Photometric data used for Feige 86

system	passband	value [mag]	type
Tycho	Bt	9.868 ± 0.023	magnitude
Tycho	Vt	9.998 ± 0.027	magnitude
Hipparcos	Hp	10.021 ± 0.002	magnitude
Gaia	G	10.0290 ± 0.0007	magnitude
Gaia	GRP	10.1652 ± 0.0012	magnitude
Gaia	GBP	9.9554 ± 0.0016	magnitude
Johnson	V	10.059 ± 0.021	magnitude
Johnson	BmV	-0.143 ± 0.014	color
Johnson	UmB	-0.646 ± 0.021	color
Stroemgren	y	10.07 ± 0.01	magnitude
Stroemgren	bmy	-0.060 ± 0.007	color
Stroemgren	m1	0.10 ± 0.01	color
Stroemgren	c1	0.315 ± 0.016	color
Stroemgren	Hbeta-B	2.700 ± 0.006	color
WISE	W1	10.517 ± 0.024	magnitude
WISE	W2	10.561 ± 0.021	magnitude
2MASS	J	10.341 ± 0.023	magnitude
2MASS	H	10.42 ± 0.04	magnitude
2MASS	K	10.501 ± 0.023	magnitude
SDSS	r	10.20 ± 0.05	magnitude
SDSS	i	10.457 ± 0.013	magnitude
box	2000-2500	8.468	magnitude
box	2500-3000	8.645	magnitude
box	1300-1800	8.162	magnitude

Table 13: Photometric data used for PHL 25

system	passband	value [mag]	type
Gaia	G	12.1618 ± 0.0008	magnitude
Gaia	GRP	12.2929 ± 0.0018	magnitude
Gaia	GBP	12.041 ± 0.007	magnitude
WISE	W1	12.645 ± 0.024	magnitude
WISE	W2	12.726 ± 0.028	magnitude
2MASS	H	12.572 ± 0.025	magnitude
2MASS	K	12.62 ± 0.03	magnitude
SDSS	g	11.994 ± 0.011	magnitude
SDSS	r	12.375 ± 0.027	magnitude
SDSS	i	12.65 ± 0.04	magnitude
Johnson	B	12.044 ± 0.012	magnitude
Johnson	V	12.166 ± 0.013	magnitude
PS1	y	12.9762 ± 0.0019	magnitude
VST	g	11.9417 ± 0.0004	magnitude
SkyMapper	v	11.984 ± 0.006	magnitude
SkyMapper	g	12.033 ± 0.006	magnitude
SkyMapper	r	12.3170 ± 0.0021	magnitude
SkyMapper	i	12.658 ± 0.007	magnitude
SkyMapper	z	12.900 ± 0.006	magnitude
VISTA	K	12.5969 ± 0.0021	magnitude

Table 14: Photometric data used for PHL 382

system	passband	value [mag]	type
Gaia	G	11.3146 ± 0.0011	magnitude
Gaia	GRP	11.4633 ± 0.0014	magnitude
Gaia	GBP	11.199 ± 0.011	magnitude
2MASS	J	11.644 ± 0.023	magnitude
SDSS	g	11.151 ± 0.027	magnitude
SDSS	r	11.53 ± 0.07	magnitude
SDSS	i	11.82 ± 0.05	magnitude
Johnson	B	11.19 ± 0.04	magnitude
Johnson	V	11.31 ± 0.04	magnitude
PS1	y	12.1374 ± 0.0011	magnitude
SkyMapper	u	11.29 ± 0.01	magnitude
SkyMapper	v	11.101 ± 0.007	magnitude
SkyMapper	g	11.1940 ± 0.0021	magnitude
SkyMapper	r	11.480 ± 0.004	magnitude
SkyMapper	i	11.8330 ± 0.0021	magnitude
SkyMapper	z	12.080 ± 0.004	magnitude

Table 15: Photometric data used for Feige 6

system	passband	value [mag]	type
Gaia	G	13.9431 ± 0.0004	magnitude
Gaia	GRP	14.0325 ± 0.0013	magnitude
Gaia	GBP	13.8440 ± 0.0028	magnitude
2MASS	J	14.20 ± 0.04	magnitude
2MASS	H	14.23 ± 0.04	magnitude
SDSS	r	14.082 ± 0.017	magnitude
SDSS	i	14.38 ± 0.04	magnitude
Johnson	B	13.88 ± 0.04	magnitude
Johnson	V	13.942 ± 0.023	magnitude
PS1	y	14.661 ± 0.004	magnitude
PS1	g	13.834 ± 0.009	magnitude
PS1	r	14.1092 ± 0.0027	magnitude
PS1	i	14.3798 ± 0.0025	magnitude
PS1	z	14.5730 ± 0.0021	magnitude
SkyMapper	u	14.237 ± 0.004	magnitude
SkyMapper	v	13.9080 ± 0.0021	magnitude
SkyMapper	g	13.840 ± 0.004	magnitude
SkyMapper	r	14.077 ± 0.004	magnitude
SkyMapper	i	14.399 ± 0.005	magnitude
SkyMapper	z	14.628 ± 0.005	magnitude

Appendix A2

Investigation of the impact of the wobbles using mock spectra

Since it was not possible to get rid of the wobbles (see Sec.2.2.2) in the spectra through modifying the data-reduction, the spectra have to be analyzed with the wobbles, which added another systematic uncertainty. Therefore, the influence of the wobbles on the derived parameters has to be explored as well. For this purpose ADS was used to produce model spectra with fixed parameters and abundances. Artificial noise at levels representing the actual observations (SNR of 100 and 200, respectively) was added to these model spectra as well. These artificial mock observations can be fitted using the same routine as for the actual observations, hence the influence of the actual fit procedure on the parameters can be explored. The deviations between the input and the derived parameters were very low and completely within the uncertainties.
Additionally wobbles can be added artificially to the mock observations by adding a sinusoidal term to the flux. Tests are performed for wobbles with amplitudes as large as 1% and 3% of the continuum flux, which corresponds to the amplitudes of the observed wobbles. In the observations the period of the wobbles seems to increase with wavelength. This is also modeled and spectra with wobbles having fixed periods, which are observed in the blue spectra, and varying periods over the entire spectrum are produced. The period is modeled as a linear function solely depending on the wavelength. The period of the wobbles is estimated by inspection by eye for six different wavelength-regions and a linear fit is performed. Wobbles with varying period are then introduced to the artificial observations through using this linear relation in the sinusoidal term.
Mock observations are produced for different parameter combinations and fits are performed in the same way as for the actual observations. For two parameter-combinations the deviations between the derived and the input abundances for the different wobble configurations are shown in Figs. 2 and 3. The resulting atmospheric parameters are listed as well.
Overall the model and derived abundances agree with each other within the typically derived uncertainties of the abundances. The effect of the wobbles on the atmospheric parameters is even lower, as deviations are lower than adopted systematic errors. Although some abundances can deviate by two orders of magnitude, this is exclusively the case for very low input abundances, which, therefore is a noise effect, that is noise spikes being interpreted as lines.
Also the continuum correction is able to get rid of the wobbles later on in the fitting

procedure. Based on the results and the later on performed continuum correction, it can be concluded that the influence of the wobbles on the derived parameters is very low and well within derived uncertainties. Therefore, the analysis can and is performed with the wobbles.
The results of the mock-spectra without wobbles show that the errors introduced through the actual fitting routine are negligible.

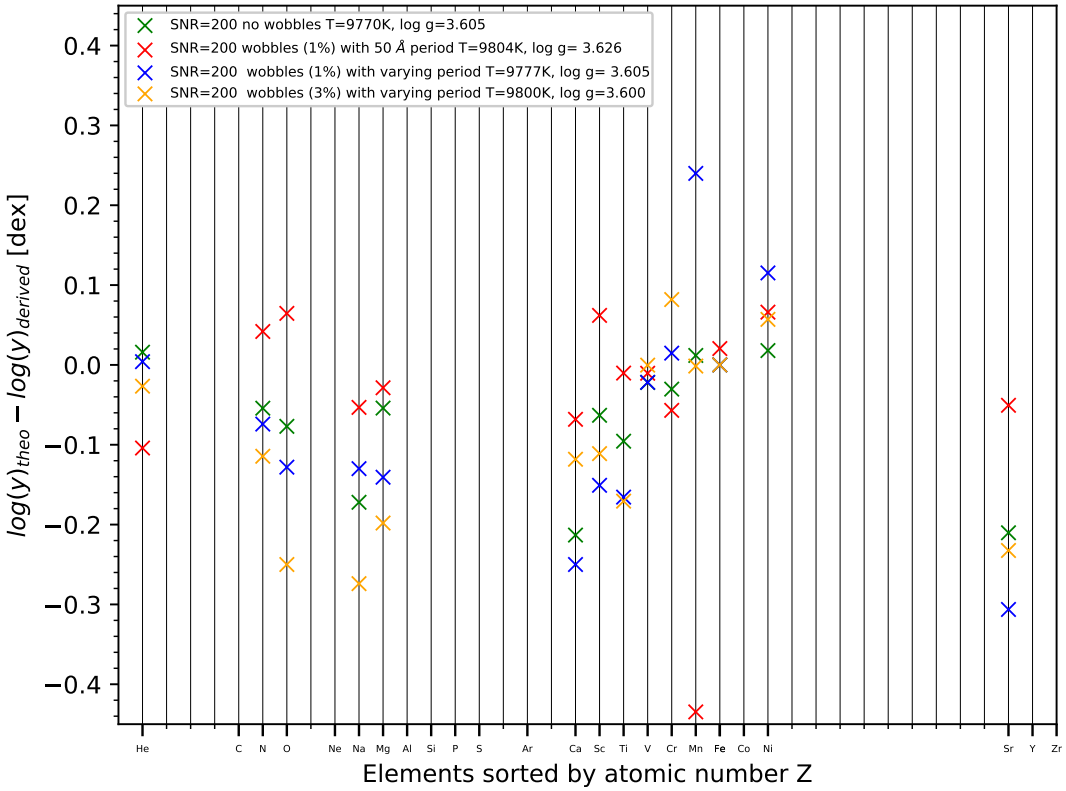

Figure 2: Differences between the input and derived atmospheric parameters and abundances for an initial atmospheric configuration of T_{eff} = 9,750 K and log(g)= 3.6

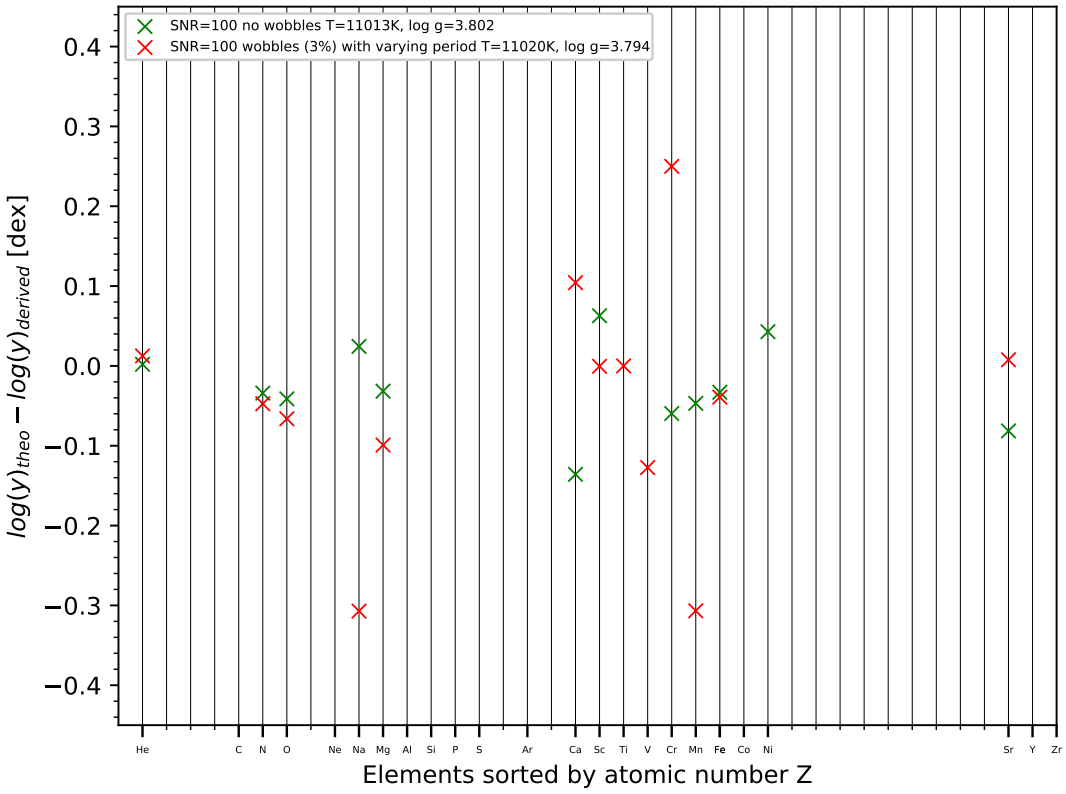

Figure 3: Differences between the input and derived atmospheric parameters and abundances for an initial atmospheric configuration of T_{eff} = 11,000 K and log(g)= 3.8

Appendix A3

Spectroscopic results

Table 16: Atmospheric parameters

	T_{eff}	log(g)	He	^{3}He	^{4}He
star	[K]	[cgs]	[dex]	[dex]	[dex]
TYC 6036-1933-1	8642 ± 90	3.33 ± 0.05	$-1.6^{+0.6}_{-1.2}$	-	-
HD 12655	9613 ± 100	3.53 ± 0.05	$-1.1^{+0.10}_{-0.60}$	-	-
HD 23342	9107 ± 100	3.43 ± 0.05	$-1.256^{+0.008}_{-0.500}$	-	-
HD 209292	11079 ± 120	3.77 ± 0.05	$-1.01^{+0.15}_{-0.22}$	-	-
HD 156758	9349 ± 100	3.45 ± 0.05	$-1.15^{+0.16}_{-0.60}$	-	-
CD-38 8806	10560 ± 110	3.68 ± 0.05	$-1.04^{+0.19}_{-0.21}$	-	-
Feige 86	15393 ± 160	4.43 ± 0.05	$-2.24^{+0.07}_{-0.06}$	$-2.998^{+0.060}_{-0.009}$	-2.33 ± 0.08
CD-48 14233	9583 ± 100	3.55 ± 0.05	$-1.33^{+0.09}_{-0.50}$	-	-
TYC 1914-687-1	8679 ± 90	3.34 ± 0.05	$-2.3^{+1.2}_{-0.5}$	-	-
PHL 25	17585 ± 200	4.57 ± 0.05	$-2.194^{+0.008}_{-0.050}$	$-2.52^{+0.05}_{-0.06}$	$-2.48^{+0.04}_{-0.06}$
HD 110942	17046 ± 180	4.74 ± 0.05	$-2.11^{+0.05}_{-0.04}$	$-3.000^{+0.022}_{-0.040}$	-2.17 ± 0.05
PHL 382	17903 ± 190	4.08 ± 0.05	-2.368 ± 0.022	$-2.439^{+0.022}_{-0.023}$	$-3.19^{+0.07}_{-0.06}$
HD 8269	9695 ± 100	3.53 ± 0.05	$-1.11^{+0.29}_{-0.14}$	-	-
Feige 6	14544 ± 150	4.16 ± 0.05	-2.43 ± 0.06	-3.00 ± 0.08	$-2.57^{+0.06}_{-0.05}$

Table 17: Dynamical parameter

star	ζ $\left[\frac{\text{km}}{\text{s}}\right]$	ξ $\left[\frac{\text{km}}{\text{s}}\right]$	v·sin(i) $\left[\frac{\text{km}}{\text{s}}\right]$	v_{rad} $\left[\frac{\text{km}}{\text{s}}\right]$
TYC 6036-1933-1	$6.47^{+0.020}_{-0.900}$	$1.4^{+0.40}_{-0.5}$	$12.34^{+0.19}_{-0.4}$	$264.27^{+0.07}_{-0.05}$
HD 12655	$0.5^{+0.5}_{-0.6}$	$1.20^{+0.15}_{-0.60}$	6.35 ± 0.08	$190.498^{+0.025}_{-0.040}$
HD 23342	$10.91^{+0.16}_{-0.21}$	$2.00^{+0.07}_{-1.10}$	$10.81^{+0.18}_{-0.15}$	293.25 ± 0.07
HD 209292	$9.593^{+0.024}_{-0.900}$	$2.00^{+0.11}_{-2.00}$	$13.255^{+0.600}_{-0.004}$	-6.85 ± 0.06
HD 156758	$6.37^{+0.05}_{-0.06}$	$2.24^{+0.06}_{-1.10}$	$15.91^{+0.19}_{-0.10}$	$-172.02^{+0.08}_{-0.05}$
CD-38 8806	$7.54^{+0.10}_{-0.05}$	$1.1^{+0.9}_{-1.1}$	$7.70^{+0.29}_{-0.06}$	$225.17^{+0.12}_{-0.10}$
Feige 86	$0.003^{+0.400}_{-0.004}$	$0.000^{+0.004}_{-0.000}$	$1.89^{+0.04}_{-0.06}$	-28.53 ± 0.06
CD-48 14233	$4.77^{+0.40}_{-0.17}$	$1.70^{+0.25}_{-0.80}$	$16.15645^{+0.40000}_{-0.00014}$	$-52.986^{+0.040}_{-0.024}$
TYC 1914-687-1	$0.756^{+0.005}_{-0.007}$	1.1 ± 0.6	$26.23388^{+0.14000}_{-0.00004}$	$-67.48^{+0.08}_{-0.06}$
PHL 25	8.3 ± 0.5	$0.0^{+0.5}_{-0.0}$	$0.0^{+2.7}_{-0.0}$	71.2 ± 1.3
HD 110942	$2.4^{+0.4}_{-0.6}$	$0.8^{+1.2}_{-0.9}$	$2.9^{+0.7}_{-0.8}$	$-20.09^{+0.06}_{-0.08}$
PHL 382	$5.4^{+1.3}_{-0.6}$	$0.4^{+1.3}_{-0.5}$	$12.75^{+0.11}_{-0.25}$	-11.0 ± 2.2
HD 8269	$6.17^{+0.09}_{-0.60}$	$1.92^{+0.09}_{-1.20}$	$3.0^{+1.5}_{-0.2}$	$44.118^{+0.026}_{-0.030}$
Feige 6	$0.004^{+0.900}_{-0.005}$	$0.2^{+0.6}_{-0.2}$	$2.45^{+0.16}_{-0.27}$	-124.269 ± 0.024

Table 18: Derived abundances given as logarithmic particle-number fraction (1)

	C	N	O	Ne
star	[dex]	[dex]	[dex]	[dex]
TYC 6036-1933-1	-	$-5.26^{+0.06}_{-0.11}$	$-4.326^{+0.024}_{-0.040}$	-
HD 12655	-	$-5.09^{+0.04}_{-0.05}$	$-4.045^{+0.040}_{-0.018}$	-
HD 23342	-	$-5.239^{+0.025}_{-0.020}$	$-4.389^{+0.070}_{-0.029}$	-
HD 209292	-	$-4.75^{+0.06}_{-0.08}$	$-4.08^{+0.11}_{-0.04}$	-
HD 156758	-	$-5.053^{+0.027}_{-0.040}$	$-4.210^{+0.080}_{-0.026}$	-
CD-38 8806	-	-4.84 ± 0.06	$-3.92^{+0.08}_{-0.06}$	-
Feige 86	$-5.517^{+0.026}_{-0.060}$	-	-4.88 ± 0.03	$-4.675^{+0.020}_{-0.017}$
CD-48 14233	-	$-5.155^{+0.022}_{-0.040}$	$-4.20^{+0.05}_{-0.04}$	-
TYC 1914-687-1	-	$-5.04^{+0.07}_{-0.10}$	$-4.352^{+0.026}_{-0.050}$	-
PHL 25	-5.4 ± 0.1	-	-	-
HD 110942	-4.72 ± 0.04	$-4.023^{+0.025}_{-0.050}$	$-4.82^{+0.05}_{-0.04}$	-4.411 ± 0.012
PHL 382	$-4.18^{+0.05}_{-0.06}$	-3.86 ± 0.06	$-4.25^{+0.06}_{-0.07}$	$-4.98^{+0.05}_{-0.06}$
HD8269	-	-5.02 ± 0.04	$-3.80^{+0.06}_{-0.05}$	-
Feige 6	-	-	$-5.500^{+0.013}_{-0.000}$	$-5.68^{+0.12}_{-0.15}$

Table 19: Derived abundances given as logarithmic particle-number fraction (2)

	Na	Mg	Al	Si
star	[dex]	[dex]	[dex]	[dex]
TYC 6036-1933-1	$-7.7500^{+0.0013}_{-0.0000}$	$-6.045^{+0.025}_{-0.040}$	-	$-6.119^{+0.014}_{-0.022}$
HD 12655	$-7.57^{+0.09}_{-0.07}$	$-5.851^{+0.025}_{-0.014}$	-	$-5.933^{+0.023}_{-0.009}$
HD 23342	-	$-6.15^{+0.07}_{-0.03}$	-	$-6.190^{+0.024}_{-0.016}$
HD 209292	-	$-5.83^{+0.14}_{-0.02}$	-	$-5.844^{+0.110}_{-0.018}$
HD 156758	$-7.741^{+0.070}_{-0.013}$	$-5.985^{+0.060}_{-0.026}$	-	$-6.059^{+0.027}_{-0.018}$
CD-38 8806	$-7.49^{+0.08}_{-0.13}$	$-5.61^{+0.05}_{-0.04}$	-	$-5.72^{+0.06}_{-0.05}$
Feige 86	-	$-5.319^{+0.024}_{-0.025}$	-	-4.98 ± 0.05
CD-48 14233	-	$-5.963^{+0.050}_{-0.027}$	-	$-5.956^{+0.024}_{-0.011}$
TYC 1914-687-1	-	$-6.012^{+0.024}_{-0.050}$	-	$-6.121^{+0.013}_{-0.027}$
PHL 25	-	-5.34 ± 0.04	-	-4.14 ± 0.04
HD 110942	-	-5.13 ± 0.06	-6.49 ± 0.04	$-4.60^{+0.10}_{-0.12}$
PHL 382	-	$-5.04^{+0.05}_{-0.08}$	$-6.22^{+0.04}_{-0.05}$	$-4.43^{+0.05}_{-0.10}$
HD 8269	$-7.44^{+0.09}_{-0.08}$	$-5.685^{+0.080}_{-0.029}$	-	$-5.818^{+0.050}_{-0.022}$
Feige 6	-	$-5.80^{+0.04}_{-0.05}$	-	$-5.16^{+0.05}_{-0.07}$

Table 20: Derived abundances given as logarithmic particle-number fraction (3)

	P	S	Ar	Ca
star	[dex]	[dex]	[dex]	[dex]
TYC 6036-1933-1	-	-	-	$-7.32^{+0.07}_{-0.06}$
HD 12655	-	-	-	$-7.25^{+0.05}_{-0.00}$
HD 23342	-	-	-	$-7.65^{+0.17}_{-0.09}$
HD 209292	-	-	-	$-7.8^{+0.4}_{-0.0}$
HD 156758	-	-	-	$-7.46^{+0.18}_{-0.10}$
CD-38 8806	-	-	-	$-7.8^{+0.5}_{-0.0}$
Feige 86	$-4.636^{+0.013}_{-0.011}$	-	-	$-5.53^{+0.05}_{-0.06}$
CD-48 14233	-	-	-	$-7.50^{+0.14}_{-0.00}$
TYC 1914-687-1	-	-	-	$-7.32^{+0.07}_{-0.06}$
PHL 25	-5.86 ± 0.05	$-6.64^{+0.19}_{-0.40}$	$-4.93^{+0.08}_{-0.10}$	$-6.19^{+0.22}_{-0.23}$
HD 110942	$-5.023^{+0.028}_{-0.040}$	$-5.051^{+0.018}_{-0.017}$	$-5.63^{+0.06}_{-0.05}$	$-5.41^{+0.15}_{-0.17}$
PHL 382	-	$-5.440^{+0.020}_{-0.021}$	$-4.746^{+0.015}_{-0.060}$	-
HD 8269	-	-	-	$-7.57^{+0.24}_{-0.13}$
Feige 6	$-5.51^{+0.05}_{-0.03}$	-	-	$-6.12^{+0.11}_{-0.22}$

Table 21: Derived abundances given as logarithmic particle-number fraction (4)

	Sc	Ti	V	Cr
star	[dex]	[dex]	[dex]	[dex]
TYC 6036-1933-1	-10.93 ± 0.07	$-8.500000^{+0.000014}_{-0.000000}$	-	$-8.0^{+0.0}_{-0.0}$
HD 12655	$-11.000^{+0.009}_{-0.000}$	$-8.500^{+0.029}_{-0.00}$	$-9.70^{+0.13}_{-0.09}$	$-8.10^{+0.07}_{-0.06}$
HD 23342	$-11.000^{+0.028}_{-0.000}$	$-8.80^{+0.09}_{-0.08}$	-	$-8.29^{+0.06}_{-0.08}$
HD 209292	-	$-9.16^{+0.09}_{-0.08}$	-	$-8.15^{+0.06}_{-0.07}$
HD 156758	$-11.00000^{+0.00006}_{-0.00000}$	$-8.65^{+0.09}_{-0.07}$	$-9.79^{+0.18}_{-0.21}$	$-8.15^{+0.06}_{-0.05}$
CD-38 8806	-	-8.77 ± 0.08	-	-7.81 ± 0.05
Feige 86	-	-6.71 ± 0.05	-	-
CD-48 14233	$-11.00^{+0.05}_{-0.00}$	$-8.76^{+0.07}_{-0.08}$	-	-7.96 ± 0.05
TYC 1914-687-1	$-10.97^{+0.10}_{-0.04}$	$-8.500^{+0.019}_{-0.000}$	-	$-8.000^{+0.019}_{-0.00}$
PHL 25	-	-	-	-
HD 110942	$-7.59^{+0.12}_{-0.11}$	-6.46 ± 0.05	-	-6.84 ± 0.12
PHL 382	-	$-6.56^{+0.10}_{-0.08}$	-	-
HD 8269	$-10.998^{+0.080}_{-0.004}$	$-8.61^{+0.09}_{-0.07}$	-	-7.82 ± 0.06
Feige 6	-	$-7.24^{+0.06}_{-0.10}$	-	-7.39 ± 0.13

Table 22: Derived abundances given as logarithmic particle-number fraction (5)

	Mn	Fe I	Fe	Ni
star	[dex]	[dex]	[dex]	[dex]
TYC 6036-1933-1	-	$-6.500^{+0.014}_{-0.000}$	$-6.460^{+0.070}_{-0.009}$	-
HD 12655	-	$-6.36^{+0.11}_{-0.08}$	$-6.281^{+0.029}_{-0.090}$	-7.35 ± 0.14
HD 23342	-	$-6.50^{+0.02}_{-0.00}$	$-6.50^{+0.06}_{-0.00}$	$-7.62^{+0.15}_{-0.17}$
HD 209292	-	$-6.28^{+0.10}_{-0.15}$	$-6.06^{+0.13}_{-0.14}$	$-6.83^{+0.06}_{-0.07}$
HD 156758	$-8.11^{+0.15}_{-0.10}$	$-6.491^{+0.090}_{-0.012}$	$-6.41^{+0.12}_{-0.10}$	$-7.48^{+0.15}_{-0.20}$
CD-38 8806	-	$-6.09^{+0.06}_{-0.07}$	$-5.93^{+0.09}_{-0.05}$	-7.04 ± 0.07
Feige 86	-6.42 ± 0.05	$-4.22^{+0.22}_{-0.40}$	$-4.02^{+0.07}_{-0.09}$	$-5.963^{+0.017}_{-0.019}$
CD-48 14233	-	$-6.50^{+0.07}_{-0.00}$	-6.39 ± 0.12	$-7.14^{+0.09}_{-0.07}$
TYC 1914-687-1	-	$-6.50^{+0.04}_{-0.00}$	$-6.385^{+0.120}_{-0.022}$	$-7.40^{+0.13}_{-0.23}$
PHL 25	-	-	$-4.80^{+0.16}_{-0.22}$	-
HD 110942	-	-	$-4.18^{+0.04}_{-0.08}$	-5.64 ± 0.05
PHL 382	-	-	$-4.528^{+0.021}_{-0.060}$	-
HD 8269	-	$-6.28^{+0.09}_{-0.11}$	$-6.008^{+0.012}_{-0.027}$	$-7.05^{+0.09}_{-0.12}$
Feige 6	-	$-4.29^{+0.20}_{-0.24}$	$-3.95^{+0.05}_{-0.07}$	-6.43 ± 0.06

Table 23: Derived abundances given as logarithmic particle-number fraction (6)

	Sr	Y
star	[dex]	[dex]
TYC 6036-1933-1	$-11.000^{+0.012}_{-0.000}$	-
HD 12655	$-11.000^{+0.007}_{-0.000}$	-
HD 23342	$-11.000^{+0.008}_{-0.000}$	-
HD 209292	$-10.84^{+0.16}_{-0.18}$	-
HD 156758	$-11.000^{+0.006}_{-0.000}$	-
CD-38 8806	$-11.00^{+0.08}_{-0.00}$	-
Feige 86	-9.18 ± 0.11	-
CD-48 14233	$-11.000^{+0.006}_{-0.000}$	-
TYC 1914-687-1	$-11.000^{+0.006}_{-0.000}$	-
PHL 25	-	-
HD 110942	-8.07 ± 0.07	-
PHL 382	-	-
HD 8269	$-11.000^{+0.006}_{-0.000}$	-
Feige 6	-	-7.9 ± 0.1

Appendix A4

Photometric results

Table 24: results from pure photometry

	$T_{\rm eff}$	log(g)	$E(B-V_P)$	Θ	z
star	[K]	[cgs]	[mag]	[rad]	
TYC 6036-1933-1	9648^{+110}_{-200}	$3.00^{+0.08}_{-0.00}$	$0.138^{+0.012}_{-0.013}$	$\left(1.407^{+0.015}_{-0.009}\right) \times 10^{-10}$	$-2.0^{+1.6}_{-0.0}$
HD 12655	9462^{+210}_{-190}	$2.98^{+0.26}_{-0.28}$	$0.029^{+0.014}_{-0.016}$	$\left(2.73^{+0.04}_{-0.05}\right) \times 10^{-10}$	$-2.0^{+2.1}_{-0.0}$
HD 23342	9400^{+170}_{-160}	$2.86^{+0.22}_{-0.23}$	0.050 ± 0.013	$(1.618 \pm 0.017) \times 10^{-10}$	$0.0^{+0.6}_{-2.1}$
HD 209292	11152^{+140}_{-150}	$3.19^{+0.16}_{-0.17}$	0.032 ± 0.007	$(9.58 \pm 0.07) \times 10^{-11}$	$-0.9^{+1.4}_{-1.2}$
HD 156758	9000^{+80}_{-00}	3.6 ± 0.4	$0.150^{+0.000}_{-0.006}$	$\left(1.867^{+0.010}_{-0.017}\right) \times 10^{-10}$	$-2.0^{+1.1}_{-0.0}$
CD-38 8806	10932^{+180}_{-400}	$3.18^{+0.22}_{-0.25}$	$0.043^{+0.015}_{-0.009}$	$\left(1.139^{+0.011}_{-0.016}\right) \times 10^{-10}$	$-2.0^{+2.5}_{-0.0}$
Feige 86	15871^{+130}_{-250}	$4.18^{+0.19}_{-0.18}$	$0.026^{+0.006}_{-0.007}$	$(9.79 \pm 0.08) \times 10^{-11}$	$0.50^{+0.00}_{-0.11}$
CD-48 14233	9643 ± 150	$3.25^{+0.14}_{-0.15}$	$0.011^{+0.011}_{-0.009}$	$\left(1.039^{+0.008}_{-0.011}\right) \times 10^{-10}$	$-1.5^{+1.6}_{-0.5}$
TYC 1914-687-1	8235^{+700}_{-070}	$3.60^{+0.21}_{-0.50}$	$0.00005^{+0.06000}_{-0.00005}$	$\left(1.432^{+0.014}_{-0.043}\right) \times 10^{-10}$	$-0.4^{+0.7}_{-1.7}$
PHL 25	16604^{+1500}_{-1400}	$3.60^{+0.18}_{-0.00}$	$0.020^{+0.023}_{-0.021}$	$\left(3.594^{+0.148}_{-0.021}\right) \times 10^{-11}$	$0.0^{+0.6}_{-2.1}$
HD 110942	19000^{+000}_{-600}	$3.60^{+0.26}_{-0.00}$	$0.089^{+0.006}_{-0.011}$	$\left(7.42^{+0.11}_{-0.06}\right) \times 10^{-11}$	$0.25^{+0.26}_{-0.90}$
PHL 382	18923^{+080}_{-800}	$3.60^{+0.14}_{-0.00}$	$0.044^{+0.007}_{-0.015}$	$\left(4.90^{+0.10}_{-0.05}\right) \times 10^{-11}$	$0.0^{+0.6}_{-1.4}$
HD 8269	9265 ± 120	$3.60^{+0.07}_{-0.08}$	0.02 ± 0.01	$(1.407 \pm 0.009) \times 10^{-10}$	$0.38^{+0.13}_{-2.40}$
Feige 6	15047^{+280}_{-230}	3.97 ± 0.19	0.034 ± 0.007	$\left(1.805^{+0.014}_{-0.015}\right) \times 10^{-11}$	$-0.9^{+1.4}_{-1.2}$

Appendix A5

Kinematic results

Table 25: Kinematic parameters for the AS-potential

star	V $\left[\frac{\text{km}}{\text{s}}\right]$	U $\left[\frac{\text{km}}{\text{s}}\right]$	L_z $-1 \cdot \left[\frac{\text{kpc}\cdot\text{km}}{\text{s}}\right]$	e [1]
TYC 6036-1933-1	11.6 ± 50.0	191.2 ± 190.0	-0.1035 ± 0.0027	0.979 ± 0.017
HD 12655	-18.5 ± 18.0	25.6 ± 40.0	0.16 ± 0.05	0.893 ± 0.006
HD 23342	-16.1 ± 60.0	212.9 ± 210.0	0.14 ± 0.05	0.972 ± 0.018
HD 209292	42.9 ± 80.0	-4.4 ± 170.0	-0.35 ± 0.13	0.81 ± 0.06
HD 156758	36.0 ± 90.0	67.1 ± 200.0	-0.29 ± 0.06	0.882 ± 0.026
CD-38 8806	-35.5 ± 100.0	-74.8 ± 230.0	0.29 ± 0.06	0.884 ± 0.029
Feige 86	106.0 ± 100.0	-95.0 ± 160.0	-0.909 ± 0.029	0.618 ± 0.015
CD-48 14233	31.2 ± 80.0	63.6 ± 200.0	-0.25 ± 0.13	0.90 ± 0.06
TYC 1914-687-1	143.2 ± 60.0	3.5 ± 120.0	-1.38 ± 0.08	0.74 ± 0.06
PHL 25	113.2 ± 70.0	-87.4 ± 110.0	-0.93 ± 0.08	0.539 ± 0.026
HD 110942	243.0 ± 12.0	43.0 ± 27.0	-2.058 ± 0.007	0.1296 ± 0.0028
PHL 382	152.0 ± 70.0	14.0 ± 110.0	-1.25 ± 0.08	0.38 ± 0.04
HD 8269	53.9 ± 80.0	-153.4 ± 170.0	-0.47 ± 0.07	0.815 ± 0.023
Feige 6	-58.9 ± 70.0	-264.3 ± 190.0	0.5 ± 0.5	0.88 ± 0.06

Table 26: Kinematic parameters for the NFW-potential

star	V $\left[\frac{\text{km}}{\text{s}}\right]$	U $\left[\frac{\text{km}}{\text{s}}\right]$	L_z $-1 \cdot \left[\frac{\text{kpc}\cdot\text{km}}{\text{s}}\right]$	e [1]
TYC 6036-1933-1	9.4 ± 50.0	191.4 ± 200.0	-0.0839 ± 0.0028	0.982 ± 0.015
HD 12655	-20.8 ± 18.0	25.6 ± 50.0	0.18 ± 0.05	0.875 ± 0.007
HD 23342	-18.4 ± 60.0	213.0 ± 200.0	0.16 ± 0.05	0.97 ± 0.02
HD 209292	40.6 ± 90.0	-4.4 ± 170.0	-0.33 ± 0.13	0.82 ± 0.06
HD 156758	33.7 ± 90.0	67.1 ± 210.0	-0.27 ± 0.06	0.89 ± 0.04
CD-38 8806	-37.8 ± 15.0	-74.7 ± 80.0	0.31 ± 0.06	0.87 ± 0.03
Feige 86	104.0 ± 100.0	-95.0 ± 170.0	-0.883 ± 0.029	0.627 ± 0.015
CD-48 14233	28.9 ± 80.0	63.7 ± 190.0	-0.23 ± 0.13	0.91 ± 0.06
TYC 1914-687-1	140.9 ± 60.0	3.5 ± 120.0	-1.35 ± 0.07	0.71 ± 0.05
PHL 25	110.9 ± 70.0	-87.4 ± 110.0	-0.91 ± 0.08	0.538 ± 0.025
HD 110942	241.0 ± 16.0	43.0 ± 21.0	-2.022 ± 0.007	0.1293 ± 0.0028
PHL 382	149.0 ± 70.0	13.0 ± 100.0	-1.22 ± 0.08	0.38 ± 0.04
HD 8269	51.6 ± 80.0	-153.4 ± 170.0	-0.45 ± 0.07	0.819 ± 0.022
Feige 6	-60.9 ± 80.0	-264.5 ± 190.0	0.5 ± 0.5	0.87 ± 0.07

Table 27: Kinematic parameters for the TF-potential

star	V $\left[\frac{\text{km}}{\text{s}}\right]$	U $\left[\frac{\text{km}}{\text{s}}\right]$	L_z $-1 \cdot \left[\frac{\text{kpc}\cdot\text{km}}{\text{s}}\right]$	e [1]
TYC 6036-1933-1	10.1 ± 50.0	191.4 ± 180.0	-0.0899 ± 0.0028	0.971 ± 0.015
HD 12655	-20.1 ± 50.0	25.6 ± 140.0	0.17 ± 0.05	0.885 ± 0.006
HD 23342	-17.7 ± 60.0	212.9 ± 210.0	0.16 ± 0.05	0.968 ± 0.019
HD 209292	41.3 ± 80.0	-4.4 ± 170.0	-0.34 ± 0.13	0.83 ± 0.06
HD 156758	34.4 ± 80.0	67.1 ± 200.0	-0.28 ± 0.06	0.890 ± 0.025
CD-38 8806	-37.1 ± 80.0	-74.7 ± 180.0	0.30 ± 0.06	0.879 ± 0.029
Feige 86	105.0 ± 100.0	-95.0 ± 160.0	-0.891 ± 0.029	0.626 ± 0.015
CD-48 14233	29.6 ± 90.0	63.6 ± 200.0	-0.24 ± 0.13	0.91 ± 0.06
TYC 1914-687-1	141.6 ± 60.0	3.5 ± 120.0	-1.36 ± 0.08	0.75 ± 0.07
PHL 25	111.6 ± 70.0	-87.4 ± 120.0	-0.92 ± 0.08	0.547 ± 0.026
HD 110942	242.0 ± 19.0	43.0 ± 20.0	-2.033 ± 0.007	0.1307 ± 0.0028
PHL 382	150.0 ± 70.0	14.0 ± 110.0	-1.23 ± 0.08	0.38 ± 0.04
HD 8269	52.3 ± 80.0	-153.4 ± 170.0	-0.45 ± 0.07	0.823 ± 0.026
Feige 6	-60.3 ± 70.0	-264.5 ± 180.0	0.5 ± 0.5	0.89 ± 0.06

Appendix A6

Spectral fits of selected objects

This appendix contains the full spectral fits of four stars. The black line is the observations and the red line the best fitting model. The four stars chosen are the following: TYC 1914-687-1, as it is one of the coolest stars in the sample and could potentially have a higher mass than predicted. HD 209292 which is the hottest A-BHB star in the sample. Feige 6 since it is a halo-BHB and finally, HD 110942 as one of the hotter newly classified B-BHB-stars. Only regions used for the fit are shown in this section. The grayed-out areas were excluded from the fit as well.

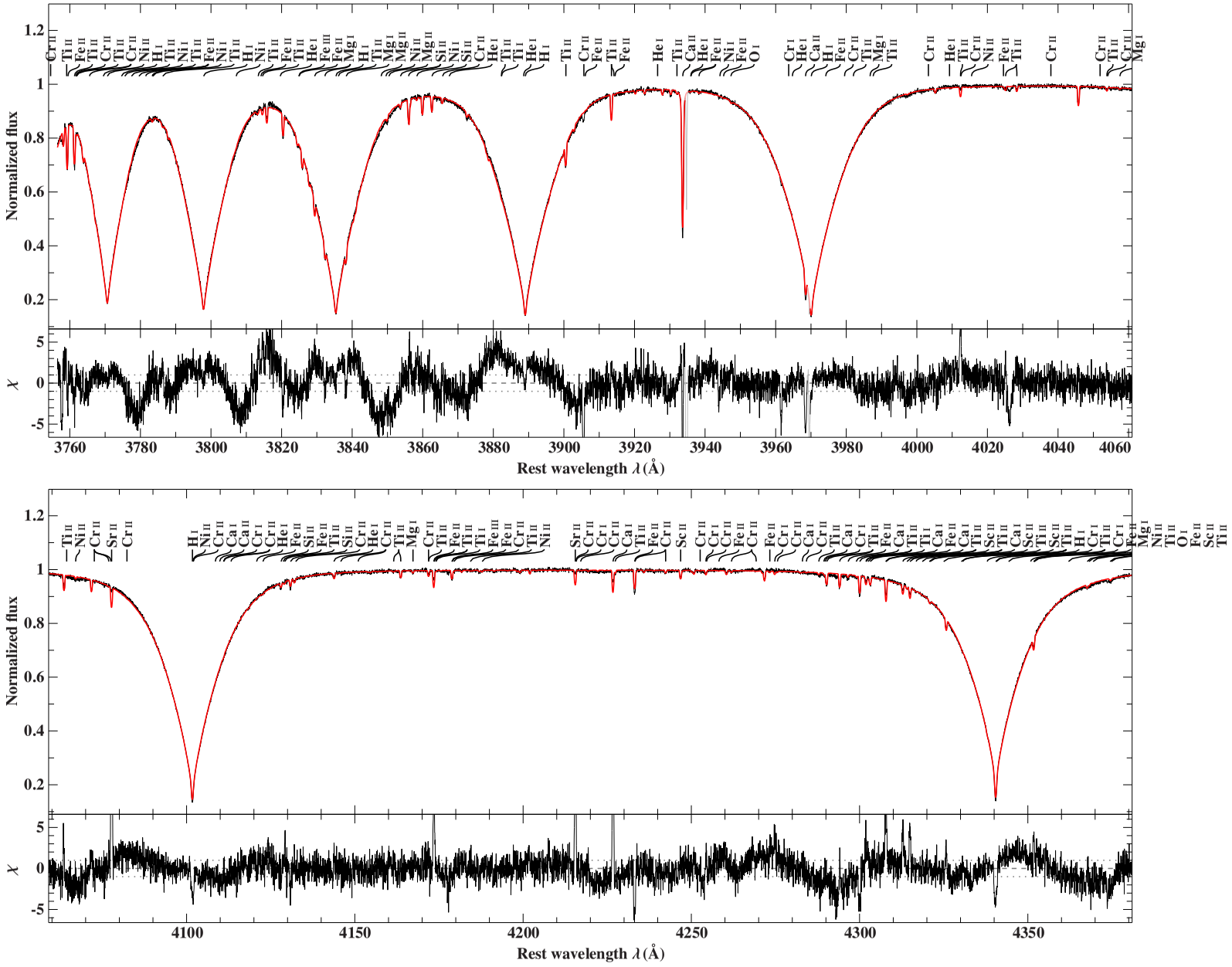

Figure 4: Spectral fit of TYC 1914-687-1, part 1

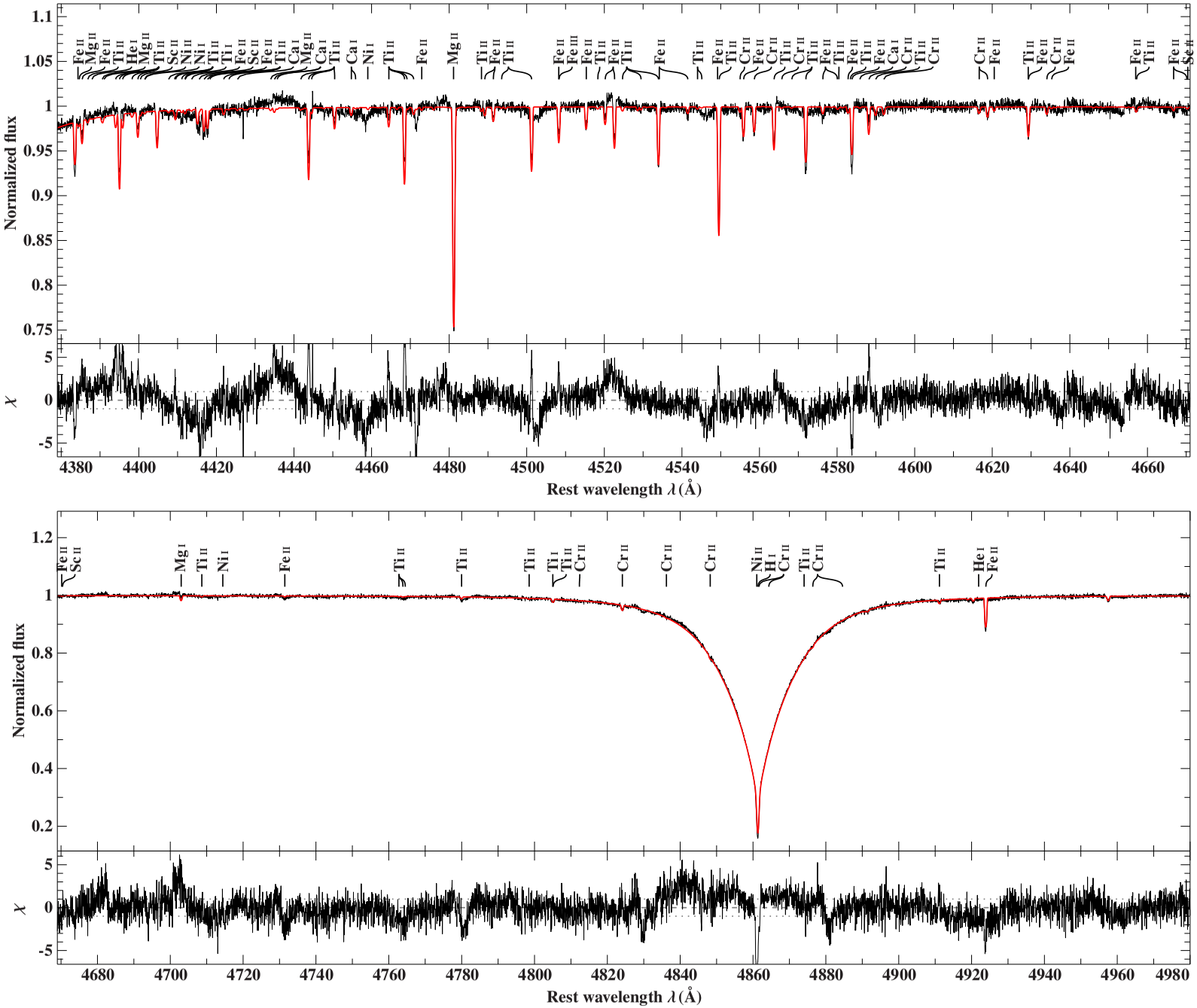

Figure 5: Spectral fit of TYC 1914-687-1, part 2

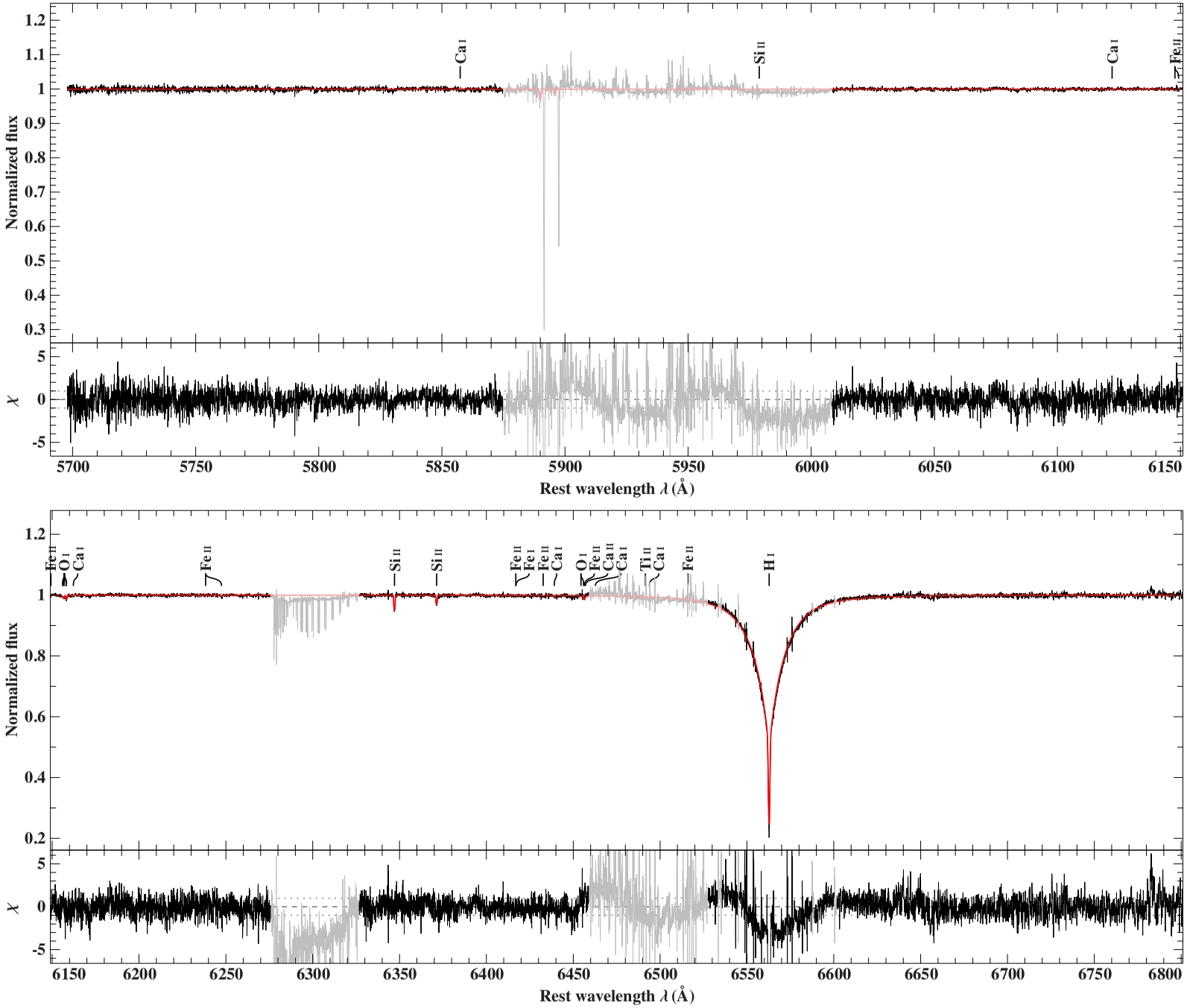

Figure 6: Spectral fit of TYC 1914-687-1, part 3

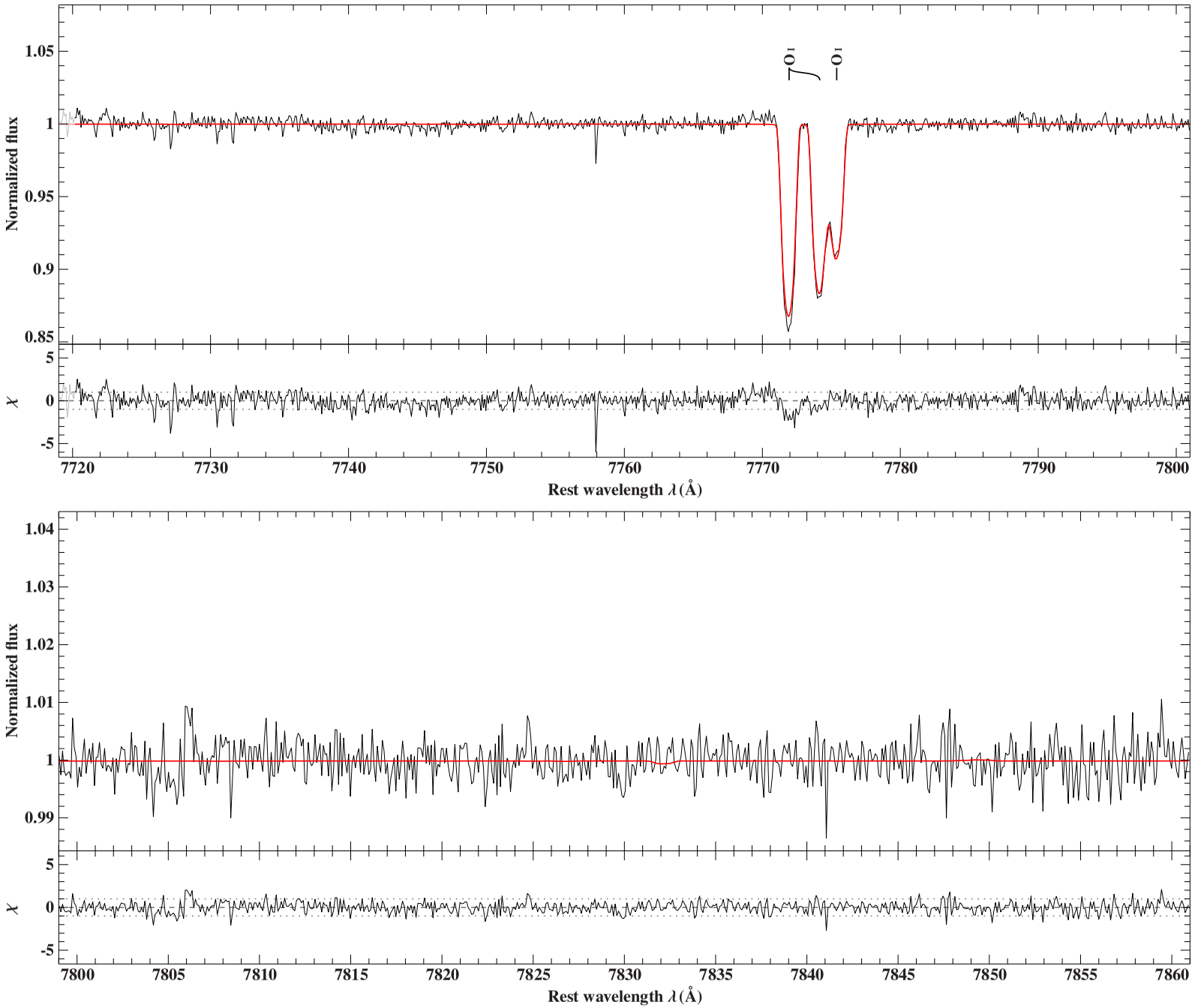

Figure 7: Spectral fit of TYC 1914-687-1, part 4

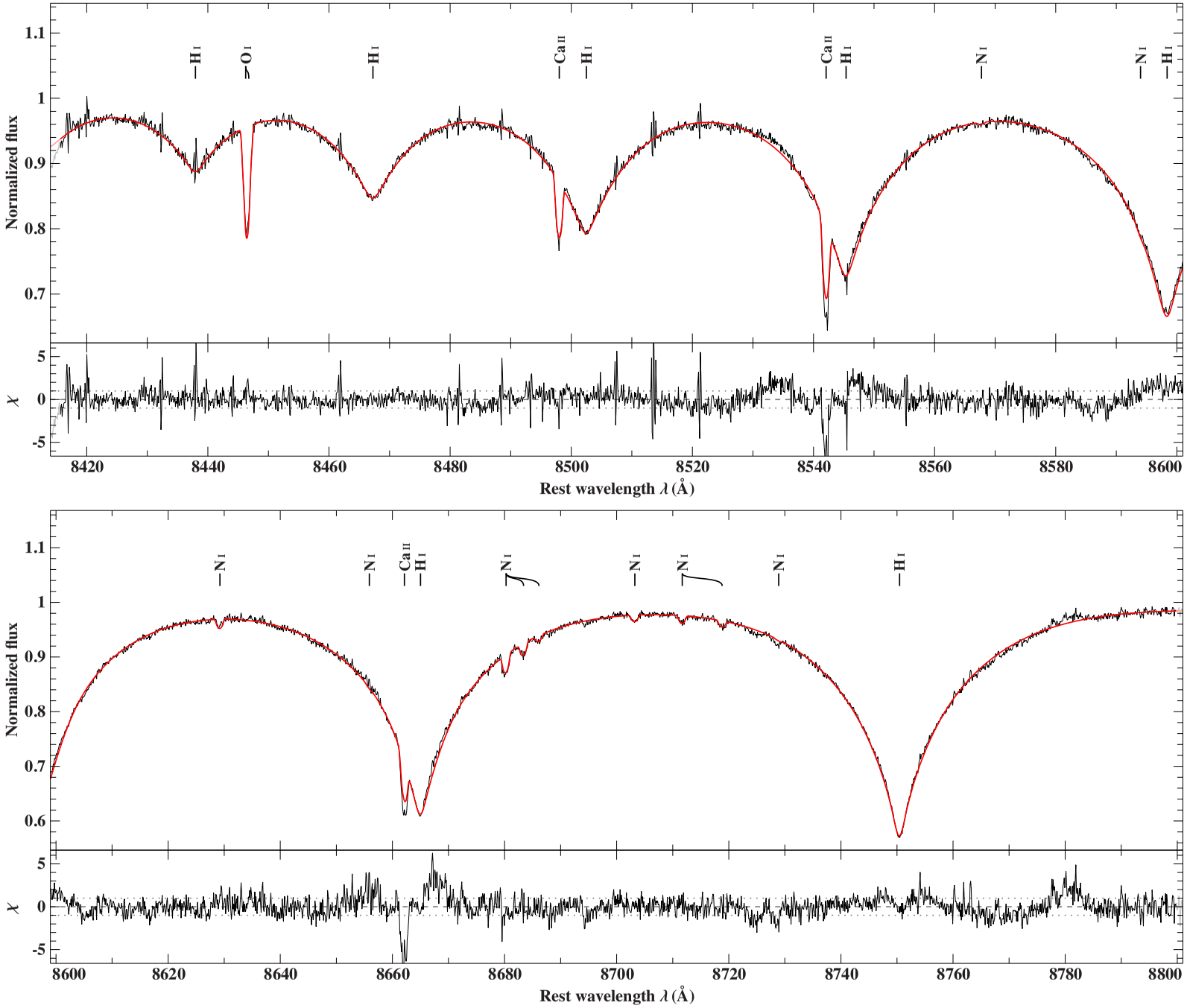

Figure 8: Spectral fit of TYC 1914-687-1, part 5

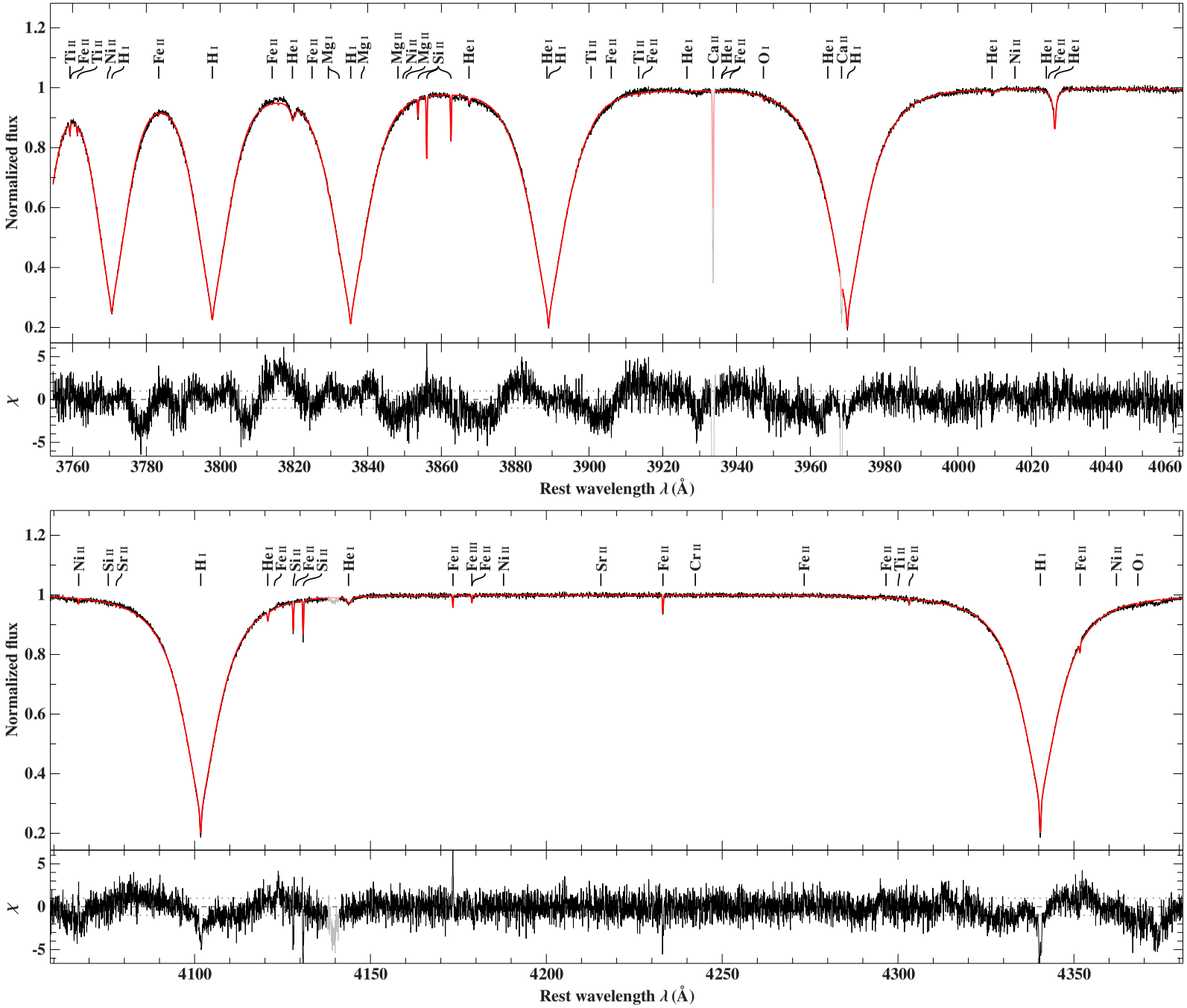

Figure 9: Spectral fit of HD 209292, part 1

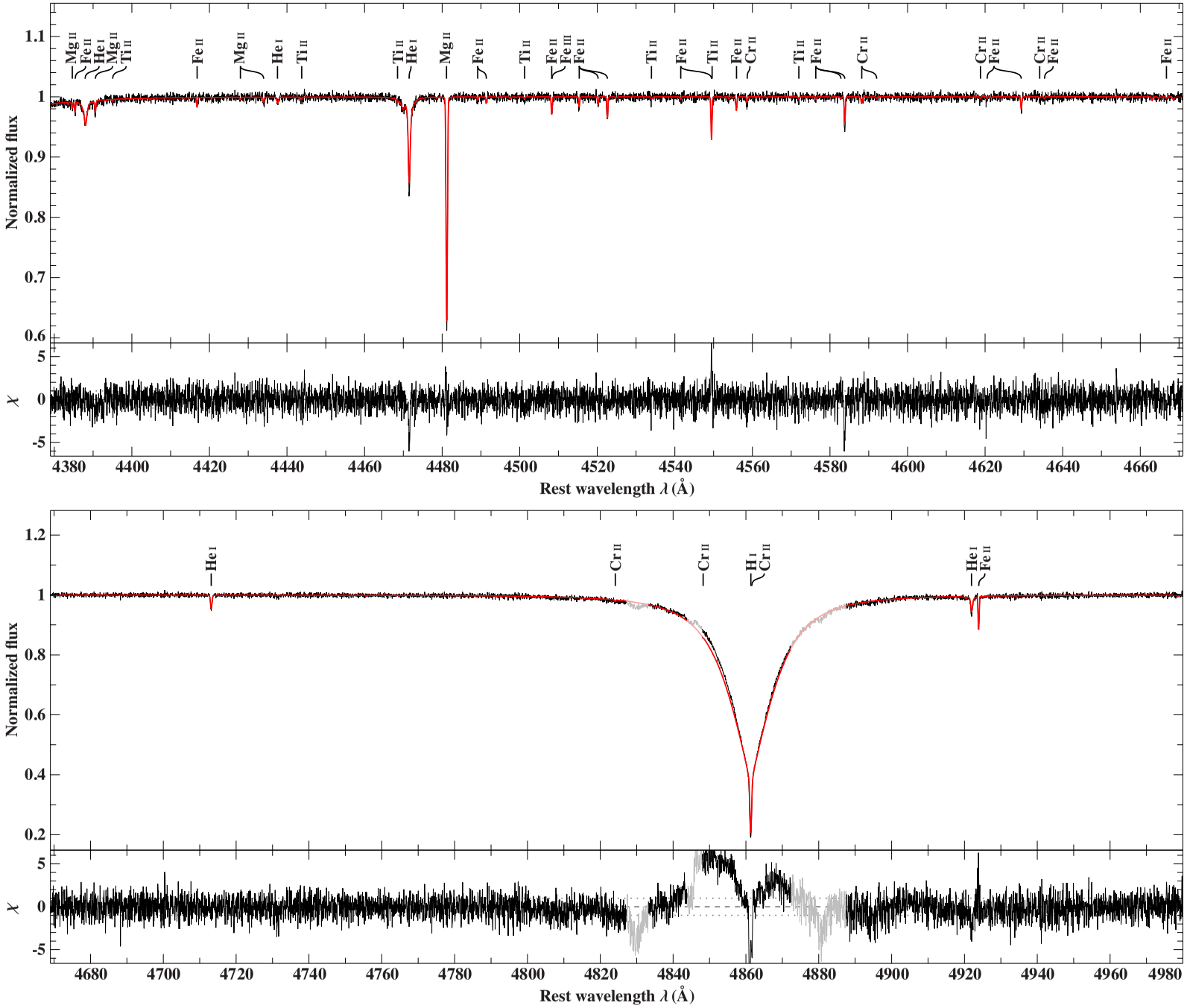

Figure 10: Spectral fit of HD 209292, part 2

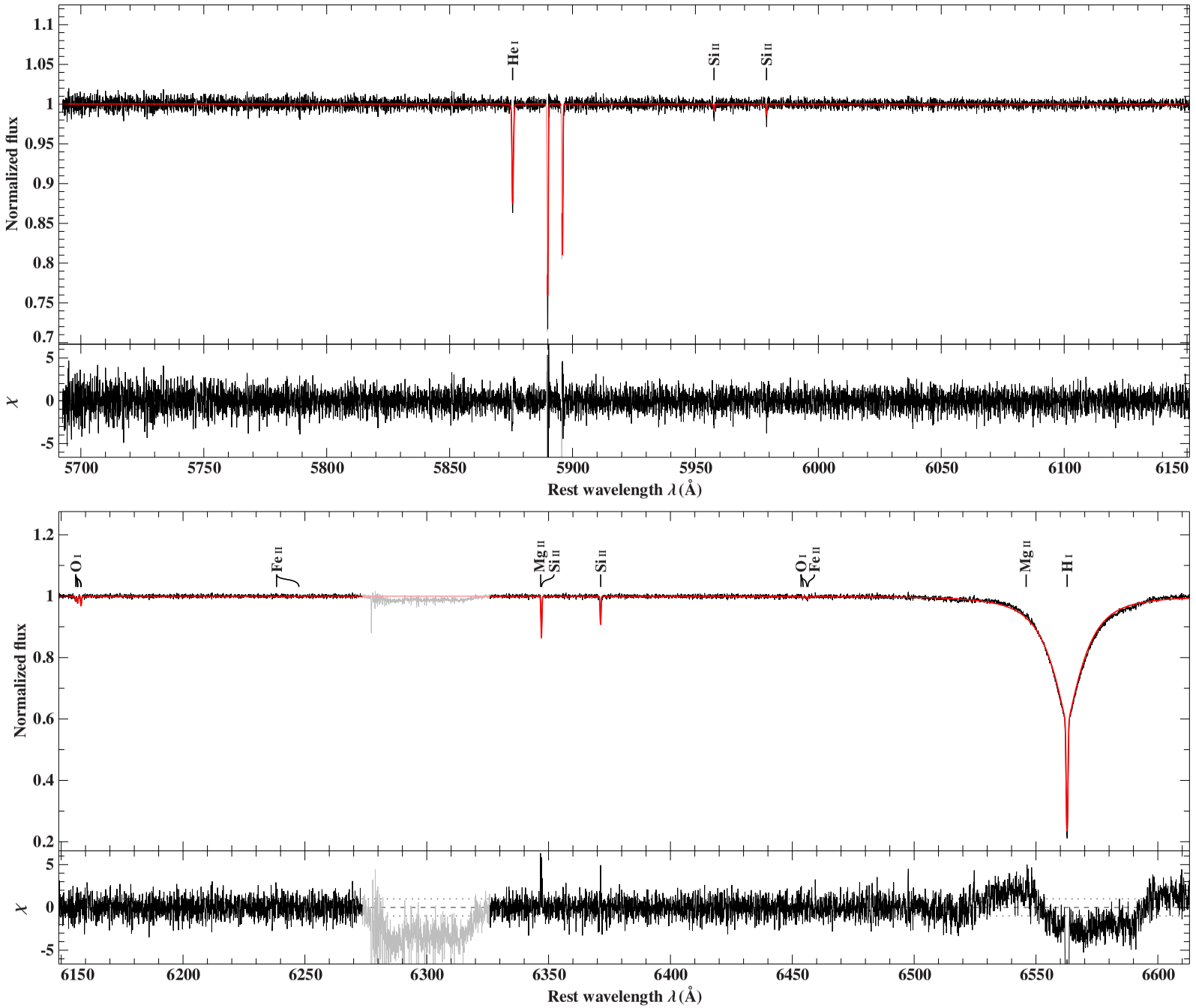

Figure 11: Spectral fit of HD 209292, part 3

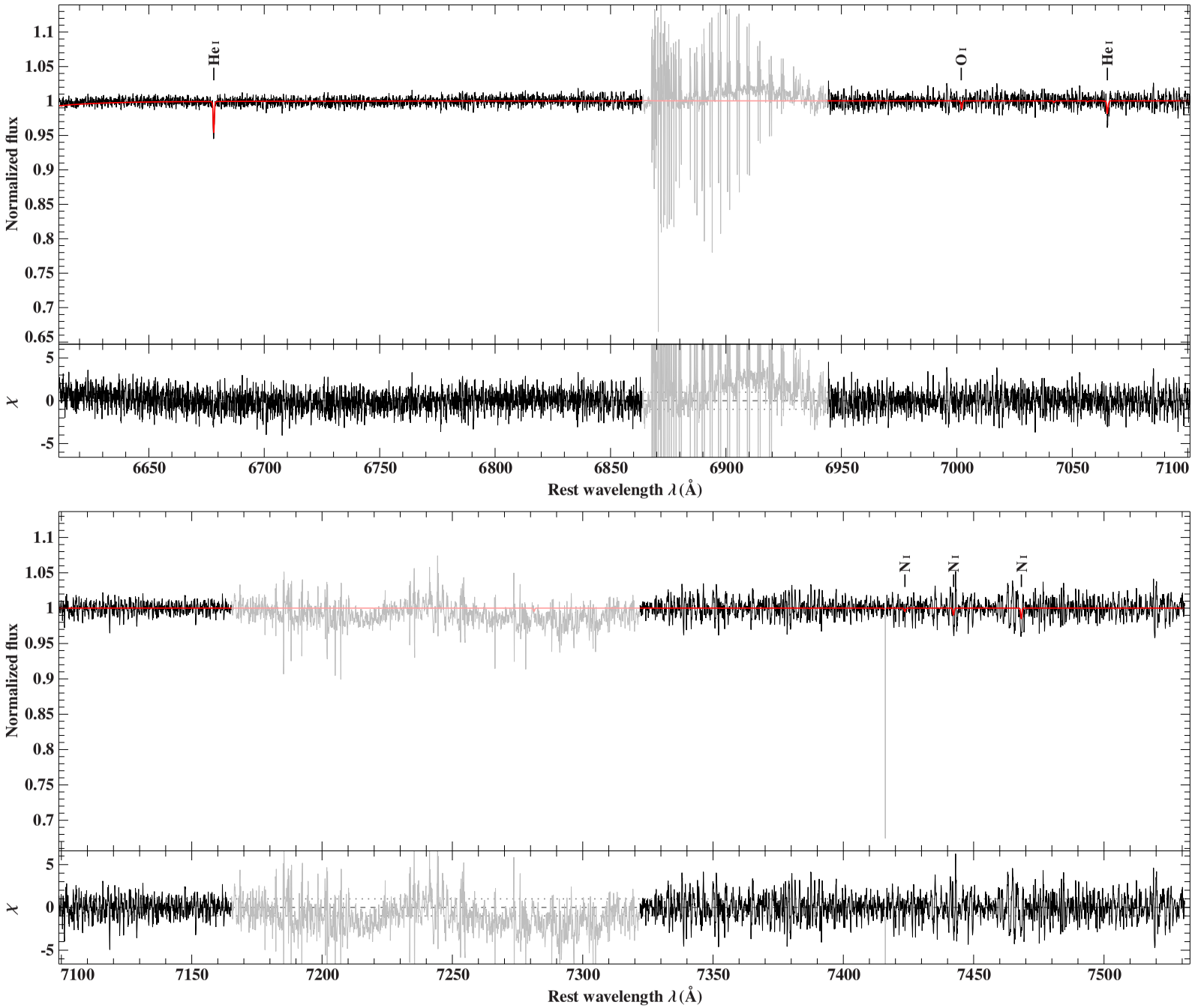

Figure 12: Spectral fit of HD 209292, part 4

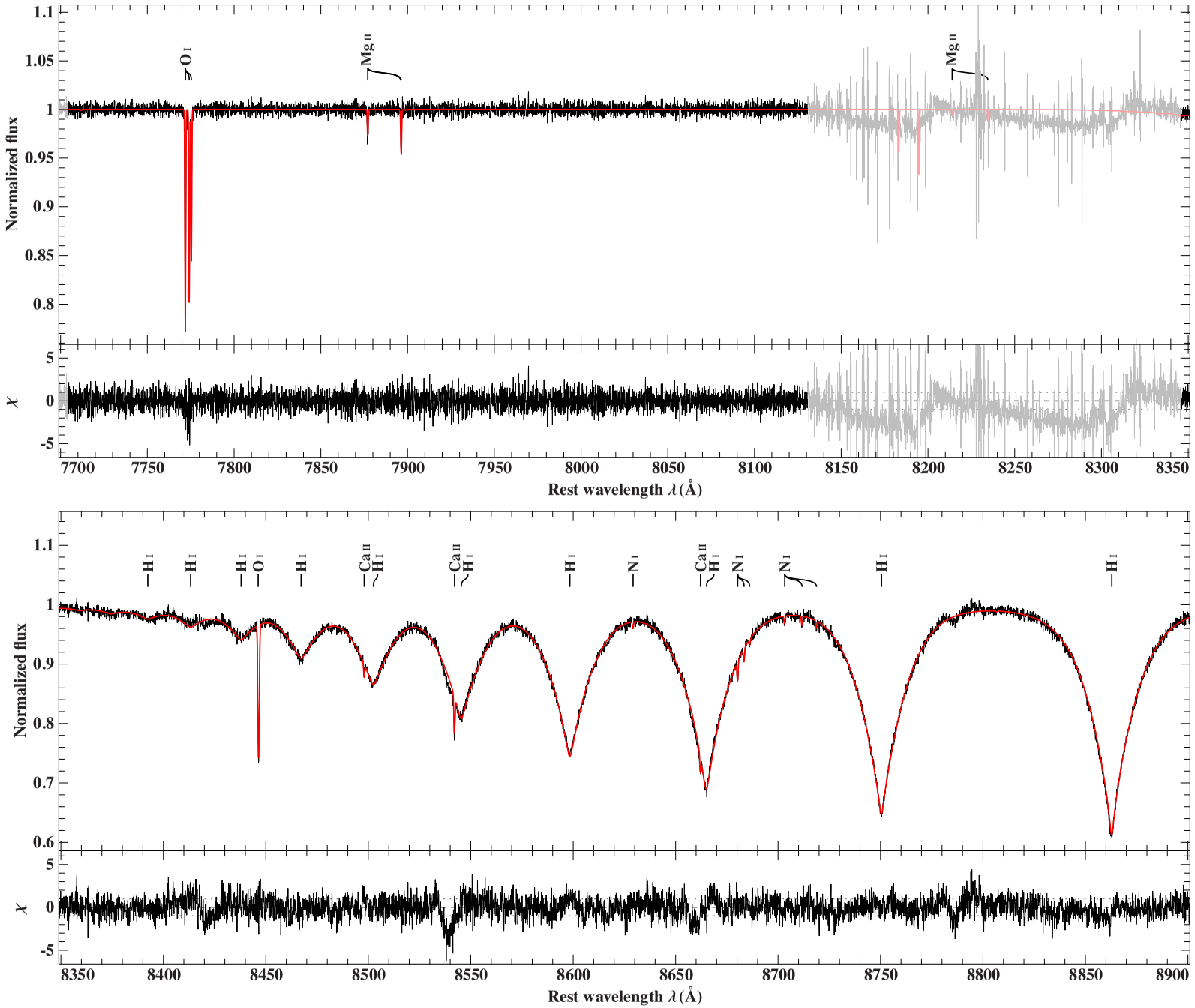

Figure 13: Spectral fit of HD 209292, part 5

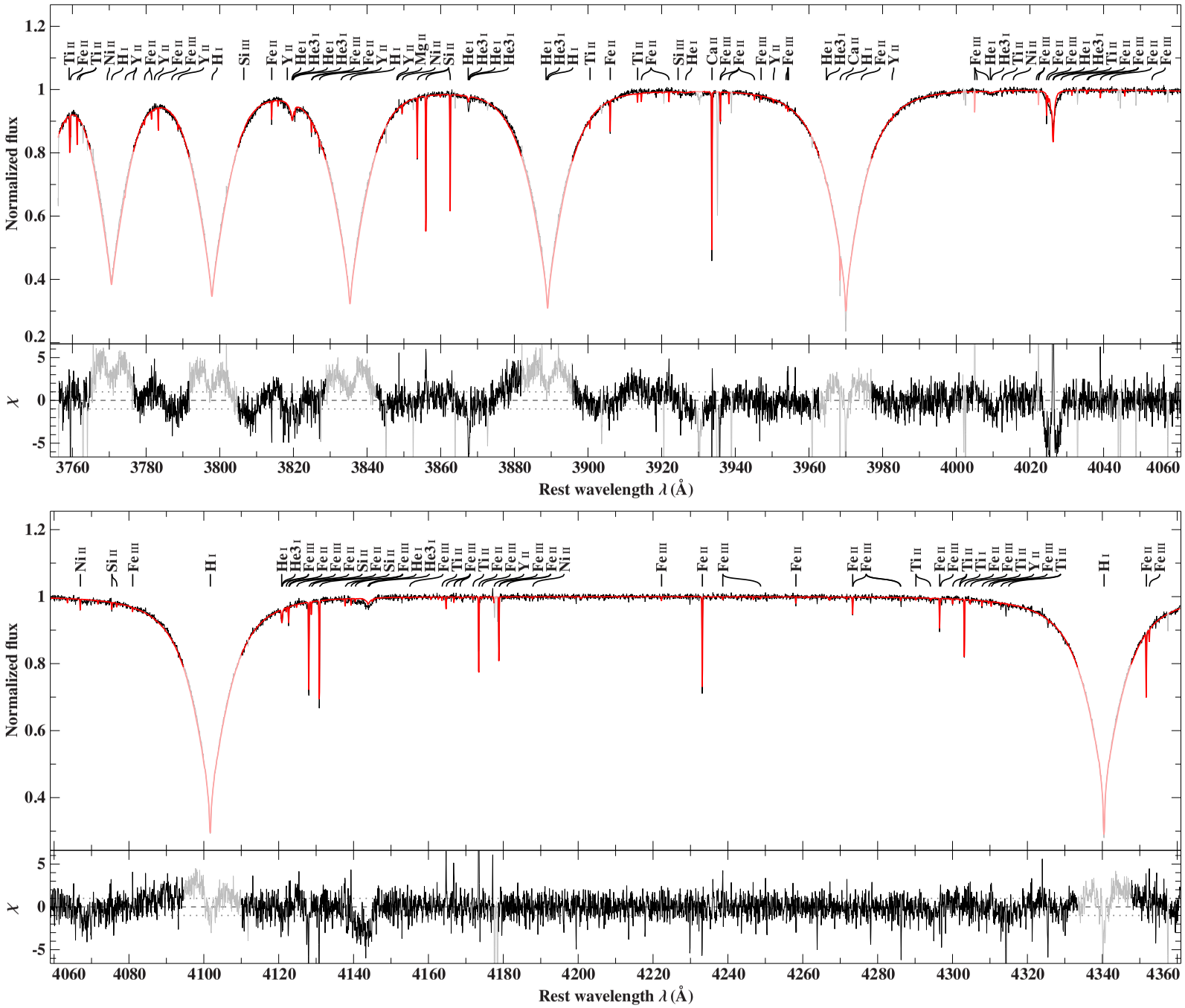

Figure 14: Spectral fit of UVES spectrum of Feige 6, part 1

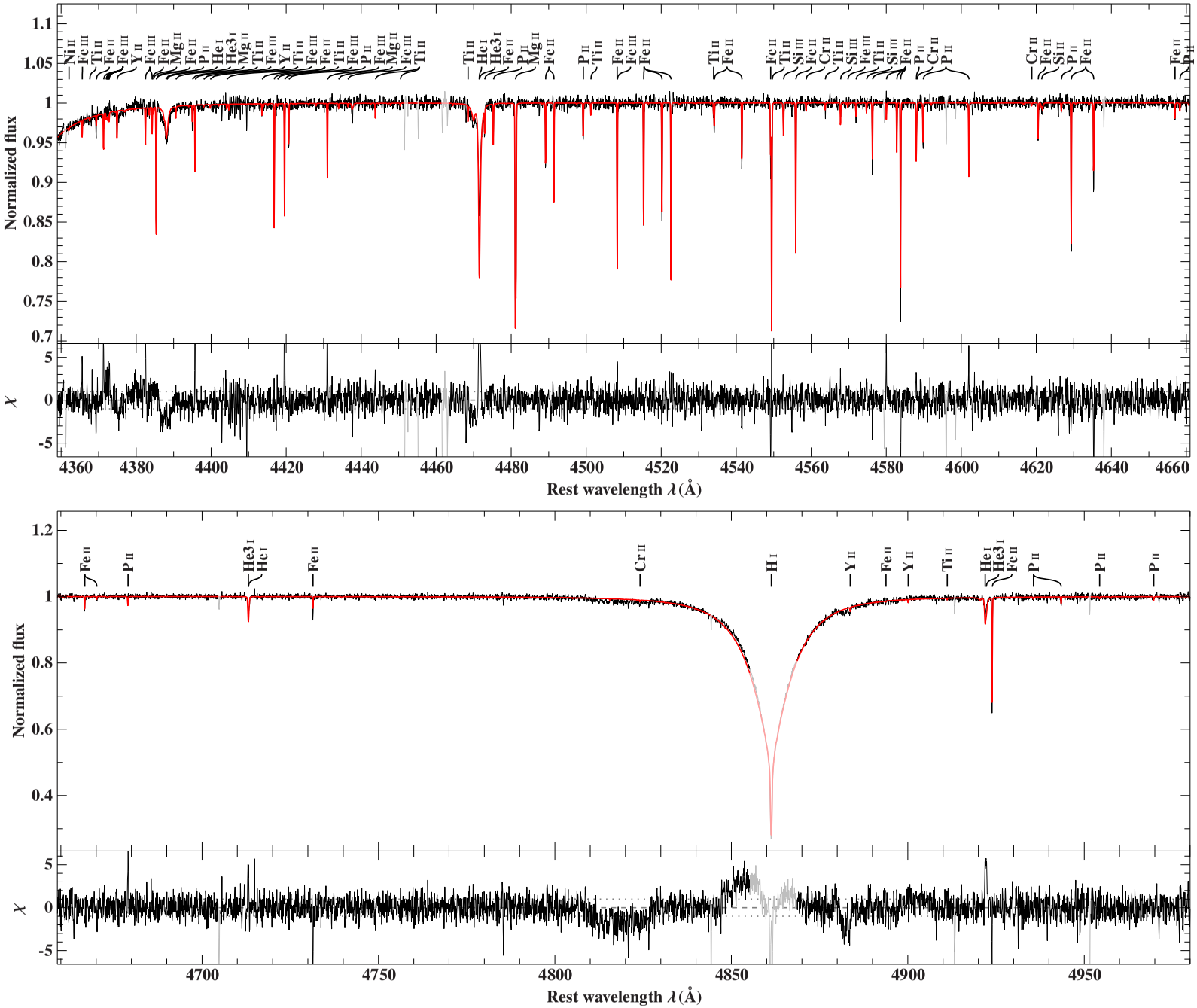

Figure 15: Spectral fit of UVES spectrum of Feige 6, part 2

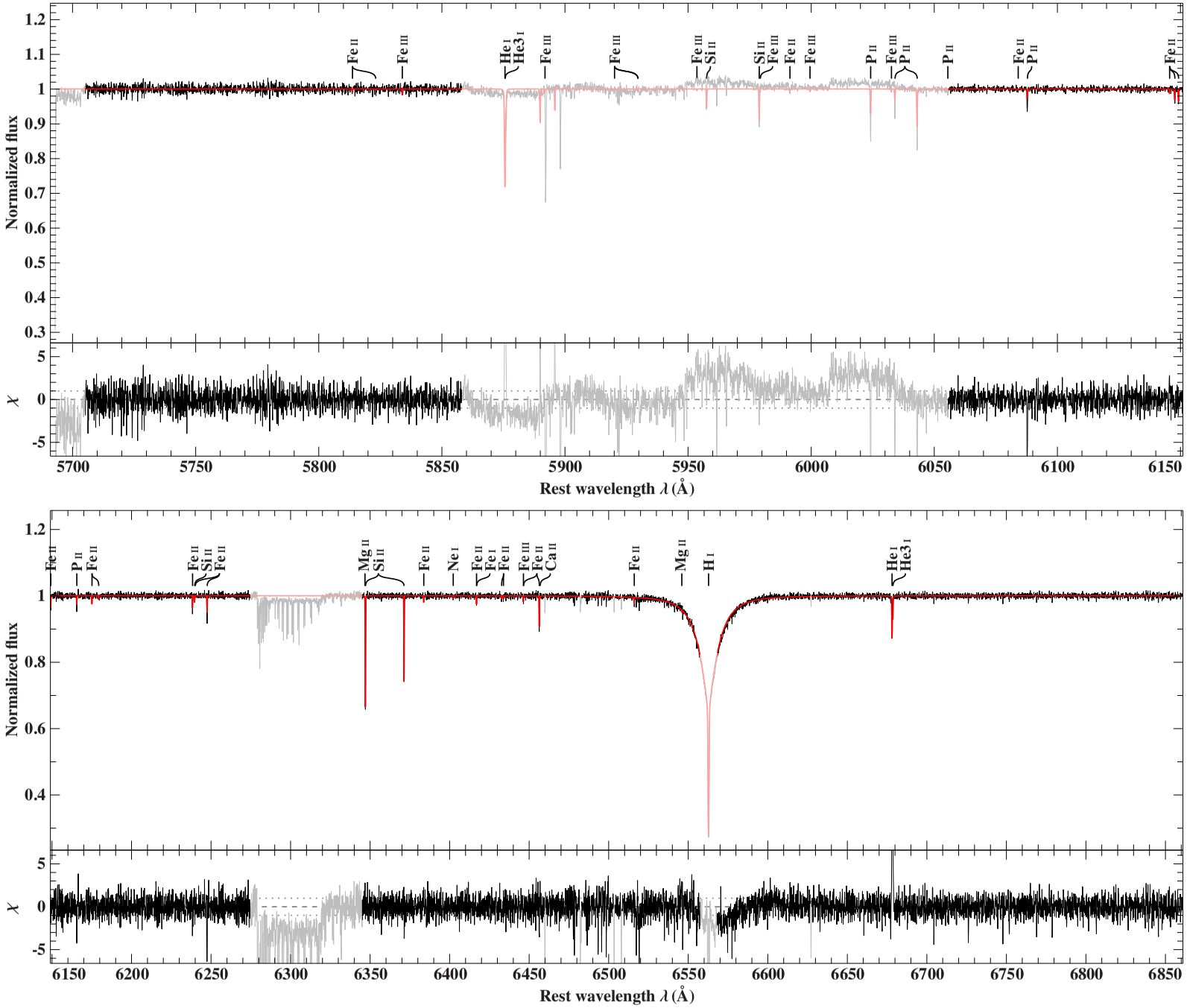

Figure 16: Spectral fit of UVES spectrum of Feige 6, part 3

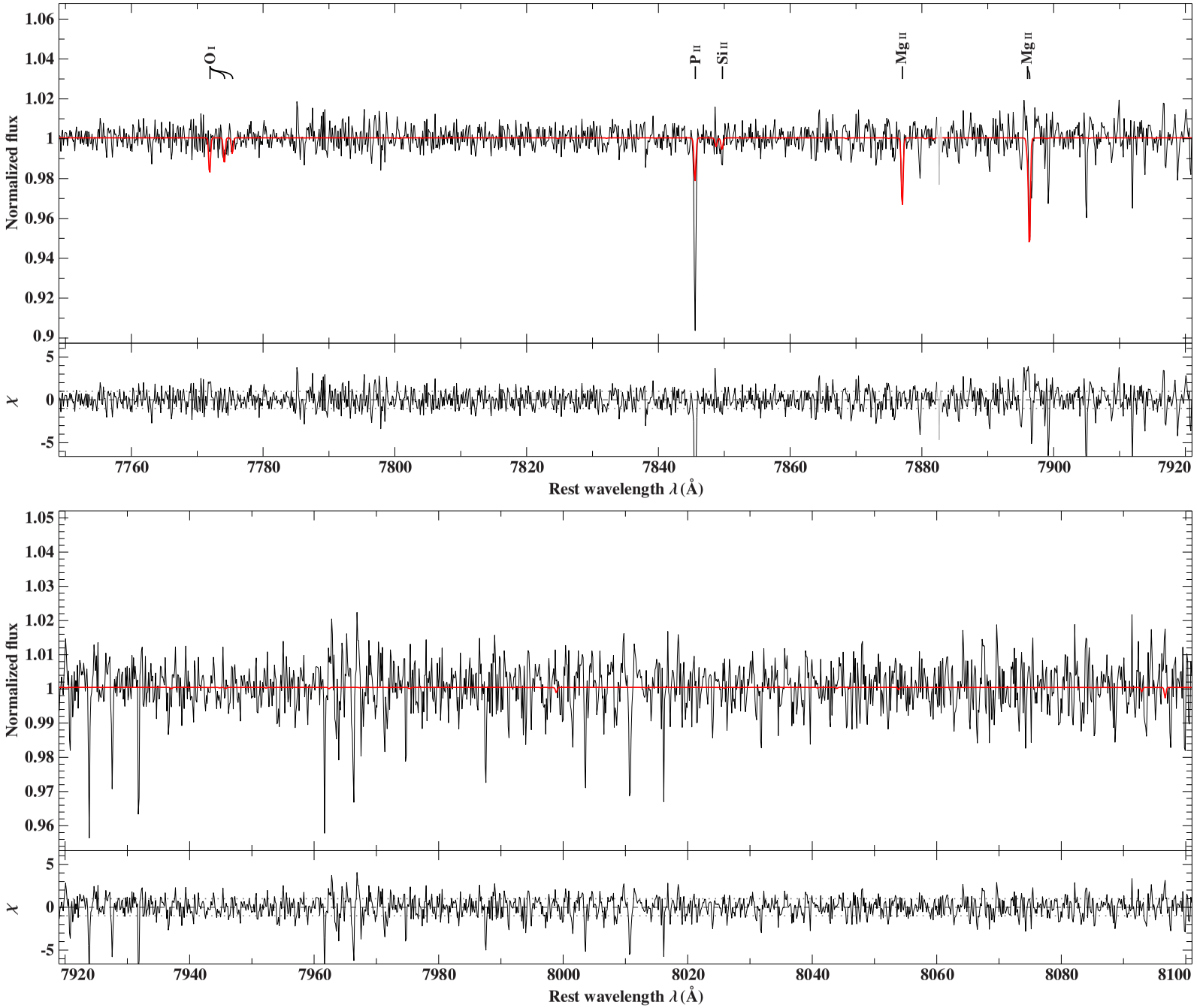

Figure 17: Spectral fit of UVES spectrum of Feige 6, part 4

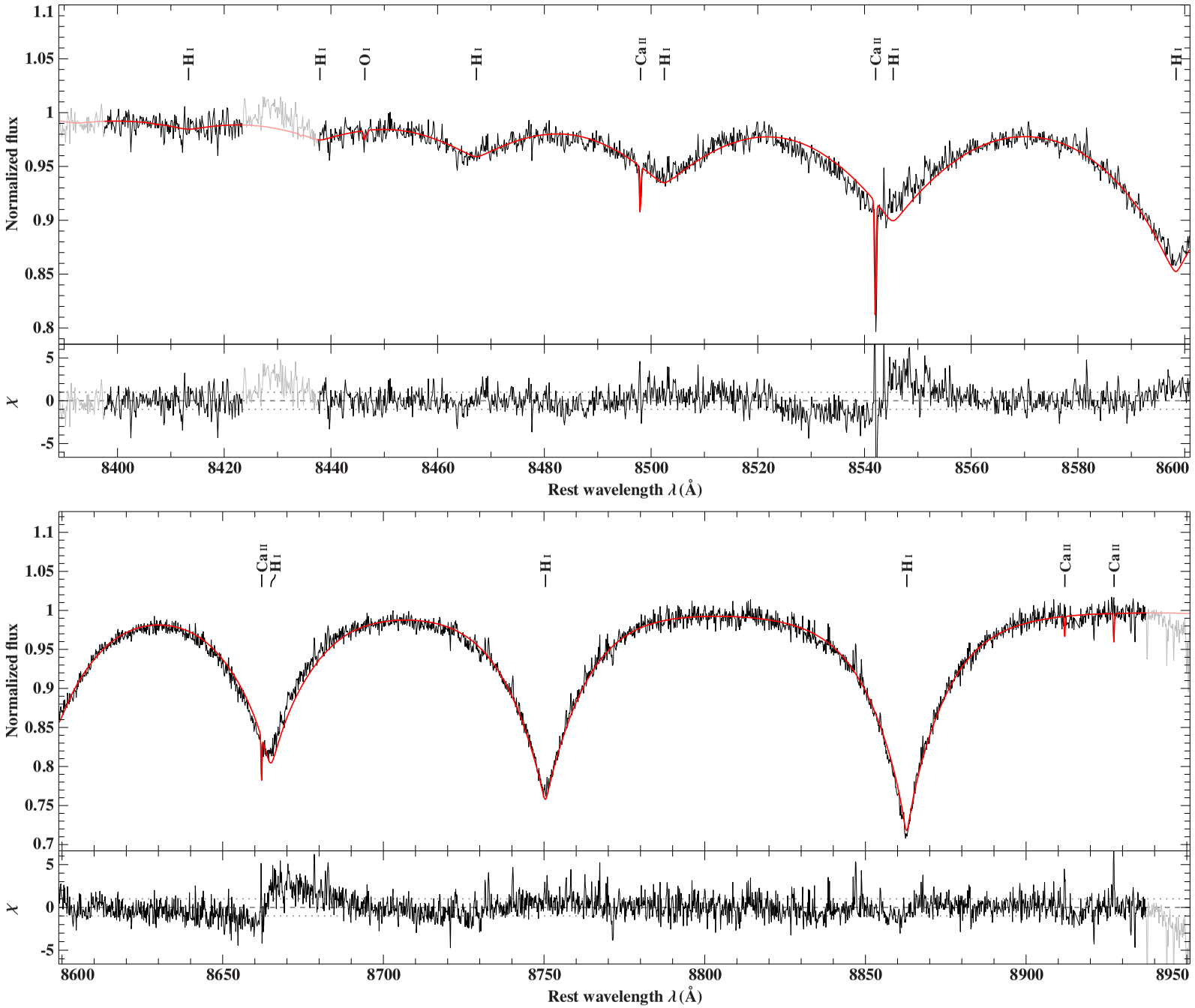

Figure 18: Spectral fit of UVES spectrum of Feige 6, part 5

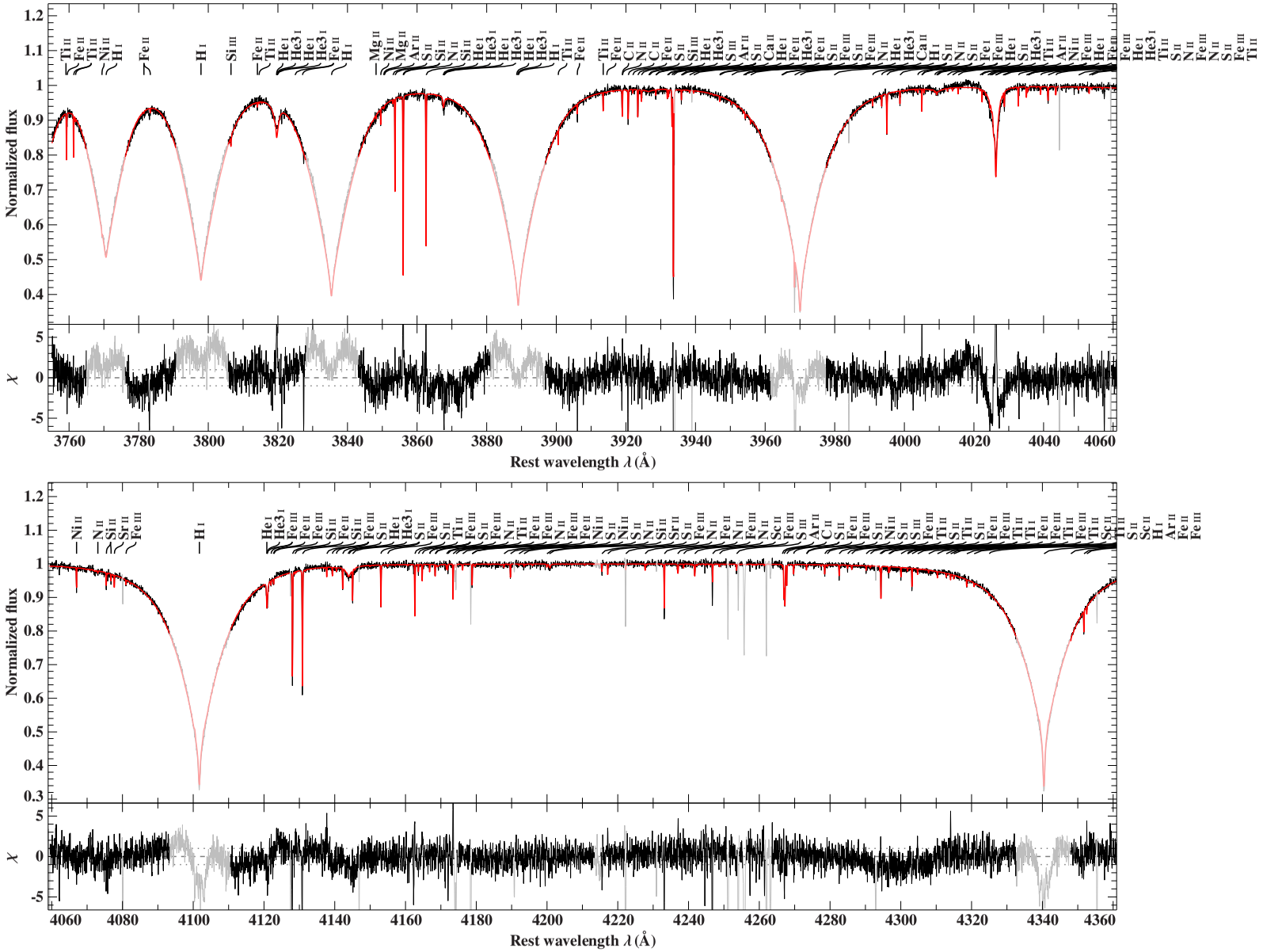

Figure 19: Spectral fit of HD 110942, part 1

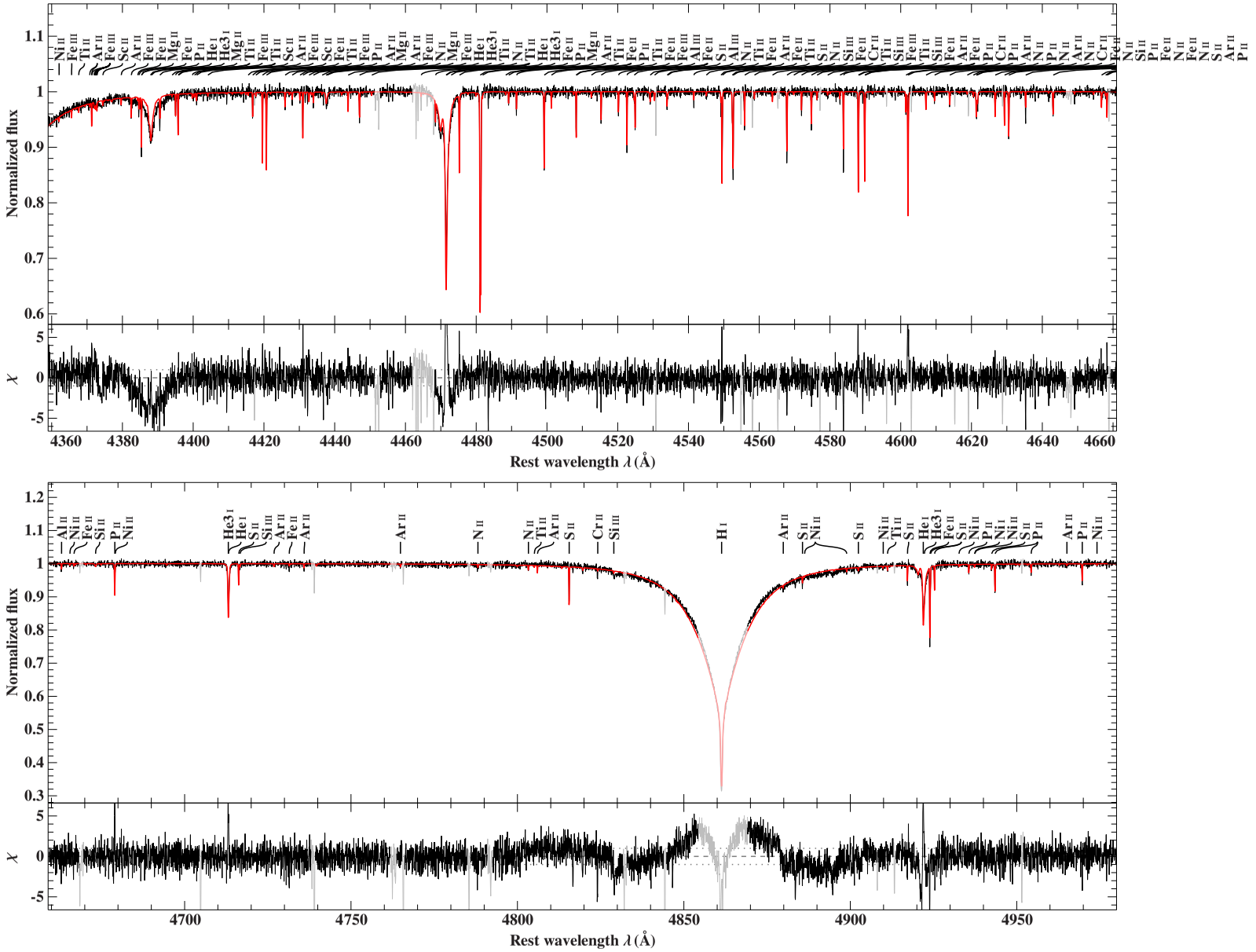

Figure 20: Spectral fit of HD 110942, part 2

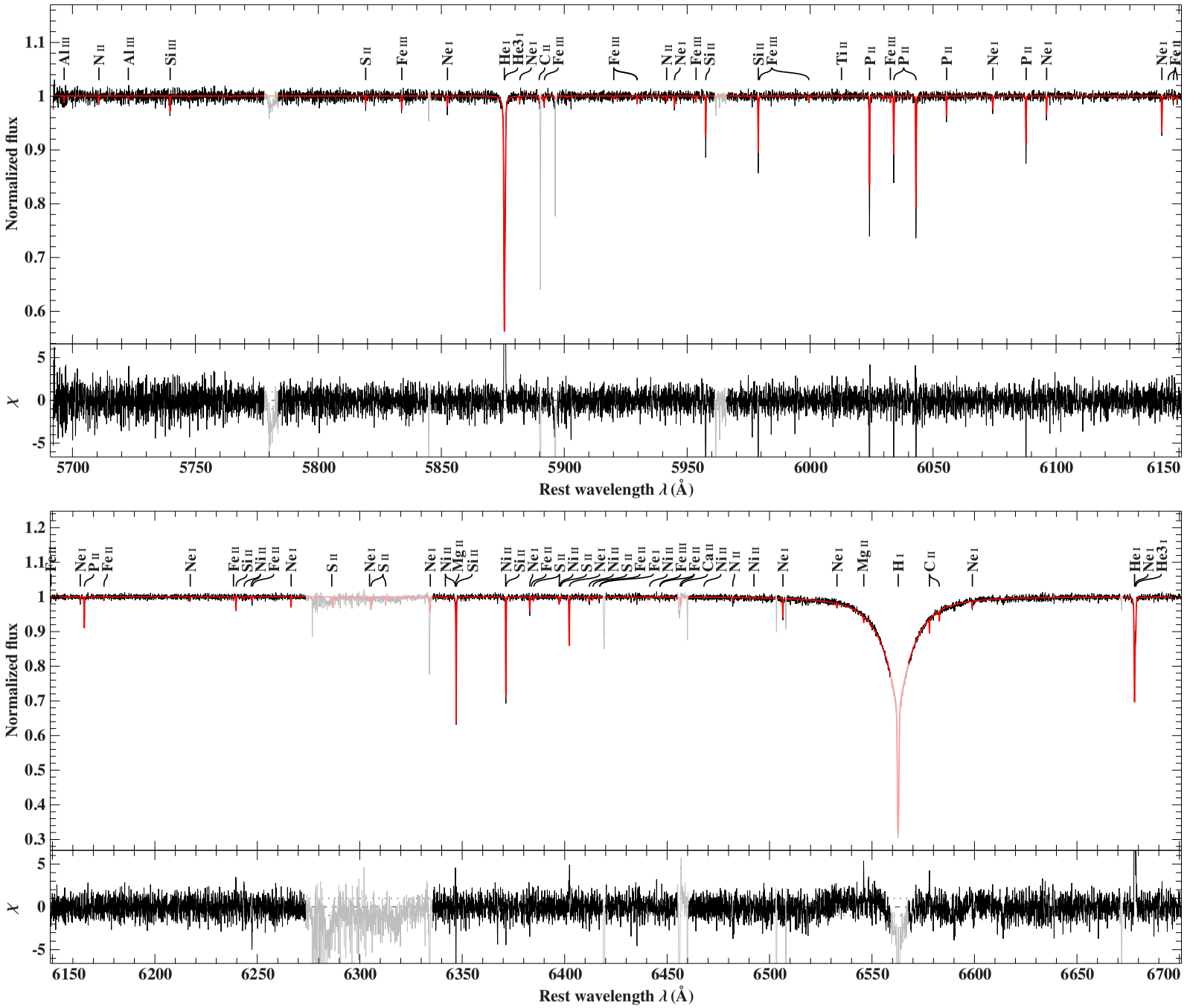

Figure 21: Spectral fit of HD 110942, part 3

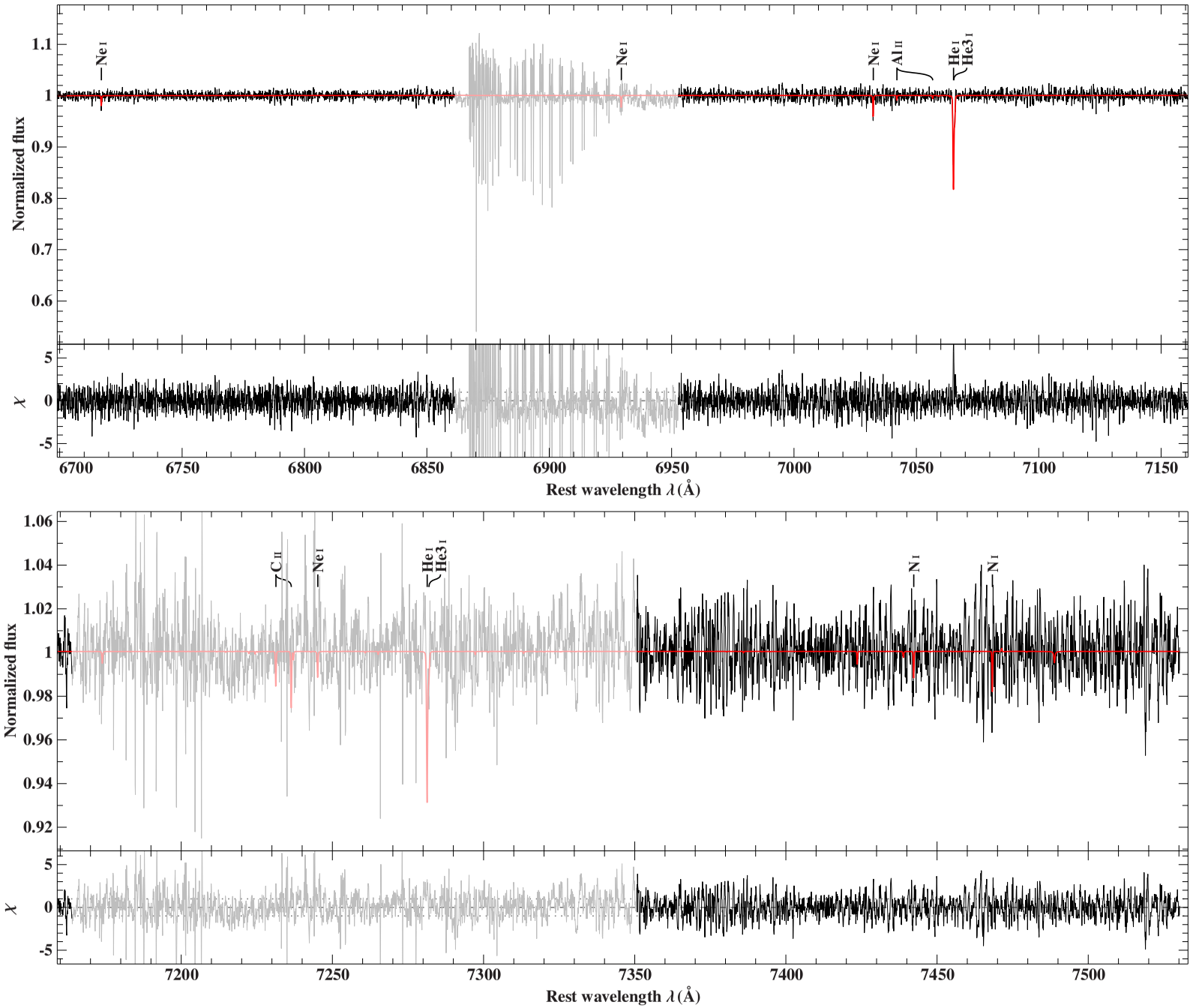

Figure 22: Spectral fit of HD 110942, part 4

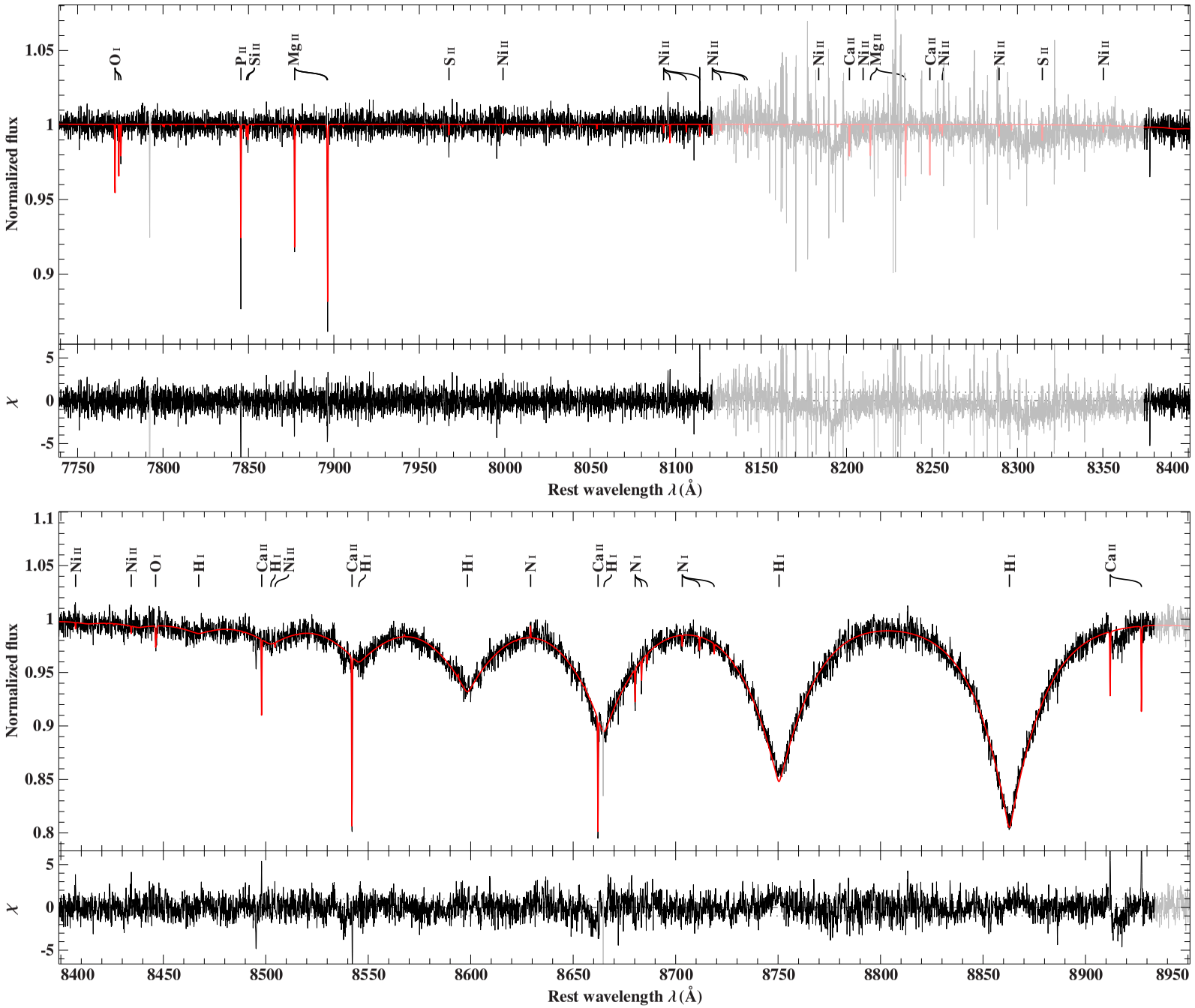

Figure 23: Spectral fit of HD 110942, part 5

Appendix A7

Additional plots

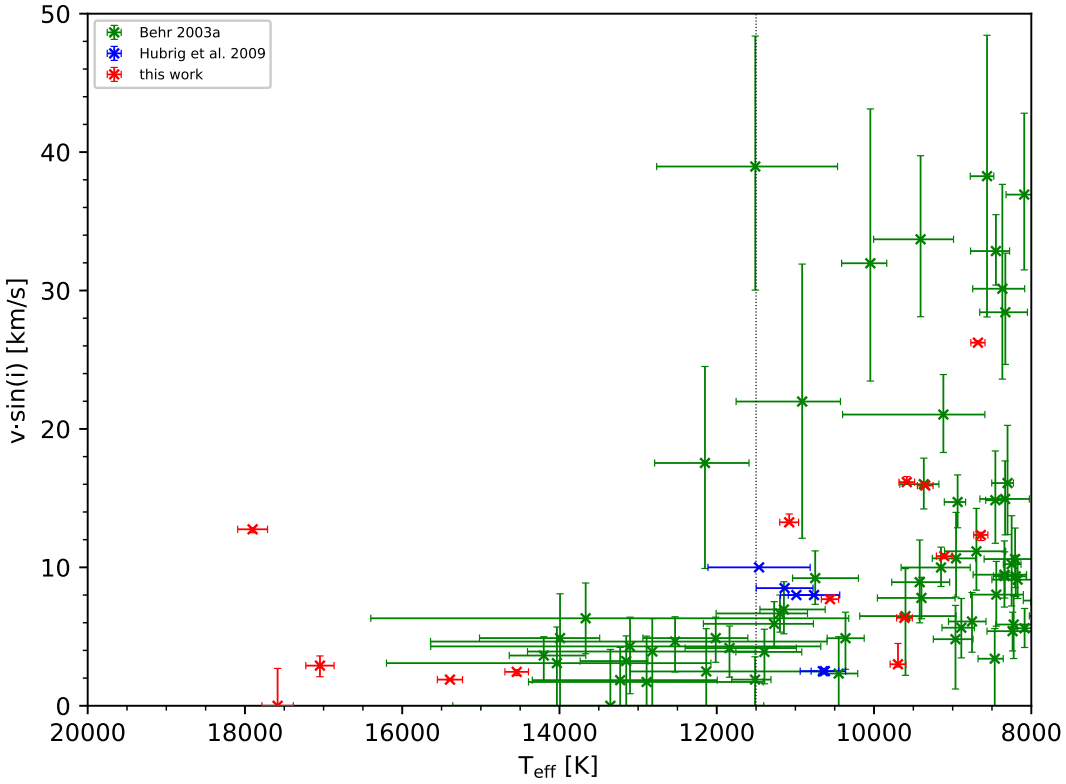

Figure 24: Projected rotational velocity vs. effective temperature compared to GC-stars (Behr 2003a; Hubrig et al. 2009)

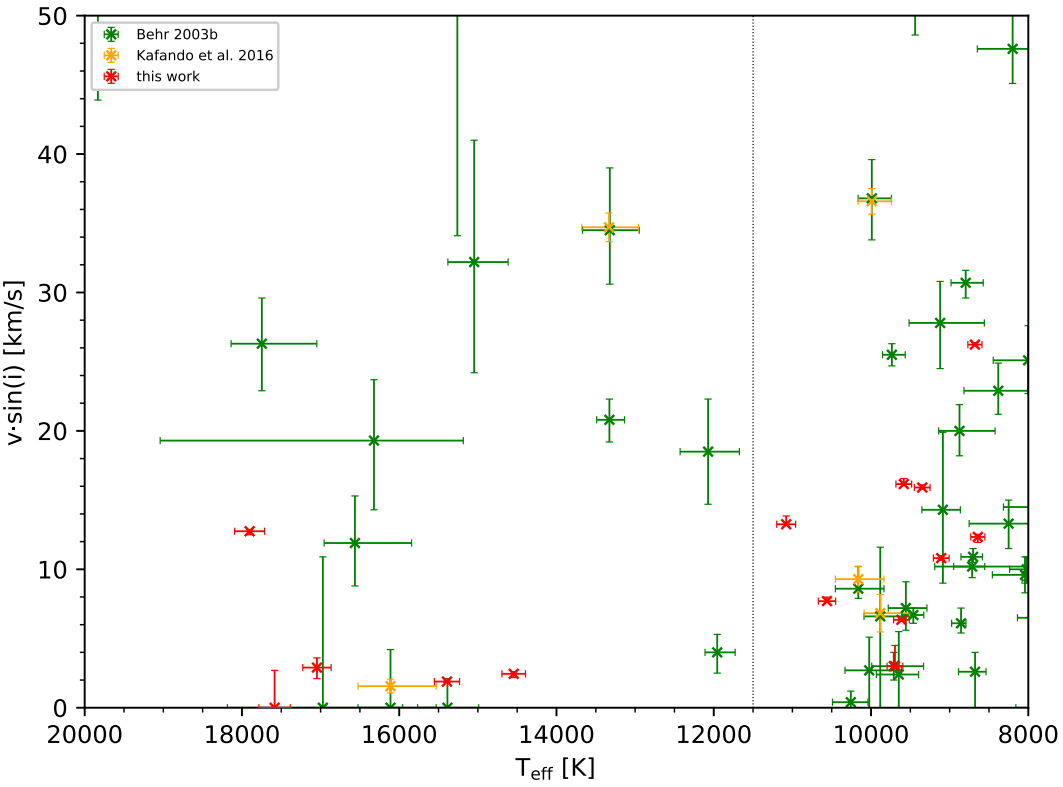

Figure 25: Projected rotational velocity vs. effective temperature compared to GC-stars (Behr 2003b; Kafando et al. 2016)

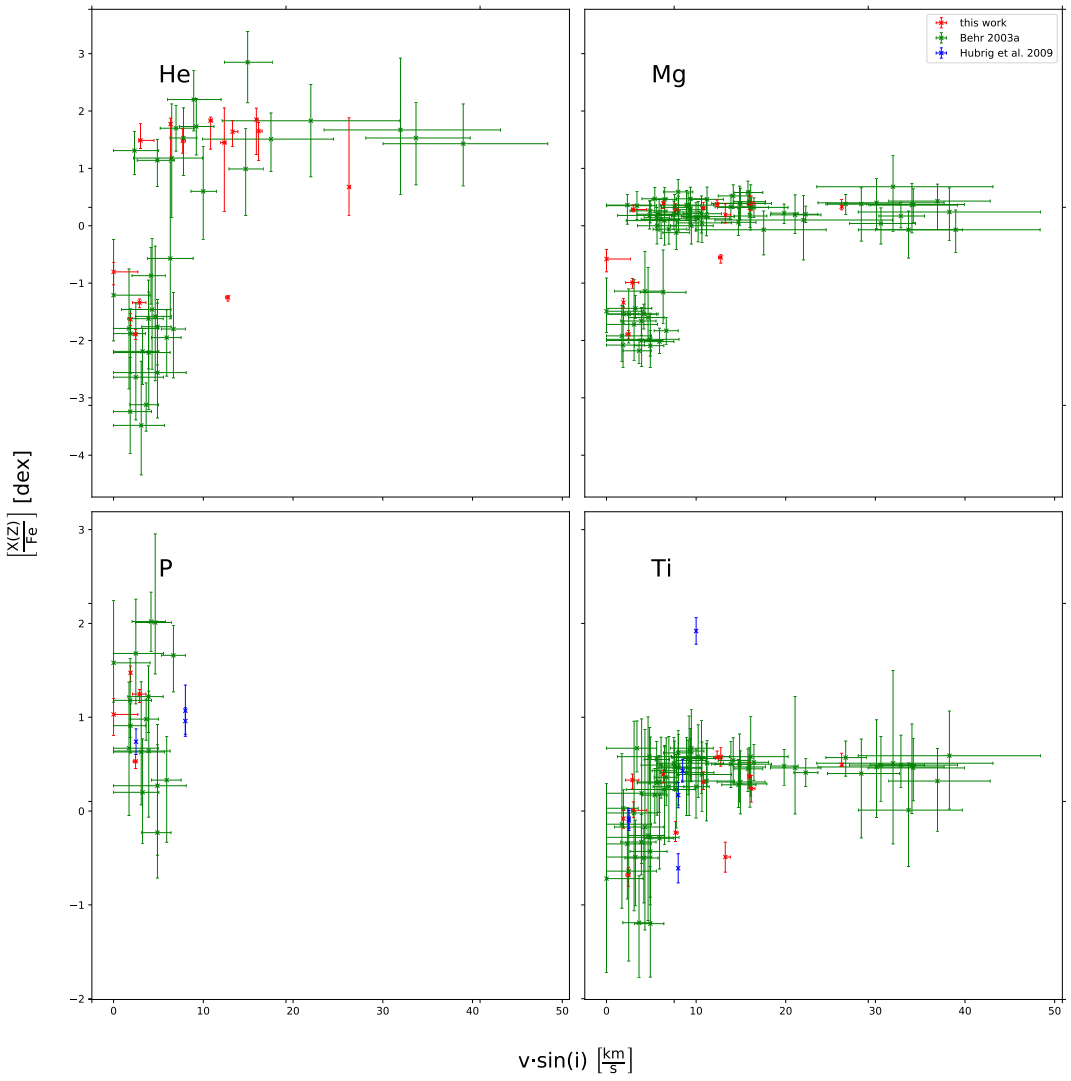

Figure 26: Correlation between projected rotational velocity and abundance compared to GC-stars (Behr 2003a; Hubrig et al. 2009)

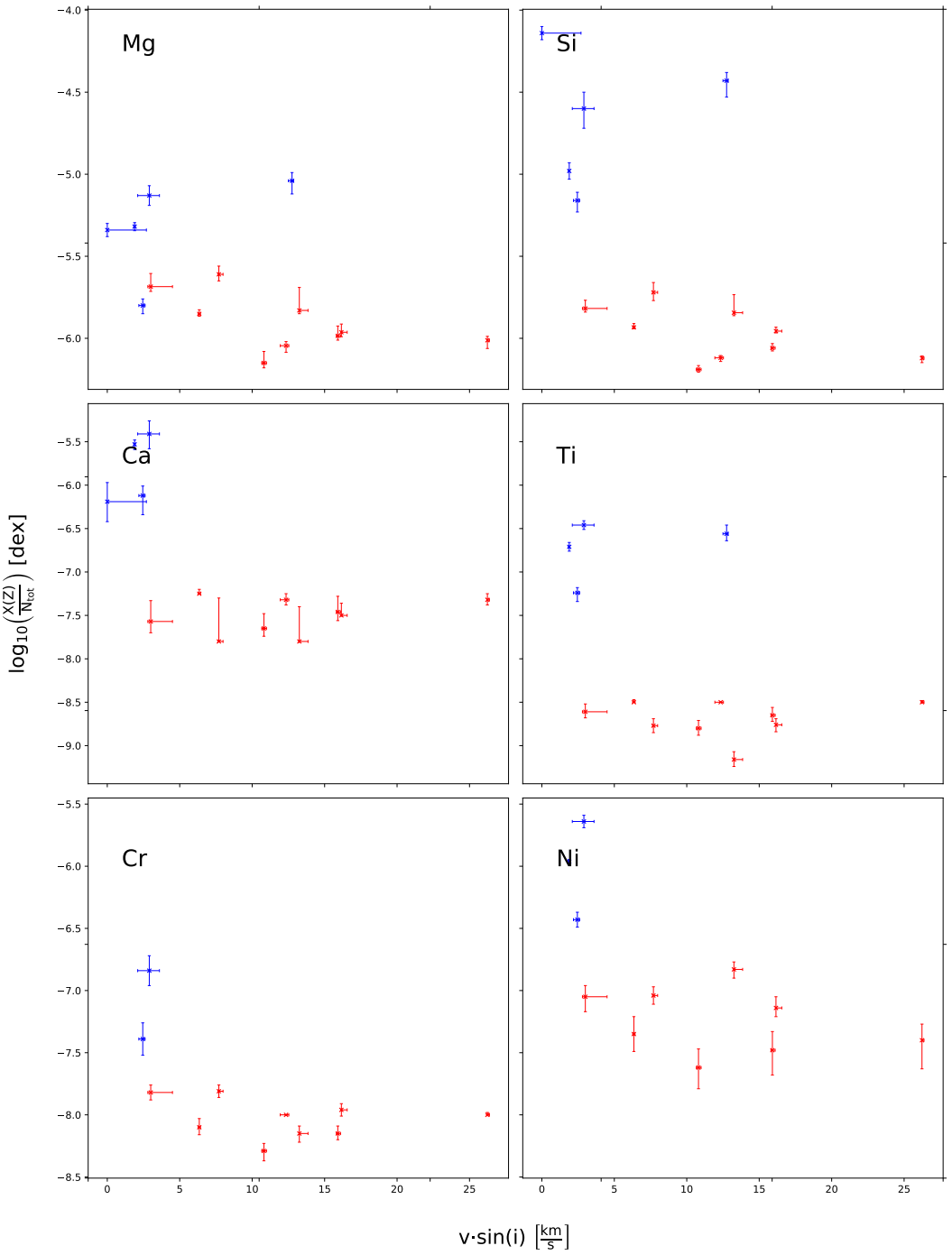

Figure 27: Correlation between projected rotational velocity and abundance

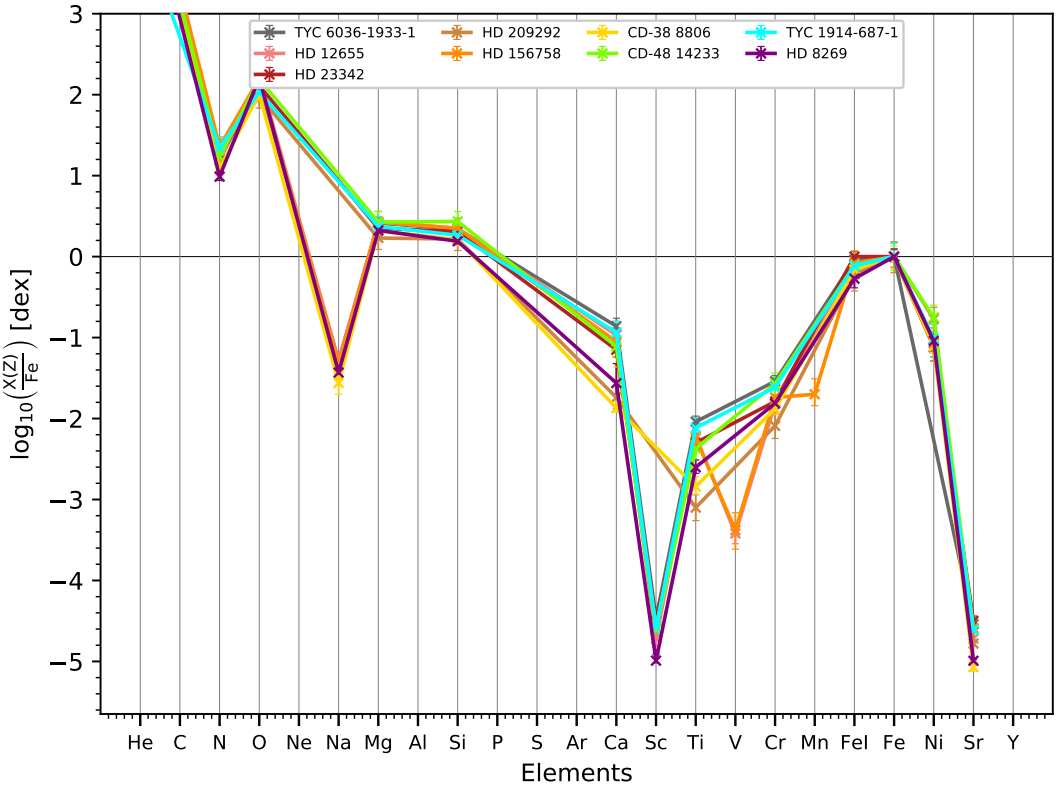

Figure 28: Element-to-iron ratios for A-BHBs

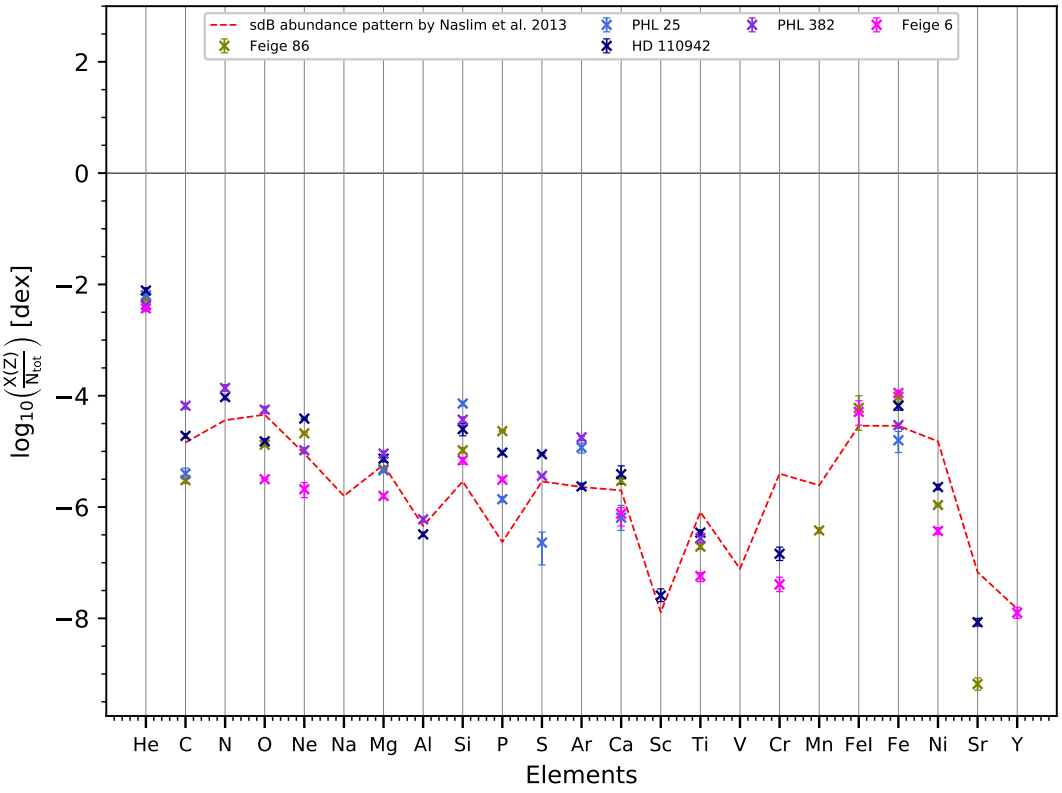

Figure 29: Abundance pattern of B-BHBs

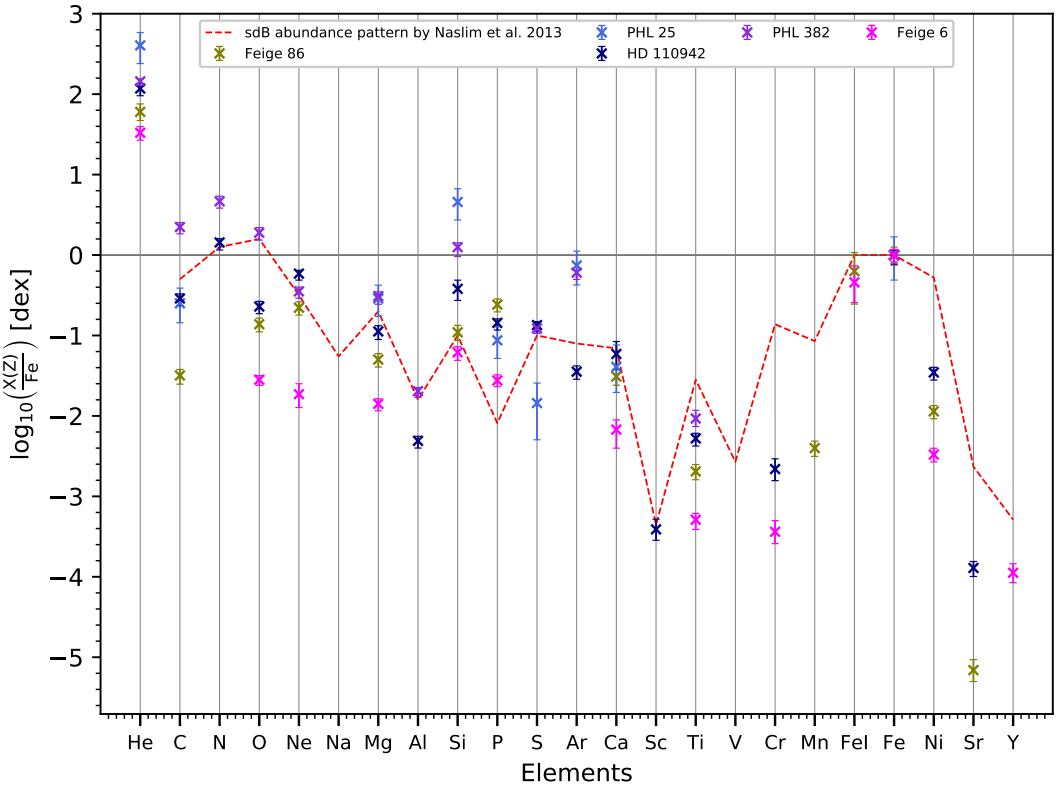

Figure 30: Element-to-iron ratios for B-BHBs

Erklärung:

Hiermit bestätige ich, dass ich diese Arbeit selbstständig und nur unter Verwendung der angegebenen Hilfsmittel angefertigt habe.

Ort, Datum	Steven Hämmerich